8-21-2014

Thermophysical Properties of Perovskite Ferroelectrics and their Applications in Energy Harvesting

Richard Perez Moyet
University of Connecticut - Storrs, richard.perez_moyet@uconn.edu

Thermophysical Properties of Perovskite Ferroelectrics and their Applications in Energy Harvesting

Richard Pérez Moyet, Ph.D.

University of Connecticut, 2014

The thermophysical properties of perovskite ferroelectrics were investigated by high accuracy determinations of the heat capacity (C_P), thermal expansion ($\Delta L/L$) and thermal conductivity (k). The ferroelectric phenomena that govern thermophysical behavior near phase transitions in these materials were investigated and compared, and were analyzed using the thermodynamic Ginzburg-Landau phenomenological theory.

For the normal ferroelectric $BaTiO_3$, the temperature dependence of the coefficients of the Landau free energy were experimentally determined from heat capacity and dielectric data and these data were used to validate predictions of low crystallographic anisotropy of polarization at inter-ferroelectric transitions. For the solid solution $Pb(Zr_{1-x}Ti_x)O_3$ (PZT) the tricritical points along the Curie line were experimentally determined and compared with predictions of a low order approximation of the Landau free energy taking into account the composition dependence of the expansion terms. Lastly, for the relaxor ferroelectric solid solutions $Pb(Zn_{1/3}Nb_{2/3})O_3$-$PbTiO_3$ (PZN-PT) and $Pb(Mg_{1/3}Nb_{2/3})O_3$-$PbTiO_3$ (PMN-PT), a method was developed to separate the reversible and root mean square (RMS) contributions to the polarization from heat capacity data.

The relaxor ferroelectric materials exhibited thermophysical properties near phase transitions that differed qualitatively from their normal ferroelectric counterparts. The anomalous behavior for the relaxor materials was associated with built-in disorder arising from random

orientation of the polarization. Quantitative comparisons of phase transition energetics for the different ferroelectric perovskites studied revealed very low transition enthalpies for the relaxor materials that were linked to very weak crystallographic anisotropy of polarization and an associated easy rotation of polarization at the inter-ferroelectric transitions between phases at the morphotropic boundary.

The easy reorientation of polarization near inter-ferroelectric transitions observed for relaxor ferroelectrics was exploited in mechanical energy harvesting. A phase transforming piezocrystal energy harvesting device was designed, built and tested under cycling stress loading conditions as functions of electrical resistive load and drive frequency. The efficiency, power and energy density were determined and found to be six times greater than those in the linear single phase region. The performance characteristics of phase transforming and resonant mode energy harvesting devices are compared and contrasted.

Thermophysical Properties of Perovskite Ferroelectrics and their Applications in Energy Harvesting

Richard Pérez Moyet

B.S., University of Puerto Rico – Mayagüez Campus, 2005

M.S., University of Puerto Rico – Mayagüez Campus, 2008

A Dissertation

Submitted in Partial Fulfillment of the

Requirements for the Degree of

Doctor of Philosophy

at the

University of Connecticut

2014

APPROVAL PAGE

Doctor of Philosophy Dissertation

Thermophysical Properties of Perovskite Ferroelectrics and their Applications in Energy Harvesting

Presented by

Richard Pérez Moyet, B.S., M.S.

Major Advisor _____

Dr. George A. Rossetti, Jr.

Associate Advisor _____

Dr. S. Pamir Alpay

Associate Advisor _____

Dr. Ramamurthy Ramprasad

University of Connecticut

2014

To my wife (Yenny) and my Daughter (Luna)

ACKNOWLEDGEMENTS

Dr. George A. Rossetti Jr.
Thanks for all the time you have devoted on my professional and personal development. It has been a lifetime learning experience and a completely new perspective of the real world. You believed in me from the very beginning and brought to me the confidence, strength and envision to walk, with firm steps, through my new upcoming future. I will never forget those wisdom words like "you have to own it" or "have to see the big picture" and your teaching philosophy of "the two big inverted triangles" in which in the first one, together with you, the scientific ideas sprout out and start to flow forming a wide range of research possibilities that are then deepened in the second big triangle by the student alone, which must be able, at that time, to converge them in his/her own innovative ideas. I will miss those times. Thanks a lot.

PhD Advisors
Thanks to Dr. S. Pamir Alpay and to Dr. Ramamurthy (Rampi) Ramprasad for your collaboration and mentoring. Thanks to Dr. Rainer J. Hebert and to Dr. Harris L. Marcus for your participation during my PhD thesis defense. Thanks to Dr. Ahmed H. Amin and Dr. Peter Finkel for your collaboration and mentoring during my summer NREIP internships at NUWC and at NRL.

Funding Agencies during my PhD
Department of Homeland Security (DHS) and Office of Naval Research (ONR)

Office partners especially Ching Chang Chung (BB), Adam A Heitmann and Jialang Zhang
Thanks guys, in many different ways, especially during my time at the office and at the laboratory for making easier to me to go through the life of a PhD student. Those times that I may spent looking for scientific or technical problem solutions were in many times significantly reduced by that unconditional help you guys gave me at some point of my career. Thanks for being part of it.

My Mom (Clara Moyet de León) and My Dad (Billy Pérez Figueroa)
Thanks for all the help, love and motivation you both always gave me. You both gave me the best gift a son can get and is the realization of becoming an essential human being to the society. A human being of values, principles, humility, respect, loveliness, craftiness, confident and prepared to build my own family and duplicate with them your legacy. I will never forget the complete devotion and passion of body, soul and heart that both of you put on my family, especially with Luna, during the final steps of my PhD. Love you so much and thanks a lot!

My brother (Bill Pérez Moyet) and sisters (Clarivette Pérez Moyet and Charon Pérez Moyet) and all my big family
Thanks for always be there to receive my calls looking for some air of motivation and to hear some words that make me feel near you guys, been relief to know everything was ok. This period has showed me how much I love you all and how strongly I would desire to be closer. But, wherever I will be, you all will be always in my heart. Thanks a lot.

My family-in-law especially my mother-in-Law (Genoveva (Geno) Quintero)
Thanks to take me as part of your lives and as another son of this beautiful family. I would like to express my most sincere and humble thanks to my mother-in-law for his unconditional, tireless and loving help with my present family Yenny and Luna. Your presence during the final steps of my PhD was essential and necessary. You helped me a lot and helped me to see the light that took me to the completeness of my PhD. I will never forget it. Thanks a lot.

My beautiful wife (Yenny P. Cardona Quintero)
Thanks for always be there and be with me, especially during this unmemorable five years of our PhD. We started this together and finished it together. All those moments of big emotions of happiness, sadness, laughing, crying, nerves, celebrations etc, we have lived them together. Coming together to this exciting adventure has been one of our best decisions. These five years have just passed and I still remember our first day in Connecticut astonished of that beautiful fall season. It is amazing to know that during this period of our lives, our beautiful Luna joined us. She is our new headlight. I want to express you my most sincere love and admiration. You always knew that I was able to do this and you taught me to believe in the "I can". But I can't imagine this without you. Love you so much.

My friends
Thanks to my friends, especially Diego, Eddy, Francisco, Tamara and Tatiana for camouflage with happiness, adventures and family-like environment the time during my PhD. You guys filled the space of my family and became my new brothers and sisters. I always was waiting for the weekends to come and for those special days that made my PhD an easy bearable path. Thanks for your friendship.

To God
Thanks God for the inspiration, imagination, creativity, motivation, dedication, productive time and all those littler factors that you allow me to have during my PhD. Thanks for allowing me to offer you those moments when I have to say thank you. Thank you for letting me get my PhD. Love you.

Table of Contents

LIST OF FIGURES

CHAPTER 1

CHAPTER 2

CHAPTER 4

CHAPTER 5

CHAPTER 6

CHAPTER 7

CHAPTER 8

CHAPTER 9

CHAPTER 10

CHAPTER 11

CHAPTER 12

LIST OF TABLES

CHAPTER 1

CHAPTER 2

CHAPTER 5

CHAPTER 6

CHAPTER 7

CHAPTER 8

CHAPTER 9

CHAPTER 10

CHAPTER 11

CHAPTER 12

APPENDIX A

LIST OF TERMS AND VARIABLES

Phases	
PE	Paraelectric
FE	Ferroelectric
PE-FE	Paraelectric to Ferroelectric
RE	Relaxor
F_T	Ferroelectric Tetragonal
F_R	Ferroelectric Rhombohedral
F_O	Ferroelectric Orthorhombic
Critical Temperatures	
T_{PF}	PE-FE Transition Temperature
$T_{FT\text{-}FO}$	F_T to F_O Transition Temperature
$T_{FO\text{-}FR}$	F_O to F_R Transition Temperature
T*	
T_C	Curie Temperature
Variables	
$C_P(T)$	Heat Capacity
$\Delta C_P(T)$	Excess Heat Capacity
H^{XS}	Excess Enthalpy
S^{XS}	Excess Entropy
G^{XS}	Excess Free energy
ΔG_L	Landau free energy (excess)
$e(T) = \Delta L/L_0$	Thermal Expansion
$D(T)$	Thermal Diffusivity
α	Thermal expansion coefficient
ϵ	Dielectric susceptibility
P_S	Spontaneous Electric Polarization
P_{rev}	Reversible contribution to the polarization
P_{RMS}	Relaxor contribution to the polarization
H_{RMS}	Relaxor contribution to the enthalpy
Ferroelectric Materials	
ABO_3	Perovskite Crystal Structure
BT	$BaTiO_3$: Barium Titanate
PT	$PbTiO_3$: Lead Titanate
PZ	$PbZrO_3$: Lead Zirconate
PZN	$Pb(Zn_{1/3}Nb_{2/3})O_3$
PMN	$Pb(Mg_{1/3}Nb_{2/3})O_3$
PIN	$Pb(In_{1/2}Nb_{1/2})O_3$
PZT	*(1-x)* $PbZrO_3$*-x*$PbTiO_3$ *(or* $PbZr_{(1-x)}Ti_xO_3$*)*

PZN-PT (or PZNT)	$(1-x)Pb(Zn_{1/3}Nb_{2/3})O_3$-$xPbTiO_3$
PMN-PT (or PMNT)	$(1-x)Pb(Mg_{1/3}Nb_{2/3})O_3$-$xPbTiO_3$
PIN-PMN-PT	$(1-x-y)Pb(In_{1/2}Nb_{1/2})O_3$-$yPb(Mg_{1/3}Nb_{2/3})O_3$-$xPbTiO_3$

Thermal Measurement Systems

DSC	Differential Scanning Calorimetry
LFA	Laser Flash Analyzer
TMA	Thermal Measurement Analyzer
P-E loop	Polarization vs Electric Field Hysteresis loop

Landau Coefficients

A_o	Isotropic temperature dependence quadratic coefficient
B_o	Isotropic temperature independence quartic coefficient
C_o	Isotropic temperature independence sextic coefficient
B_1	Anisotropic temperature independence quartic coefficient
B_2	Anisotropic temperature dependence quartic coefficient
C_1	Anisotropic temperature independence sextic coefficient
C_2	Anisotropic temperature dependence sextic coefficient
C_3	Anisotropic temperature independence sextic coefficient

CHAPTER 1

INTRODUCTION

Energy harvesting is a process in which energy captured from an external source is used to provide power in a device. These external sources may be human body motion, air flow, vibration, temperature gradient, pressure variations, ambient light indoor, etc. Among them, mechanical energy sources are very attractive for the energy harvesting process[1], since they generate the highest amount of power when compared with other energy sources, as shown in Figure 1.1.

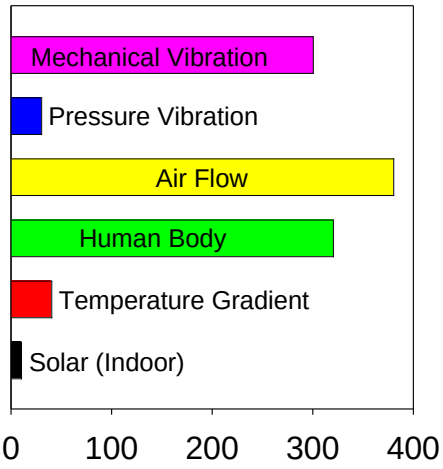

Figure 1. 1 Comparison of various potential power sources.[1]

A typical piezoelectric energy harvesting device uses mechanical vibration energy obtained from a piezoelectric material operating in resonance mode to generate electrical energy, which is then stored and used to provide power.[2] The resonance mode of vibration in a piezoelectric material is typically derived from cantilever configurations, shown in Figure 1.2. In these configurations, an input mechanical energy, induced by the kinetic energy of a proof mass at the tip of the cantilever, produces resonance vibrations generating electrical energy as a result of the direct piezoelectric effect. The resonance bandwidth of a cantilever should be wide enough to accommodate the uncertain variance of ambient vibration.[3] It can be increased from nonlinear resonator energy harvesters by hardening or softening the resonance bandwidth of the beam

structure. Ultra wide bandwidth (>20%) from the center frequency has been demonstrated in a monolithic MEMS-based nonlinear resonant piezoelectric micro energy harvester which generated a power of more than 22 μW with a power density of (1100.0 μW/mm^3).[3]

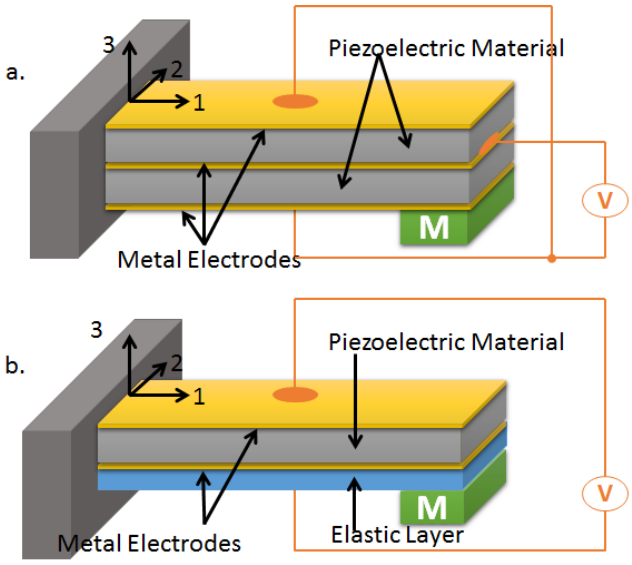

Figure 1. 2 Basic configuration for a piezoelectric energy harvesting. (a) Bimorph configuration and (b) Unimorph configuration.[1]

The most widely exploited piezoelectric materials currently in use for these applications are the ferroelectric morphotropic phase boundary (MPB) solid solutions $PbZrO_3$-$PbTiO_3$ (PZT). In resonance-mode piezoelectric energy harvesting the key material parameters are the electromechanical coupling factors (k_{ij}) and the piezoelectric coefficient (d_{ij}).[4] Extremely high dielectric properties, $d_{33} >= 1500\ pC/N$ and $k_{33} \geq 0.92$ have been demonstrated in solid solution relaxor ferroelectric single crystal materials $Pb(Zn_{1/3}Nb_{2/3})O_3$-$PbTiO_3$ (PZN-PT) and $Pb(Mg_{1/3}Nb_{2/3})O_3$-$PbTiO_3$ (PMN-PT) around the MPB compared with PZT polycrystalline ceramic materials.[5–7] However, the bandwidth of resonance mechanical vibration, stress levels, and the Curie temperature, all of which can lead to depolarization, are some of the limitations for a resonance-mode piezoelectric energy harvesting application.[2] The piezoelectric material in a linear or nonlinear resonance mode energy harvesting process operate well below phase transitions in order to avoid large swings in load impedance, high electric field drive, and hysteresis losses.[8] Its thermal stability during operation is limited by its Curie temperature (T_C). Similarly, the poled state must

be maintained during operation, which limits the stress levels and temperatures that can lead to depolarization.

A new method for electromechanical energy conversion was demonstrated based on the ferroelectric to ferroelectric (inter-ferroelectric) phase transition in the engineering domain MPB solid solution d_{32}-mode $xPb(In_{1/2}Nb_{1/2})O_3$-$(1-x-y)Pb(Mg_{1/3}Nb_{2/3})O_3$-$yPbTiO_3$ (PIN-PMN-PT) relaxor ferroelectric single crystal.[9] The inter-ferroelectric phase transition that was considered was an induced ferroelectric orthorhombic (F_O) phase transition from the ferroelectric rhombohedral (F_R) phase due to an engineering domain single crystal ferroelectric material cut along (110) and electrically poled along [110]. Compared with the pseudobinary MPB solid solutions ferroelectrics, this ternary relaxor ferroelectric single crystal composition has a higher T_C and coercive field (E_C).[10–12] Essentially, as shown in Figure 1.3a, this energy conversion method was based on two isopolarization processes, where mechanical compression and an applied reverse electric field drive the single crystal close to an induced F_O phase transition, and two isobaric processes, where the change in polarization and strain are allowed by bleeding charge from the electrodes during the induced F_R-F_O phase transition.[13] The reversible F_O-F_R phase transition on decompression could be due to compensation charges on charge domain walls that pull the polarization to the F_R state.[10] The energy density per cycle obtained from the inter-ferroelectric phase transformation is more than an order of magnitude larger than the energy density from cantilever configurations. Also, the power density from this method is comparable to the cantilever mode which operates at much higher frequencies.

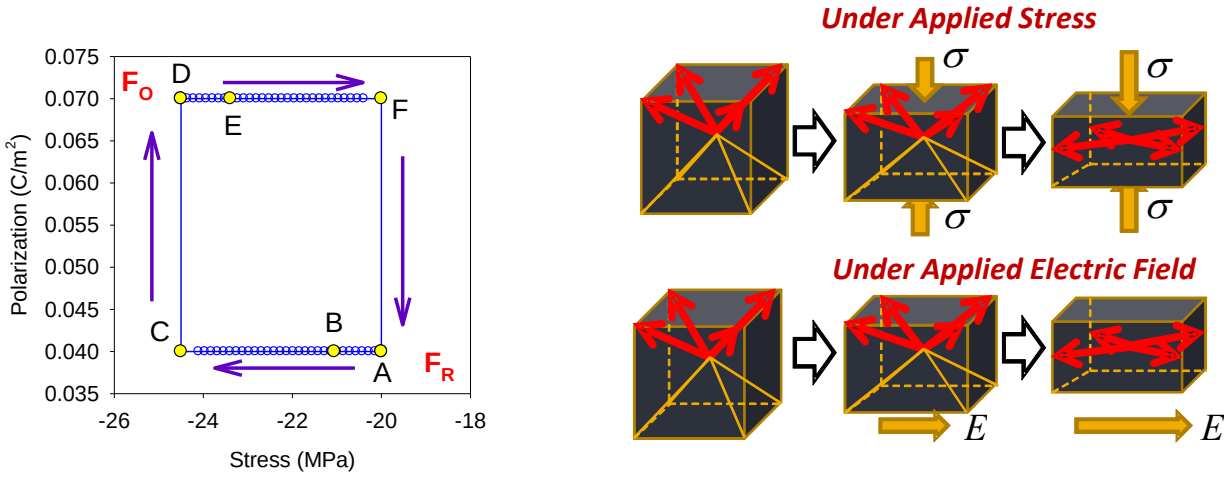

(a) (b)

Figure 1. 3 (a) Polarization rotation from ferroelectric rhombohedral to ferroelectric orthorhombic as a function of a uniaxial stress and applied electric field. (b) Energy harvesting cycle from an stress-induced inter-ferroelectric phase transition in an engineering domain single crystal.[14,15]

The polarization orientation and rotation of the [111] engineering domain single crystal is represented in Figure 1.3b, where a simultaneous electrical bias along [110] and a uniaxial stress along [001] cause an easy polarization rotation from a poled [111] to [110] direction for composition at the MPB. Then, in this method the electric energy output was obtained from a reversible cycling process through the F_R-F_O phase transition triggered by simultaneous application of an electric bias and a reversible mechanical stress driven at 1 Hz, out of the resonance frequency of PIN-PMN-PT single crystal. The polarization rotation through the inter-ferroelectric phase transition may occur subject to a change of temperature, composition, applied stress and/or applied electric field.[9] A stress-electric field-temperature diagram has been demonstrated for the ferroelectric single crystal materials PMN-32PT[16] and PIN-PMN-PT[9].

Figure 1.4 shows the stress-electric field-temperature diagram for the F_R-F_O inter-ferroelectric transition in PIN-PMN-PT single crystal. It is to be noted that the width of the hysteresis region around F_R-F_O phase transition appears to remain constant, indicating that the energy barrier between the F_R and F_O phases is nearly independent of whether the transformation is thermally, electrically, or mechanically driven within this range of loadings.[9] This diagram shows that the inter-ferroelectric phase transition can be triggered by the simultaneous application of external fields.

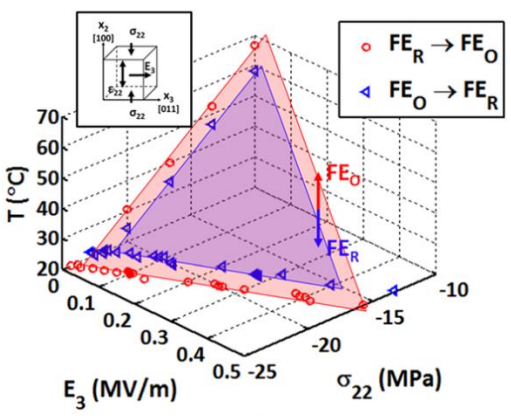

Figure 1. 4 Temperature, stress and electric field diagram for [011] oriented PIN-PMN-PT showing the phase transition hysteresis.[15]

Ferroelectric crystals that display this kind of phase transformation around the F_R side of the MPB include PZT, PZN-xPT, PMN-xPT and ternary solid solutions PIN-PMN-PT. The MPB separates the ferroelectric tetragonal into ferroelectric rhombohedral phases and intercepts the Curie line. In resonance mode energy harvesting the F_T-phase with composition close to the MPB is commonly used instead of the F_R-phase due to high strain levels. In this case, due to thermal stability, high Curie temperatures are desired. In the inter-ferroelectric phase transition-mode electromechanical energy conversion process, or phase transition energy harvesting, the inter-ferroelectric phase transition is then used. The electrical energy output used is directly associated with the energy at the inter-ferroelectric phase transition. During an inter-ferroelectric transition, both modulus and direction of polarization change. In the particular case of a d_{32}-mode PIN-PMN-PT engineering domain single crystal, it was as a result of an induced-electric field in the [011] direction[10] due to an inter-ferroelectric polarization rotation from the poled [111] ferroelectric

rhombohedral (F_R) phase across the MPB.[8] This method benefits from the output electric energy that results from an easy polarization rotation across the MPB[17–22] and their engineering polarization orientation.[23]

In this work, a comprehensive study of the phase transition energetics in the perovskite-type structure in normal ferroelectric materials $BaTiO_3$ (BT), $PbTiO_3$ (PT) and solid solution PZT, as well as the relaxor ferroelectric solid solution PMN-PT, PZN-PT and PMN-PIN-PT are shown. Each chapter of this research work individually investigates each of these ferroelectric materials and their associated phase transition phenomena. Table 1.1 summarizes the ferroelectric phenomena investigated in the different ferroelectric materials.

Table 1. 1 Perovskite-Type Ferroelectric Materials and their phase transition and ferroelectric phenomena individually investigated in this research work.

Line Compound	**Solid Solution Morphotropic Phase Boundary**			
Single	Binary			Ternary
Normal Ferroelectric		Relaxor Ferroelectrics		
$BaTiO_3$ (Single Crystal)	PZT (Ceramic)	PZN-PT (Single Crystal)	PMN-PT (Single Crystal)	PIN-PMN-PT (Single Crystal)
• Pretransitional (fluctuation phenomena) • Determination of the Landau Coefficients by heat capacity. • Crystallographic anisotropic of the polarization at the inter-ferroelectrics phase transitions	• Tricritical behavior in solid solution system around the MPB.	• Reversible and relaxor contribution to the polarization. • Depoling switching events in poled crystals	• Reversible and relaxor contribution to the polarization. • Energetic Field-Induced phase transition and their contribution to the polarization.	• Domain engineering single crystals. • Stress induce phase transition • Energy Harvesting. • Fatigue process

The phase transition energetics and thermal transport properties in these ferroelectric materials are also compared based on similar experimental conditions. It was mainly based on heat capacity measurements from DSC signal. In each of the ferroelectric materials investigated, phenomena associated with the ferroelectric behavior of the phase transition energetic are also investigated in more detail. As for example, in BT there is controversy related to the order and temperature dependence of the coefficients in the Landau polynomial which is very important information for modeling purposes. In PZT there is a big discussion about the location of the tricritical point and the coexistence of low symmetry ferroelectric phases around the MPB. Contributions to the reversible and root mean square (RMS) polarization in relaxor ferroelectric materials are also demonstrated. Also, the thermal and transport signature of the induce-phase transition and observed thermal poling events in relaxor materials is revealed. Finally, for application purposes, the energy conversion comparison between typical resonance mode energy harvesting and an inter-ferroelectric phase transformation is demonstrated.

REFERENCES

1. Priya, S. Advances in Energy Harvesting Using Low Profile Piezoelectric Transducers. *J. Electroceramics* **19,** 165–182 (2007).

2. Kim, S.-G., Priya, S. & Kanno, I. Piezoelectric MEMS for energy harvesting. *MRS Bull.* **37,** 1039–1050 (2012).

3. Hajati, A. & Kim, S.-G. Ultra-wide bandwidth piezoelectric energy harvesting. *Appl. Phys. Lett.* **99,** 083105 (2011).

4. Kim, H., Priya, S., Stephanou, H. & Uchino, K. Consideration of impedance matching techniques for efficient piezoelectric energy harvesting. *IEEE Trans. Ultrason. Ferroelectr. Freq. Control* **54,** 1851–9 (2007).

5. Kuwata, J., Uchino, K. & Nomura, S. Dielectric and Piezoelectric Properties of 0.91Pb(Zn1/3Nb2/3)O3-0.09PbTiO9 Single Crystals. *Jpn. J. Appl. Phys.* **21,** 1298–1302 (1982).

6. Kuwata, J., Uchino, K. & Nomura, S. Phase transitions in the Pb(Zn1/3Nb2/3)O3-PbTiO3 System. *Ferroelectrics* **37,** 579–82 (1981).

7. Park, S.-E. & Shrout, T. R. Ultrahigh strain and piezoelectric behavior in relaxor based ferroelectric single crystals. *J. Appl. Phys.* **82,** 1804 (1997).

8. Finkel, P., Amin, A., Lofland, S., Yao, J. & Viehland, D. Phase switching at low field and large sustainable strain output in domain engineered ferroic crystals. *Phys. Status Solidi* **209,** 2108–2113 (2012).

9. Dong, W. D., Finkel, P., Amin, A. & Lynch, C. S. Stress dependence of thermally driven pyroelectric charge release during FER-FEO phase transformations in [011] cut relaxor ferroelectric crystals. *Appl. Phys. Lett.* **100,** 262909 (2012).

10. Amin, A., McLaughlin, E., Robinson, H. & Ewart, L. Mechanical and thermal transitions in morphotropic PZN-pT and PMN-PT single crystals and their implication for sound projectors. *IEEE Trans. Ultrason. Ferroelectr. Freq. Control* **54,** 1090–5 (2007).

11. Zhang, S., Luo, J., Hackenberger, W. & Shrout, T. R. Characterization of Pb(In(12)Nb(12))O(3)-Pb(Mg(13)Nb(23))O(3)-PbTiO(3) ferroelectric crystal with enhanced phase transition temperatures. *J. Appl. Phys.* **104,** 64106 (2008).

12. Zhang, S. *et al.* Electromechanical characterization of [Formula: see text] crystals as a function of crystallographic orientation and temperature. *J. Appl. Phys.* **105,** 104506 (2009).

13. Dong, W. D., Finkel, P., Amin, A. & Lynch, C. S. Giant electro-mechanical energy conversion in [011] cut ferroelectric single crystals. *Appl. Phys. Lett.* **100,** 042903 (2012).

14. Dong, W. D., Finkel, P., Amin, A. & Lynch, C. S. Giant electro-mechanical energy conversion in [011] cut ferroelectric single crystals. *Appl. Phys. Lett.* **100,** 042903 (2012).

15. Dong, W. D., Finkel, P., Amin, A. & Lynch, C. S. Stress dependence of thermally driven pyroelectric charge release during FER-FEO phase transformations in [011] cut relaxor ferroelectric crystals. *Appl. Phys. Lett.* **100,** 262909 (2012).

16. McLaughlin, E. A., Liu, T. & Lynch, C. S. Relaxor ferroelectric PMN-32%PT crystals under stress and electric field loading: I-32 mode measurements. *Acta Mater.* **52,** 3849–3857 (2004).

17. Heitmann, A. A. & Rossetti, G. A. Polar Anisotropy and Inter-Ferroelectric Transitions in Barium Titanate and its Solid Solutions. *Integr. Ferroelectr.* **126,** 155–165 (2011).

18. Heitmann, A. A. & Rossetti, G. A. Thermodynamics of polar anisotropy in morphotropic ferroelectric solid solutions. *Philos. Mag.* **90,** 71–87 (2010).

19. Ishibashi, Y. Theory of the Morphotropic Phase Boundary. *Ferroelectrics* **267,** 191–199 (2002).

20. Khachaturyan, a. G. Ferroelectric solid solutions with morphotropic boundary: Rotational instability of polarization, metastable coexistence of phases and nanodomain adaptive states. *Philos. Mag.* **90,** 37–60 (2010).

21. Rossetti, G. A., Khachaturyan, A. G., Akcay, G. & Ni, Y. Ferroelectric solid solutions with morphotropic boundaries: Vanishing polarization anisotropy, adaptive, polar glass, and two-phase states. *J. Appl. Phys.* **103,** 114113 (2008).

22. Rossetti, G. A. & Navrotsky, A. Calorimetric Investigation of Tricritical Behavior in Tetragonal Pb (Zr x Ti 1 ⁄ x) O 3. *J. Solid State Chem.* **144,** 188–194 (1999).

23. Fu, H. & Cohen, R. Polarization rotation mechanism for ultrahigh electromechanical response in single-crystal piezoelectrics. *Nature* **403,** 281–3 (2000).

CHAPTER 2

BACKGROUND

2.1 Phase transition energetics in perovskite-type crystal structures.

The phase transition energetics in ferroelectric (FE) materials has recently become a major topic of research due to the discovery of high dielectric susceptibility, high piezoelectric coefficient and electromechanical coupling factor found around the morphotropic phase boundary (MPB) of solid solution ferroelectric materials.[1] The typical MPB solid solution ferroelectric materials under investigation for potential technological applications include the binaries normal ferroelectric $PbZrO_3 - PbTiO_3$ (PZT)[2], relaxor ferroelectrics $Pb(Zn_{1/3}Nb_{2/3})O_3 - PbTiO_3$ (PZN-PT)[3] and $Pb(Mg_{1/3}Nb_{2/3})O_3 - PbTiO_3$ (PMN-PT)[4], as well as the ternary solid solution relaxor ferroelectric $Pb(In_{1/2}Nb_{1/2})O_3 - Pb(Mg_{1/3}Nb_{2/3})O_3 - PbTiO_3$ (PIN-PMN-PT)[5]. PZT ceramics are widely used in electro-active devices and in other technological applications due to the piezoelectric, elastic, and dielectric maxima properties that occur near the MPB.[2] The relaxor materials possess very large dielectric constants, attractive for capacitors; exceptional large electrostrictive coefficients, important for sonar, sensor, actuators and micropositioners; and large electro-optic constants, useful for information storage, shutters and optical modulators.[6]

Two characteristics between these solid solution ferroelectric materials are the contribution of the normal ferroelectric $PbTiO_3$ (PT), which displays a ferroelectric tetragonal (F_T) phase below its Curie temperature (T_C), and a parent paraelectric (PE) cubic phase with a perovskite-type crystal structure (ABO_3). In general, ferroelectric perovskite-type structures have a high symmetry m3m point group cubic PE-phase, a non-polar centrosymmetric phase, at high temperature and transitions to a ferroelectric state with a lower symmetry, where some of the atoms are slightly

displaced when below T_C. A prototype for a ferroelectric material with an oxide perovskite-type structure is $BaTiO_3$ (BT). In BT the ferroelectric phase transitions from the cubic PE to the F_T–phase (with point group 4m) at T_C = 120 °C (PE–F_T), to the ferroelectric orthorhombic (F_O) phase (with point group mm) at 5 °C (F_T-F_O) and to the ferroelectric rhombohedral (F_R) phase (with point group 3m) at -90 °C (F_O-F_R).[7] These sequence of phase transitions may be understood from distortions of the parent cubic PE-phase, as shown in Figure 2.1.[7]

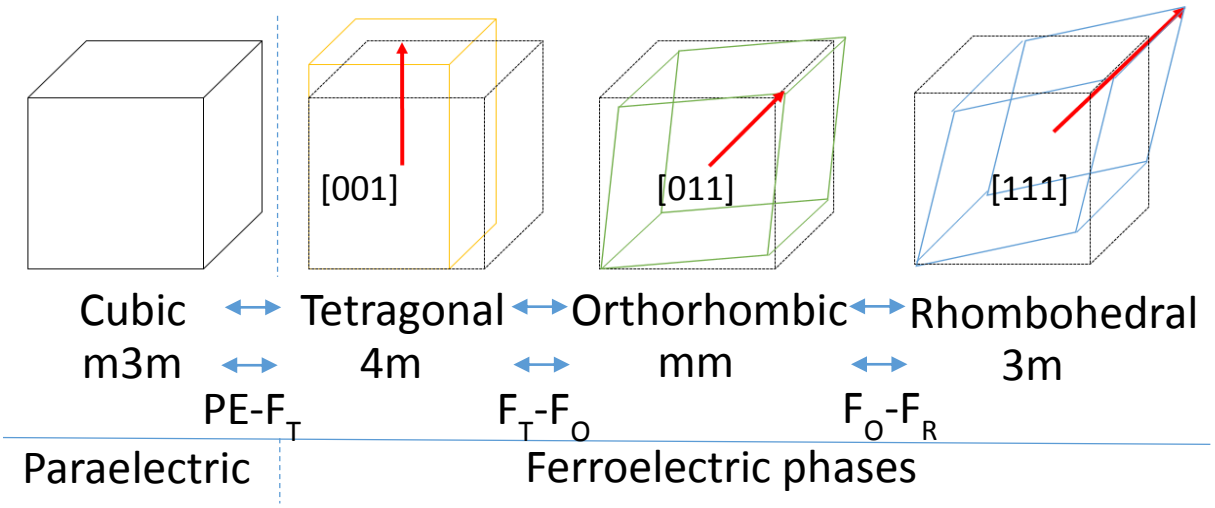

Figure 2. 1 Phase transition in $BaTiO_3$, a conventional ferroelectric material.[7]

Similarly, phase transitions in solid solution ferroelectric materials may be classified as PE-FE (PE-F_α or PE-F_β) or FE-FE (inter-ferroelectric: F_α-F_β) both occurring in the temperature-composition phase diagram. The subscripts α and β represent crystallographic ferroelectric phases, typically ferroelectric rhombohedral (F_R) and ferroelectric tetragonal (F_T). In the PE-FE phase transition a spontaneous polarization suddenly occur as a step function (first-order phase transition) or as a continuous function (second-order phase transition) of the applied field. The relative displacements of atoms during the structural phase transformation in each of the unit cells of the crystal result in the appearance of a pyroelectric effect.[8] In the case of an inter-ferroelectric

phase transition the spontaneous polarization (P_S) may rotates between the different ferroelectric phases. Some examples of inter-ferroelectric transitions may include: F_T-F_R across the MPB, F_{R3m}-F_{R3c} in the PZT phase diagram and induced-field inter-ferroelectric phase transitions typically found in relaxor ferroelectrics.

2.2 Ginzburg-Landau thermodynamic theory: 1st- and 2nd-order phase transition, tricritical point and inter-ferroelectric phase transition.

The Ginzburg-Landau thermodynamic theory (known as the Landau theory) is an excellent theoretical tool for the study of phase transition energetics. Due to symmetrical considerations of the prototype paraelectric cubic phase in ferroelectric oxides with perovskite-type structures, it is convenient to follow the Devonshire approach to the Landau theory[9,10]. In general this thermodynamic theory is based on the thermodynamic potential of a system in the vicinity of a phase transition.[11] It is the most common approach to study the phenomenology of any symmetry-breaking structural phase transition and it is independent of any atomic model.[9] The Landau theory considers the case in which a high symmetry phase undergoes a transition to a phase of lower symmetry. The symmetry group *m3m* admits seven proper lower-symmetry ferroelectric phases: one tetragonal (*4mm*), one rhombohedral (*3m*), one orthorhombic (*mm2*), three monoclinic (*m*), and one triclinic (*1*).[12]

The simplest conceivable theoretical situation of the Landau theory utilizes with the assumption that the polarization is directed along one of the crystallographic axes only (i.e. that spontaneous polarization occurs along this direction and the applied field is restricted to this direction also), that all stresses are zero and that the non-polar phase is centrosymmetric.[13] Under these conditions and at zero applied electric field, the low order approximation to the Landau free

energy, as a function of the polarization (**P**), temperature (T) and composition (c), can be written as:

$$G(\boldsymbol{P};T,c) - G_0(T,c) = \Delta G_L(\boldsymbol{P};T,c) = \frac{1}{2}A(T)P^2 + \frac{1}{4}B_0P^2 + \frac{1}{6}C_0P^2 \quad (2.1)$$

where the polarization is the order parameter, *A(T)* is the quadratic coefficient and B_0 and C_0 are the high order Landau coefficients. The order parameter is taken to be exactly zero in the high symmetry phase while assuming a non-zero value in the low symmetry phases. The order parameter is mostly independent of the details of the transition mechanism.[14] *A(T)* is assumed to vary linearly with temperature in the form $A(T) = \frac{1}{2}A_0(T - T_C)$, related to the Curie-Weiss law in such a way that T_C is the transition temperature (for a 2nd-order transition) or the lower metastability limit of the upper phase (for a 1st-order transition).[15] B_0 determines the order of the PE-FE phase transition and C_0 considers the stability of the Landau thermodynamic potential. Due to the symmetrical considerations of the prototype paraelectric cubic phase in the perovskite crystal structure (centrosymmetric non-polar phase), all odd-rank tensor coefficients in the Landau free energy are taken to be zero.[13]

2.2.1 First-order phase transition

Following the simple notation of Equation 2.1, $B_0 < 0$ for a 1st-order phase transition in which a spontaneous jump in the polarization at T_C will occur. As shown in Figure 2.2a, for a PE-F_T phase transition as an example, a 1st-order phase transition undergoes through different critical temperatures that range from $T_C < T < T^*$. Above T^* the stable centrosymmetric phase with a single energy minimum is observed. At $T = T^*$ the ferroelectric phase can exists as a metastable state. Below T_C the polar tetragonal phase, with two equal energy minima, is then obtained. The FE- and PE-phases are in equilibrium at the PE-FE phase transition temperature (T_{PF}) where the

free energy of both phases are equal and zero. A further decrease in temperature leads to a stable ferroelectric phase at T_C.

2.2.2 Second-order phase transition

The conditions for a 2nd-order phase transition from the *m3m* symmetry group is given by $B_0 > 0$. For a 2nd-order transition the structure undergoes a continuous phase transformation as the temperature approaches T_C, as shown in Figure 2.2b. In the 2nd-order phase transition, the metastable minimum at T^* and the coexisting phases at T_{PF} are not observed.

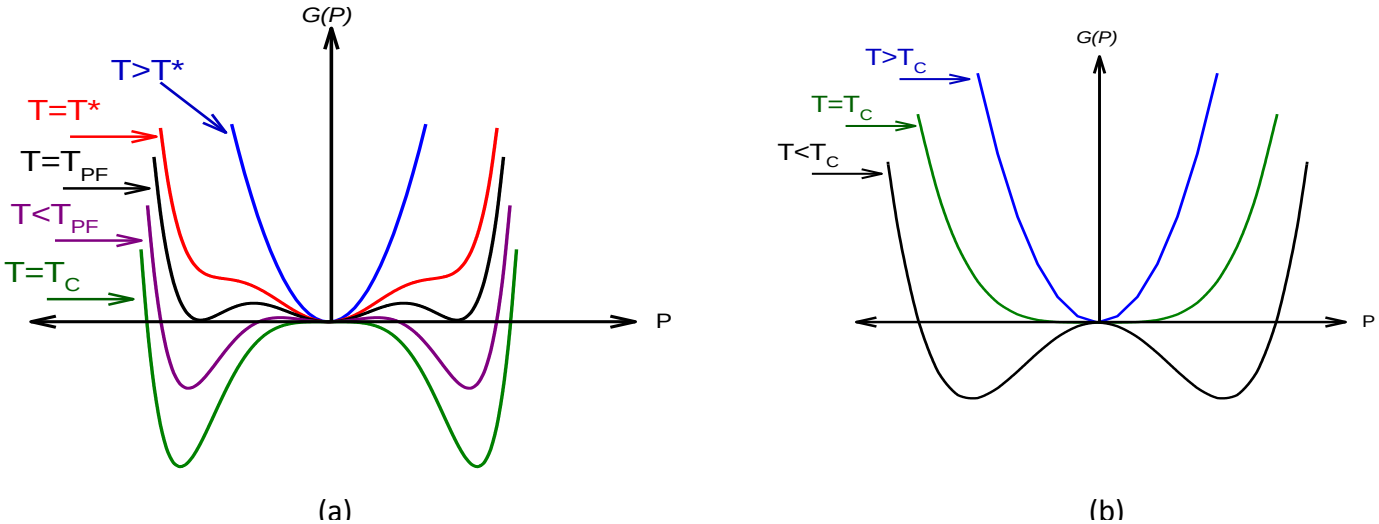

Figure 2. 2 The quality temperature dependence of the free energy as a function of the polarization order parameter at different critical temperatures between the two stable phases (in this case from PE-F_T) near a (a) first order phase transition and (b) second order phase transition.

2.2.3 Tricritical point

The quartic order Landau coefficient change sign when transits from a 1st- to 2nd-order phase transition as a function of composition or pressure. At $B_0 = 0$, the line of the 1st- to 2nd-order phase transition meet defining a tricritical point. The tricritical point occurs under the condition that the quartic coefficient changes sign and occurs in crystals which are placed under hydrostatic pressures or when the chemical composition of the crystal is altered by ion substitution (i.e. the quartic coefficient changes sign as a function of composition or pressure). A particular example of a phase transition through a tricritical point is that found around the Curie line in PZT.[16,17]

2.2.4 Inter-ferroelectric phase transition

In a ferroelectric to ferroelectric (inter-ferroelectric) phase transition a change in both the modulus and direction of the polarization occur, as shown in Figure 2.3. During the inter-ferroelectric transition, the polarization is reoriented from one crystallographic orientation to another. Inter-ferroelectric phase transitions may occur subject to a change of temperature, composition, applied stress and/or applied electric field. As an example, during an inter-ferroelectric transition from F_T to F_R the spontaneous polarization is reoriented from the pseudocubic <001> directions to the <111> directions. The inter-ferroelectric phase transition will be driven by the high order anisotropic Landau coefficients and may or may not be temperature dependent, depending on the convergence of the Landau polynomial.[18,19]

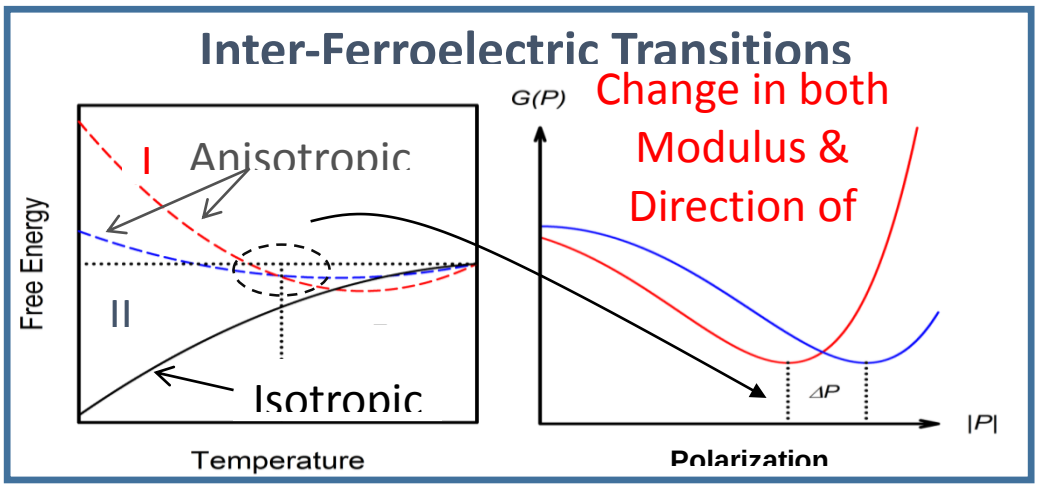

Figure 2. 3 Anisotropic dependence of an inter-ferroelectric phase transition.

2.3 Phase transition ferroelectric phenomena

In a big picture, ferroelectrics may be classified by their phase transition phenomenon. The different phenomena may reveal a more clear understanding of recent topics of controversy in this field. Some of these phenomena are listed below and will be will be the focus of subsequent chapters:

2.3.1 High crystallographic anisotropy of polarization in normal ferroelectrics such as $BaTiO_3$ and $PbTiO_3$.

A normal ferroelectric displays a long range order interaction of the dipoles moments.[6] The phase transitions in normal ferroelectrics have been attributed to a high crystallographic anisotropy of polarization dependence and may be understood from the different orientation of the spontaneous polarization relative to the cubic perovskite-type structure.[2] Transparent FEs exhibit strong optical anisotropy across T_C.[6] Some ferroelectric properties that defined a normal ferroelectric material, shown in Table 2.1, are (i.) a high remanent polarization (P_R) due to the

manifestation of the cooperative nature of the FE phenomenon, (ii.) the vanishing of the temperature dependence of polarization at T_C which may occur as a 1st- or 2nd-order phase transition, (iii.) the peak in dielectric susceptibility, or dielectric constant (ϵ'), represented as a sharp transition peak in single crystals and (iv.) that they obey the Curie-Weiss Law $\left(\epsilon' = C/(T - T_C)\right)$ in the high temperature paraelectric phase.

2.3.2 Order-disorder phase transition due to random dipolar distribution found in relaxor ferroelectrics.[20]

The phase transition in relaxor ferroelectrics had been attributed to a diffuse phase transition due to the order-disorder of the dynamic slowing down of strong frequency dispersion of random dipolar fluctuations within the polar nanodomain. Relaxor-like behavior occurs due to local structural disorder in the arrangement of cations in one or more crystallographic sites of the structure.[21,22] Also, it can be observed as dipolar nanoregions forming dipolar glass-like state due to inhomogeneous distribution of the polarization which suppress, long range FE order.[6] The signature of a relaxor state, shown in Table 2.1, is a broad frequency-dependent peak in the real part of the temperature-dependent dielectric susceptibility.[6] The peak at the phase transition temperature, which shifts to high temperature with increasing frequency, is defined as a dynamic freezing or glass-like transition temperature (T_m). The remanent polarization is very small due to the manifestation of the random orientation of domains with the presence of some degree of cooperative freezing of nanodomain orientations. The temperature dependence of the polarization decreases smoothly through the dynamic transition temperature T_m and retains finite values to rather high temperatures due to the fact that polar nanodomains persist to well above T_m. A strong

deviation from the Curie-Weiss law is observed in relaxor ferroelectrics. Additionally, there is no structural phase transition and no optical anisotropy across T_m.

Table 2. 1 Contrast between the properties of a normal and relaxor ferroelectrics.[6]

	Normal Ferroelectric	***Relaxor Ferroelectric***
Polarization vs Electric Field	• Macro-size Ferroelectric domains	• Nano-size polar domains
Polarization Behavior	• No polar domains above T_c	• Nano-size polar domain persist well above T_m
Dielectric Constant	• Sharp narrow transitions • Fallows Curie-Weiss law • Now frequency dependence	• Very broad peaks • Strong deviation from Curie-Weiss law • Strong frequency dispersion
Structural Transformation	• First and second-order phase transition with macroscopic symmetry change at T_C	• No structural phase transition across T_m. • Critical slowing down of dipolar motion below Tm
Optical	• Strong optical anisotropy across T_C	• No optical anisotropy below T_m

2.3.3 Normal-to-relaxor ferroelectric phases transformation "crossover" in solid solution ferroelectric materials.[6]

A phase transformation or "crossover" from normal to relaxor ferroelectric behavior may occur after the nanodomains first nucleate as decreasing temperature, the so call Burns temperature (T_B) or depolarization temperature (T_d).[23] If the nanodomains grow as to become microdomains, then the sample will undergo a static, cooperative FE phase transition at T_C. In the other hand, if they do not grow large enough as to percolate then sample will exhibit a dynamic slowing down of their polarization distribution at $T \ll T_m$ leading to an isotropic relaxor state with random orientation of the polar domains.[6] The relaxor to normal ferroelectric crossover may also occurs as a function of hydrostatic pressure.[24] In this case, the energy barrier to dipole reorientation decrease as a function of the applied pressure, due to an easy orientation of smaller domains

(nanodomains), giving rise to a relaxor responses. Also, this crossover may occurs as a field-induced nano-to-macrodomain transition. The presence of a biasing field in a relaxor state aligns the nanodomains and increases them leading to an onset of long-range ferroelectric order.[6]

2.3.4 Induced-field (or also crystallographically designed) phase transformation in ferroelectric engineering domain single crystals.[25–27]

A domain-engineered crystal is one which has been poled by the application of a sufficiently high field along one of the possible polar axes of the crystal other than the zero field polar axis, creating a set of domains in which the polarizations are oriented such that their angles to the poling direction are minimized.[28] Taking in consideration the zero field polar axis of the F_R (3m), F_O (mm2) and F_T (4mm) the three possible sets of poling directions are $\langle 111\rangle_C$, $\langle 101\rangle_C$ and $\langle 001\rangle_C$, respectively relative to the perovskite crystal structure denote as "C". Table 2.2 shows six possible domain-engineered structures formed by cutting and poling a perovskite crystal along those directions different from its zero field polar axis.[25]

Table 2. 2 Engineered and monodomain states in perovskite single crystals (C denotes reference to the pseudocubic unit cell).[25]

Crystal class	Polar direction	Poling direction	Polar directions for the resultant set of equivalent domain variants	Domain-engineered structure
Rhombohedral 3m	$\langle 111\rangle_C$	$[111]_C$	$[111]_C$	1R
		$[101]_C$	$[111]_C$, $[1\bar{1}1]_C$	2R
		$[001]_C$	$[111]_C$, $[11\bar{1}]_C$, $[1\bar{1}1]_C$, $[1\bar{1}\bar{1}]_C$	4R
Orthorhombic mm2	$\langle 101\rangle_C$	$[111]_C$	$[101]_C$, $[011]_C$, $[110]_C$	3O
		$[101]_C$	$[101]_C$	1O
		$[001]_C$	$[101]_C$, $[011]_C$, $[\bar{1}01]_C$, $[0\bar{1}1]_C$	4O
Tetragonal 4mm	$\langle 001\rangle_C$	$[111]_C$	$[001]_C$, $[010]_C$, $[100]_C$	3T
		$[101]_C$	$[001]_C$, $[100]_C$	2T
		$[001]_C$	$[001]_C$	1T

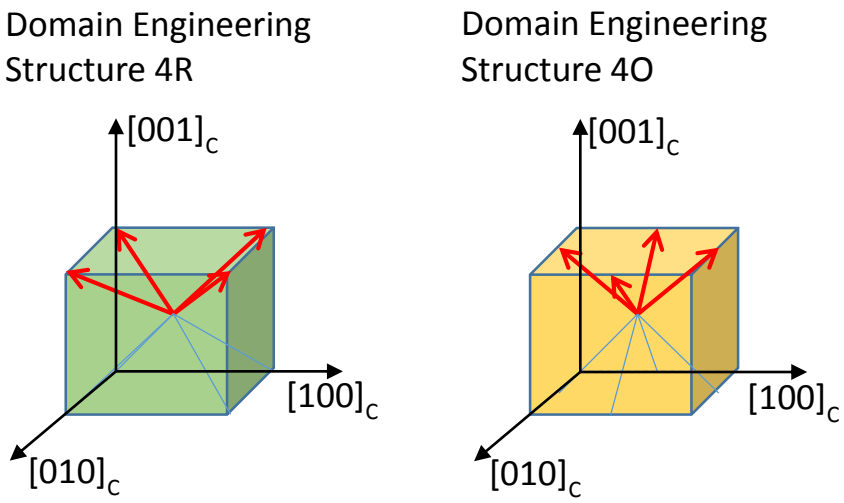

Figure 2. 4 Domain engineering structure 4R and 4O corresponding to the [001] poled rhombohedral and orthorhombic crystals.[29]

Three monodomain structures 1R, 1C and 1T are also produced by poling a perovskite-type crystal along its zero field polar axis. For the purpose of illustration, Figure 2.4 shows the domain engineering structure of the rhombohedral and orthorhombic crystals poled along [001]. Giant piezoelectric properties, d_{33}>2000 pC/N and k_{33} > 92%, had been found in engineered domain ⟨001⟩ relaxor based piezoelectric single crystals such as PMN-PT and PZN-PT with rhombohedral structure near the MPB due to a rotation of ⟨111⟩ polarization toward the ⟨001⟩ direction.[1] In this case the engineered domain structure is represented by 4R, shown in Figure 2.4. A minimum energy polarization rotation path from the ⟨111⟩ to ⟨001⟩ direction was theoretically revealed, which shows large piezoelectric coefficients due to a large induced strain level from a small applied electric field.[30] This giant piezoelectric properties had been shown to be inversely proportional to the mechanical quality factor, Q, which is the inverse of mechanical loss of crystals.[31] This combination of high piezoelectric properties and low Q make single crystals excellent for non-resonant actuators and high frequency medical ultrasound transducers.[1,32–34] Zhang et al demonstrated that 2R in PMN-30PT has a d_{33} = 1050 pC/N and Q_{33} = 600 which lies

between 1R (d_{33} = 90 pC/N, Q_{33} = 1130) and 4R (d_{33} = 1500 pC/N and Q_{33} = 120) engineered domain structures. This was a result of the overall reduced domain wall mobility due to high stability of 2R compared to 1R and 4R under applied cycling electric field[35], may be as a consequence of 109^o domain parallel to (110) phase, and its proximity to the MPB.[31] Interesting work by Wen Dong demonstrated the giant electro-mechanical energy conversion PIN-PMN-PT relaxor single crystal ferroelectric material domain engineering cut and poled along <110> plane but uniaxially pressed along [001] direction.[26,36]

2.3.5 Inter-ferroelectric phase transition as a consequence of an easy polarization rotation through low symmetry ferroelectric phases,[30] or due to a low crystallographic anisotropy of the polarization.[16,18,37–40]

There is also the phenomena of inter-ferroelectric phase transitions, especially through the MPB. It had been shown, in the proximity of the MPB, that the morphology of polar nanodomain (PND) colonies naturally assemble along {110} and {010} in order to minimize the elastic energy.[41] It was predicted from the conformal miniaturization theory applied to ferroelectric systems with miniaturized domains close to the MPB, such as PZN-PT and PMN-PT crystals. In this case, abnormal small domain wall energy γ or extreme domain wall density were considered.[42] This theory assume a nanodomain mixture of F_R- and F_T-phases based on the adaptive state theory of martensites.[43] The polarization rotation also results from the domain wall energy within adjacent domains. Since the domain size $\lambda_o \propto \sqrt{\gamma}$[13], the domain structures near the MPB line is reduced to nanoscale dimensions. This, in particular, had been demonstrated in the PZT solid solution system as a function of composition, but it also easily applied to other MPB systems. In PZT, it was demonstrated that the crystallographic anisotropy of the polarization vanishes at the MPB or that

the free energy becomes degenerated with respect to the direction of the polarization vector, as shown in Figure 2.5.[16] It was as a consequence of the anisotropy contribution to the quartic term Landau coefficient that tend to zero as the wall energy within the domain tend to zero as proposed by Rossetti et al.[16] The material remains polarized but it is in fact a ferroelectric glass with no preferential polarization direction.[16]

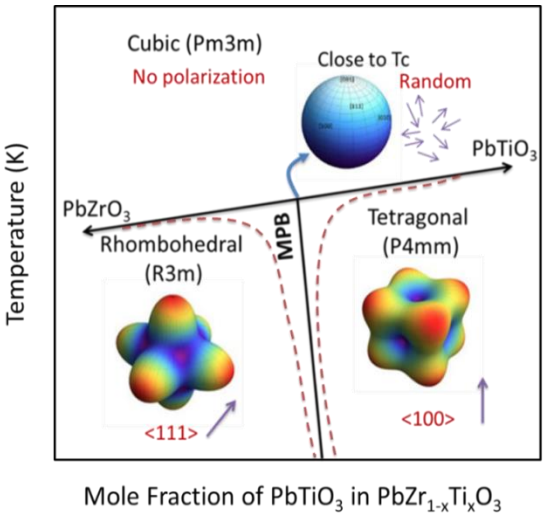

Figure 2. 5 Free energy surface degeneration due to the vanishing of the crystallographic anisotropy of polarization as approaching the MPB in the PZT. As propose by Rossetti et al.[16]

2.4 Thermal and transport properties in ferroelectric materials

The phase transition energetics of perovskite-type structure ferroelectrics had been extensively investigated around their electric properties such as the dielectric susceptibility, pyroelectricity and the P-E hysteresis loop. However, far less attention has been given to their thermal properties such as heat capacity ($C_P(T)$), thermal conductivity ($k(T)$), thermal diffusivity ($D(T)$) and thermal expansion ($\Delta L(T)$) or thermal strain ($\varepsilon(T)$).

There is an intimate relation of the thermal conductivity and the ferroelectricity, resulting from a singular behavior of the thermal vibration of ions shifted to cause the ferroelectric behavior.[48] In the case of the relaxor materials some polar nanoregions (PNRs) had been demonstrated where its onset of polarization, or the T_d, had been determined from acoustic emission measurements,[49] thermal expansion,[21] heat capacity and thermal conductivity,[45,46] birefringence,[50] neutron scattering[51] etc. Thermal properties in relaxor ferroelectric materials had been demonstrated to be comparable with that of glasses or amorphous materials where short range dipolar interaction are involved.[18,21,44–47] A built-in disorder is related with the diffuse phase transition in relaxor compounds associated with the presence of PNR's which damp the polar transverse optic phonon mode that drop precipitously into the transverse acoustic branch.[51–54] Order-disorder-like ordering of PNRs as a function of PT concentration had been proposed in this materials due to observation of no change in local structure, in overall, as the crystal structure undergoes a series phase transitions.[55,56] A plateau transition in thermal conductivity, which may provide a thermal boundary resistant at the boundary of ferroelectric domain, and a shift to the left in C_P/T^3 behavior associated with glass-like thermal conduction has been observed in relaxor materials.[45,57] Also, it has been observed an anomaly in the high temperature C_P associated with nucleation and growth of PNRs which completely merged into ferroelectrics domains below the transition.

In general, the phase transitions are accompanied by a change in the volume and entropy of the crystal.[8] The free energy of the system can be directly obtained from the calculated excess enthalpy ($H^{XS}(T)$) and entropy ($S^{XS}(T)$) of the system obtained from excess heat capacity $\Delta C_P(T)$ measurement, as shown in Equation 2.2.

$$\Delta G(T,c) \cong \Delta G_L(\boldsymbol{P};T,c) = \int \Delta C_P(T)\partial T - T\int \frac{\Delta C_P(T)}{T}\partial T = H^{XS}(T) - TS^{XS}(T) \quad (2.2)$$

Considering an intrinsic behavior of the free energy of a system, $\Delta G(T, c)$ for a ferroelectric material is related to $\Delta G_L(\boldsymbol{P}; T, c)$ with similar boundary conditions as in Equation 2.1. The heat capacity of a system can give information of the thermal properties of the material such as the free energy, the thermal properties of a poled ferroelectric state, the relaxor thermal stability etc. In general, the heat capacity integrates overall volume contributions to the free energy occurring on the time scale of the measurements, and variations in the heat capacity anomalies near phase transitions are extremely sensitive to the underlying defect structure.[14] Intrinsic and extrinsic contributions from the phase transition energetics may be revealed as a function of temperature from $C_P(T)$ measurements such as the energy associated with the intrinsic crystal and domain reconfiguration, respectively.

2.5 References

1. Park, S.-E. & Shrout, T. R. Ultrahigh strain and piezoelectric behavior in relaxor based ferroelectric single crystals. *J. Appl. Phys.* **82,** 1804 (1997).

2. Jaffe, B., Cook, W. R. & Jaffe, H. *Piezoelectric Ceramics*. 53–183 (Academic Press, 1971).

3. Kuwata, J., Uchino, K. & Nomura, S. Phase transitions in the Pb(Zn1/3Nb2/3)O3-PbTiO3 System. *Ferroelectrics* **37,** 579–82 (1981).

4. Noheda, B., Cox, D., Shirane, G., Gao, J. & Ye, Z.-G. Phase diagram of the ferroelectric relaxor (1-x)PbMg1/3Nb2/3O3-xPbTiO3. *Phys. Rev. B* **66,** 054104 (2002).

5. Wang, D., Cao, M. & Zhang, S. Phase diagram and properties of Pb(In1/2Nb1/2)O3–Pb(Mg1/3Nb2/3)O3–PbTiO3 polycrystalline ceramics. *J. Eur. Ceram. Soc.* **32,** 433–439 (2012).

6. George A. Samara. The relaxational properties of compositionally disordered ABO3 perovskites. *J. Phys. Condens. Matter* **15,** R367–R411 (2003).

7. Jona, F. & Shirane, G. *Ferroelectric Crystals*. (1962).

8. Strukov, B. A. & Levanyuk, A. P. *Ferroelectric Phenomena in Crystals: Physical Foundations*. (Springer-Verlag, 1998).

9. Devonshire, A. F. XCVI. Theory of barium titanate. *Philos. Mag. Ser. 7* **40,** 1040–1063 (1949).

10. Devonshire, A. F. CIX . Theory of barium titanate — Part II. *Philos. Mag. Ser. 7* **42,** 1065–1079 (1951).

11. Landau, L. D. & Lifshitz, E. E. *Statistical Physics*. (Pergamon Press Ltd, 1958).

12. Shuvalov, L. A. . *J. Phys. Soc. Japan* **28,** 38 (1970).

13. Lines, M. E. & Glass, A. M. *Principles and Applications of Ferroelectrics and Related Materials*. (Clarendon Press, 1977).

14. E. Salje. in *Phys. Prop. Thermodyn. Behav. Miner.* (Salje, E.) 75–119 (Dordrecht: Reidel, 1988).

15. Jorge, I., Ivantchev, S., M.J., P.-M. & Alverto, G. Devonshire-Landau free energy of BaTiO 3 from first principles. *cond-mat.mtrl-sci* 1–7 (2000).

16. Rossetti, G. A. & Khachaturyan, A. G. Inherent nanoscale structural instabilities near morphotropic boundaries in ferroelectric solid solutions. *Appl. Phys. Lett.* **91,** 072909 (2007).

17. Eremkin, V. V., Smotrakov, V. G. & Fesenko, E. G. Structural Phase Transitions in PbZr1-xTixO3 Crystals. *Ferroelectrics* **110,** 137=144 (1990).

18. Rossetti, G. A., Khachaturyan, A. G., Akcay, G. & Ni, Y. Ferroelectric solid solutions with morphotropic boundaries: Vanishing polarization anisotropy, adaptive, polar glass, and two-phase states. *J. Appl. Phys.* **103,** 114113 (2008).

19. Lu, X., Li, H. & Cao, W. Landau expansion parameters for BaTiO3. *J. Appl. Phys.* **114,** 224106 (2013).

20. Maureen L. Mulvihill *et al.* The Role of Processing Variables in the Flux Growth of Lead Zinc Niobate-Lead Titanate Relaxor Ferroelectric Single Crystals. *Jpn. J. Appl. Phys.* **35,** 3984–3990 (1996).

21. Cross, L. E. Relaxor Ferroelectrics. *Ferroelectrics* **76,** 241–267 (1987).

22. G. A. Smolenskii, Isupov, V. A., Agranovskaya, A. I. & Popov, S. N. Ferroelectrics with Difuse Phase Transitions. *Sov. Phys. Solid State* **2,** 2584 (1961).

23. Burns, G. & Dacol, F. H. Crystalline ferroelectrics with glassy polarization behavior. *Phys. Rev. B* **28,** 2527–2530 (1983).

24. G. A. Samara, Venturini, E. L. & Schmidt, V. H. Dielectric properties and phase transitions of [Pb(Zn1/3Nb2/3)O3]0.905(PbTiO3)0.095: Influence of pressure. *Phys. Rev. B* **63,** 184104 (2001).

25. Matthew, D., Damjanovic, D., Hayem, D. & Setter, N. Domain engineering of the transverse piezoelectric coefficient in perovskite ferroelectrics. *J. Appl. Phys.* **98,** 014102 (2005).

26. Dong, W. D., Finkel, P., Amin, A. & Lynch, C. S. Giant electro-mechanical energy conversion in [011] cut ferroelectric single crystals. *Appl. Phys. Lett.* **100,** 042903 (2012).

27. Liu, T. & Lynch, C. S. Domain Engineered Relaxor Ferroelectric Single Crystals. *Contin. Mech. Thermodyn.* **18,** 119–135 (2006).

28. Bell, a. J. Phenomenologically derived electric field-temperature phase diagrams and piezoelectric coefficients for single crystal barium titanate under fields along different axes. *J. Appl. Phys.* **89,** 3907 (2001).

29. Zhang, S. & Li, F. High performance ferroelectric relaxor-PbTiO3 single crystals: Status and perspective. *J. Appl. Phys.* **111,** 031301 (2012).

30. Fu, H. & Cohen, R. Polarization rotation mechanism for ultrahigh electromechanical response in single-crystal piezoelectrics. *Nature* **403,** 281–3 (2000).

31. Zhang, S., Sherlock, N. P., Jr., R. J. M. & Shrout, T. R. Crystallographic dependence of loss in domain engineered relaxor-PT single crystals. *Appl. Phys. Lett.* **94,** 162906 (2009).

32. Zhang, R., Jiang, B. & Cao, W. Single-domain properties of 0.67Pb(Mg[sub 1/3]Nb[sub 2/3])O[sub 3]–0.33PbTiO[sub 3] single crystals under electric field bias. *Appl. Phys. Lett.* **82,** 787 (2003).

33. Zhang, S. *et al.* Field-induced piezoelectric response in Pb(Mg1/3Nb2/3)O3–PbTiO3 single crystals. *Solid State Commun.* **137,** 16–20 (2006).

34. Lebrun, L. *et al.* Investigations on ferroelectric PMN-PT and PZN-PT single crystals ability for power or resonant actuators. *Ultrasonics* **42,** 501–5 (2004).

35. Abplanalp, M. *et al.* Scanning force microscopy of domain structures in Pb(Zn1/3]Nb2/3)O3-8% PbTiO3 and Pb(Mg1/3Nb2/3)O3-29% PbTiO3. *J. Appl. Phys.* **91,** 3797 (2002).

36. Dong, W. D., Finkel, P., Amin, A. & Lynch, C. S. Stress dependence of thermally driven pyroelectric charge release during FER-FEO phase transformations in [011] cut relaxor ferroelectric crystals. *Appl. Phys. Lett.* **100,** 262909 (2012).

37. Khachaturyan, a. G. Ferroelectric solid solutions with morphotropic boundary: Rotational instability of polarization, metastable coexistence of phases and nanodomain adaptive states. *Philos. Mag.* **90,** 37–60 (2010).

38. G. A. Rossetti, Zheng, W. & Khachaturyan, A. G. Phase coexistence near the morphotropic phase boundary in lead zirconate titanate solid solutions. *Appl. Phys. Lett.* **88,** 072912 (2006).

39. Heitmann, A. A. & Rossetti, G. A. Thermodynamics of polar anisotropy in morphotropic ferroelectric solid solutions. *Philos. Mag.* **90,** 71–87 (2010).

40. Heitman, A. Design and Modeling of High Power Density Acoustic Transducer Materials for Autonomous Undersea Vehicles. (2012).

41. Bai, F., Li, J. & Viehland, D. Domain engineered states over various length scales in (001)-oriented Pb(Mg1⁄3Nb2⁄3)O3-x%PbTiO3 crystals: Electrical history dependence of hierarchal domains. *J. Appl. Phys.* **97,** 054103 (2005).

42. Jin, Y. M., Wang, Y. U., Khachaturyan, A. G., Li, J. F. & Viehland, D. Adaptive ferroelectric states in systems with low domain wall energy: Tetragonal microdomains. *J. Appl. Phys.* **94,** 3629 (2003).

43. Khachaturyan, A. G., Shapiro, S. M. & Semenovskaya, S. Adaptive phase formation in martensitic transformation. *Phys. Rev. B* **43,** 10832 (1991).

44. Moriya, Y., Kawaji, H., Tojo, T. & Atake, T. Specific-Heat Anomaly Caused by Ferroelectric Nanoregions in Pb(Mg1/3Nb2/3)O3 and Pb(Mg1/3Ta2/3)O3 Relaxors. *Phys. Rev. Lett.* **90,** 205901 (2003).

45. Tachibana, M. & Takayama-Muromachi, E. Thermal conductivity and heat capacity of the relaxor ferroelectric [PbMg1/3Nb2/3O3]1−x[PbTiO3]x. *Phys. Rev. B* **79,** 100104 (2009).

46. Tachibana, M., Sasame, K., Kawaji, H., Atake, T. & Takayama-Muromachi, E. Thermal signatures of nanoscale inhomogeneities and ferroelectric order in [PbZn1/3Nb2/3O3]1−x[PbTiO3]x. *Phys. Rev. B* **80,** 094115 (2009).

47. Viehland, D., Jang, S. J., Cross, L. E. & Wuttig, M. Freezing of the polarization fluctuations in lead magnesium niobate relaxors. *J. Appl. Phys.* **68,** 2916 (1990).

48. Ikushi, Y., Nomura, S. & Sawada, S. Thermal Conductivity of $BaTiO_3$ Ceramics. *J. Phys. Soc. Japan* **13,** 1550–1551 (1958).

49. Dul'kin, E., Roth, M., Janolin, P.-E. & Dkhil, B. Acoustic emission study of phase transitions and polar nanoregions in relaxor-based systems: Application to the PbZn1⁄3Nb2⁄3O3 family of single crystals. *Phys. Rev. B* **73,** 012102 (2006).

50. Ziębińska, a, Rytz, D., Szot, K., Górny, M. & Roleder, K. Birefringence above T c in single crystals of barium titanate. *J. Phys. Condens. Matter* **20,** 142202 (2008).

51. Gehring, P. M., Park, S. & Shirane, G. Soft Phonon Anomalies in the Relaxor Ferroelectric Pb(Zn1/3Nb2/3)0.92Ti0.08O3. *Phys. Rev. Lett.* **84,** 5216–5219 (2000).

52. Hirota, K., Wakimoto, S. & E. Cox, D. Neutron and X-ray Scattering Studies of Relaxors. *J. Phys. Soc. Japan* **75,** 111006 (2006).

53. Gehring, P., Park, S.-E. & Shirane, G. Dynamical effects of the nanometer-sized polarized domains in Pb(Zn1/3Nb2/3)O3. *Phys. Rev. B* **63,** 224109 (2001).

54. Gehring, P., Wakimoto, S., Ye, Z.-G. & Shirane, G. Soft Mode Dynamics above and below the Burns Temperature in the Relaxor Pb(Mg1/3Nb2/3)O3. *Phys. Rev. Lett.* **87,** 277601 (2001).

55. Jeong, I.-K., Lee, J. K. & Heffner, R. H. Local structural view on the polarization rotation in relaxor ferroelectric (1−x)Pb(Zn1⁄3Nb2⁄3)O3–xPbTiO3. *Appl. Phys. Lett.* **92,** 172911 (2008).

56. Guo, Z. *et al.* X-ray probe of the polar nanoregions in the relaxor ferroelectric 0.72Pb(Mg1⁄3Nb2⁄3)O3–0.28PbTiO3. *Appl. Phys. Lett.* **91,** 081904 (2007).

57. Swartz, E. & Pohl, R. Thermal boundary resistance. *Rev. Mod. Phys.* **61,** 605–668 (1989).

CHAPTER 3

OBJECTIVES

3.1 Statement of Problem and Objectives

The main objectives of this study are:

i. To measure and compare the energies of paraelectric to ferroelectric and inter-ferroelectric phase transitions in both conventional and relaxor ferroelectric materials.

ii. To interpret the measured energies using the Landau theory of phase transitions to determine the change in polarization at the inter-ferroelectric transitions.

iii. To use this information to compare the changes in polarization at inter-ferroelectric transitions of different ferroelectric materials.

iv. To investigate the energy conversion capability of single crystal materials in an electro-mechanical energy conversion processes using inter-ferroelectric phase transitions.

3.2 Methodology and Approach

To accomplish these objectives, the phase transitions in polycrystalline PZT and in the single crystal $BaTiO_3$, PZN-PT and PMN-PT ceramic ferroelectric materials were investigated by heat capacity measurements. The heat capacity can be used to determine the thermal evolution of the order parameter as well as other relaxations of the structure that can influence the nature of a phase transition. In order to extract all these contributions:

i. The hard-mode contributions to C_P were estimated using both Debye and empirical models.

ii. The excess heat capacity associated with transitions between the parent cubic phase and the lower symmetry ferroelectric phases was determined.

iii. The enthalpies, entropies and transition temperatures of the paraelectric to ferroelectric and inter-ferroelectric phase transitions were determined from an analysis of the excess heat capacity.

Relaxor ferroelectrics display contributions to the heat capacity that deviate from the expected hard-mode behavior over a wide temperature range away from the structural phase transition points. To study this:

i. This deviation was associated with the thermal evolution of the relaxor polarization that arises due to the relaxor nature of the transitions and vanishes above the Burns temperature.
ii. By subtracting the contributions of the relaxor polarization to the excess heat capacity, the enthalpies and entropies of the displacive transitions along the Curie line were determined.
iii. Parameters associated with the relaxor nature of phase transitions, e.g. the Burns temperature, were determined.

Using relations that follow from the Ginzburg-Landau theory of weak first-order transitions, the reversible polarization was computed and used to determine:

i. The temperature evolution of the excess entropy and reversible polarization.
ii. The coefficients of the appropriate Landau polynomial.
iii. The “jumps” in reversible polarization at the transition points and the thermal hysteresis of the transitions.

Finally, the ternary solid solution relaxor ferroelectric PIN-PMN-PT, which displays high thermal and electrical stability in comparison with PMN-PT and PZN-PT, was used to study the electro-mechanical energy conversion through an inter-ferroelectric phase change cycling process. To investigate a stress-induced phase transition in a domain engineered PIN-PMN-PT single crystal:

i. High pre-stress condition close to the induced F_O-phase transition was applied to reduce the stress during the cycling process.
ii. Different frequencies and electrical resistance loading were investigated.
iii. The jump in polarization at the phase transition was determined.
iv. The mechanical to electrical energy conversion was also investigated.
v. The results were compared with resonance energy harvesting from PZT.

CHAPTER 4:

EXPERIMENTAL METHODS

4.1 Electrical Characterization Measurements

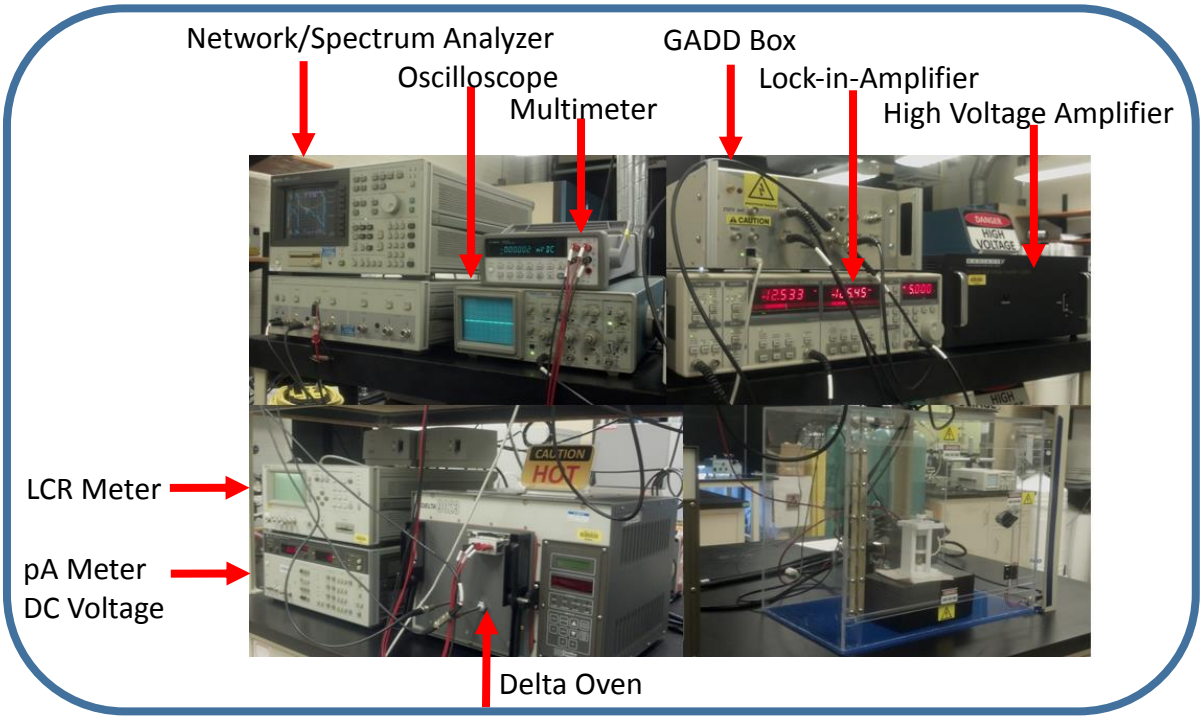

Figure 4. 1 Dielectric Multi-Spectroscopy System

A comprehensive dielectric and piezoelectric measurement system at the University of Connecticut (shown in Figure 4.1) was used for the electrical characterization of the materials. This system consists of a HP Agilent 4282A LCR meter, a Delta Design 9023 oven, a HP Agilent 4195A Network Spectrum Analyzer, an Agilent 34401A digital multimeter, a SR830 Lock-In amplifier, a Trek Precision High Voltage amplifier and a custom-built charge voltage converter (GADD box). Pyroelectric measurements are were also conducted by using a HP Agilent 4140B picoammeter. Custom designed software developed by Paul Moses at the Penn State MRL allows for the interconnection and data acquisition from the individual measurement systems listed above.

4.1.1 Dielectric Permittivity

The relative dielectric permittivity, loss tangent and the change in polarization were obtained from weak-field dielectric characterization from the capacitance, loss and pyroelectric current, respectively. The measurements were taken as a function of temperature, frequency and a weak applied electric field. The isothermal frequency sweeps from 100 Hz to 1 MHz under a field of 0.1 V using the HP Agilent 4282A LCR meter. The samples were placed in a custom built dielectric test fixture, shown in Figure 4.2, inside a Delta Design 9023 Oven, capable of operating from liquid nitrogen temperature op to 300 ^{o}C.

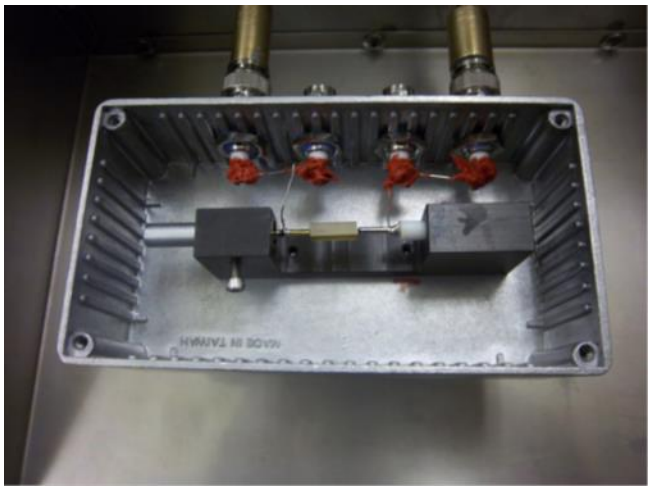

Figure 4.2 Dielectric Test Fixture

In order to equilibrate the temperature of the sample with the oven temperature, it was held constant for three minute prior to each the measurement in a temperature range of -50 ^{o}C to 250 ^{o}C. The temperature of the sample was determined from the resistance, as measured with an Agilent 34401A digital multimeter, of a resistance temperature interfaced detector (RTD) sensor placed adjacent to the sample. From the 1 mm thick silver paste electrode plate as a parallel plate

capacitor treatment, the relative permittivity was found from the measured capacitance by Equation 4.1.

$$\varepsilon_r = \frac{1}{\varepsilon_0}\left(\frac{d}{A}\right) C \tag{4.1}$$

where $\varepsilon_o = 8.85x10^{-12}\ F/m$ is the permittivity of free space, A is the sample area, d is the sample thickness and C is the capacitance.

4.1.2 Pyroelectricity

The same measurement set up were used to measure the pyroelectric current from -50 °C to 250 °C at a ramp rate of 1 degree per minute, however the a HP Agilent 4140B picoammeter connected to the low side of the sample, while the connection to the high side was terminated to a 50 Ω ground, was used to measure the charge build up. The pyroelectric current was subsequently measured at every half degree. The change in polarization as a function of temperature was determined by following the Byer-Rondy method.[1]

4.1.3 Polarization vs Electric field (Ferroelectric Hysteresis Loop)

Simultaneous acquisition of the ferroelectric hysteresis loops, polarization (P) vs applied electric field (E) (P-E loop) and strain (S) vs E (S-E loop) were obtained from a strong-field dielectric property measurement system consisted of a modified Sawyer-Tower circuit under full computer control. The P-E and S-E ferroelectric hysteresis loops were measured under the application of a bipolar field of 1500 V.

4.2 Thermal and Transport Property Measurements

4.2.1 Heat Capacity Measurement

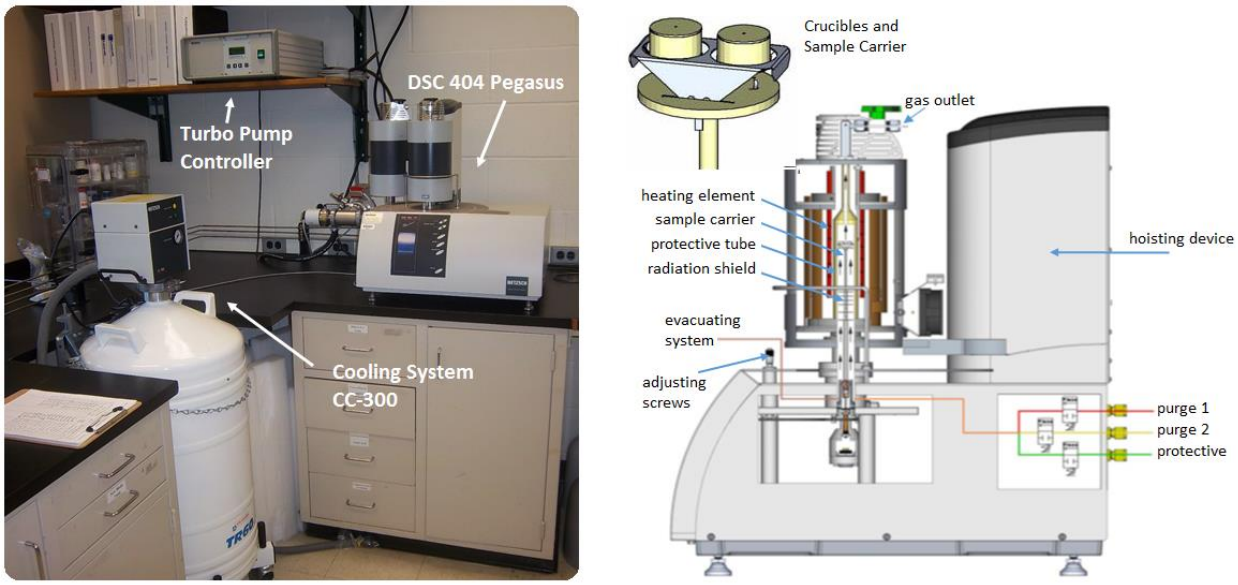

Figure 4. 3 Differential Scanning Calorimeter

The Differential Scanning Calorimeter (DSC) system "DSC 404 F1 Pegasus" from Netzsch, shown in Figure 4.3, in a temperature range from100 to 1000 K at 10 K/min with 20 points per degree Kelvin was used to determine the heat capacity ($C_P(T)$). The specimens were placed in good thermal contact within covered platinum crucibles. The DSC was conducted in two temperature ranges. The low temperature range (100 to 823 K) was conducted under Hellium using the Silver-furnace with the E-type furnace carrier (calibrated with Bi, CsCl, Hg, In, dSn and Zn). Gas Nitrogen, as a result of the evaporation of the liquid Nitrogen from the CC-300 cooling system, was used during the cooling process with the low temperature range experimental conditions. The high temperature range (303 to 1000 K) was carried out under Argon using the Platinum-furnace with the S-type furnace carrier (calibrated with In, Bi, Al, Ag and Au). Both gas flow rates were 50 ml/min. Alumina spacers were used below the Pt crucibles to avoid the Pt surface of the S-type furnace carrier to stick to the crucible due to high temperature treatment. Two sets of data (low

and high temperature ranges) were stitched together after careful calibration of the baseline. The accuracy of the data (absolute average error ~1 %) was verified by comparing the measured heat capacity of Alumina with the heat capacity of the standard material (NSB standard table)[2] as shown in Figure 4.4.

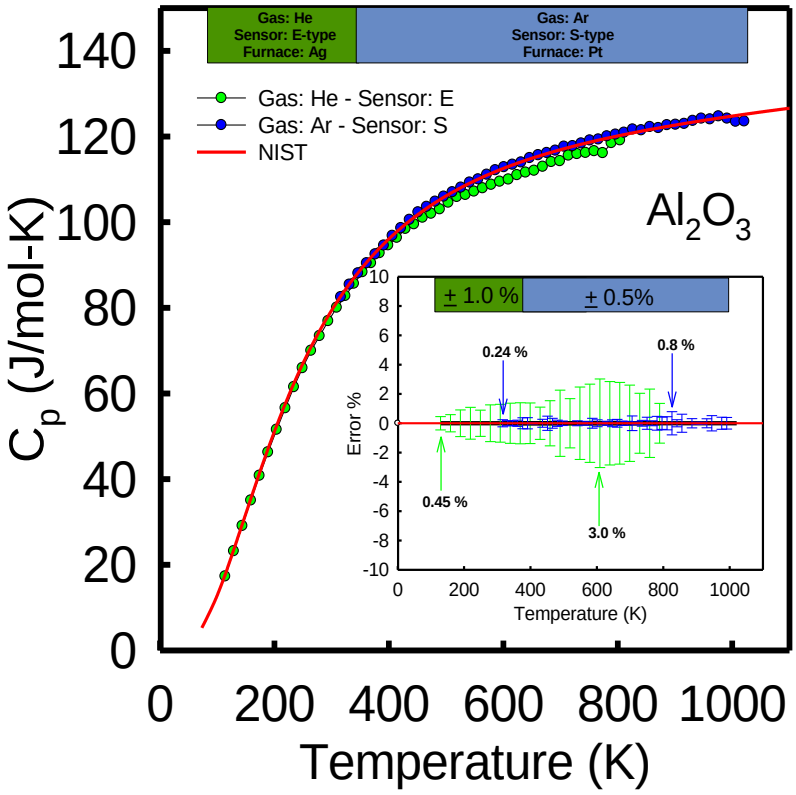

Figure 4. 4 Heat capacity of AlO3 polycrystalline – Determination of error in the DSC measurement.

To determine the heat capacity, ASTM E 1269[3] ratio method was used by using NIST SRM-720[2] data for a single crystal Al_2O_3 calibration standard. The ASTM E 1269 ration method consist in three consecutive measurements under the same experimental conditions and temperature specifications. First, a baseline ($DSC_{baseline}$) is a run were crucible are empty. In the

second measurement, $DSC_{standard}$, a standard material is kept in the sample crucible. The third measurement, DSC_{sample}, is made with the actual sample in the sample crucibles. The ration method equation is given by Equation 4.2:

$$C_P(T) = \frac{m_{standard}}{m_{sample}} \frac{DSC_{sample} - DSC_{Baseline}}{DSC_{standard} - DSC_{Baseline}} C_{P-standard} \quad (4.2)$$

where m_{sample} and $m_{standard}$ are the mass of the sample and the standard material, respectively. The $C_{P-standard}$ is the heat capacity of the standard material. The ASTM method (ASTM E 1269) also requires three measurements with an identical temperature program, including isothermal segments at the beginning and the end. Also, for accurate heat capacity measurements, the baseline run may be repeated twice to ensure stability and reproducibility.

4.2.2 Thermal Expansion

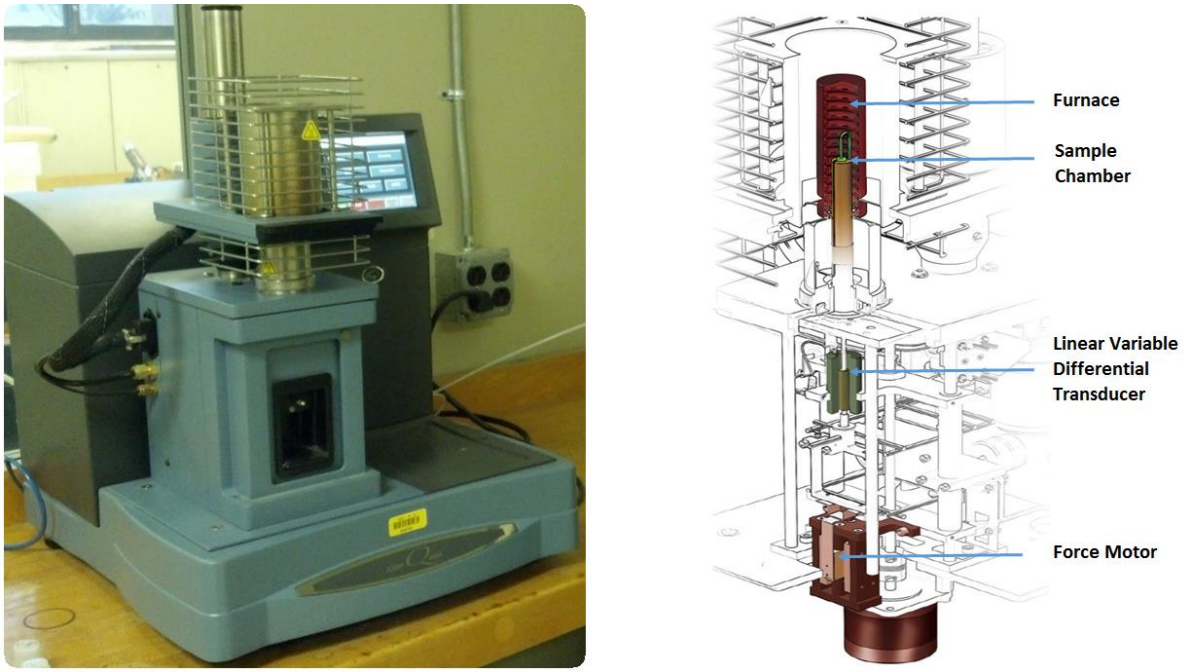

Figure 4. 5 Thermal Measurement Analyzer (TMA) system "TMA Q400 V7.4.

The Thermal Measurement Analyzer (TMA) system "TMA Q400 V7.4" thermochemical analyzer, shown in Figure 4.5, from 278 to 803 K at 2 K/min was used to measure the dimension change, $\Delta L = L(T) - L_o$, of the material. The Q400 TMA sample measurement system consists of a precision, moveable-core, linear variable differential transducer (LVDT), which generates an accurate output signal that is directly proportional to a sample dimension change.

The gas Nitrogen flow rate and mechanical load were 100 mL/min and 0.05 N, respectively. ASTM E-831[4] was used to calibrate the system with Sn, In, Zn, Al (for the cell constant) standards. The absolute average experimental error for the thermal expansion was ~5.0%. The thermal expansion was easily obtained from Equation 4.3

$$e_{ij}(T) = \Delta L / L_o \tag{4.3}$$

where the direction of the measurement to the single crystal materials were considered. The thermal expansion coefficients was obtained from Equation 4.4:

$$\alpha = \frac{\partial e_{ij}(T)}{\partial T} \tag{4.4}$$

Since the thermal expansion, or thermal strain, was determined for ferroelectric materials, its absolute value was obtained by considering zero dimension change at the paraelectric to ferroelectric phase transition temperature. The linear thermal expansion of the high temperature paraelectric phase was then extrapolated to this phase transition point.

4.2.3 Thermal Diffusivity

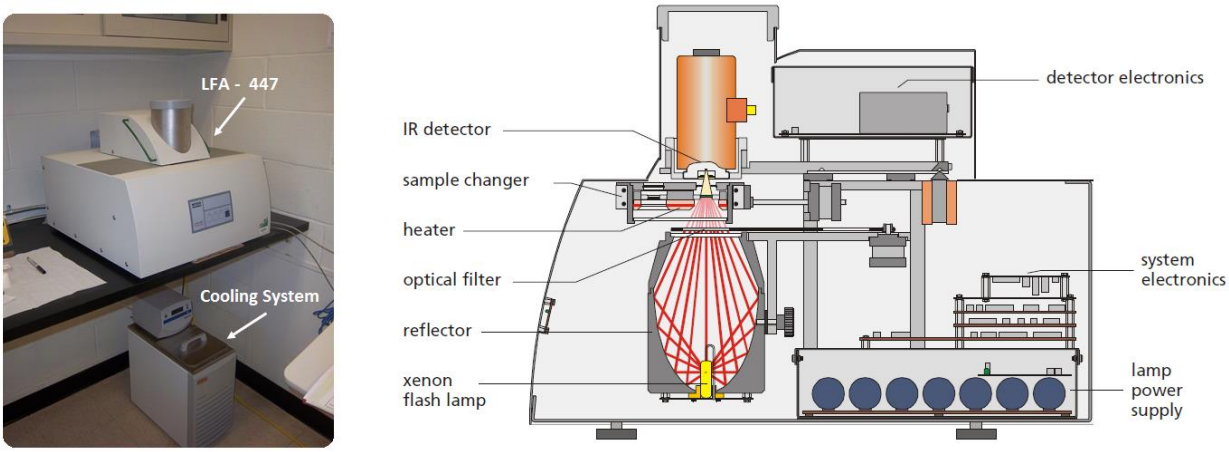

Figure 4. 6 Thermal Measurement Analyzer (TMA) system "TMA Q400 V7.4.

The Laser Flash Analyzer (LFA) system "Nano-Flash LFA 447" from Netzsch, shown in Figure 4.6, in a temperature range of 298 K to 573 K was used to measure the thermal diffusivity *D(T)*. Parallel surfaces perpendicular to the thickness of the specimen were Au-sputter coated and spray coated with graphite spray (DGF 123). The specimens were place in an 8 mm square stainless steel sample holder with a 6 x 6 sample requirement dimension. The initial LFA parameters used were: 100% light filter, 304 volts, long pulse width, 10 gain pre-amp and 5002 gain main-amp. The temperature stability was reach by the use of a water chiller and liquid Nitrogen which also protect the IR detector located at the back sample surface.

The standard deviation of the measurement correspond to seven accepted data point of the heat from the laser flash accurate measured at the back of the sample surface. For the accuracy of the measurement, 1 mm Alumina sample, shown in Figure 4.7, was also run, at the same time, with the same experimental conditions as the interest material. The average experimental error (~1.0 %), was determined by compared the measured standard Alumina with Netzsch data table.

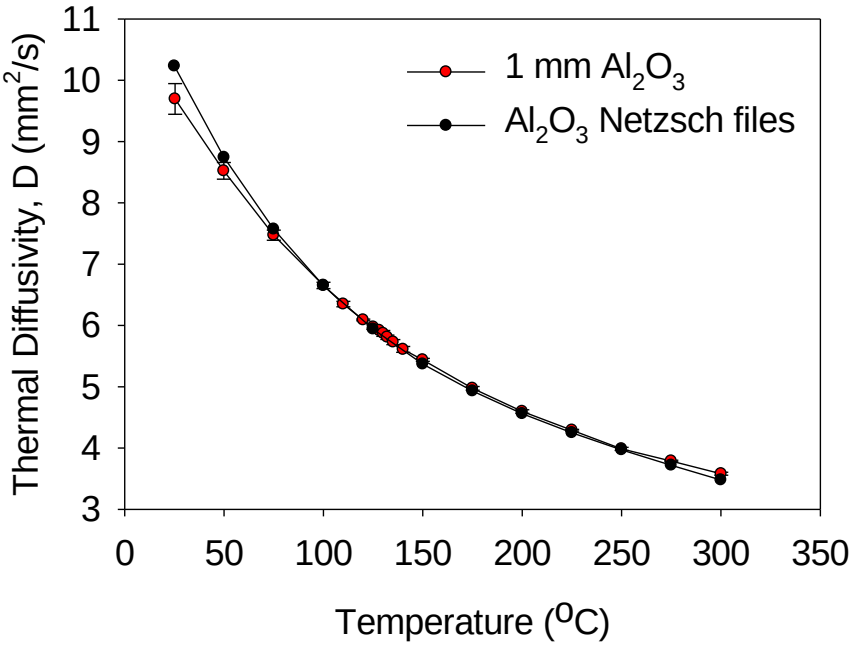

Figure 4. 7 Measured thermal diffusivity of Al_2O_3 standard compared with standard tables from Netzsch.

The thermal diffusivity from the LFA, results from a thermal transient problem of heat conduction through a slab where in the initial boundary conditions pulse of radiant energy Q (cal/cm^2) is instantaneously and uniformly absorbed in the small depth g at the front surface x = 0 of a thermally insulated solid of uniform thickness L (cm).[5] The solution to the transient equation $\left(\frac{\partial T}{\partial t} = k\frac{\partial^2 T}{\partial x^2}\right)$ is given by Equation 4.5.

$$T(x,t) = \frac{Q}{DCL}\left[1 + 2\sum_{n=1}^{\infty} cos\left(\frac{n\pi x}{L}\right)\frac{\sin(n\pi g/L)}{n\pi g/L} \times exp\left(\frac{-n^2\pi^2}{L^2}\alpha t\right)\right] \quad (4.5)$$

Since and since g is very small number for opaque materials (considering the coating of the material) $\sin\left(\frac{n\pi g}{L}\right) \approx \frac{n\pi g}{L}$ and at the back of the surface (x = L), $\cos(n\pi) = (-1)^n$. Then,

Equation 4.5 may be re-expressed in dimensionless form for the temperature profile at the rear surface:

$$V = 1 + 2\sum_{n=1}^{\infty}(-1)^n \exp(-n^2\omega) \tag{4.6}$$

where $V = \frac{T(L,t)}{T_{max}}$ and $\omega = \frac{\pi^2 \alpha t}{L^2}$. T_{max} represents the maximum temperature at the rear surface given by $T_{max} = \frac{Q}{DCL}$.[6] The profile given by Equation 4.6 is given in Figure 4.8a, similar profile given by the LFA for an accepted data point is also shown in Figure 4.8b.

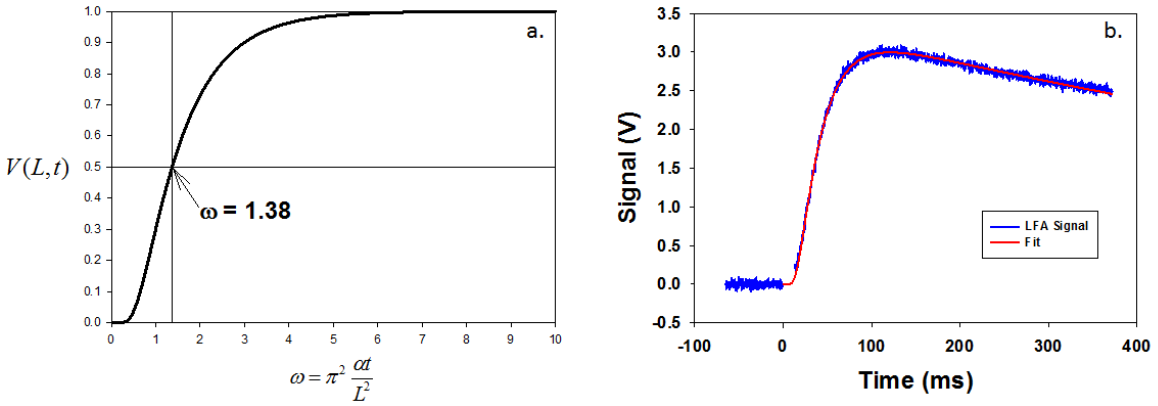

Figure 4. 8 Measured thermal diffusivity of Al_2O_3 standard compared with standard tables from Netzsch.

A way to determine the thermal diffusivity, $\alpha(T)$, is then from the time required $(t_{1/2})$ for the back surface to reach half of the maximum temperature rise V = 0.5, which gives as a result of $\omega = 1.38$, shown in Equation 4.7.

$$\alpha = \frac{1.38L^2}{\pi^2 t_{1/2}} \tag{4.7}$$

Where $t_{1/2}$ is obtained from the half time in the voltage signal vs. time profile, shown in Figure 4.8b. In order to obtain the thermal diffusivity as a function of temperature, the voltage signal vs. time profile must be determined for each interested temperatures in the accessible temperature range.

4.3 Summary

In this experimental method chapter it was discussed the main measurement techniques that were used to characterize the ferroelectric single crystal materials and to measure their temperature dependence property behavior and the energetic at their different phase transitions. This chapter was divided into the electrical characterization techniques (dielectric permittivity, ferroelectric hysteresis loop and Pyroelectricity) and the thermal and transport measurement systems (DSC, TMA and LFA). All the equipment in each measure techniques are available in the Institute of Material Sciences at the University of Connecticut – Storrs campus

All this measurements techniques were discussed in general with the purpose to be referenced in the following chapters. In the case of the electrical measurement systems, a comprehensive dielectric and piezoelectric measurement system, controlled by a custom computer software, was able to characterize the materials as a function of temperature, frequency and electric field. The single crystals were characterized by their ferroelectric hysteresis loop (P-E loop and S-E loop), their dielectric permittivity and loss and their pyroelectric current.

In the case of the thermal and transport properties, they were investigated by conducting DSC, TMA and LFA measurements. In this case, the different required parameters and thermal analysis technique were presented. Also the average experimental error and calibration to the different measurement systems were shown. The calibration of the system is typically based on

the phase transition change of standards materials. For the DSC measurement technique the ASTM E 1269 ratio method was considered to determine the heat capacity. It consists of three different runs (baseline, standard and sample) with the same experimental conditions and temperature history. The very large temperature range considered in this thermal measurement technique was available by data stich of two measured temperature ranges. From TMA measurement technique, the thermal expansion was easily obtained by taking in consideration the dimension change of the sample as a function of temperature. The expansion of the materials is capture by a linear variable differential transducer which generates an accurate output signal that is directly proportional to a sample dimension change. Finally, from a LFA measurement technique the thermal diffusivity was determined. In this technique it is considered the heat conduction through a slab heat where in the initial boundary conditions pulse of radiant energy is instantaneously and uniformly absorbed in the small depth at the front surface of a thermally insulated solid of uniform thickness.[5]

4.4 References

1. Byer, R. L. & Roundy, C. B. . *Ferroelectrics* **3,** 333–338 (1972).

2. Ditmars, D. A. & Douglas, T. B. Measurement of the Relative Enthalpy of Pure alpha-A1203 (NBS Heat Capacity and Enthalpy Standard Reference Material No. 720) from 273 to 1173 K. *J. Res. Nat. Stand. Sec. A.* **75A,** 401–402 (1971).

3. ASTM Standard E 1269. *Standard Test Method for Determining Specific Heat Capacity by Differential Scanning Calorimetry*. *ASTM Int.* (2011). doi:10.1520/E1269-11

4. ASTM Standard E 831. *Standard Test Method for Linear Thermal Expansion of Solid Materials by Thermomechanical Analysis*. (2013). doi:10.1520/E0831

5. Carslaw, H. S. & Jaeger, J. C. *Conduction of Heat in Solids*. 101 (Oxford University, 1959).

6. Parker, W. J., Jenkins, R. J., Butler, C. P. & Abbott, G. L. Flash Method of Determination Thermal Diffusivity, Heat Capacity, and Thermal Conductivity. *J. Appl. Phys.* **32,** (1961).

CHAPTER 5

PHASE TRANSITON ENERGYETIC IN $BaTiO_3$ SINGLE CRYSTAL

5.1 Introduction

The energetic at phase transitions in ferroelectric materials has brought significant attention to potential technological application such as thermal sensing and energy harvesting. In the case of $BaTiO_3$, a fundamental ferroelectric material, the sequence of phase transitions (paraelectric (PE, m3m point group) cubic – ferroelectric tetragonal (F_T, 4mm point group) – ferroelectric orthorhombic (F_O, mm point group) – ferroelectric rhombohedral (F_R, 3m point group)) may be understood from distortions of its original parent cubic perovskite-type crystal structure in the PE-phase.[1] Intrinsic and extrinsic contributions from the phase transition energetics may be revealed as a function of temperature from heat capacity measurements such as the energetic associated with the intrinsic crystal and domain reconfiguration, respectively. In general, the heat capacity integrates overall volume contributions to the free energy occurring on the time scale of the measurements and variations in the heat capacity anomalies near phase transitions are extremely sensitive to the underlying defect structure.[2]

Energetic at the different phase transitions obtained from heat capacity measurements, in this case it is associated with the excess contribution to the enthalpy (ΔH^{XS}), in $BaTiO_3$ single crystal had been reported.[3–12] However, the limits of integration under the different phase transitions had been, in most of the cases, chosen arbitrarily which results in an inconsistent measure of comparison. Sometimes it is a consequence of the measured temperature range, crystal growth method, crystal defect concentration or an inaccurate measurement technique.[7] As an example, Todd and Lorenson report the energetic at the ferroelectric to ferroelectric (inter-

ferroelectric) phase transition of $BaTiO_3$ single crystal obtained from the derivative limit.[3] Shirane and Takeda used broken lines or dash lines as a linear background to set the integration limits for the transition energies.[4] Egorov et al., obtained the energy of the phase transition from the temperature limits where the temperature dependences of the DSC signal change respect to the peak area.[6]

In this chapter, I will present a highly accurately measurement of the heat capacity of $BaTiO_3$ single crystal in a wide temperature range. In order to get the anomalous associated with the energetic at phase transition, the measured C_P was subtracted from the C_P-background associated with the hard mode behavior of the C_P obtained from the Debye function or empirical equation. Information at the different phase transitions (PE-F_T, F_T-F_O, F_O-F_R) will be determined, such as T_{max}, T_{onset} and the different phase transition limits, enthalpies and entropies. Due to the large temperature range to the anomalous contribution to the heat capacity associated with the phase transition, different limit of integration were then defined. Lastly, at the paraelectric phase transition, pretransitional features observed as a tail from the heat capacity measurements were also discussed based on the fluctuation phenomena[13,14] and local polar nanoregions[15–17] in the symmetric paraelectric phase.

5.2 Results and Discussion

5.2.1 Dielectric Characterization

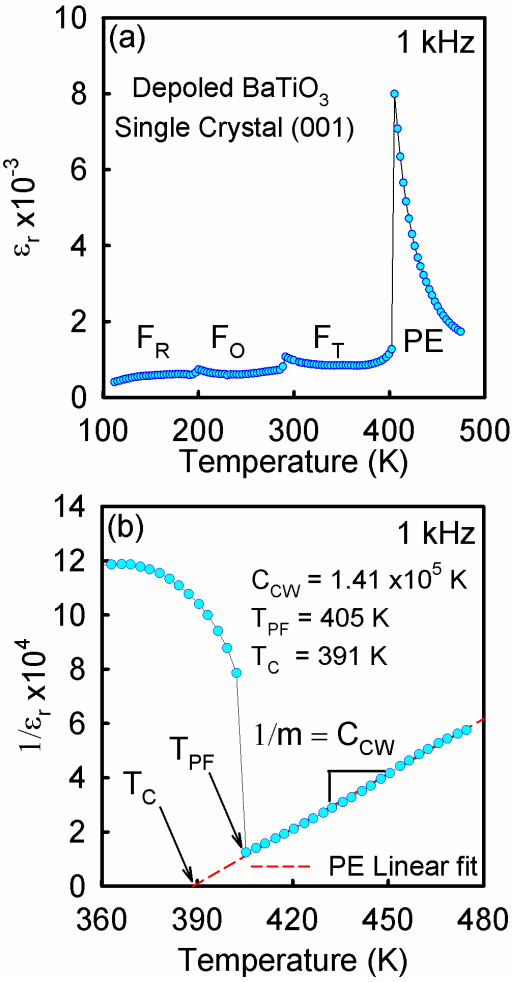

Figure 5. 1 (a) Dielectric permittivity of $BaTiO_3$ depoled single crystal. (b) Inverse dielectric permittivity analysis around the Paraelectric to ferroelectric transition.

Dielectric permittivity and thermal expansion were used characterized the $BaTiO_3$ single crystal. The characterization of $BaTiO_3$ single crystal, by relative dielectric permittivity measurement in a wide temperature range, is shown in Figure 5.1a. The well know ferroelectric transitions of $BaTiO_3$ single crystal were observed as sharp transition peaks at 197 K, 288 K and

405 K corresponding to the ferroelectric orthorhombic, F_O, to the ferroelectric rhombohedra, F_R, (T_{FO-FR}), to the ferroelectric tetragonal, F_T, to F_O (T_{FT-FO}) and to the cubic paraelectric, PE, to F_T (T_{PF}) phase transition temperatures, respectively. The measured relative dielectric permittivity, shown in Figure 5.1a, compares well with that measured along the c-axis by Merz.[18] The inverse relative dielectric permittivity of $BaTiO_3$ single crystal around the PE-F_T phase transition region is shown in Figure 5.1b. From the slope of a line fitted to the high temperature PE-phase of the inverse relative dielectric permittivity, the Curie-Weiss constant ($C_{C-W} = 1.41x10^5\ K^{-1}$) was obtained. Its intersection to the temperature-axis gives the Curie temperature ($T_C = 391\ K$). A clear jump in the inverse relative dielectric permittivity was observed at the PE-F_T phase transition which it is characteristic of a 1st-order phase transition in normal ferroelectric materials. It was observed at $T_{PF} = 405\ K$. These three parameters (C_{C-W}, T_C and T_{PF}) are compared with literature Table 5.1.

5.2.2 Characterization by thermal strain

The depoled $BaTiO_3$ single crystal was also characterized by its thermal strain, e_{ij}, along the [100], e_{11}, and along [001], e_{33}, directions relative to the thermal strain of the PE-phase, shown in Figure 5.2. The linear thermal strain of the PE-phase with an average thermal expansion coefficient, $\alpha = 12.56\ \mu m/mK$ from several measurements, typically value of a ceramic material, compared well with literature,[4,5,19–21] shown in Table 5.1.

A linear fit to the high temperature PE-phase was extrapolated to lower temperatures and set it to pass through zero thermal strain at T_{PF}. A sharp PE-F_T transition was observed at $T_{PF} = 403\ K$, which agrees well with that found from the dielectric measurement, compared in Table 5.1. The measured strain was compared with the strain obtain from a- and c-lattice parameters of

$BaTiO_3$ single crystal obtained by Key and Vousden,[5] Shebanov,[19] both from X-ray diffraction data, and Jaffe and Cook.[22] The temperature dependence of the thermal strain to this literature is in extremely good agreement.

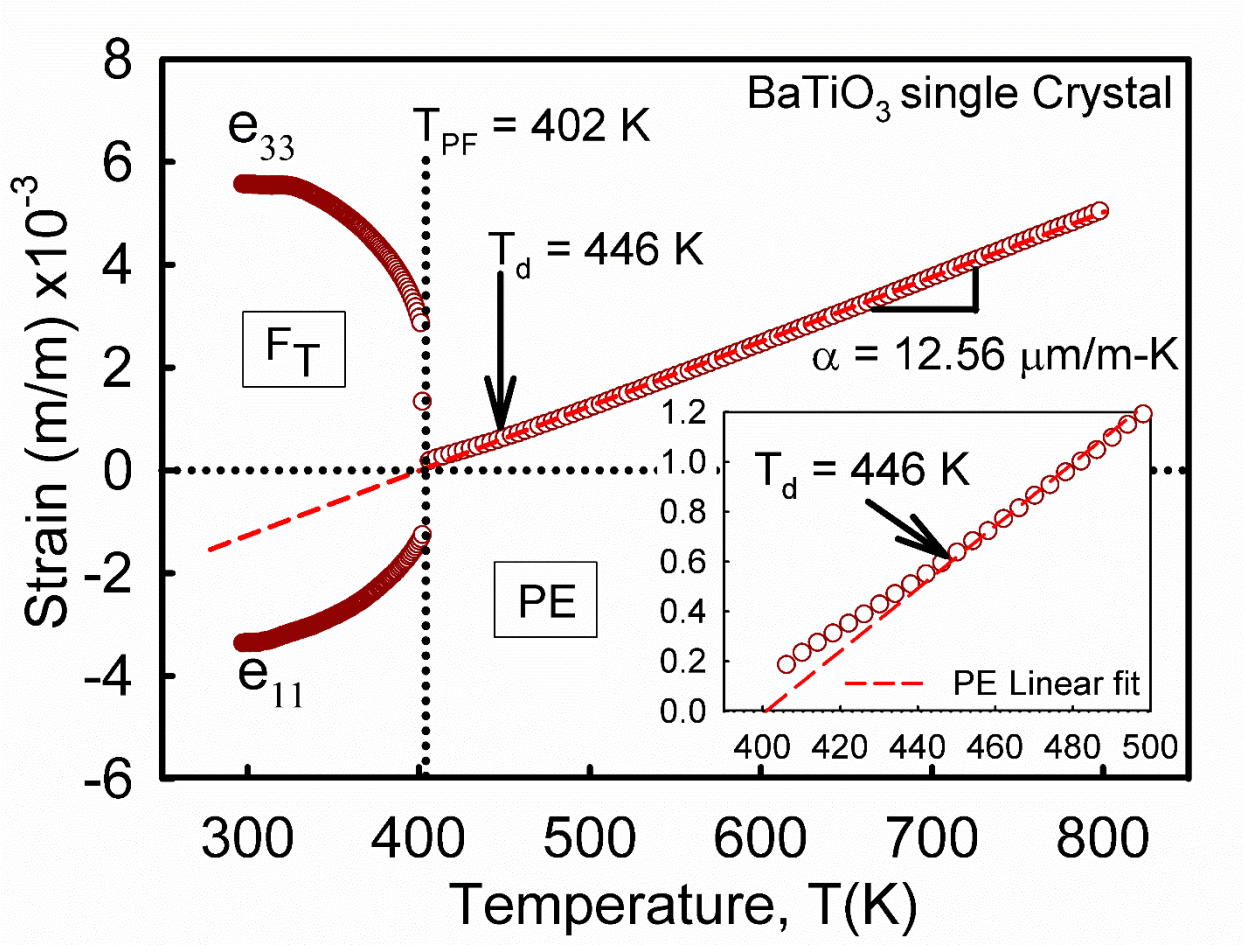

Figure 5. 2 Thermal strain for depoled $BaTiO_3$ single crystal. Inset: observation of the Burns temperature.

Table 5. 1 Thermodynamic properties of depoled $BaTiO_3$ single crystal.

	Property	Units	
Curie temperature	T_C	K	391[a], 378 – 393[11,18,23–25]
PE-F$_T$ transition	T_{PF}	K	405[a], 402[b], 403[24]
Burns temperature	T_d	K	460[b], 446[c], 420 – 453[15,26,27]
Curie-Weiss Constant	$C_{C\text{-}W}$ x10^5	K	1.41[a], 1.51 – 2.07[4,28–30]
Debye temperature	θ_D(K)	K	555[c], 432 – 485[31–34]
Thermal expansion coefficient	α (PE-phase)	$\mu m/mK$	12.56[b], 9.80 – 16.0[4,5,19–21]

[a]This study from dielectric measurement.
[b]This study from thermal expansion measurement.
[c]This study from heat capacity measurement.

5.2.3 Thermal analysis to the phase transition from heat capacity

The highly accurately measured C_P of $BaTiO_3$ single crystal is shown in Figure 5.3. It is to be noted the high sensitivity of the measurement, especially at the structural phase transformations over the full measured temperature range. Structural changes at phase transitions may be revealed by the C_P measurement. The inter-ferroelectric phase transition temperatures as well as the PE-F_T phase transition were observed as sharp peaks and correlated well with dielectric measurements in Figure 5.1a. The peaks maxima from the C_P-data were located at $T_{FO\text{-}FR}$ = 199 K, $T_{FT\text{-}FO}$ = 290 K and T_{PF} = 405 K. The inter-ferroelectric phase transition temperatures also agree well with the one obtained from Todd and Lorenson on $BaTiO_3$ single crystal material.[3]

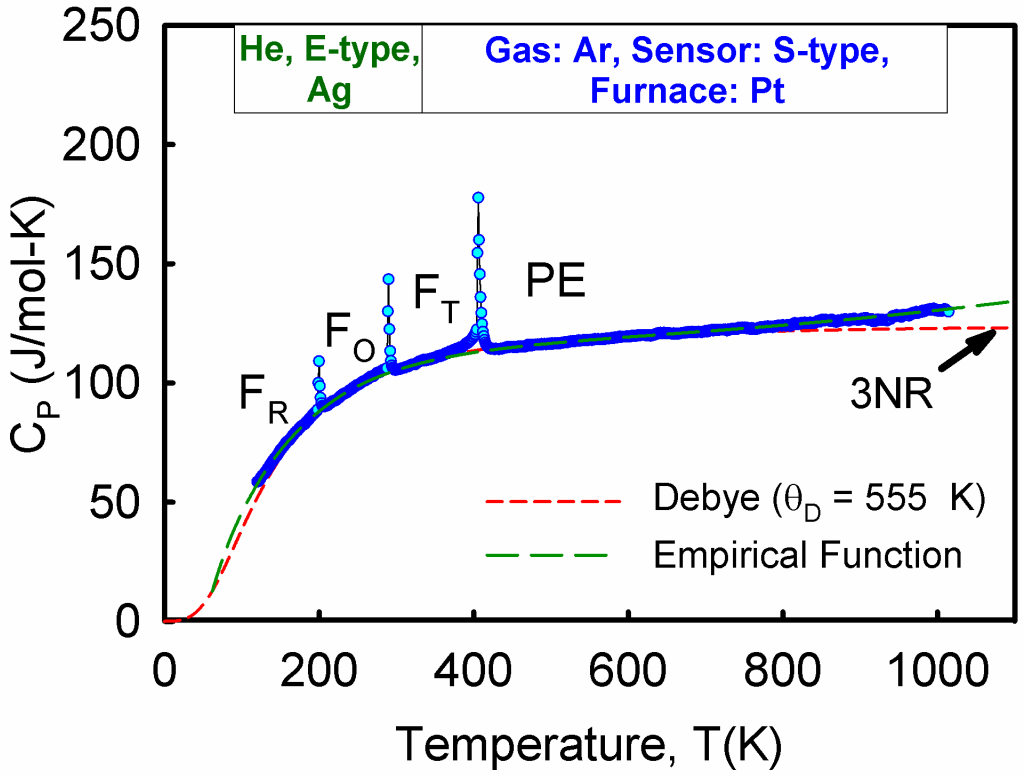

Figure 5. 3 Heat capacity of depoled $BaTiO_3$ single crystal in a wide temperature range. Short- and long-dash lines indicate the fit to the Debye function and to an empirical equation, respectively.

The C_P-data of $BaTiO_3$ single crystal was analyzed by two methods: (a) A typical direct thermal analysis in order to determine temperatures, enthalpies and entropies at phase transitions and (b) by the application of a thermodynamic potential to the intrinsic C_P, or the excess C_P (ΔC_P), to determine the excess free energy of the system. The latter was relative to C_P-background obtained by the Debye function and empirical equation. In the first method, the "Proteus Analysis Software from Netzsch" for thermal analysis was used. A detail description of the direct thermal analysis is shown in Figure 5.4. At each inter-ferroelectric phase transitions and at the PE-F_T phase transition, the peak maxima temperature (T_{max}), the onset temperature (T_{Onset}), offset temperature (T_{Offset}) and the temperatures at which the slope of the derivative of C_P change from zero as

approaching the phase transition from the left ($T_{d\text{-}L}$) and from the right ($T_{d\text{-}R}$) were determined. These temperatures and the corresponding enthalpies and entropies delimited from T_{Onset} - T_{Offset} and $T_{d\text{-}L}$ - $T_{d\text{-}R}$, are shown in Table 5.2. Comparison with literature of the transition temperatures and the corresponding enthalpies and entropies for each phase transition are also shown in Table 5.2. The main reason of Table 5.2 is to show the different ways those thermodynamics quantities had been reported in literature. As a consequence, the transition temperature as T_{Onset} is usually report in literature and it agree well with the one found in this study for the different phase transitions. It is to ben noted that in $BaTiO_3$ single crystal the different between the T_{onset}, T_{max} and $T_{d\text{-}L}$ is relatively small due to sharp peaks of the phase transitions. Those transition temperatures may be affected by structural defects.

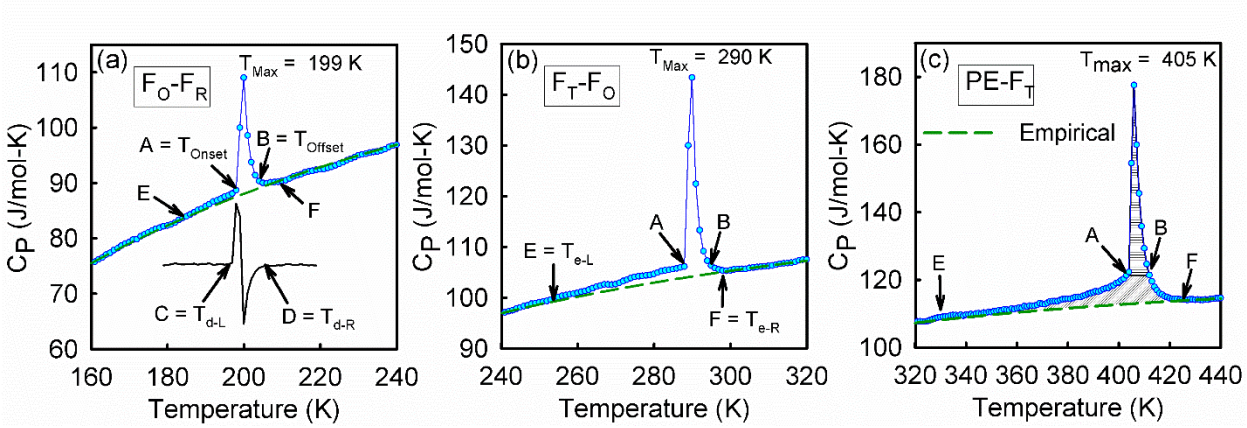

Figure 5. 4 Analysis of around phase transitions of the heat capacity data. (a) F_O-F_T transition, (b) F_T-F_O transition and (c) PE-F_T transition. The temperature limits ($T_{d\text{-}L}$ and $T_{d\text{-}R}$) and ($T_{e\text{-}L}$ and $T_{e\text{-}R}$) correspond to the non-zero value of the derivative (D) of heat capacity from the left (L) and from right (R) of the transition peak. Those transition temperatures are the temperature limits from the intersection of the heat capacity with the empirical function from the left and from the right.

Hatta and Ikushima shown transition temperature for the PE-F_T transition at 408.33 K and 397.72 K for top seeded solution technique and flux method, respectively.[7] It may be associated with different processing methods or the temperature increment during the DSC run experiment. In general, the heat capacity integrates overall volume contributions to the free energy occurring on the time scale of the measurements and variations in the heat capacity anomalies near phase transitions are extremely sensitive to the underlying defect structure.[2]

Before further comparisons, an additional temperature limits were determined. These temperature limits correspond to a deviation of the C_P associated with the phase transition, the excess heat capacity (ΔC_P), to the hard-mode behavior of the C_P, described by an empirical equation ($C_P(Empirical)$ or Debye function $C_P(Debye)$, from the left ($T_{e\text{-}L}$) and from the right ($T_{e\text{-}R}$) of each of the phase transition. In order to get ΔC_P, $C_P(Debye)$ and $C_P(Empirical)$ were used as C_P-backgrounds to fit the hard-mode behavior (no phase transition) of the C_P-data, as shown in Figure 5.3. The hard-mode behavior obtained for $BaTiO_3$ single crystal compared well with that obtained from Todd and Lorenson[3] measured in the low temperature range and from Coughlin[35] in the high temperature range for $BaTiO_3$ single crystal material. In Coughlin works the single crystal used is a piece of the same crystal used by Todd and Lorenson.

First, the Debye function (Equation 5.1) may be found to be valid at the low temperature regime, T^3 -law, and at the high temperature where all modes of vibration are considered, the Dulong Petit Limit.[36] It is to be noted, in Figure 5.3, that the high temperature C_P-data reaches the Dulong-Petit limit (3NR).

$$\boldsymbol{C_P(Debye) = C_P(\theta_D) = 9NR\left(\frac{T}{\theta_D}\right)^3 \int_0^{\theta_D/T} \frac{x^4 e^x}{(e^x-1)^2} dx} \qquad (5.1)$$

In Equation 5.1, N is the number of atoms per unit cell, R is the gas constant and θ_D is the Debye temperature. The Debye temperature for $BaTiO_3$ had been mostly obtained from the low

temperature C_P and it is in good agreement with the T^3 – law. Discrepancies around this law had been verified by Villar et al.[34] They measured the C_P of crystalline ferroelectrics at low temperatures. It was described the Debye phonon contribution as $T \to 0\,K$ for ferroelectric materials with sharp dielectric transitions with T, $T^{3/2}$ and T^3 terms due to susceptibility for dipolar impurities of the low temperature C_P (T < 4 K). However, their data are well described by the T^3 –law showing that there is no indication of an additional "excess-heat" or additional terms (T or $T^{3/2}$) concluding that the previously found anomalies are not intrinsic volume properties. Table 5.1 shows reported θ_D which range from 432[31] to 485.[34]

In our attempt to determine θ_D from the experimental C_P-data, it is first considered the free energy in each ferroelectric phases and the PE-phase. From the fit of the Debye function to the different phases, the following θ_D were obtained: θ_D(F_R-phase) = 535 K, θ_D(F_O-phase) = 557 K, θ_D(F_T-phase) = 565 K and θ_D(PE-phase) = 580 K. As can be observed, θ_D decrease toward lower symmetry ferroelectric phases. It had been demonstrated that the extrapolation of volume expansion of the PE-phase of $BaTiO_3$ single crystal to lower temperatures lies very close to the volume expansion of the low temperature F_R-phase.[5,37] From this consideration, the Debye function was fitted to the hard-mode behavior of the C_P-data which does not include phase transition and no excess C_P from the phase transformation. It gives θ_D = 555 K which well described the hard-mode behavior of the C_P-data, shown as red short dash line in Figure 5.3. Recently, from DFT-GGA calculation, it was found θ_D = 513 K determined from the calculated lattice parameters and the relation between θ_D and the elastic constant.[38] The difference in previously reported θ_D may be a consequence to the surface-to-volume effect.[31,34]

At high temperature the Debye function, by using θ_D = 555 K, lies on the experimental C_P-data demonstrating the Dulong-Petit limit 3NR. However, a deviation from 3NR is observed after

around 800 K. In this case, the assumption of $C_v \cong C_P$ is no longer hold and the expansivity coefficient need to be taken into consideration.

Then, in way to better fit the hard mode behavior of the C_P-data in each of the phases, two $C_{P-Empirical}$ functions were used as C_P-backgrounds, shown as green long dash line in Figure 5.3. The $C_{P-Empirical}$ function is given by Equation 5.2:

$$\boldsymbol{C_{P-Empirical} = a + bT^{-1} + cT^{\frac{1}{2}} + dT + eT^{2} + fT^{-2}} \quad (5.2)$$

where the pre-factors a, b, c, d, e and f are given for two temperature ranges: for the low temperature range $(C_{P-Empirical})_L$ (0 to 305 K) a = -118.22, b = -926.286, c = 23.0536, d = -0.5756, e = 0, f = 0, and for the high temperature range $(C_{P-Empirical})_H$ (305 to 1012 K) a = 365.6705, b = -32.719, c = -13.2313, d = 0.2147, e = 0 and f = 1,210,44.0. Using $C_{P-Empirical} = \left(C_{P-Empirical}\right)_L + \left(C_{P-Empirical}\right)_H$ and the experimental C_P-data, the excess C_P $\left(\Delta C_P = C_P - C_{P-Empirical}\right)$ was then computed, shown in Figure 5.5a. The red dash line in Figure 5.5a corresponds to the hard-mode behavior.

In Figure 5.4c, using as an example the PE-F_T phase transition, shows how the $C_{P-Empirical}$ (green dash-line) intercepts the C_P-data. The C_P-data above this line describes the contribution of the phase transition to C_P, or (ΔC_P). The same analysis was carried out for the F_O-F_R and F_T-F_O inter-ferroelectric phase transitions shown in Figure 5.4a and 5.4b, respectively. The corresponding enthalpy and entropy for each phase transition using $T_{e\text{-}L}$ and $T_{e\text{-}R}$ as limit of integration are also shown in Table 5.2.

Table 5. 2 Thermal properties from heat capacity measurement of depoled $BaTiO_3$ single crystal

		Contribution between Onset/offset limits				Contribution between derivative limits				Contribution between the limits of $C_P(Empirical)$ intercepting the C_P-data			
Phase Transition	T_{max} (K)	A^a (K)	B^a (K)	H^b A-B[a]	S^b A-B[a]	C^a (K)	D^a (K)	H^b C-D	S^b C-D	E^a (K)	F^a (K)	H^b E-F	S^b E-F
F_O-F_R	199	198	200	47	0.237	198	202	71	0.358	188	207	90	0.475
F_T-F_O	290	288	291	87	0.302	288	292	152	0.528	273	295	177	0.648
PE-F_T	405	403	409	124	0.308	403	414	187	0.463	361	422	364	1.007

Literature values

	$T_{transition}$ (K)	$H_{Transition}$ (J/mol)	$S_{Transition}$ (J/mol-K)
O-R	183 - 202[3–5]	33.4 - 59.8[3,4,39]	0.167 - 0.158[3,4,39]
T-O	273 – 289[3–6]	64.8 - 108.7[3,4,6,11,39]	0.226 - 0.4[3,6,11,39]
C-T	397-408[5–9,12]	221.5 - 232[6,9]	0.502 - 0.55[4,6,11,39]

[a]The notations A-B, C-D and E-F are temperature limits of integration corresponding to the onset (A) and offset (B) temperatures, to the change in the derivative of C_P with temperature from a constant value from the left (C) and from the right (D) around the peak transition and to the intersection of the empirical function with the C_P-data from the left (E) and from the right (F) of the a transition peak, respectively.
[b]Enthalpy (H) and entropy (S) units are J/mol and J/mol-K, respectively.

As a consequence, there were revealed three different transition energies for each phase transition. Those transition energies are delimited by the temperature limits: T_{Onset}-T_{Offset}, $T_{d\text{-}L}$ - $T_{d\text{-}R}$ and $T_{e\text{-}L} - T_{e\text{-}R}$. It is of relevant since all contributions to the inter-ferroelectric and PE-F_T phase transitions may be quantifies and better compare with literature. As an example, Todd and Lorenson report the energy for the inter-ferroelectric phase transition of $BaTiO_3$ single crystal obtained from the derivative limit.[3] Shirane and Takeda used broken lines or dash lines as a linear background to set the integration limits for the transition energies.[4] Egorov et al obtained the energy of transition from the temperature limits where the temperature dependences of the DSC signal change respect to the peak area.[6] It is the same as the deviation from zero of the derivative of C_P approaching the phase transition from the left or from the right. In average, for the PE-F_T phase transition, the transition temperatures, enthalpies and entropies determined from the limit of integration respect to the derivative of C_P ($T_{d\text{-}L}$ - $T_{d\text{-}R}$) are in good agreement with those reported

from literature. However, for the inter-ferroelectric transition (F_T-F_O and F_O-F_R), the T_{Offset}-T_{Onset} temperature limits for the determination of the enthalpies, entropies and transition temperatures are in better agreement with literature. The energy obtained from these limit of integration (T_{Offset}-T_{Onset} and or $T_{d\text{-}L}$ - $T_{d\text{-}R}$) is associated with the energy at the phase transformation, related to the latent heat. However, as the temperature is increased, before this abrupt changes in energy, there is an incrementing energy associated with the intrinsic crystal and domain reconfiguration. It is revealed as a tail, in the C_P-data, before the phase transition with $T_{e\text{-}L}$ as its onset. The energy obtained from $T_{e\text{-}L} - T_{e\text{-}R}$ is then the total energy of the transition.

The excess free energy ($G^{XS}(T)$) of the system may be determined from Equation 5.3:

$$\boldsymbol{G^{XS}(T) = \int \Delta C_P(T) dT - T\left[\int \frac{\Delta C_P(T)}{T} dT\right]} \quad (5.3)$$

where the first integral term corresponds to the excess enthalpy, $H^{XS}(T)$, and the second integral term to the excess entropy, $S^{XS}(T)$. The excess thermodynamic properties $H^{XS}(T)$, $S^{XS}(T)$ and $G^{XS}(T)$ are shown as a function of temperature in Figure 5.5b, 5.5c and 5.5d, respectively. It is to be noted a sharp and clear jump in enthalpy and entropy at the phase transition points. Also, it was observed the temperature dependence behavior of the thermodynamic properties, especially from the curvature of the F_T-phase. At the inter-ferroelectric phase transition, the change in the slope of the $G^{XS}(T)$ is very small. In other words, the $G^{XS}(T)$ of $BaTiO_3$ single crystal, appears to be continuous between ferroelectric phases. It is an indication of the small variation in the volume expansion as previously discussed.

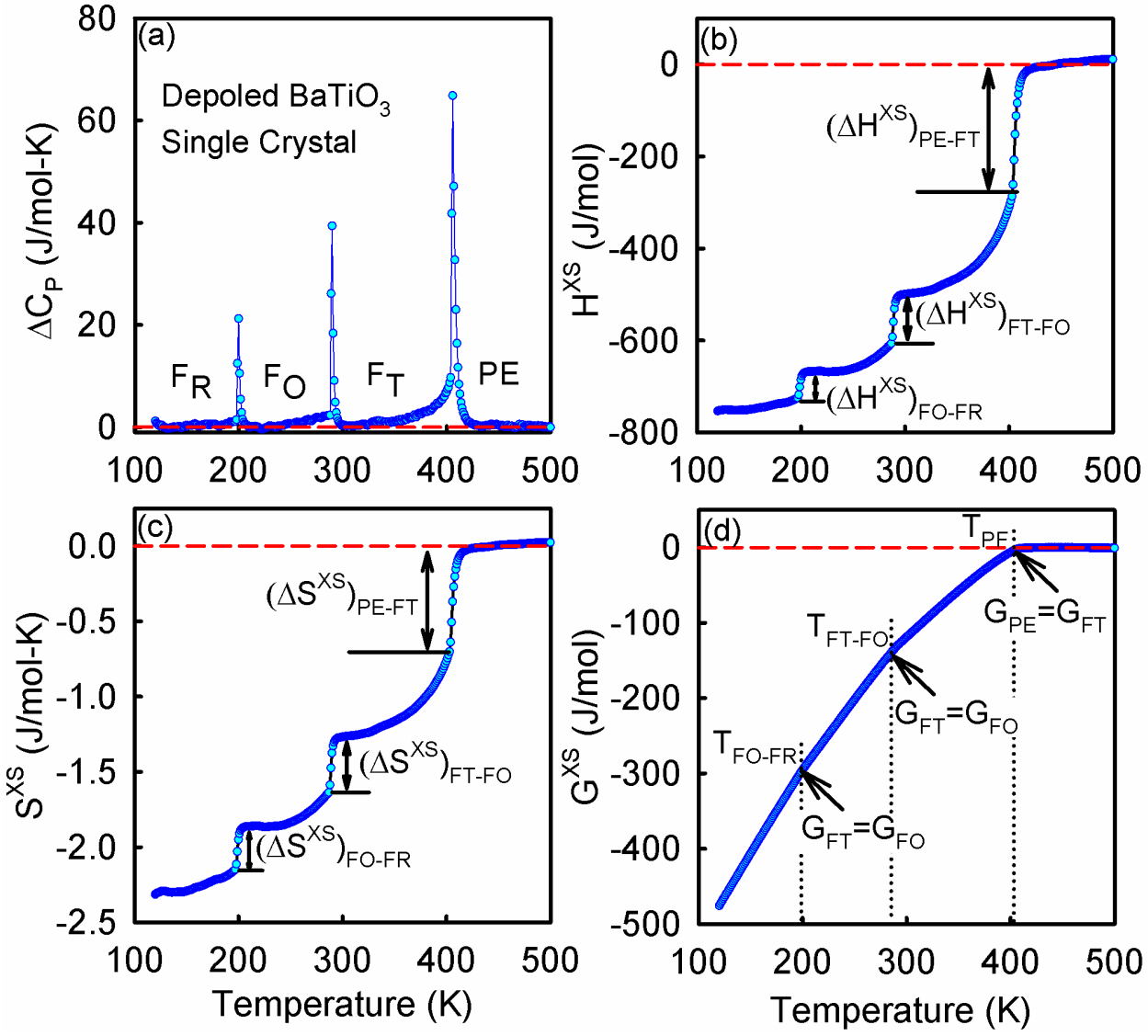

Figure 5. 5 Excess thermodynamic quantities associated with the phase transition as a function of temperature. (a) excess heat capacity (ΔC_P), (b) excess enthalpy (H^{XS}), (c) excess entropy (S^{XS}) and (d) excess free energy (G^{XS}).

The abrupt change in the heat capacity at T_{PF} is followed, from T_{peak}, by a "tail" up to $T_{e\text{-}R}$ in the paraelectric phase. It had been demonstrated to be associated with intrinsic properties of the $BaTiO_3$ single crystal.[13,14] This pretransitional phenomena has been observed in the temperature dependence of the birefringence,[15,40] thermal expansion,[16,41] second harmonic generation[42],

Brillion frequency shit[43,44] and had been associated with the appearance of local polar nanoregions in the symmetric paraelectric phase.[15,17,45] This pretransitional phenomenon was also observed from the thermal expansion shown in Figure 5.2. The inset in Figure 5.2, shows a deviation of the PE-phase to the fit line at 460 K. This deviation is commonly found in relaxor ferroelectric materials and is associated with their onset of polarization.[16] This depolarization temperature, T_d, had been found by optical index of refraction in cubic $BaTiO_3$ by Burns and Dacol below 453.15 K in which they noticed a marked deviation from linearity associated with local polarization and elastic distortions due to electro-optic effect.[27] This temperature is also call the Burns temperature (T_B), Recently, A. Ziebinska et al., found the $BaTiO_3$ single crystal was birefringence over a very broad temperature range and those birefringence disappears in the 433.15 – 443.15 K range[15]. They associated it with the disappearing of a stable precursor clusters possible originated from a specific temperature where order-disorder and displacive phase transition coexist. One could infer that, even dough it is a normal ferroelectric material, the onset of polarization in this system is 45 to 60 degree after T_{PF}. This temperature, especially in a normal ferroelectric material such as $BaTiO_3$, had been shown as structural defects in the material. However, Gorev et al, shows a deviation of the strain from regular behavior and the appearance of nonzero polarization in the solid solution $Ba_{1-x}La_xTi_{1-x/4}O_3$ near 420 K, which remain almost unchanged for the lanthanum concentration increase.[26]

The analytical form of the temperature dependence of the corresponding physical quantities of this pretransitional phenomenon had been given by the measurement elastic stiffness, as a logarithmic temperature dependence,[44] and measurements of the heat capacity, as a $(T - T_0)^{-1/2}$ dependence[13], for $BaTiO_3$ single crystal. The latter, is related to the fluctuation phenomena in multiaxial ferroelectrics (such as $BaTiO_3$).[14] Grabovsky et al., shown the intrinsic contribution of

this pretransitional phenomenon in the paraelectric phase from based on the single crystal grown by Remeika-type and top-seeded solution growth (TSSG) crystal methods comparison. Since the $(T - T_0)^{-1/2}$ dependence to the excess heat capacity, where T_0 was used as the paraelectric to ferroelectric phase transition temperature (T_{PF}), the theory of the fluctuation phenomena for the nonferroelectric and for the multiaxial ferroelectric such as $BaTiO_3$[14]

$$\Delta C_P^{fl} = \frac{k_B T^2 \alpha^{3/2}}{8\pi\delta^{3/2}}(T - T_0)^{-1/2} \quad (5.4)$$

where k_B is the Boltzmann constant, $\alpha = 4\pi/C_{C-W}$ and C_{C-W} is the Curie-Weiss constant and δ is a correlation parameter that has a direct relation to the form of the vibrational spectrum of the crystal and is determined by the interaction of atoms which are displaced during the phase transition of the sublattices.[14] In thin films, this parameter determines the domain wall width and the polarization profile.[13] Our best fit to Equation 5.4 in the high temperature data above T_{peak} gives $\delta = 0.53x10^{-16}\ cm^2$, which compared well with 0.45x10^{-16} and 0.66x10^{-16} obtained by Grabovsky for the TSSG and Remeika crystal growth methods, respectively. Also, it compared well with the unit cell parameter a = 0.384 nm (~ 0.4 nm for $BaTiO_3$) by the classical relation $\delta \sim \alpha T_C a^2$.[30]

5.3 Summary

High accurately measurements of the heat capacity in $BaTiO_3$ single crystal were determined in a wide temperature range and agree well with that of Todd et al.,[3] and Coughlin,[35] which had been referenced by many authors as a base for theoretical models. The quality of the single crystal was characterized by its dielectric permittivity and thermal strain. The transition temperatures at the different phase transitions (PE-F_T, F_T-F_O and F_O-F_R) were determined from heat capacity, dielectric permittivity and thermal expansion and are shown in Table 5.1 and Table 5.2. The

anomalous contribution, associated with the phase transition, to the heat capacity was separated from its hard mode behavior by fitting the C_P-background to the Debye function and empirical equation. By assuming low energy contribution at the inter-ferroelectric phase transition, a continuous function to $G^{XS}(T)$, the fit to the Debye function gives θ_D = 555 K, which is in good agreement with that determined from the calculated lattice parameters and the relation between θ_D and the elastic constant.[38] Due to the deviation of the C_P to the Dulong-Petit limit, an empirical equation was then considered. As a consequence different limits of integration from ΔC_P were investigated and the $S^{XS}(T)$ and $H^{XS}(T)$ corresponding to the different limit of integration around the phase transition were determined. In general, for the PE-F_T phase transition, the transition temperatures, enthalpies and entropies determined from the limit of integration respect to the derivative of C_P ($T_{d\text{-}L}$ - $T_{d\text{-}R}$) are in good agreement with those reported from literature. However, for the inter-ferroelectric transition (F_T-F_O and F_O-F_R), the T_{Offset}-T_{Onset} temperature limits for the determination of the enthalpies, entropies and transition temperatures are in better agreement with literature. The energy contribution from those limits of integration are related to the Latent heat while the energy contribution determined from $T_{e\text{-}L} - T_{e\text{-}R}$ are related to the total energy of the phase transition. Lastly, the pretransitional phenomena observed as a "tail" in the symmetric paraelectric phase was attribute for some authors as local polar nanoregions. However, it was also found that it was associated with the fluctuation phenomena in multiaxial ferroelectrics.[13,14] Our fitting to the C_P data at the "tail" gives the parameter $\delta = 0.53x10^{-16}\ cm^2$ which is good agreement with that found by Grabovsky et al.[13] The classical relation $\delta \sim \alpha T_C a^2$ was also hold for $BaTiO_3$ single crystal.

5.4 References

1. Jona, F. & Shirane, G. *Ferroelectric Crystals*. (1962).

2. E. Salje. in *Phys. Prop. Thermodyn. Behav. Miner.* (Salje, E.) 75–119 (Dordrecht: Reidel, 1988).

3. Todd, S. S. & Lorenson, R. E. Heat Capacities at Low Temperatures and Entropies at 298.16 K of Orthotitanates of Barium and Strontium. *J. Am. Ceram. Soc.* **74,** 3764 (1952).

4. Shirane, G. & Takeda, A. Transition Energy and Volume Change at Three Transitions in Barium Titanate. *J. Phys. Soc. Japan* **7,** 1–4 (1952).

5. Key, H. F. & Voudsen, P. . *Philos. Mag.* **40,** 1019 (1949).

6. Egorov, V. M., Smirnova, E. P. & Lemanov, V. V. Calorimetry of $(1 - x)BaTiO_3$-xBa(Mg1/3Nb2/3)O3 solid solutions. *Phys. Solid State* **49,** 1528–1531 (2007).

7. Hatta, I. & Ikushima, A. Temperature Dependence of the Heat Capacity in BaTi03. *J. Phys. Soc. Japan* **41,** 558–564 (1976).

8. Lee, S., Rossetti, G. a., Liu, Z.-K. & Randall, C. a. Intrinsic ferroelectric properties of the nonstoichiometric perovskite oxide Ba[sub 1−x]Ti[sub 1−y]O[sub 3−x−2y]. *J. Appl. Phys.* **105,** 093519 (2009).

9. Bai, Y., Ding, K., Zheng, G.-P., Shi, S.-Q. & Qiao, L. Entropy-change measurement of electrocaloric effect of $BaTiO_3$ single crystal. *Phys. Status Solidi* **209,** 941–944 (2012).

10. Viehland, D., Jang, S. J., Cross, L. E. & Wuttig, M. Freezing of the polarization fluctuations in lead magnesium niobate relaxors. *J. Appl. Phys.* **68,** 2916 (1990).

11. Blattner, H., Kanzig, W. & Merz, W. . *Helv. Phys. Acta* **22,** 35 (1949).

12. Morimoto, K., Sawai, S., Hisano, K. & Yamamoto, T. Simultaneous measurement of specific heat, thermal conductivity, and thermal diffusivity of modified barium titanate ceramics. *Thermochim. Acta* **442,** 14–17 (2006).

13. Grabovsky, S. V, Shnaidshtein, I. V, Takesada, M., Onodera, A. & Strukov, B. A. Calorimetric study of multiaxial fluctuations in ferroelectric BaTiO 3 in nonpolar cubic phase. *cond-mat.mtrl-sci* 2–6 (2013).

14. Strukov, B. A. & Levanyuk, A. P. *Ferroelectric Phenomena in Crystals: Physical Foundations*. (Springer-Verlag, 1998).

15. Ziębińska, a, Rytz, D., Szot, K., Górny, M. & Roleder, K. Birefringence above T c in single crystals of barium titanate. *J. Phys. Condens. Matter* **20,** 142202 (2008).

16. Cross, L. E. Relaxor Ferroelectrics. *Ferroelectrics* **76,** 241–267 (1987).

17. Dul'kin, E., Roth, M., Janolin, P.-E. & Dkhil, B. Acoustic emission study of phase transitions and polar nanoregions in relaxor-based systems: Application to the PbZn1⁄3Nb2⁄3O3 family of single crystals. *Phys. Rev. B* **73,** 012102 (2006).

18. Merz, W. J. The Electric and Optical Behavior of $BaTiO_3$ Single-Domain Crystals. *Phys. Rev.* **76,** (1949).

19. Shebanov, L. A. X-Ray Temperatures Study of Crystallographic Characteristics of Barium Titanate. *Phys. Status Solidi* **65,** 321–325 (1981).

20. Choi, K. J. . *Science (80-.).* **306,** 1005 (2004).

21. Edwards, J. W. . *J. Am. Chem. Soc.* **73,** (1951).

22. Jaffe, B., Cook, W. R. & Jaffe, H. *Piezoelectric Ceramics*. 53–183 (Academic Press, 1971).

23. Sawada, S. & Shirane, G. Specif Heat and Thermal Expansion of $BaTiO_3$. *J. Phys. Soc. Japan* **4,** 52–56 (1948).

24. Wang, Y. L. *et al.* Landau thermodynamic potential for BaTiO[sub 3]. *J. Appl. Phys.* **101,** 104115 (2007).

25. Kanzig, W. & Meier, R. . *Helv. Phys. Acta* **22,** 585 (1949).

26. Gorev, M. V., Flerov, I. N., Sciau, P. & Guillemet-Fritsch, S. Thermal Expansion of (Ba1-xLax)Ti1-x/4O3 Solid Solutions. *Phys. Solid State* **51,** 746–752 (2009).

27. Burns, G. & Dacol, F. H. Crystalline ferroelectrics with glassy polarization behavior. *Phys. Rev. B* **28,** 2527–2530 (1983).

28. Merz, W. J. Double Hysteresis Loop of $BaTiO_3$ at the Curie Point. *Phys. Rev.* **91,** 513–517 (1953).

29. Drougard, M. E. & Young, D. R. . *Phys. Rev.* **95,** 1152 (1954).

30. Bednyakov, P. S., Shnaidshtein, I. V. & Strukov, B. a. Investigation of the dielectric properties of $BaTiO_3$ single crystals of different qualities by the thermal noise method. *Phys. Solid State* **53,** 350–357 (2011).

31. Lawless, W. N. . *Phys. Rev. B1* **36,** 134 (976).

32. Hortal, M. The Speciic-Heat of $BaTiO_3$ at Low-Temperatures. *Ferroelectrics* **54,** 653–656 (1984).

33. Footer, M. C. & Anderson, A. C. . *Ferroelectrics* **62,** 11 (1985).

34. Villar, R., Gmelin, E. & Grimm, H. Specific Heat of Crystalline ferroelectric at low temperatures. *Ferroelectrics* **69,** 165–178 (1986).

35. Coughlin, J. P. & Orr, R. L. High Temperature Heat Contents of Meta- and Orthotitanates of Barium and Strontium. *J. Am. Ceram. Soc.* **75,** 530–531 (1953).

36. Debye, P. . *Ann. Phys.* **39,** 789–839 (1912).

37. Kwei, G. H., Lawson, A. C., Billinge, J. L. & Cheong, S.-W. Structure of the Ferroelectric Phase of Barium Titanate. *J. Phys. Chem.* **97,** 2368–2377 (1993).

38. Sanna, S., Thierfelder, C., Wippermann, S., Sinha, T. P. & Schmidt, W. G. Barium titanate ground- and excited-state properties from first-principles calculations. *Phys. Rev. B* **83,** 054112 (2011).

39. Volger, J. . *Philips Res. Repts.* **6,** 21 (1952).

40. Takagi, M. & Ishidate, T. Anomalous birefringence of cubic $BaTiO_3$. *Solid State Commun.* **113,** 423–426 (2000).

41. Rusek, K. *et al.* Non-Linear Properties of BaTiO 3 above T C. *Ferroelectrics* **375,** 165–169 (2008).

42. Pugachev, a. M. *et al.* Broken Local Symmetry in Paraelectric BaTiO_{3} Proved by Second Harmonic Generation. *Phys. Rev. Lett.* **108,** 247601 (2012).

43. Ko, J.-H. *et al.* Elastic softening and central peaks in BaTiO[sub 3] single crystals above the cubic-tetragonal phase-transition temperature. *Appl. Phys. Lett.* **93,** 102905 (2008).

44. Ko, J.-H. *et al.* Logarithmic temperature variations of the elastic constant of barium titanate near the ferroelectric phase transition. *Curr. Appl. Phys.* **12,** 1185–1189 (2012).

45. Namikawa, K. *et al.* Direct Observation of the Critical Relaxation of Polarization Clusters in $BaTiO_3$ Using a Pulsed X-Ray Laser Technique. *Phys. Rev. Lett.* **103,** 197401 (2009).

CHAPTER 6

THERMODYNAMIC THEORY OF THE PHASE TRANSITION ENERGETIC OF BARIUM TITANATE FROM HEAT CAPACITY

6.1 Introduction

The thermodynamic theory of $BaTiO_3$ had been well established by Devonshire who first try to unify the sequence of crystallographic ferroelectric phase transformation through the observed changes in dielectric, thermal and piezoelectric properties.[1,2] The crystallographic sequence of phase transformation in $BaTiO_3$ (paraelectric (PE) cubic – ferroelectric tetragonal (F_T) – ferroelectric orthorhombic (F_O) – ferroelectric rhombohedral (F_R)) can be perceived from its original parent cubic (m3m point group) perovskite-type crystal structure PE-phase. Distortions relative to the original cubic perovskite-type crystal structure, as the temperature is decrease, results in low symmetry ferroelectric phases with crystallographic point groups 4mm, mm, 3m which had been found to occur at the transition temperatures 120 ^oC (the Curie temperature = T_C), 5 ^oC and -90 ^oC, respectively.[3] This three crystallographic distortions give rise to the spontaneous polarization, P_s, with six equivalent directions along $\langle 100 \rangle$, eight along $\langle 110 \rangle$ and 12 along $\langle 111 \rangle$ directions, respectively.

The spontaneous polarization is often used as the thermodynamic order parameter for ferroelectric materials under certain boundary conditions. In the simplest approximation it can be associated with the excess entropy of the system. Within the scope of the Ginzburg-Landau thermodynamic theory, Salje demonstrated from heat capacity measurements, the relative magnitude of the 2-4-6 Landau polynomial coefficients in its low order approximation, close to T_C, for phase transition energetic represented as a first-order transition, second order-transition and

tricritical points.[4] The range of applicability below T_C, from this approach, had been found to be of several degrees (~10 degrees) from different perovskite-type ferroelectric crystals.[5] This method had been successfully applied to the energetic in Lead Titanate single crystal.[6]

Alternative expressions from the original 2-4-6 polynomial as applied by Devonshire to $BaTiO_3$ bulk single crystal have been reported to provide varying degrees of agreement with experiment.[1,2,7–11] It includes temperature independent 2-4-6 Landau polynomial by Devonshire,[1,2] temperature dependent 2-4-6 polynomial by Buessem et al[10]., and modified by Bell,[7,8] temperature independent 2-4-6-8 polynomial by Li et al.,[11] and temperature dependent 2-4-6-8 polynomial by Wang et al..[9] In general, any form of the Landau polynomial provide similar very small transitions points or a continuous polarization at ferroelectric to ferroelectric (inter-ferroelectric) transitions.[12,13] A. A. Heitmann and G. A Rossetti, proposed a low crystallographic anisotropy at inter-ferroelectric phase transitions in $BaTiO_3$, and showed that the polarization is nearly continuous across all temperatures.[12–14] It was previously demonstrated from the pseudocubic lattice parameter in $BaTiO_3$ single crystal.[15] Similar conclusion had been shown in morphotropic phase boundary ferroelectric systems between the low symmetry ferroelectric rhombohedral and tetragonal phases.[16,17]

In the case of the order of the Landau polynomial, it was shown that an accurate description of the free energy of $BaTiO_3$ can be achieved by truncated the polynomial to six-order and to include necessary temperature parameters.[12,18] Recently, Xiaoyan Lu et al., shown the convergence of the 6-order Landau polynomial convergence, in reduce form, for bulk single crystal ferroelectrics to the complex polarization-electric field and dielectric-electric field loops in temperatures around T_C. They also stand out, based on the number of terms in the Landau expansion and their temperature dependence, that those Landau parameters given by Buessem et

al.[10] and modified by Bell et al.,[8] were more reasonable for single bulk crystal. However, more accurate parameters for bulk single crystal still need further investigation.

In this chapter, the temperature dependence coefficients of the 2-4-6 Landau polynomial, based on the crystallographic anisotropy of polarization approach, were determined from an accurate wide temperature range measurements of the heat capacity of $BaTiO_3$ single crystal. Carefully analyses of the heat capacity together with the dielectric permittivity around the PE-F_T, the temperature dependence of the excess entropy in the F_T-phase and the weakly F_T-F_O and F_O-F_R first-order phase transitions points were subsequently followed in order to determine the coefficients of the Landau thermodynamic potential. The calculated excess entropy ($S^{XS}(T)$) excess enthalpy ($H^{XS}(T)$) and excess free energy ($G^{XS}(T)$) from the Landau free energy, ΔG_L, were compared with those determined from experiment and the temperature dependence of the calculated polarization was compared with literature from those based on bulk single crystal. A relative stability phase diagram of the quartic and sextic order Landau coefficients proposed by Heitmann and Rossetti,[13,14] based on the isotropic and anisotropic contributions to the free energy, were used to demonstrate the low crystallographic anisotropic of polarization between ferroelectric phases. Finally, the excess contribution to the thermal strain in $BaTiO_3$ single crystal was used to verify the Landau coefficients in the low order approximation close to the T_C and to validate the determined temperature dependence of the of the polarization. Thereby, the electrostriction coefficients along the different crystallographic directions in the F_T-phase were also determined.

6.2 Results

6.2.1 Crystallographic anisotropy of polarization

The Devonshire notation of the Ginzburg-Landau theory for perovskite ferroelectric materials may be re-express in terms of the isotropic and anisotropic contribution to the total free energy by fallowing similar approach as used by Khachaturyan and Rossetti[13,17,19] and also used in the following references.[12,16,20,21] Since of the experimental conditions to determined ΔC_P, the boundary conditions in which the total free energy is under no applied stress and no applied electric field may be considered, which results in the Landau free energy $\left(\Delta G_L(T, \boldsymbol{P})\right)$. In this case, the calculated excess free energy from the heat capacity $G^{XS}(T, \boldsymbol{P})$, shown previously in Equation 5.5, must be equal to the $\Delta G_L(T, \boldsymbol{P})$.

In the Devonshire notation to the Landau free energy,[1,2] the contribution to the polarization may be separated, $\boldsymbol{P} = \boldsymbol{n}P$, where $\boldsymbol{n} = \{n_1, n_2, n_3\}$ is a unit vector in the direction of the polarization, $\boldsymbol{P}$, and $P = |\boldsymbol{P}|$ its magnitude. The direction of the polarization vector, $\boldsymbol{n}$, may be treated as an internal thermodynamic variable that relax as a function of temperature (or composition) to its equilibrium value, $\boldsymbol{n}_\theta^{eq}$, where θ is the ferroelectric phase. The easy polarization or the equilibrium direction, $\boldsymbol{n}^{eq}$, follows $\boldsymbol{n}_1^2 + \boldsymbol{n}_2^2 + \boldsymbol{n}_3^2 = 1$. Consequently, if the easy polarization directions are parallel to a 4-fold, 2-fold or 3 fold axis then for F_T-phase $\boldsymbol{n}_T^{eq} = \{0,0,1\}$, for the F_O-phase $\boldsymbol{n}_O^{eq} = \left\{\frac{1}{\sqrt{2}}, \frac{1}{\sqrt{2}}, 0\right\}$ and for the F_R-phase $\boldsymbol{n}_R^{eq}[111] = \left\{\frac{1}{\sqrt{3}}, \frac{1}{\sqrt{3}}, \frac{1}{\sqrt{3}}\right\}$, respectively.[14] From the Devonshire notation, after substitution of $\boldsymbol{P} = \boldsymbol{n}P$ and factorization, the Landau free energy can be re-write as:

$$\Delta G_L(T, P, n) = \frac{1}{2}A_o(T - T_C)P^2 + \frac{1}{4}[B_1 + B_2\boldsymbol{\Gamma_4}]P^4 + \frac{1}{6}[C_1 + C_2\boldsymbol{\Gamma_6} + C_3\boldsymbol{\Gamma_6'}]P^6 \qquad (6.1)$$

where A_o, related to the Curie-Weiss constant, and T_C were obtained from the dielectric permittivity measurement, previously determined from Equation 5.1 and shown in Table 5.1,

$B_1, C_1\ and\ C_3 = constant, \quad B_2 = f(T) = B_2' + B_2''(T - T_C), \quad C_2 = f(T) = C_2' + C_2''(T - T_C),$ $\boldsymbol{\Gamma_4} = (\boldsymbol{n}_1^4 + \boldsymbol{n}_2^4 + \boldsymbol{n}_3^4), \boldsymbol{\Gamma_6} = (\boldsymbol{n}_1^6 + \boldsymbol{n}_2^6 + \boldsymbol{n}_3^6)$ and $\boldsymbol{\Gamma_6'} = (\boldsymbol{n}_1^2\boldsymbol{n}_2^2\boldsymbol{n}_3^2)$. The temperature dependence of the quartic and sextic terms of $\Delta G_L(T, P, \boldsymbol{n}) = G^{XS}(T, P, \boldsymbol{n})$ were determined from the temperature evolution of the $S^{XS}(T)$, previously experimentally determined and shown in Equation 5.5, in the F_T-phase, $S_T^{XS}(T)$, to be discuss in following sections. The excess entropy and the equation of state are given by Equation 6.2 and Equation 6.3, respectively.

$$\left[\frac{\partial G^{XS}(T,P,\boldsymbol{n})}{\partial T}\right]_P = -S^{XS}(T, P, \boldsymbol{n}) \tag{6.2}$$

$$\left[\frac{\partial G^{XS}(T,P,\boldsymbol{n})}{\partial P}\right]_T = 0 \tag{6.3}$$

where in general the polarization for the different ferroelectric phases (ϕ) can be represented as

$$P_\phi^2(T, \boldsymbol{n}) = \frac{-[B_1 + B_2\boldsymbol{\Gamma_4}] + \sqrt{[B_1 + B_2\boldsymbol{\Gamma_4}]^2 - 4A_o(T - T_C)[C_1 + C_2\boldsymbol{\Gamma_6} + C_3\boldsymbol{\Gamma_6'}]}}{2[C_1 + C_2\boldsymbol{\Gamma_6} + C_3\boldsymbol{\Gamma_6'}]} \tag{6.4}$$

Now, $G^{XS}(T, P, \boldsymbol{n})$ can be easily separates in the isotropic contribution, $[G^{XS}(T, P)]_{ISO}$, which is independent of the polarization direction similar to a polar glass, and in the anisotropic contribution, $\left[G_\phi^{XS}(T, P, \boldsymbol{n})\right]_{ANISO}$, which includes the equilibrium direction dependence of the polarization vector. From Equation 6.1 and 6.4:

$$[G^{XS}(T, P)]_{ISO} = \frac{1}{2}A_o(T - T_C)P^2 + \frac{1}{4}B_1P^4 + \frac{1}{6}C_1P^6 \tag{6.5}$$

$$\left[G_T^{XS}\left(T, P_T, n_T^{eq}\right)\right]_{ANISO} = \frac{1}{4}B_2P_T^4 + \frac{1}{6}C_2P_T^6 \tag{6.6}$$

$$\left[G_O^{XS}\left(T, P_O, n_O^{eq}\right)\right]_{ANISO} = \frac{1}{8}B_2P_O^4 + \frac{1}{24}C_2P_O^6 \tag{6.7}$$

$$\left[G_R^{XS}\left(T, P_R, n_R^{eq}\right)\right]_{ANISO} = \frac{1}{12}B_2P_R^4 + \frac{1}{54}\left(C_2 + \frac{1}{3}C_3\right)P_R^6 \tag{6.8}$$

which mean that A_o, B_1 and C_1 are the isotropic coefficients and B_2, C_2 and C_3 are the anisotropic ones. The polarization, P, for $[G^{XS}(T, P)]_{ISO}$ is the total polarization corresponding to Equation

6.1. For comparison, Table 6.1 shows the relationship of the isotropic and anisotropic Landau coefficients by this approach, Equation 6.1, with the Devonshire notation.

Table 6. 1 Comparison of the Landau coefficients from the Devonshire notation and Equation 6.1

α_1	$A_o(T-T_C)/2$
α_{11}	$(B_1+B_2)/4$
α_{111}	$(C_1+C_2)/6$
α_{12}	$B_1/2$
α_{112}	$C_1/2$
α_{123}	$(6C_1+C_3)/6$

6.2.2 Low order approximation to the Landau free energy

Equation 6.1 results asymptotically accurate as approaching T_C. It corresponds to the low order approximation of the Landau theory as $T \to T_C$. As approaching the discontinuous PE-F_T phase transition, it fallows from Equation 6.1 that:

$$G_T^{XS}(T \to T_C, P_T) = \frac{1}{2}A_o(T-T_C)P_T^2 + \frac{1}{4}B_oP_T^4 + \frac{1}{6}C_oP_T^6 \tag{6.9}$$

where $B_o = B_1 + B_2'$ and $C_o = C_1 + C_2'$, consistently with Equation 6.1. In this particular case, the experimental data close to PE-F_T transition in Equation 5.5a, by rearranging Equation 6.9 from Equation 6.2, may be analyzed by Equation 6.10:[4]

$$F(S^{XS}) = \frac{4}{3}\left[1 - \left(\frac{3T_{PF}S^{XS}(T\to T_C)}{2L} - 1\right)^2\right] = \frac{T-T_C}{T_{PF}-T_C} \tag{6.10}$$

where $L = 260\ J/mol$ is the latent heat at the first-order phase change. Close to T_{PF}, the function $F(S^{XS})$, shown in Figure 6.1, can be represented by straight line in the temperature range where $0 < F(S^{XS}) < 1$. A linear fit on this region is associated with the last term in Equation 6.10 where $T_C = 391\ K$ can be found at $F(S^{XS}) = 0$ and $T_{PF} = 405\ K$ can be obtained from the slope $m =$

$(T_{PF} - T_C)^{-1}$. In the left side of Equation 6.10, the initial input parameter $T_{PF} = 405\ K$ came from the inverse dielectric permittivity, Equation 5.1b, and the parameters L and $S^{XS}(T)$, from the experimental data in Figures 4.5b and 4.5c, respectively. It is to be noted that the parameter L, initially $L = 287\ J/mol$, is an adjustable parameter. It is related to the thermodynamic equilibrium at the phase transition which may be reach, theoretically, with an extremely slow temperature rate during experiment. By using $L = 260\ J/mol$, the relation among critical temperatures $T^* = T_{PF} + (T_{PF} - T_C)/4 = 407.7\ K$ is satisfied [A1]. The temperature T* is the highest temperature for which the zero field ferroelectric phase can exist in a metastable state.[22]

Also, the experimental data in Equation 5.5a close to T_{PF}, may be represented by $\Delta C_P = T(\partial S^{XS}(T \to T_C)/\partial T)$. In the general form for a first-order transition,[4,5] it can be rewrite as:

$$\left(\frac{\Delta C_P(T \to T_C)}{T}\right)^{-2} = \frac{4\left(B_o^2 - 4A_o(T_{PF} - T_C)C_o\right)}{A_o^4} + \frac{16C_o}{A_o^3}(T_{PF} - T) \qquad (6.11)$$

The left side of Equation 6.11 is plot in Figure 6.1b in the same temperature range as $F(S^{XS})$. It was fitted to a linear regression in which its extrapolation to the temperature axis gives $T^* = 408\ K$ in agreement with the relation among critical temperatures. It follows, from the right side of Equation 6.11, that the jump (Δ) at T_{PF}, which defines the discontinuity, and the slope (λ) are given by $\Delta = \frac{4\left(B_o^2 - 4A_o(T_{PF} - T_C)C_o\right)}{A_o^4} = 2.68\ x10^{-6}$ and $\lambda = \frac{16C_o}{A_o^3} = -6.84\ x10^{-7}$, respectively.

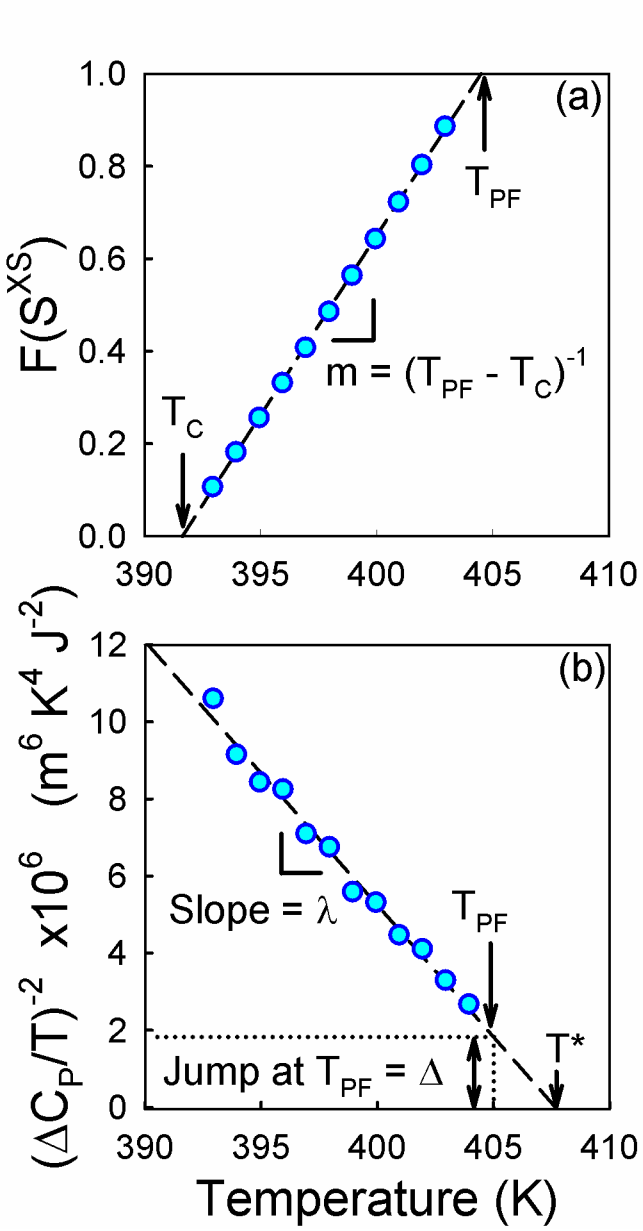

Figure 6.1: Low order approximation of Landau coefficients. (a) FSXS as a function of temperature. (b) Inverse of the squared of excess heat capacity over temperature as a function of temperature.

Simultaneous solution of Δ and λ give the high order Landau coefficients $B_o = 11.1x10^8 \frac{J}{m^5C^4}$ and $C_o = 2.21x10^{10} \frac{J}{m^9C^6}$ obtained from the low order approximation of ΔG_L. Table 6.2 shows a comparison of B_o and C_o with that obtained by Lee S. et al. from the defect concentration of the

intrinsic partial Schottky defects due to non- stoichiometry in $BaTiO_3$ as state by the Ginzburg–Landau theory of weak first-order phase transitions.[23]

Table 6. 2 Thermodynamic properties of the depoled $BaTiO_3$ single crystal

	Property	Units	
Second rank Landau pre-factor	A_o x10^5	Jm/C^2K^1	8.02[a], 8.17[23]
Fourth-rank Landau coefficient	B_o x10^8	Jm^5/C^4	-11.1[c, d], -9.85[b], -9.4[23]
Sixth-rank Landau coefficient	C_o x10^{10}	Jm^9/C^6	2.21[c, d], 2.30[b], 2.0[23]
Electrostriction Q_{ij}	Q_{11}	m^4/C^2	0.1015[b,c], 0.11 – 0.115[8,24–26]
	Q_{12}	m^4/C^2	-0.0338[b,c], -0.0452 - -0.033[8,24–26]

[a]This study from dielectric measurement.
[b]This study from thermal expansion measurement.
[c]This study from heat capacity measurement.
[d]Coefficient obtained from the low order approximation of the Landau theory.

6.2.3 Temperature dependence Landau coefficients

An extension from the above analysis far from the PE-F_T transition to lower symmetry phases, may results in an over estimation of the thermodynamic properties shown in Equation 5.5. To account for the temperature behavior far from the PE-F_T phase transition, it is necessary to expand the quartic and, if is necessary, the sextic terms of the Landau free energy as a function of temperature as was shown in Equation 6.1. The free energy of the F_T-phase is given by Equation 6.5 plus Equation 6.6. For the F_T-phase, since $B_o = B_1 + B_2'$ and $C_o = C_1 + C_2'$ were found from the previous low order approximation analysis, the only unknown coefficients are B_2'' and C_2''. In fact, these two Landau coefficients describe the temperature dependence of the thermodynamic properties. Taking this in consideration, the experimental entropy in the F_T-phase, shown in Equation 5.5c, can be described from Equation 6.2, resulting in the following expression:

$$\left\{-\boldsymbol{S_T^{XS}(T)}\right\}_{\boldsymbol{EXP}} = \left\{-\boldsymbol{S_T^{XS}(T)}\right\}_{\boldsymbol{CAL}} = \frac{\mathbf{1}}{\mathbf{2}}\boldsymbol{A_o P_T^2} + \frac{\mathbf{1}}{\mathbf{4}}\boldsymbol{B_2'' P_T^4} + \frac{\mathbf{1}}{\mathbf{6}}\boldsymbol{C_2'' P_T^6} \quad (6.12)$$

where $P_T^2 = P_T^2\left(T, \boldsymbol{n}_T^{eq} = \{0,0,1\}\right)$ determined from Equation 6.3. From a dynamic nonlinear regression fit of Equation 6.12 to the experimental $S_T^{XS}(T)$ data, in Equation 5.5c, the coefficients B_2'' and C_2'' were easily determined. Since the temperature dependence of the Landau free energy can be described by coefficients B_2'' and C_2'', the solution to Equation 6.1 was then found by equating thermodynamic relationships at inter-ferroelectric phase transitions. At F_T-F_O phase transition it is true that:

$$\boldsymbol{G_O^{XS}\left(T = T_{T-O}, P_O(T = T_{T-O}), n_O^{eq}\right) = G_T^{XS}\left(T = T_{T-O}, P_O(T = T_{T-O}), n_T^{eq}\right)} \quad (6.13)$$

and also that

$$\boldsymbol{\left\{\Delta S_{T-O}^{XS}\right\}_{EXP} = S_T^{XS}(T = T_{T-O}) - \left(\frac{1}{2}A_o P_O^2 + \frac{1}{8}B_2'' P_O^4 + \frac{1}{24}C_2'' P_O^6\right)_{T=T_{T-O}}} \quad (6.14)$$

where the only unknowns B_2' and C_2' can be found by simultaneous solution of Equation 6.13 and Equation 6.14. Similarly, it is true that at F_O-F_R phase transition:

$$\boldsymbol{G_R^{XS}\left(T = T_{O-R}, P_R(T = T_{O-R}), n_R^{eq}\right) = G_O^{XS}\left(T = T_{O-R}, P_O(T = T_{O-R}), n_O^{eq}\right)} \quad (6.15)$$

where C_3 can be determined. Table 6.3 shows the determined Landau coefficients as described in Equation 6.1.

Table 6. 3 Coefficients of $BaTiO_3$ Landau thermodynamic potential as described by the Equation 6.1

Coefficients		Units
A_o	8.02x10^5	Jm/C^2
B_1	-1.92x10^7	Jm^5/C^4
C_1	1.52x10^{10}	Jm^9/C^6
B_2'	-1.09x10^9	Jm^5/C^4
B_2''	9.54x10^6	Jm^5/KC^4
C_2'	6.83x10^9	Jm^9/C^6
C_2''	-1.68x10^8	Jm^9/KC^6
C_3	-2.00x10^{10}	Jm^9/C^6

Using these coefficients, the thermodynamic properties, $H^{XS}(T)$, $S^{XS}(T)$ and $G^{XS}(T)$, for all equilibrium and non-equilibrium ferroelectric phases were calculated and plotted in Figure 6.2a, 6.2b and Equation 6.2c, respectively. From the $H^{XS}(T)$ and $S^{XS}(T)$ it can be observed the temperature dependence captured from the F_T-phase as well as the very small jumps at the inter-ferroelectric transitions. Also, it was observed the vanishing at $T = T_C$ of $H^{XS}(T)$ and $S^{XS}(T)$ of the non-equilibrium F_R- and F_O-phases. From the $G^{XS}(T)$, in Figure 6.2c, it was revealed the temperature behavior of the equilibrium and non-equilibrium ferroelectric phases as well as the relative small variation in the free energy slope from one ferroelectric phase to other. The inset in Figure 6.2c shows the behavior of the free energy for the non-equilibrium F_R- and F_O-phases and the equilibrium F_T-phase. It is observed, graphically, the relationship among the critical temperatures T^*, T_C and T_{PF}.

The calculated temperature behavior of $H^{XS}(T)$, $S^{XS}(T)$ and $G^{XS}(T)$, shown in Figure 6.2a, 6.2b and 6.2c, which are in excellent agreement with the experimentally determined thermodynamic properties shown in Equation 5.5b, 4.5c and 4.5d, respectively. By using the Equation 6.4, relative to each ferroelectric phase, with the coefficients in Table 6.3, it is then possible to determine the temperature behavior of the polarization, shown in Figure 6.2d. The non-equilibrium ferroelectric phases are also shown as dot-lines. The jump in polarization ($\Delta P_{\alpha-\beta}$, where α and β are different phases) between the phases reveals the presence of a spontaneous polarization at the PE-F_T phase transition and a crystallographic anisotropy of polarization at the inter-ferroelectric phase transitions. The spontaneous polarization was found to be $\Delta P_{PE-FT}(T = T_{PF} = 405K) = 0.18\, C/m^2$, in good agreement with Merz $P_s(C/m^2) = 0.155 \pm 0.015$.[27] Very small change in polarization between ferroelectric phases or very small polarization jumps at inter-ferroelectric transition were determined; $\Delta P_{FT-FO}(T = T_{FT-FO}) = 0.022\ C/m^2$ and

$\Delta P_{FO-FR}(T = T_{FO-FR}) = 0.011\ C/m^2$. These very small jumps at inter-ferroelectric transition confirm the vanishing of crystallographic anisotropy of polarization in which near-polarization continuity between ferroelectric phases may be assumed.[13,17,19]

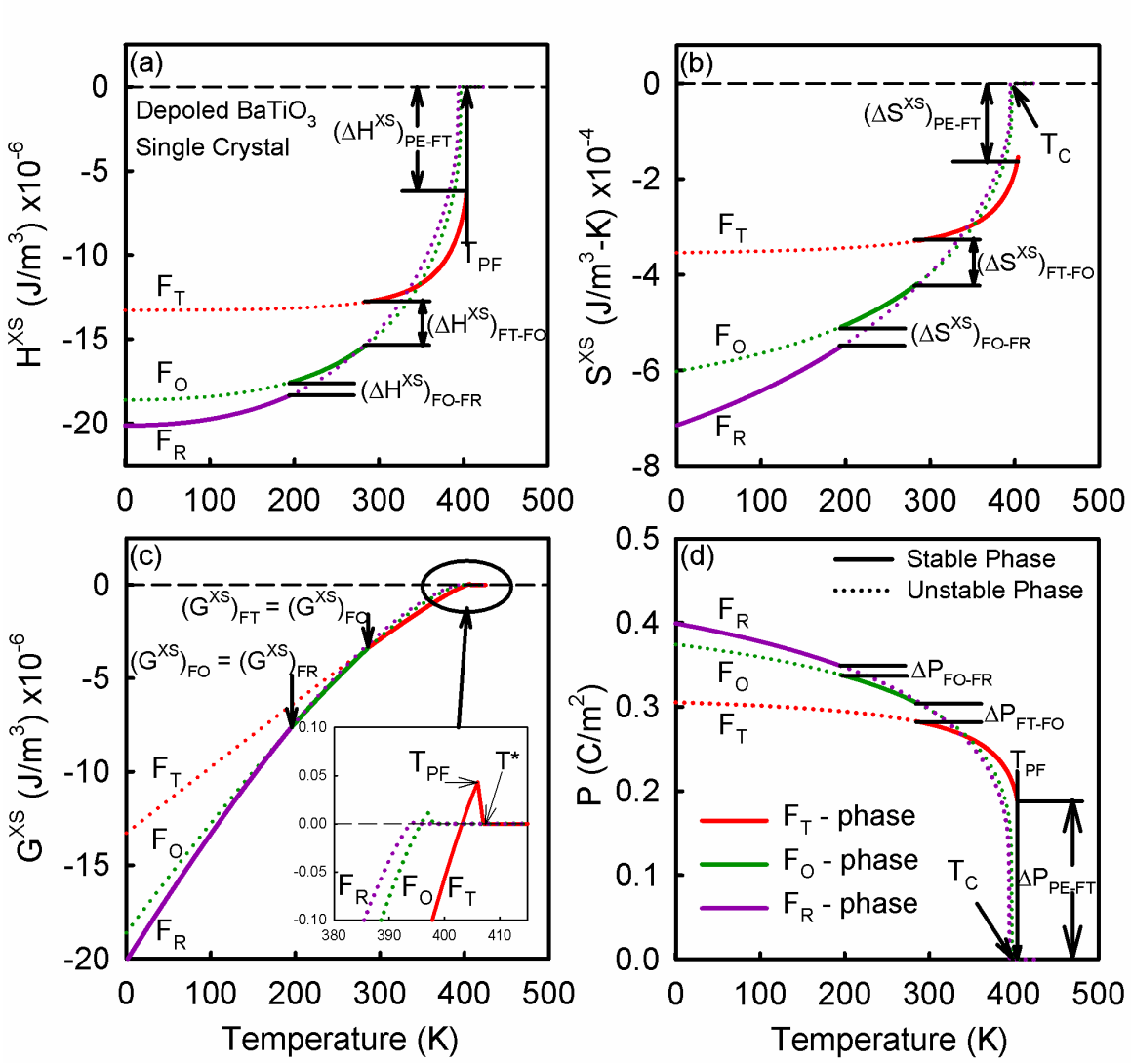

Figure 6.2: Calculation of excess thermodynamic quantities associated with the phase transitions as a function of temperature. (a) Excess enthalpy (H^{XS}), (b) Excess entropy (S^{XS}), (c) excess free energy (G^{XS}) and (d) reversible polarization.

6.3 Discussion

6.3.1 Temperature dependence of the polarization and Landau coefficients

The calculated temperature dependence of the polarization for $BaTiO_3$ single crystal is compared in Figure 6.3 with several other polarization from the Landau expression that had been previously reported from literature. It was compared by the polarization determined from the temperature independent 2-4-6 Landau polynomial propose by Devonshire,[1,2] a temperature dependent 2-4-6 Landau polynomial given by Bell,[8] a temperature independent 8^{th} order polynomial determined by Li et. al.,[11] and a temperature dependent 8^{th} order polynomial proposed by Wang et. al..[9] Independently of the polynomial order and its temperature dependence, the polarization is nearly continuous across all temperatures. In this study, the Landau polynomial was consider as a temperature dependent in the quadratic, quartic and sextic terms in order to reproduce and have a better agreement with the experimentally determined thermodynamic properties, shown in Equation 5.5.

Several observations may be address from this comparison. The jump in polarization at the inter-ferroelectric transitions compare well with that determined by Devonshire. Comparing with Bell and Cross, the jump in polarization at the inter-ferroelectric transition is about two times the ones found in this study. On the other hand, the temperature dependence of the polarization in this study is comparable with that of Bell and Cross which it is captured by the F_T-phase. The polarization behavior from the 8^{th}-order Landau Polynomial approach by Wang et al., seems to underestimate the polarization behavior. Inversely, the temperature independent 8^{th} order Landau Polynomial approach by Li Y. L. et al, seems to overestimate the polarization behavior as was the case for the low order approximation analysis discussed previously. In the low order approximation, high order terms are considered temperature independents. Table 6.4 compares the

Landau coefficients determined in this study for $BaTiO_3$ single crystal as in Devonshire notation. The Landau coefficients in Devonshire notation shown in Table 6.4 are those in Table 6.3 transformed by using Table 6.1.

It is to be noted, in Table 6.4, the similarities of the temperature dependence landau coefficient terms from the Bell and Cross Landau potential and the determined unintentionally from this study. It was also recently shown by Xiaoyan Lu et al., by the convergence of the 6 order Landau polynomial based on the complex polarization-electric field and dielectric-electric field loops in temperatures around the Curie temperature.[18] These temperature dependence coefficient terms were required to obtain the same temperature dependence or the same excess entropy curvature revealed for the F_T-phase, as previously shown in Equation 5.5c. Since it was no trivial, it was also verified the temperature dependence of α_{12} for the 2-4-6 Landau potential. However, in this case, all curvatures of the calculated thermodynamic properties, $H^{XS}(T)$, $S^{XS}(T)$ and $G^{XS}(T)$, were bent down, as the temperature decrease, from the experimental data previously shown in Equation 5.5, which results in a polarization decrease toward lower temperatures.

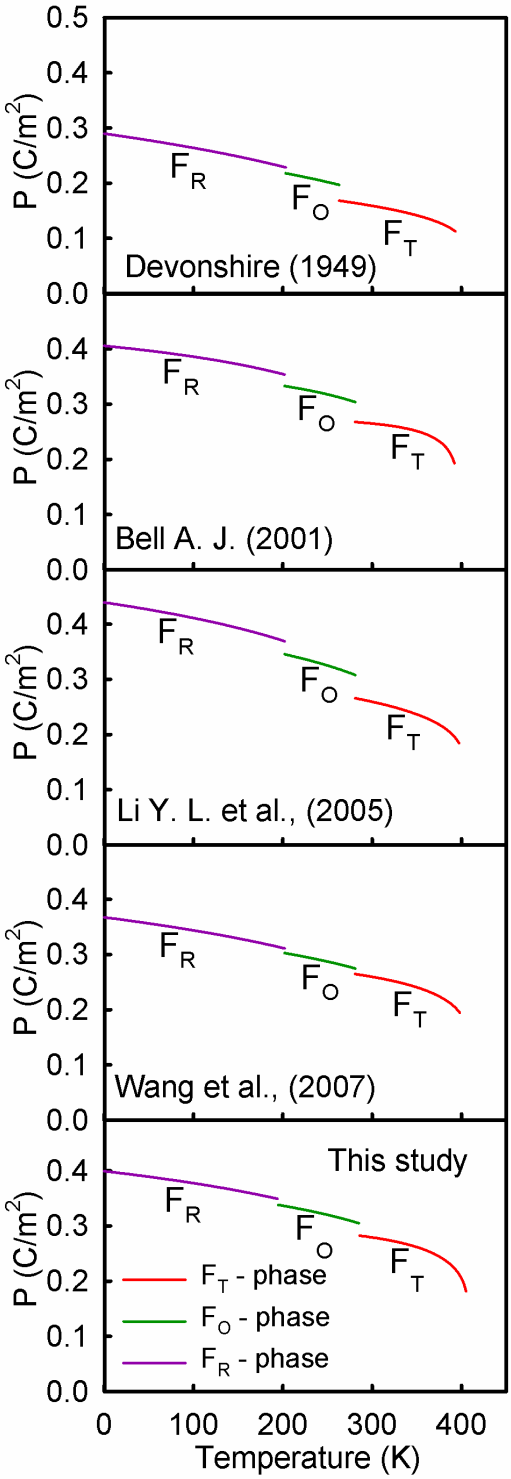

Figure 6.3 Comparison of the behavior and polarization jumps of the calculated reversible polarization as a function of temperature with references[1,8,9,11]

Table 6. 4 Coefficients of $BaTiO_3$ Landau thermodynamic potential as in Devonshire notation, where T is temperature in K

Coefficient	Units	This study	Wang et al.[a]	Li, Cross and Chen[b]	Bell and Cross[c]	Devonshire[d]
α_1	Jm/C^2	$(4.01x10^5)$*(T-Tc)	$(3.61x10^5)$*(T-391)	$(4.124x10^5)$*(T-388)	$(3.34x10^5)$*(T-381)	(1x10-4)*(T-118)
α_{11}	Jm^5/C^4	$-2.764x10^8 + (2.385x10^6)$*(T-Tc)	$-1.83x10^9 + (4x10^6)$*T	$-2.097x10^8$	$-2.02x10^8 + (4.69x10^6)$*(T-393)	$-4.4x10^{-12}$
α_{12}	Jm^5/C^4	$-9.161x10^6$	$-2.24x\ 10^9 + 6.7\ x10^6$T	$7.974x10^8$	$3.23x10^8$	$3.7x10^{-21}$
α_{111}	Jm^9/C^6	$3.675x10^9 + (-2.804x10^7)$*(T-Tc)	$1.39x10^{10} + (-\ 3.2x10^7)$*T	$1.294x10^9$	$2.76x10^9 + (-5.52x10^7)$*(T-393)	$5.3x10^{-12}$
α_{112}	Jm^9/C^6	$7.609x10^9$	$-2.2x10^9$	$-1.95x10^9$	$4.47x10^9$	-
α_{123}	Jm^9/C^6	$1.189x10^{10}$	$5.51x10^{10}$	$-2.5x10^9$	$4.91x10^9$	-
α_{1111}	Jm^{13}/C^8	-	$4.84x10^{10}$	$3.863x10^{10}$	-	-
α_{1112}	Jm^{13}/C^8	-	$2.53x10^{11}$	$2.529x10^{10}$	-	-
α_{1122}	Jm^{13}/C^8	-	$2.80x10^{11}$	$1.637x10^{10}$	-	-
α_{1123}	Jm^{13}/C^8	-	$9.35x10^{10}$	$1.367x10^{10}$	-	-
[a]Wang et al.[9]		[b]Li et al.[11] [c]Bell[8] (Bell and Cross[7])			[d]Devonshire[1,2] (Devonshire coefficients are in CGS units.)	

Using the coefficients for the Landau thermodynamic potential determined in this study as in Equation 6.1, shown in Table 6.3, and the different contributions to the excess free energy, Equations 6.5-6.8, the behavior of $\left[G_\alpha^{XS}\left(T, P_T, \boldsymbol{n}_\alpha^{eq}\right)\right]_{ANISO}$ and $[G^{XS}(T,P)]_{ANISO}$ may by verify. Figure 6.4 shows both energies contribution as a function of temperature. The polarization used in this analysis is the total polarization, determined by Equation 6.4, corresponding to the total excess free energy, Equation 6.1. From the anisotropic excess free energy, in Figure 6.4, it is possible to observe the stability of the different ferroelectric phases. As an example, from $T_{FO\text{-}FR}$ to $T_{FT\text{-}FO}$ the anisotropic excess free energy of the F_O-phase (dark green short-dash line) is more stable than the anisotropic excess free energy of the F_R-phase (dark pink long-dash line) which is more stable than that of the F_T-phase (red dash-dot-dot line). However, from the isotropic excess free energy (black solid-line), it is observed that it increases toward lower symmetry ferroelectric phases. Or contrariwise, that the anisotropic excess free energy decreases. In this manner, the

small jump in polarization at inter-ferroelectric transitions may be as a consequences of both crystallographic isotropic and anisotropic of polarization contributions. In general, the isotropic excess free energy for both inter-ferroelectric transition in $BaTiO_3$ single crystal (F_O-F_R and F_T-F_O) is higher in magnitude than the anisotropic excess free energy. Nevertheless, at the F_O-F_R transition the isotropic excess free energy is higher in magnitude than at the F_T-F_O transition, resulting in a relative smaller jump in polarization compared with F_T-F_O transition.

6.3.2 Isotropic and anisotropic contribution to the free energy

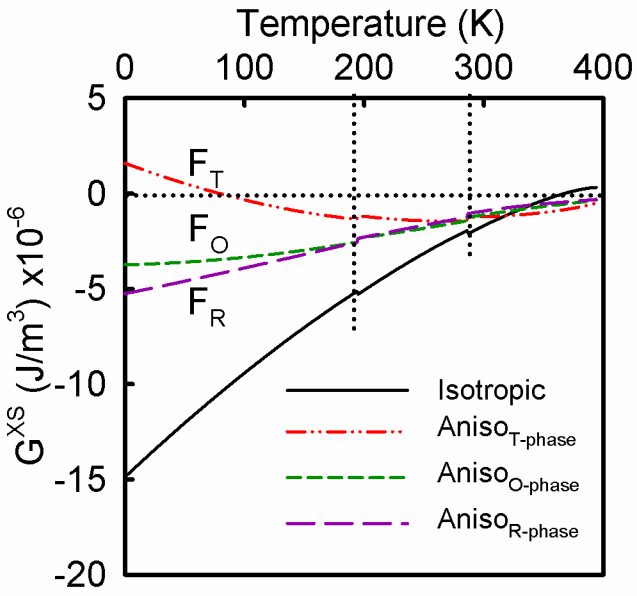

Figure 6.4: Contribution of the isotropic and anisotropic part of the excess free energy as a function of temperature.

The relative stability diagram, associated with the anisotropic excess free energy for the different ferroelectric phases, is shown in Figure 6.5. It was constructed from the theoretical work of Adam and Rossetti.[12] In this dimensionless diagram, the equilibrium values of the polarization vectors for the special symmetry ferroelectric phase (F_T-F_O-F_R)[28] in the 2-4-6 Landau potential

were substituted into the anisotropic contribution of the excess free energy, as shown from Equation 6.6 to Equation 6.8.

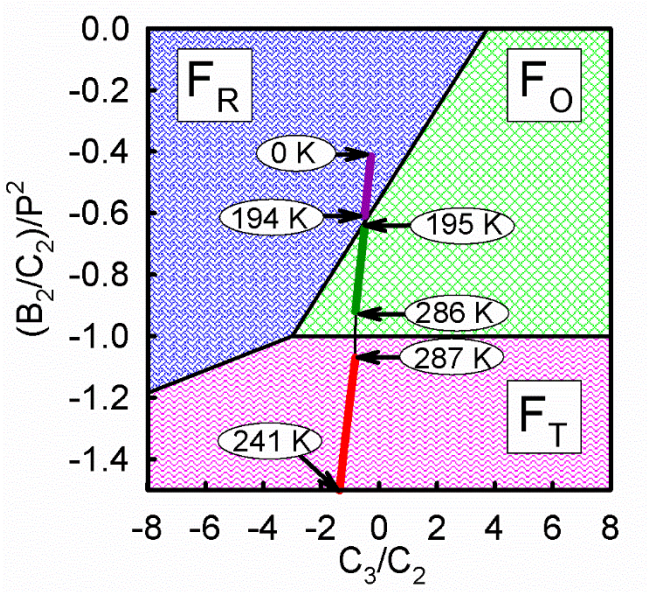

Figure 6.5 Dimensionless relationship of the determined anisotropic Landau coefficients for $BaTiO_3$ single crystal on the relative stability diagram of the excess free energy, Equation 6.6 to Equation 6.8, respect to the quartic and sextic anisotropic Landau coefficient as demonstrate by Adam and Rossetti.[12]

By using Equation 6.6 to Equation 6.8, it is possible to demonstrated that the inequality

$$\frac{B_2}{C_2 P^2} < -1 \tag{6.16}$$

is satisfied when F_T phase is more stable than the F_O, which that occurs when $\left[G_T^{XS}(T, P_T, \boldsymbol{n}_T^{eq})\right]_{ANISO} < \left[G_O^{XS}(T, P_O, \boldsymbol{n}_O^{eq})\right]_{ANISO}$. Also, when the F_R phase is more stable than the F_O phase, under the condition where $\left[G_R^{XS}(T, P_R, \boldsymbol{n}_R^{eq})\right]_{ANISO} < \left[G_O^{XS}(T, P_O, \boldsymbol{n}_O^{eq})\right]_{ANISO}$, it is also satisfy that

$$\frac{B_2}{C_2 P^2} > \frac{4}{27}\frac{C_3}{C_2} - \frac{5}{9} \tag{6.17}$$

Similarly, when $\left[G_T^{XS}\left(T, P_T, \boldsymbol{n}_T^{eq}\right)\right]_{ANISO} < \left[G_R^{XS}\left(T, P_R, \boldsymbol{n}_R^{eq}\right)\right]_{ANISO}$, or when the F_T phase is more stable than the F_R phase, then

$$\frac{\boldsymbol{B_2}}{\boldsymbol{C_2 P^2}} < \frac{\mathbf{1}}{\mathbf{27}}\frac{\boldsymbol{C_3}}{\boldsymbol{C_2}} - \frac{\mathbf{8}}{\mathbf{9}} \tag{6.18}$$

Additionally, it is important to note that the topology of the relative stability diagram shown in Figure 6.4 was constructed independent of both composition and temperature.[12] However, as stated by Heitmann and Rossetti, the addition of a particular dependence of the coefficients on temperature, pressure, or composition must still satisfy the conditions in Equations 6.16 through 6.18. In this study, the quartic and sextic anisotropic Landau coefficients (B_2 and C_2) were considered temperature dependent. As a consequence, the relationship between the anisotropic Landau coefficients of $BaTiO_3$ single crystal, in the relative stability diagram, is not revealed as a vertical line passing through the different ferroelectric phases. In this particular case, $(B_2/C_2)/P^2$ as a function of C_3/C_2 shift to the left as temperature is increase. Two very important points may be extracted from this result. First, independently of the temperature dependence of the anisotropic Landau coefficients, the relationship in Equation 6.16 to Equation 6.18 were all hold for the case of $BaTiO_3$ single crystal. And second, the anisotropic at the F_O-F_R transition is smaller compared with F_T-F_O transition, revealed by the jump from one stable anisotropic ferroelectric phase to another. It is a consequence of the determined Landau potential free energy which results in small jumps from the calculated polarization in this study.

6.3.3 Alternative analysis from thermal expansion

The polarization of a ferroelectric system may also be calculated from a thermal strain experimental technique, if the electrostriction coefficients, Q_{ij}, are known. The calculated polarization, shown in Figure 6.2d, and the square root of the thermal strain in the F_T phase are

proportionally related. The constant of proportionality, relative to the different crystallographic orientations, is Q_{ij}. Figure 6.6 shows $\sqrt{-S^{XS}}$, $\sqrt{-e_{11}^{XS}}$ and $\sqrt{e_{33}^{XS}}$ around the PE-F_T transition obtained experimentally from the C_P and the thermal strain, respectively. The excess thermal strain, e_{ij}^{XS}, was obtained from the subtraction of e_{ij} to the linear fit of the high temperature PE-phase thermal strain extrapolated to lower temperatures. All those three square roots are proportional to polarization. Similar temperature dependence behavior is observed when compare all three. A interest observation was related to the tail observed in $\sqrt{-S^{XS}}$ after T_{PF}. This tail has an onset temperature close to T_d, as was found from the thermal strain as the temperature decrease. It is important to note that the C_P-background was fitted to the high temperature PE-phase to where no contribution from the phase transitions or excess heat capacity was considered. Then, from the C_P analysis at the PE-F_T transition, the onset of polarization can be obtained where the entropy of the system, as the temperature is decrease, deviate from zero or from the PE-phase.

From the thermal strain data it can be demonstrated that in the c-direction, $e_{33}^{XS} = Q_{11}P_T^2$, and in the a-direction, $e_{11}^{XS} = -Q_{12}P_T^2$, where the polarization is that in the F_T phase, shown in Figure 6.2d. Figure 6.6b shows e_{ij}^{XS} as a function of the calculated polarization in the temperature range from 360 K to T_{PF} (T_{PF} = 402 K as found from thermal expansion). The slopes are associated with the electrostriction coefficients $Q_{11} = 0.1015\ m^4/C^2$ and $Q_{12} = -0.0338\ m^4/C^2$ relative to e_{33}^{XS} and e_{11}^{XS} as a function to the squared of the calculated polarization, respectively. The determined Q_{ij} are in good agreement with those found from Yamada et al., ($Q_{11} = 0.1\ m^4/C^2\ and\ Q_{12} = -0.034\ m^4/C^2$).[25] In general, the determined Q_{ij} are between the ranges of those found from literature compared in Table 6.2.

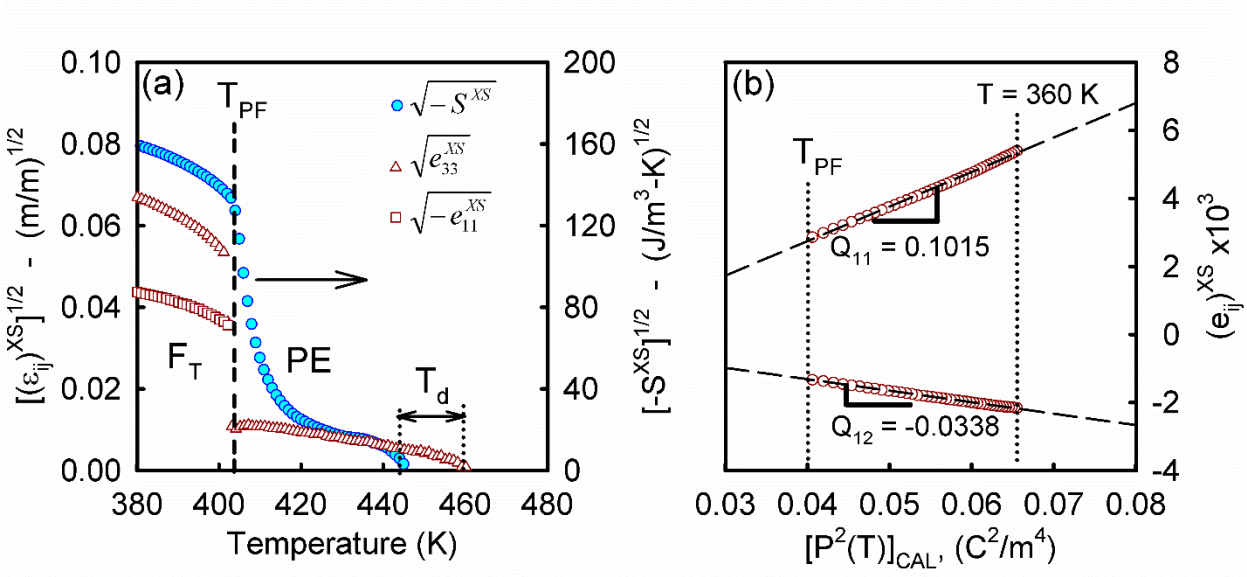

Figure 6.6: (a) Square root of the excess thermal strain and excess entropy around the PE-F_T transition as a function of temperature. (b) Determination of the electrostriction Q_{11} and Q_{12} for $BaTiO_3$ single crystal from the thermal strain as a function of the calculated polarization.

Using the determined Q_{11} and Q_{12}, the low order approximation Landau coefficients, B_o and C_o may be also determined from the following expressions:

$$B_o = \frac{-4A_o(T_{PF}-T_C)}{\Delta P^2} \tag{6.19}$$

$$C_o = \frac{3A_o(T_{PF}-T_C)}{\Delta P^4} \tag{6.20}$$

where the spontaneous polarization $\Delta P^2 = 0.194\ C/m^2$ and $\Delta P^2 = 0.168\ C/m^2$ where determined from $\sqrt{\Delta e_{33}^{XS}/Q_{11}}$ and $\sqrt{-\Delta e_{11}^{XS}/Q_{12}}$ at PE-F_T phase transition, respectively. Equations 6.19 and 6.20 are asymptotically accurate close to T_{PF}. The low order Landau coefficients, $B_o = -9.85x10^8\ Jm^5/C^4$ and $C_o = 2.30x10^{10}\ Jm^9/C^6$, found from this approach were compared in Table 6.2 with those determined from the heat capacity analysis and with literature. The values obtained for B_o and C_o, in the analysis of the thermal expansion, and also Q_{ij}, are additional validations to the spontaneous polarization and its temperature dependence. The determination of the calculated temperature dependence of the polarization was achievable from the application of

the Landau theory by using the Khachaturyan and Rossetti approach, to the heat capacity on $BaTiO_3$ single crystal.

6.3.4 Comparison of the crystallographic anisotropy of polarization with the pseudocubic lattice parameters by Kwei et al.[15]

Another relevant result from the calculated polarization in Figure 6.2d is the small jump at inter-ferroelectric transition, as previously discussed. These small jumps are a consequence of the crystallographic anisotropic of polarization which determined the symmetry of the stable ferroelectric phases. It had been demonstrated that the volumetric change in thermal expansion between ferroelectric phases is also small.[15,29] From the lattice parameters determined from Jaffe it can be demonstrated that the extrapolation of the a-lattice parameter from the cubic PE-phase, a_c, to the lower symmetry ferroelectric phase in $BaTiO_3$ single crystal, a_c(F_R-phase), is very close to the a-lattice parameter from the F_R-phase, a_R. Kwei et al., present a detail crystal structural Rietveld refinement of $BaTiO_3$ single crystal extracted from the relative displacement of the ionic sublattices obtained from a powder neutron diffraction data.[15] A continuity between ferroelectric phases is observed from the point charge contribution to the polarization determined by Kwei et al., shown in Figure 6.7a (black open cycles). It is revealed by the least square fit (black dash line) across all measured temperature range by Kwei et al. It was concluded from their report that the domain size of the F_R-phase and F_O-phase is considerably smaller than the F_T-phase and that fluctuations at inter-ferroelectric transitions reduce the structural coherence. It was revealed as an increase in the microscopic strain as the transition is approached from their data.

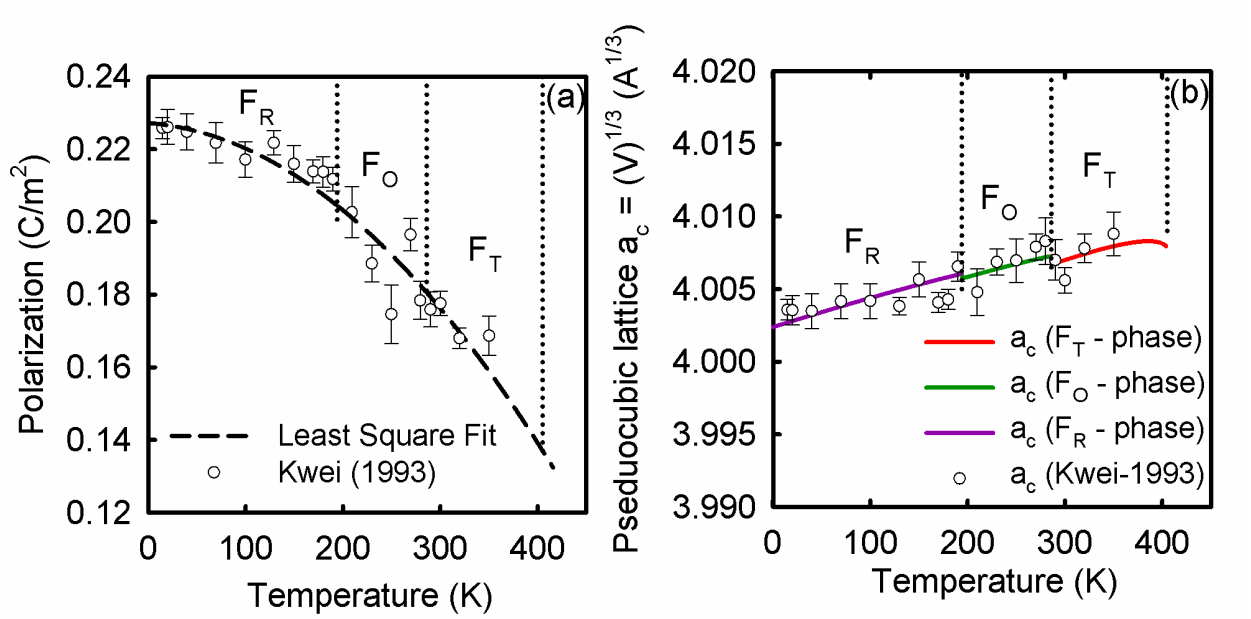

Figure 6.7: (a) Point charge contribution of the polarization as a function of temperature and the least squared fit (Dash line) to the data. (b) Calculated pseudocubic lattice parameter (solid lines) for the depoled $BaTiO_3$ single crystal as a function of temperature. The experimental data (open cycles) in both figures is taken from Kwei et. al.[15]

Furthermore, it was also determined, from Kwei et. al., the lattice parameters and the cell volume as a function of temperature for the three ferroelectric phases. The cell volume expansion is proportional to the square of the polarization. For the special case of $BaTiO_3$, due to the equilibrium directions of the polarization vector along [001], [110] and [111] for F_T, F_O and F_R, respectively, it can be demonstrated that:

$$\boldsymbol{V(T) = a_c^3(T)[1 + (Q_{11} + 2Q_{12})P^2(T)]} \tag{6.21}$$

where $a_c^3(T)$ is the pseudocubic lattice parameter and may be obtained from the high and low symmetry ferroelectric phases respectively from the following expressions:

$$\boldsymbol{a_c(at\ F_T - phase) = \frac{a_T}{1+Q_{12}P_T^2}} \tag{6.22}$$

$$\boldsymbol{a_c(at\ F_R - phase) = \frac{a_R}{1+\frac{1}{3}(Q_{11}+2Q_{12})P_R^2}} \tag{6.23}$$

The lattice parameters a_T and a_R correspond to the F_T and F_R phases obtained experimentally from Kwei et. al., respectively. The result from Equations 6.22 and 6.23 were fitted to a linear regression in order to obtain $a_c^3(T)$ for any desired temperature in the same temperature range of the calculated polarization in Figure 6.2d. Since Q_{ij} were also determined, from Figure 6.5b, a comparison of the pseudocucbic lattice parameter of $BaTiO_3$ single crystal obtained from Equation 6.21 and those determined by Kwei et. al. (open cycles), are shown Figure 6.7b. In addition to the excellent agreement with Kwei et. al., and the calculated pseudocubic lattice parameters obtained in this study, it is to be noted, from Figure 6.7b, the continuity in $a_c^3(T)$ between ferroelectric phases. It indicates that small crystallographic anisotropy at inter-ferroelectric transitions is also a consequence of small atomic structural displacements.

6.4 Summary

The Devonshire notation to the Landau free energy in perovskite-type crystal structure ferroelectric materials was reformulated following the approach by Khachaturyan and Rossetti[16] based on the crystallographic anisotropic of the polarization. In this manner, the isotropic and anisotropic contributions to the free energy can be easily separated. Based on this approach and by using the dielectric permittivity and the excess contribution to the heat capacity in $BaTiO_3$ single crystal, the complete set of Landau coefficients were determined. The low order approximation Landau coefficients, asymptotically accurate as approaching T_C, were first obtrained. It is related with derived expression from the free energy associated with a first-order phase transition at the PE-F_T phase transformation. By using these coefficients as input parameters, the experimental temperature dependence of the excess entropy, the experimental change in entropy at the inter-ferroelectric transitions and relation that fallow the anisotropy contribution to the Landau free

energy of the different ferroelectric phases the complete set of Landau coefficients to the 2-4-6 Landau thermodynamic potential were determined for $BaTiO_3$ single crystal. Thereby, the temperature dependence of the polarization was determined. It is the first time that the complete set of the Landau coefficients to the Landau free energy are determined from heat capacity measurements. The temperature dependence of the Landau coefficients in the quartic and sextic terms agree well with those determined by Buessem et al.[10] and subsequently modified by Bell et al.[8] It was shown by Xiaoyan Lu al. that those ones were reasonable for $BatiO_3$ single crystal compared with other references.[18]

The crystallographic anisotropic of polarization was investigated by following similar approach by Heitmann et. al.[13,14] It was demonstrated that the jumps in polarization at the inter-ferroelectric phase transition points were extremely small, which it was proposed for a low crystallographic anisotropic of polarization at these phase transitions points. It was a consequence of the large contribution of the isotropic part of the free energy in comparison to the anisotropic part around this phase transition regions. This extremely small jumps in the polarization at the inter-ferroelectric transition validated the conditions to the proposed relative stability phase diagram of the ferroelectric phases in $BaTiO_3$,[14] formulated as a continuous path of the polarization towards low symmetry ferroelectric phases. Alternatively, from the linear relationship of the excess thermal expansion and the calculated temperature dependence of the polarization, the electrostriction coefficients were also determined. They are comparable with those determined by Yamada et al.[25] and are between the ranges from those found in literature shown in Table 6.2. Then, by using the jump in polarization determined from $\sqrt{\Delta e_{33}^{XS}/Q_{11}}$ and $\sqrt{-\Delta e_{11}^{XS}/Q_{12}}$ at the PE-F_T phase transition, the Landau coefficients to the low order approximation of the Landau free energy were determined and compare well with those determined from heat capacity. Finally, since

Q_{ij} and the temperature dependence of the polarization were determined, the continuity toward low symmetry ferroelectric phases of the pseudocucbic lattice parameter of $BaTiO_3$ single crystal was compared with that obtained experimentally from Kwei et al.[15] which also demonstrated the continuity to the point charge contribution to the polarization.

6.5 References

1. Devonshire, A. F. XCVI. Theory of barium titanate. *Philos. Mag. Ser. 7* **40,** 1040–1063 (1949).

2. Devonshire, A. F. CIX . Theory of barium titanate — Part II. *Philos. Mag. Ser. 7* **42,** 1065–1079 (1951).

3. Jona, F. & Shirane, G. *Ferroelectric Crystals*. (1962).

4. E. Salje. in *Phys. Prop. Thermodyn. Behav. Miner.* (Salje, E.) 75–119 (Dordrecht: Reidel, 1988).

5. Aleksandrov, K. S. & Flerov, I. N. . *Sov. Phys. Solid State* **21,** 195 (1979).

6. Rossetti, G. a & Maffei, N. Specific heat study and Landau analysis of the phase transition in PbTiO 3 single crystals. *J. Phys. Condens. Matter* **17,** 3953–3963 (2005).

7. Bell, A. J. & Cross, L. E. A phenomenological gibbs function for $BaTiO_3$ givin correct E field dependence of all ferroelectric phase changes. *Ferroelectrics* **59,** 197–203 (1984).

8. Bell, a. J. Phenomenologically derived electric field-temperature phase diagrams and piezoelectric coefficients for single crystal barium titanate under fields along different axes. *J. Appl. Phys.* **89,** 3907 (2001).

9. Wang, Y. L. *et al.* Landau thermodynamic potential for BaTiO[sub 3]. *J. Appl. Phys.* **101,** 104115 (2007).

10. Buessem, W. R., Cross, L. E. & Goswami, A. K. Phenomenological Theory of High Permittivity in Fine-Grained Barium Titanate. *J. Am. Ceram. Soc.* **49,** 33–36 (1966).

11. Li, Y. L., Cross, L. E. & Chen, L. Q. A phenomenological thermodynamic potential for $BaTiO_3$ single crystals. *J. Appl. Phys.* **98,** 064101 (2005).

12. Heitman, A. Design and Modeling of High Power Density Acoustic Transducer Materials for Autonomous Undersea Vehicles. (2012).

13. Heitmann, A. A. & Rossetti, G. A. Thermodynamics of polar anisotropy in morphotropic ferroelectric solid solutions. *Philos. Mag.* **90,** 71–87 (2010).

14. Heitmann, A. A. & Rossetti, G. A. Polar Anisotropy and Inter-Ferroelectric Transitions in Barium Titanate and its Solid Solutions. *Integr. Ferroelectr.* **126,** 155–165 (2011).

15. Kwei, G. H., Lawson, A. C., Billinge, J. L. & Cheong, S.-W. Structure of the Ferroelectric Phase of Barium Titanate. *J. Phys. Chem.* **97,** 2368–2377 (1993).

16. Rossetti, G. A. & Khachaturyan, A. G. Inherent nanoscale structural instabilities near morphotropic boundaries in ferroelectric solid solutions. *Appl. Phys. Lett.* **91,** 072909 (2007).

17. Rossetti, G. A., Khachaturyan, A. G., Akcay, G. & Ni, Y. Ferroelectric solid solutions with morphotropic boundaries: Vanishing polarization anisotropy, adaptive, polar glass, and two-phase states. *J. Appl. Phys.* **103,** 114113 (2008).

18. Lu, X., Li, H. & Cao, W. Landau expansion parameters for $BaTiO_3$. *J. Appl. Phys.* **114,** 224106 (2013).

19. Khachaturyan, a. G. Ferroelectric solid solutions with morphotropic boundary: Rotational instability of polarization, metastable coexistence of phases and nanodomain adaptive states. *Philos. Mag.* **90,** 37–60 (2010).

20. Ishibashi, Y. Theory of the Morphotropic Phase Boundary. *Ferroelectrics* **267,** 191–199 (2002).

21. G. A. Rossetti, Zheng, W. & Khachaturyan, A. G. Phase coexistence near the morphotropic phase boundary in lead zirconate titanate solid solutions. *Appl. Phys. Lett.* **88,** 072912 (2006).

22. Lines, M. E. & Glass, A. M. *Principles and Applications of Ferroelectrics and Related Materials*. (Clarendon Press, 1977).

23. Lee, S., Rossetti, G. a., Liu, Z.-K. & Randall, C. a. Intrinsic ferroelectric properties of the nonstoichiometric perovskite oxide Ba[sub 1−x]Ti[sub 1−y]O[sub 3−x−2y]. *J. Appl. Phys.* **105,** 093519 (2009).

24. Wang, J. J., Meng, F. Y., Ma, X. Q., Xu, M. X. & Chen, L. Q. Lattice, elastic, polarization, and electrostrictive properties of BaTiO[sub 3] from first-principles. *J. Appl. Phys.* **108,** 034107 (2010).

25. Yamada, T. Electromechanical Properties of Oxygen-Octahedra Ferroelectric Crystals. *J. Appl. Phys.* **43,** 328 (1972).

26. Hlinka, J. & Márton, P. Phenomenological model of a 90° domain wall in $BaTiO_3$-type ferroelectrics. *Phys. Rev. B* **74,** 104104 (2006).

27. Merz, W. J. The Electric and Optical Behavior of $BaTiO_3$ Single-Domain Crystals. *Phys. Rev.* **76,** (1949).

28. Shuvalov, L. A. . *J. Phys. Soc. Japan* **28,** 38 (1970).

29. Jaffe, B., Cook, W. R. & Jaffe, H. *Piezoelectric Ceramics*. 53–183 (Academic Press, 1971).

CHAPTER 7

PHASE TRANSITION ENERGETIC AND TRICRITICAL BEHAVIOR IN LEAD ZIRCONATE-TITANTE (PZT) CERAMICS FROM HEAT CAPACITY MEASUREMENTS

Note: The original version of this chapter had been submitted for publication under:
Ching-Chang Chung, Richard Pérez Moyet and George A. Rossetti, Jr. "Tricritical Behavior of Lead Zirconate-Titanate: A Heat Capacity Study"

7.1 **Introduction**

In this chapter it is of interest to investigate the location of two tricritical points across the Curie line of the PZT phase diagram. In ferroelectric materials, a critical point may exist where the line of second-order phase transition passes over to a line of first-order phase transition. For this purpose, tricritical behavior in lead zirconate-titanate (PZT) was investigated by heat capacity measurements using differential scanning calorimetry (DSC) in the temperature range 310K–950K. By empirical observations, the characteristic changes in the shapes of the heat capacity curve and vanishing of the transition enthalpies for $0.25 \leq x \leq 0.55$ confirmed the occurrence of two tricritical points. The observed linear dependence of the excess entropies on composition agree with the predictions of a truncated 2-4-6 Landau polynomial, which was used to self-consistently locate these points. Theoretically, by the application of the 2-4-6 Landau polynomial, one tricritical point was located near the composition $x = 0.22$ and a second near the composition $x = 0.51$. Prediction of the composition dependence of the Landau polynomial was confirmed by direct analysis of the experimental data to the low temperature limit close to the Paraelectric to ferroelectric (PE-FE) phase transition.

7.2 **Experimental**

The experimental detail of the ceramic powder $PbZr_{1-x}Ti_xO_3$ ($0.0 \leq x \leq 1.0$) samples preparation is given by Ching-Chang Chung et al.,[1] However, for consistency of this chapter, a brief description of the experimental details will be shown. Powders of $PbZr_{1-x}Ti_xO_3$ ($0.0 \leq x \leq 1.0$) were prepared using a modification of a sol-gel method described previously[2,3] The phase composition of the samples was assessed from powder x-ray diffraction patterns at room temperature using a Bruker D8 Advance diffractometer (CuKα radiation) operating at a scan rate of 4°/min in an auto-repeat mode that averaged the data from 4-6 scans in the range of 15° – 90° 2θ. The peak positions were determined by fitting the reflections to Pearson VII line profile shape functions. The crystal lattice parameters of the tetragonal (a, c) and rhombohedral (a, α) phases were determined from the positions of the (002)/(200) and (111)/($\bar{1}$11) and (200) reflections, respectively, and were used to compute the x-ray density (ρ_X). The apparent densities (ρ_A) of the sintered disks were computed from weight and volume measurements made using an analytical balance (resolution of 0.01 mg) and an electronic digital caliper (resolution of 0.01 mm). The percent theoretical densities ($\%TD = \rho_A / \rho_X$ x 100) were computed from these two measurements. The average grain sizes (D) of the sintered disks were estimated by the linear intercept method by sampling >90 grains from a series of electron micrographs acquired at a magnification of 3000X using a JEOL 6335F field emission scanning electron microscope. The room-temperature dielectric constant of the sintered disks was determined from capacitance measurements recorded at 0.1 V and 1 kHz using a HP 4282A complex impedance analyzer. For these measurements, the disks were electroded using colloidal silver paste that was allowed to cure for 24 h at room temperature.

Heat capacity measurements were made using a Netzsch DSC 404 F1 Pegasus high temperature differential scanning calorimeter equipped with a Pt-wound furnace and Type-S sensor. The measurements were made at a scan rate of 10 K/min. under dry argon flowing at 50 mL/min using covered platinum crucibles. The data were collected in both heating and cooling runs using a data acquisition interval of 50 points/K. Heat capacities (C_P) were determined using the ASTM E 1269 ratio method using a sapphire disk calibrated to the NIST SRM 720 reference data for a synthetic sapphire standard. The sensitivity polynomial was verified at the time of data collection by comparing the C_P measured on the sapphire disk to the C_P measured on a dense alumina disk. The measurements were found to agree within 1% over the entire temperature range of the measurements, 310K–950K; The baseline. The temperature calibration was verified from data collected on Hg, In, Sn, Bi, Zn and Cscl standards with melting points spanning this temperature range (234K - 918K). For the $PbZr_{1-x}Ti_xO_3$ solid solution compositions, the measurements were performed on sintered disks. For the $PbTiO_3$ and $PbZrO_3$ end member compounds, the measurements were performed on powders that were densely packed into the Pt crucibles to ensure good thermal contact. Three measurements were performed on each sample investigated and the C_P data for the measurements was averaged.

7.3 **Results and Discussion**

7.3.1 **Specimen Characterization**

The $PbZr_{1-x}Ti_xO_3$ specimens were characterized by the room-temperature x-ray diffraction and dielectric permittivity at 1 kHz. The x-ray diffraction and heat capacity measurements were obtained from specimens in powder (p) form for the composition x = 0 and x = 1.0 due to the volatilization of the oxides and the cracking during cooling from the sintering temperature,

respectively. For the solid solution compositions ($0.10 \leq x \leq 0.80$) all measurements were perform on sintered disks (SD). Representative x-ray diffraction patterns of the sintered disks is presented in Figure 7.1 for compositions belonged to the space group R3m or cell double (R3C) rhombohedral phases (x = 0.30), to near the MPB revealing the mixture of the Tetragonal and Rhombohedral phases (x = 0.48) and to the Tetragonal phase (x = 0.70). Sharp Bragg reflections to high diffractions orders with no evident secondary phases were observed. The reflections were indexed by the space group R3m for composition belonged to the rhombohedral phase and with the space group P4mm for the tetragonal phase. For the composition near the MPB (x = 0.48) it was a mixture of the tetragonal and Rhombohedral phases.

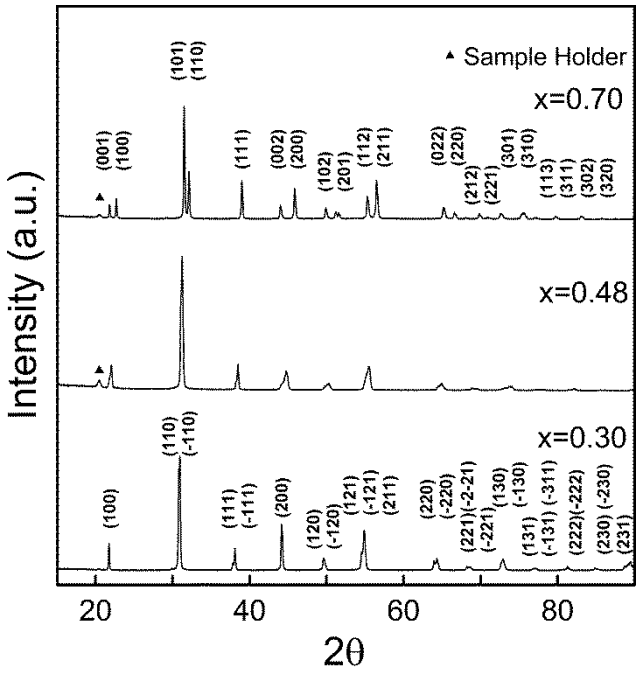

Figure 7. 1 Powder x-ray diffraction patterns collected on unannealed sintered disks of $PbZr_{1-x}Ti_xO_3$ with varying composition (x) showing: (a) the rhombohedral composition with x = 0.3, the tetragonal composition with x = 0.70 and a two phase mixture of tetragonal and rhombohedral phases with x – 0.48. The indexing shown on the patterns from bottom to top is for the rhombohedral (R3m) and tetragonal (P4mm) symmetries, respectively.

Figure 7.2(a) shows the crystal lattice parameters of the unannealed specimens. Included on the plot are the cube roots of the primitive cell volumes (Ω) for the orthorhombic (P*bam*) phase $\left(a^{"} = \sqrt[3]{abc}/8 = \sqrt[3]{\Omega}\right)^4$, the rhombohedral phase $\left(a \approx \sqrt[3]{\Omega}\right)$ and the tetragonal phase $\left(a' = \sqrt[3]{a^2c} = \sqrt[3]{\Omega}\right)$. The linear variation of the primitive cell volume with composition agree well with previous high-resolution powder x-ray and neutron studies.[5–7] The crystal lattice parameters, the primitive cell volume as well as the percent theoretical density and grain size for all samples studied were reported in Table 7.1.

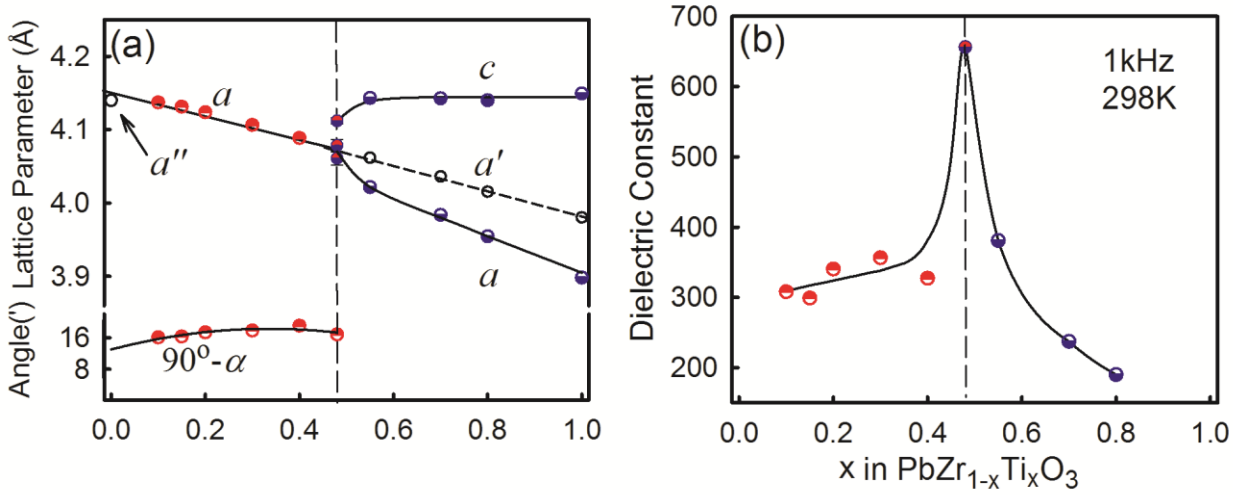

Figure 7. 2 (a) Crystal lattice parameters of unannealed $PbZr_{1-x}Ti_xO_3$ powders (x = 0.00, 1.00) and sintered disks ($0.10 \leq x \leq 0.80$) *versus* composition at room temperature. The cube root of the primitive cell volume in the tetragonal (P4*mm*) phase ($a' = \sqrt[3]{a^2c}$) and the orthorhombic (P*bam*) phase ($a'' = \sqrt[3]{abc}/8$) are also shown. (b) Room-temperature dielectric constant of the unannealed sintered disks *versus* composition at 1 kHz. The solid lines shown in (a) and (b) are guides to the eye.

The room-temperature dielectric constant measured at 1 kHz is presented in Figure 7.2(b). The expected behavior of the composition dependence of the dielectric constant is also in good agreement with early work carried out on unmodified $PbZr_{1-x}Ti_xO_3$ by Jaffe et al.[8] An abrupt change in dielectric constant from the rhombohedral phase was observed as decrease x from the

MPB, while a more continuous change was observed at the tetragonal phase as increasing x from the MPB. A sharp maxima ($K \sim 680$) was observed at the composition located near the MPB.

Table 7. 1 Crystal lattice parameters (a, b, c, α) and primitive cell volume (Ω) of unannealed $PbZr_{1-x}Ti_xO_3$ powders and sintered disks

x	Phase	Form	a (Å)	b (Å) or α	c (Å)	Ω (Å^3)
0.00	O [a]	P [b]	5.85	11.77	8.23	70.82(3) [c]
0.10	R	SD	4.14	89.73°	-	70.81(1)
0.15	R	SD	4.13	89.73°	-	70.51(1)
0.20	R	SD	4.12	89.71°	-	70.13(1)
0.30	R	SD	4.11	89.70°	-	69.24(1)
0.40	R	SD	4.09	89.70°	-	68.35(0)
0.48	R +T	SD	4.08	89.72°		67.83(8)
0.48	R +T	SD	4.06		4.11	67.83(8)
0.55	T	SD	4.02	-	4.14	67.01(1)
0.70	T	SD	3.98	-	4.14	65.75(1)
0.80	T	SD	3.95	-	4.14	64.75(3)
1.00	T	P	3.89	-	4.14	62.94(1)

[a] O: Orthorhombic (P*bam*), R: Rhombohedral (R3*m* /R3*c*), T: Tetragonal (P4*mm*)
[b] P: Powder, SD: Sintered disk
[c] Estimated uncertainty in the least significant digit

7.3.2 **Heat Capacities**

The heat capacity of the $PbZr_{1-x}Ti_xO_3$ powders (x = 0.00, 1.00) and sintered disks ($0.10 \leq x \leq 0.80$) is shown in Figure 7.3. The heat capacities of specimens with high $PbZrO_3$ content (x = 0.0, 0.1 and 0.15) were measured in a temperature range from room temperature to ~750 K. However, for composition with high $PbTiO_3$ content (x = 0.2, 0.3, 0.4, 0.48, 0.55, 0.7, 0.8 and 1.0) the temperature range was from room temperature to ~900 K. Four key observations may be extracted from the C_P raw data as presented in Figure 7.3. First, sharp peaks corresponding to the Paraelectric to Ferroelectric (PE-FE) phase transition were observed to decrease from a C_P behavior of a first

order phase transition to a second order one from the end members ($x = 1.0, x = 0.0$) towards the MPB region. Second, due to the compositional dependence of the order of the phase transition, the C_P-data may be divided in three regions: first-order phase transition in the rhombohedral phase, second order phase transition of compositions around the MPB and first order phase transition in the tetragonal phase. Third, the high temperature C_P-data, 100 degrees after the PE-FE phase transition to be consistent, were observed below the Dulong-Petit limit as the $PbTiO_3$ content decreases. Finally, the inter-ferroelectric phase transitions corresponding to $R3m - R3c$ were possible to be detected from a C_P measurement, for the following compositions: (x = 0.1, 0.15, and 0.2).

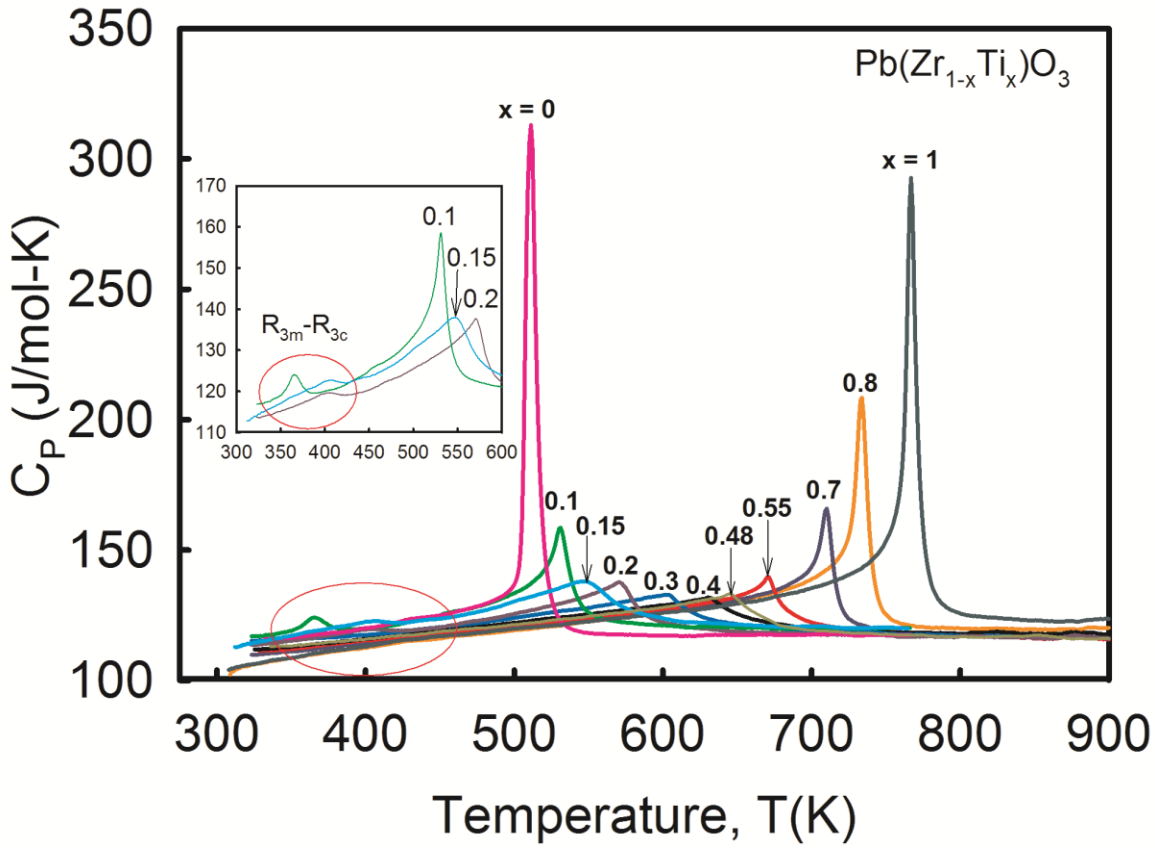

Figure 7. 3 Heat capacity data versus temperature of unannealed $PbZr_{1-x}Ti_xO_3$ powders (x = 0.00, 1.00) and sintered disks ($0.10 \leq x \leq 0.80$). The inset shows the inter-ferroelectric FR_{3m} - FR_{3C} phase transition peak during heat capacity. The heat capacity data were collected on heating.

Since the onset temperature for the weak first-order PE-FE phase transition of the compositions from ($0.15 < x < 0.55$) depends on the temperature range it was determined, then, in order to be consistent, the peak temperature (T_{Peak}) was used as the phase transition temperature in the PE-FE phase as well as in the $R3m - R3c$ inter-ferroelectric phase transition. By using T_{Peak}, the Temperature-Composition phase diagram of $PbZr_{1-x}Ti_xO_3$ was then constructed, shown in Figure 7.4.

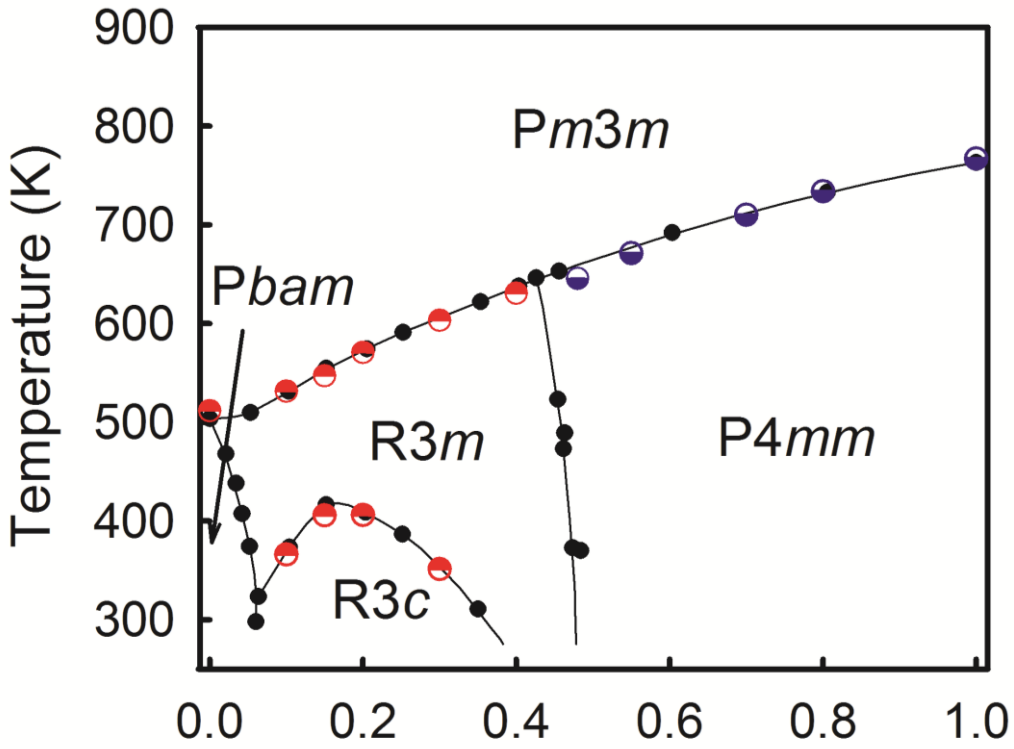

Figure 7. 4 Transition temperatures (half-filled circles) for unannealed $PbZr_{1-x}Ti_xO_3$ powders (x = 0.00, 1.00) and sintered disks ($0.10 \leq x \leq 0.80$) superimposed on the conventional phase diagram adapted from Jaffe et al.[8] The heat capacity data were collected on heating.

The excellent agreement with the accepted phase diagram by Jaffe et al., can be observed.[8] The open upper half blue circles belong to the Tetragonal phase while the open lower half red circles belong to the Rhombohedral phase. Figure 7.5 presents the heat capacity *versus* temperature curves acquired from measurements made on heating for all of the compositions listed in Table

7.1. In this figure, the curves are displaced relative to one another so that the shapes and intensities of the anomalies in heat capacity near the phase transitions can be more easily compared. Heat capacity intervals of 50 J/mol-K are shown by the tick marks on the vertical axis to facilitate this comparison.

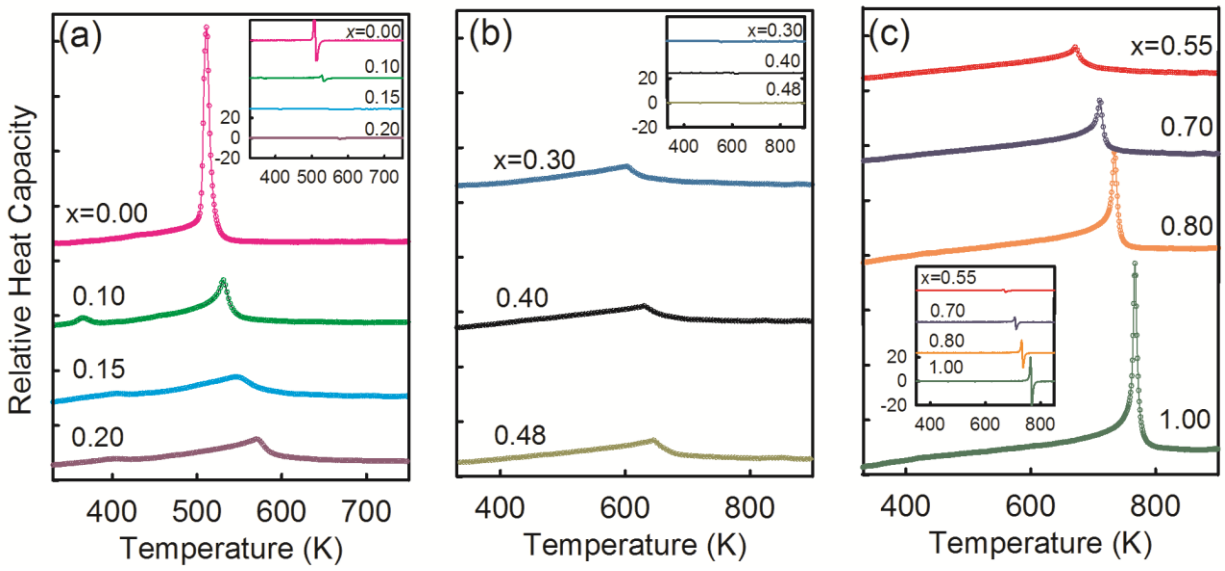

Figure 7. 5 Relative heat capacity *versus* temperature of unannealed $PbZr_{1-x}Ti_xO_3$ powders (x = 0.00, 1.00) and sintered disks ($0.10 \leq x \leq 0.80$) in three ranges of composition (a) $0.00 \leq x \leq 0.20$ (b) $0.30 \leq x \leq 0.40$ and (c) $0.55 \leq x \leq 1.00$. The heat capacity data were collected on heating. The insets show the first derivative of the heat capacity *versus* temperature curves. The tick marks on the vertical axes represent intervals of 50 J/mol-K.

Several observations concerning the RR and PE-FE transitions can be made from the data shown in Figure 7.5. As shown in Figure 7.5(a), for the zirconium-rich compositions with $0.0 \leq x \leq 0.20$, the RR and PE-FE (R3*m* ↔ P*m*3*m*) transitions all showed a marked decrease in intensity with increasing *x*. In this range of composition the variation of the heat capacity with temperature near the FE-PE transitions was characteristic of weak first-order transitions close to second order. As shown in Figure 7.5(b), as the titanium content is increased in the range $0.30 \leq x \leq 0.48$, the PE-FE phase transitions R3*m* ↔ P*m*3*m* (x = 0.30, 0.40) and P4*mm* ↔ P*m*3*m* (x = 0.48) showed almost

no change in intensity with increasing *x*, and the variation of the heat capacity with temperature near the PE-FE phase transitions was characteristic of second-order transitions. As shown in Figure 7.5(c), for the titanium-rich compositions with $0.55 \leq x \leq 1.0$, the FE-PE phase transitions (P4*mm* ↔ P*m*3*m*) showed an increase in intensity with increasing *x*. In this range of composition the variation of the heat capacity with temperature near T_{PF} was again characteristic of first-order transitions. The data in Figure 7.5 strongly support previous reports[9,10] that the $PbZr_{1-x}Ti_xO_3$ system exhibits two lines of first-order PE-FE transitions separated by a line of second-order transitions. This observation can be better appreciated by comparing the first derivatives of the heat capacities with temperature, as shown in the insets of the figure and also in Figure 7.6. The first derivative curves showed sharp symmetric extrema that decreased markedly in intensity on moving away from end member compounds with either increasing values of *x* from *x* = 0.0 or decreasing values of *x* from *x* = 1.0.

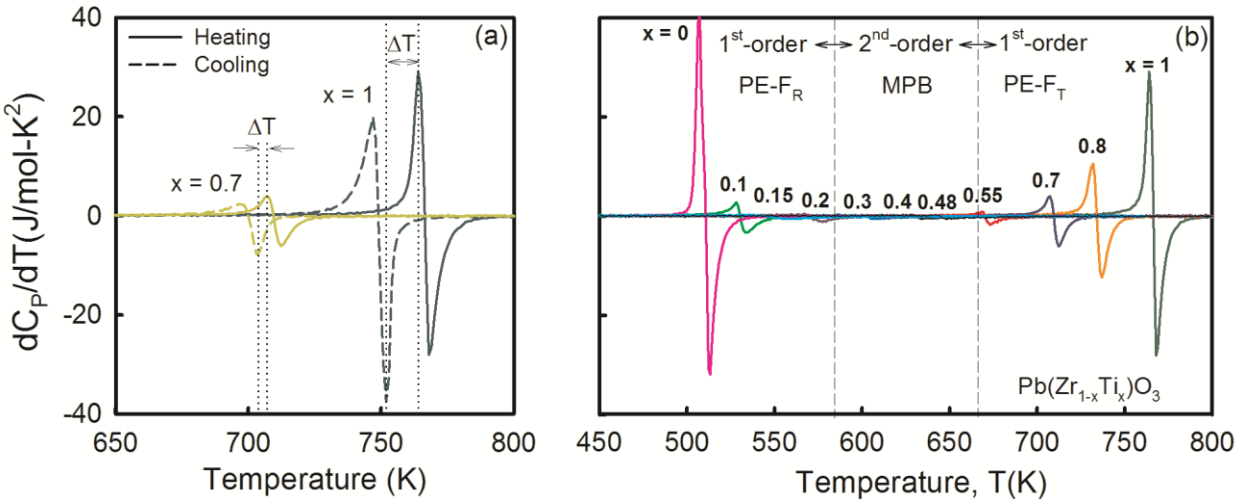

Figure 7. 6 The first derivative of the heat capacity *versus* temperature curves of unannealed $PbZr_{1-x}Ti_xO_3$ powder ($x = 0.00, 1.00$) and sintered disks ($0.10 \leq x \leq 0.80$) showing characteristic behaviors of first order to a second order phase transition as moving away from end member compounds. (a) Decrease in thermal hysteresis from heating and cooling heat capacity measurements. (b) Decrease in the intensity of sharp symmetric extrema.

The last key observation was refers to the behavior of the high temperature heat capacity, 100 temperature degree after the PE-FE phase transition to be consistent, which lies below the Dulong Pettit Limit (3NR). It is also apparent from Figure 7.3 and Figure 7.5 that for all compositions investigated, the heat capacity in the cubic phase at $T > T_{PF}$ was nearly constant to highest temperature (T_{max}) of the measurements (T_{max} = 773K for $x \leq$ 0.20 or T_{max} = 950K for $0.30 \leq x \leq 1.0$). Because the heat capacity above T_{PF} was essentially constant, a single value for each composition was obtained by averaging the heat capacity over the range of temperature T_{PF} + 100K $< T < T_{max}$. The results are plotted in Figure 7.7(a).

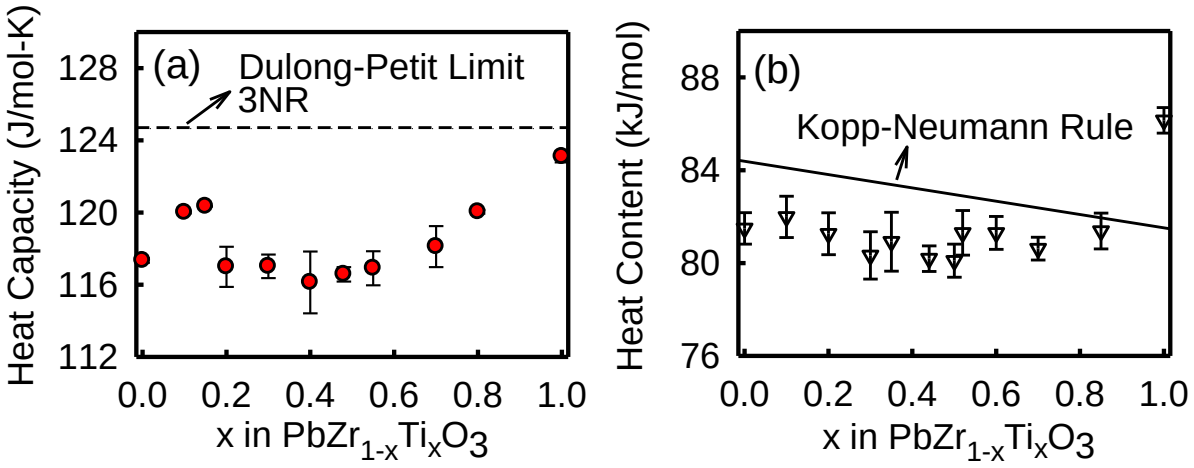

Figure 7. 7 Heat capacity for the cubic phase of unannealed $PbZr_{1-x}Ti_xO_3$ powders (x = 0.00, 1.00) and sintered disks ($0.10 \leq x \leq 0.80$) *versus* composition determined by averaging the data collected above the temperature of the ferroelectric to paraelectric transition at $T > T_{FP}$ + 100 K. The heat capacity data were collected on heating. The dashed line shows the heat capacity predicted by the law of Dulong and Petit (b) The heat content of $PbZr_{1-x}Ti_xO_3$ *versus* composition adapted from Rane M. et al.[11] The solid line shows the heat content predicted by the Kopp-Neumann additivity rule.

These results show that the heat capacity of the cubic phase of lead titanate (x = 1.0) is very close to that predicted by the law of Dulong and Petit, $C_P \sim C_V = 3nR$, where n = 5 is the number of atoms per formula unit and R is the universal gas constant. This result has been reported previously in single crystal[12] lead titanate specimens. The good agreement with the Dulong and Petit limit

indicated that the heat capacity of cubic lead titanate has an essentially constant heat capacity representative of full equipartition excitation of vibrational modes. Also as observed previously, substitution of the larger zirconium atom for titanium resulted in a marked decrease in heat capacity for decreasing x in the range $0.55 \leq x \leq 1.0$.[12] As shown in Figure 7.7(a), for $0.0 \leq x \leq 0.55$ the heat capacity of the cubic phase is essentially independent of composition, although some small increase for the zirconium-rich compositions near $x = 0.10$ is evident.

To better understand the observed dependence of the cubic heat capacities on composition, they are compared with previously measured heat contents ($H_{ttd} = H_{973K} - H_{298K}$) determined by transposed temperature drop calorimetry.[11] As shown in Figure 7.7(b), it is seen that the reported variation of the heat contents with composition is strikingly similar to that observed for the heat capacities of the cubic phase. The variation of the heat contents with composition in $PbZr_{1-x}Ti_xO_3$ has been rationalized by comparing with the Neumann-Kopp additivity rule.[11] This is shown as the solid line in the figure and represents the composition weighted average of the heat contents of the component binary oxide compounds. The positive deviation from the Neumann-Kopp rule for lead titanate can be attributed to the vertex-shared Ti-O octahedra in the perovskite structure, which are free to rotate, as compared with the edge-shared Ti-O octahedra in rutile.[13] In contrast, negative deviation from the Neumann-Kopp rule for lead zirconate can be attributed to the regular six-fold coordination and shorter Zr-O bond length in the perovskite structure as compared with the distorted seven-fold coordination for zirconium in baddeleyite.[14] Hence, a higher heat capacity is expected for the titanium-rich compositions. The present measurements confirm that this is indeed the case for the cubic phase of $PbZr_{1-x}Ti_xO_3$, as shown by the experimental data reported in Figure 7.7(a).

7.3.3 **Transition temperature, Entropies and Enthalpies**

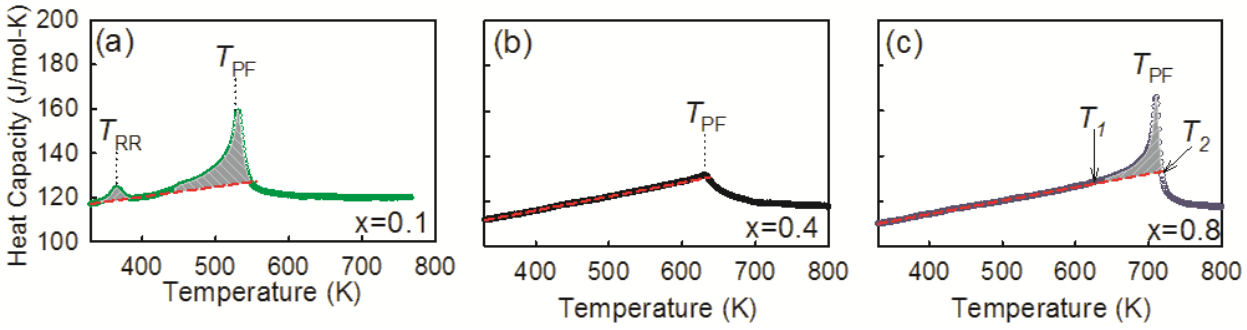

Figure 7. 8 Heat capacity *versus* temperature for unannealed of $PbZr_{1-x}Ti_xO_3$ sintered disks with the compositions (a) x = 0.10, (b) x = 0.40 and (c) x = 0.80 measured on heating. T_{RR} and T_{FP} denote the temperatures of the peaks in the heat capacity at the rhombohedral cell doubling (R3*c* ↔ R3*m*) and ferroelectric to paraelectric (R3*m* ↔ P*m*3*m*) phase transitions, respectively. The dashed line shows the background heat capacity used for the estimation of the transition enthalpies.

Because the shapes and intensities of the heat capacity curves changed markedly with composition in the regions near the rhombohedral cell doubling and ferroelectric to paraelectric transitions, as shown on Figure 7.3 and Figure 7.5, the transition temperatures and enthalpies were determined using the simplest method that enabled a valid and reproducible comparison among the different samples investigated. The transition temperatures, T_{RR} and T_{PF}, were determined by locating the maxima in the heat capacity curves using a second derivative test. The transition enthalpies, ΔH_{RR} and ΔH_{PF}, were determined by integrating the heat capacities $[C_P(T)]$ relative to linear background function $[C_P^0(T)]$ fitted to the data in ranges of temperature $T_1 < T_{PF}$ away from the transitions and extrapolated to temperature $T_2 > T_{PF}$,

$$\Delta H_i = \int_{T_1}^{T_2} [C_P(T) - C_P^0(T)]dT . \qquad (7.1)$$

Figure 7.9a and Figure 7.9b shows the excess heat capacity, $\Delta C_P = C_P(T) - C_P^0(T)$, and excess entropy, $S^{XS} = \int (\Delta C_P(T)/T)dT$, for all the unannealed compositions studied following the method shown in Figure 7.8. This ΔC_P and S^{XS} corresponds to the heat content at the phase transitions.

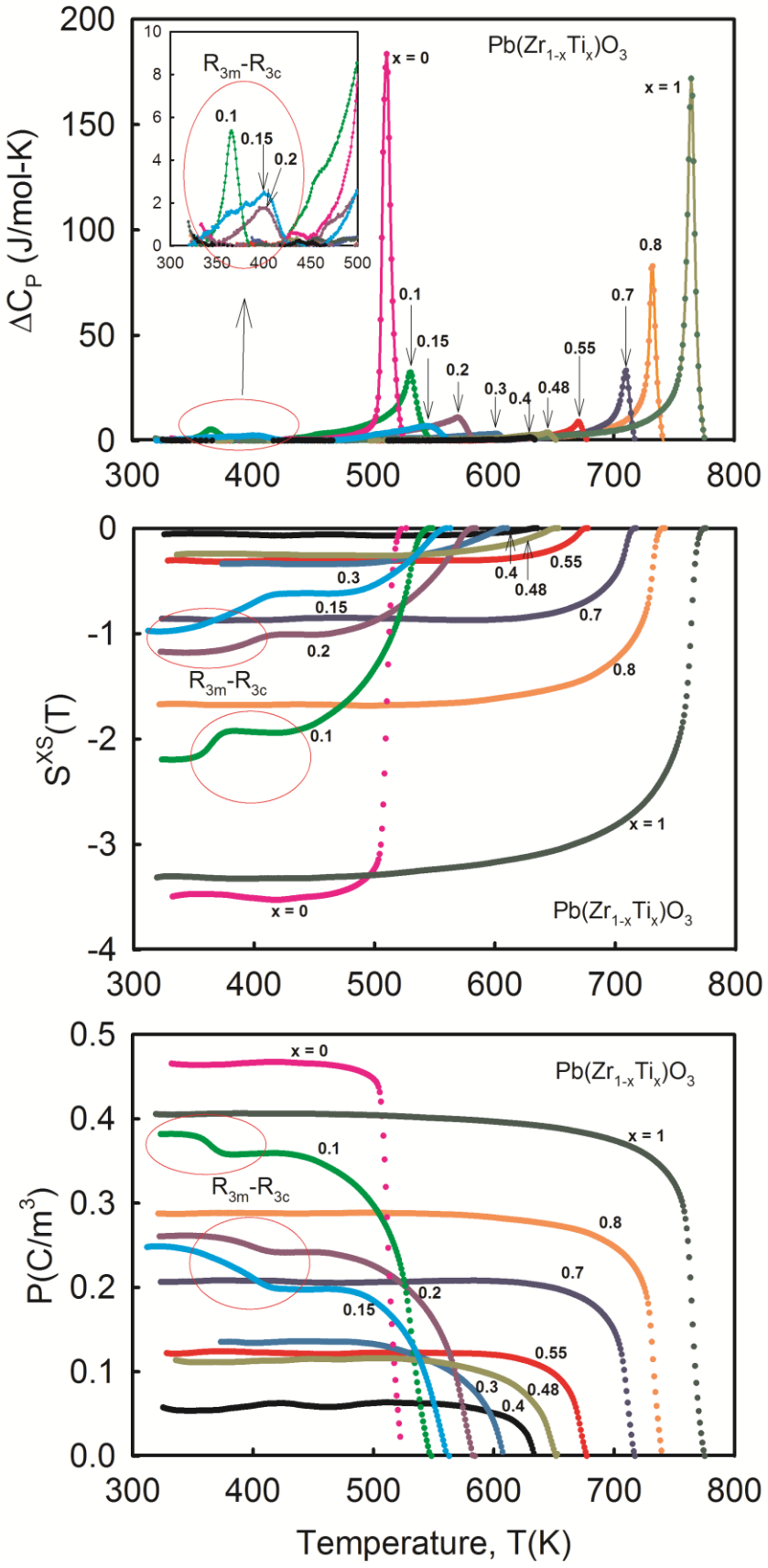

Figure 7. 9
Excess thermodynamic properties of unannealed $PbZr_{1-x}Ti_xO_3$ powder ($x = 0.00, 1.00$) and sintered disks ($0.10 \leq x \leq 0.80$) determined as shown in Figure 7.6.
(a) Excess heat capacity as a function of temperature. (Inset shows the F_{R3m}-F_{R3C} inter-ferroelectric phase transitions).
(b) Excess entropy as a function of temperature.
(c) Calculated reversible polarization as a function of temperature.

The method of determining the transition temperatures and enthalpies is illustrated on Figure 7.8c. Using this method the transition entropies $\Delta S_i = \Delta H_i / T_i$ were computed. The transition temperatures, enthalpies and entropies determined from data acquired on heating are collected in Table 7.2 for the rhombohedral cell doubling and ferroelectric to paraelectric transitions of all compositions investigated.

Table 7. 2 Transition temperatures (T_i), transition enthalpies (ΔH_i) and transition entropies (ΔS_i) acquired on heating for the ferroelectric to paraelectric (FP) and rhombohedral cell doubling (RR) phase transitions in unannealed $PbZr_{1-x}Ti_xO_3$ powders and sintered disks

x	Form	T_{FP} (K)	T_{RR} (K)	ΔH_{FP} (kJ/mol)	ΔH_{RR} (J/mol)	ΔS_{FP} (J/mol-K)	ΔS_{RR} (J/mol-K)
0.00	P [a]	511 ±1[b]	-	1.72 ±0.09 [a]	-	3.37 ±0.58 [c]	-
0.10	SD	531 ±1	366 ±1[b]	0.86 ±0.08	72.2 ±4.4[b]	1.61 ±0.46	0.20 ±0.04 [c]
0.15	SD	547 ±1	406 ±2	0.36 ±0.05	60.7 ±3.0	0.66 ±0.26	0.15 ±0.02
0.20	SD	571 ±1	406 ±1	0.47 ±0.05	59.5 ±1.5	0.82 ±0.29	0.15 ±0.01
0.30	SD	603 ±1	351 ±4	-	6.5 ±4.0	-	0.03 ±0.03
0.40	SD	630 ±1	-	-	-	-	-
0.48	SD	646 ±1	-	-	-	-	-
0.55	SD	671 ±1	-	0.11 ±0.01	-	0.16 ±0.03	-
0.70	SD	710 ±1	-	0.65 ±0.05	-	0.91 ±0.25	-
0.80	SD	734 ±1	-	1.06 ±0.01	-	1.44 ±0.04	-
1.00	P	767 ±1	-	1.88 ±0.01	-	2.45 ±0.05	-

[a] P: Powder, SD: Sintered disk
[b] Standard deviation about the mean
[c] Error propagated using three times the standard deviation in ΔH_i and an estimated absolute error in T_i of ±3 K

The errors for the transitions temperatures and enthalpies listed in Table 7.2 represent the standard deviations about the mean value of the three measurements preformed. Because the transition entropies are used in the Landau analysis of phase transition behavior described below, the errors in the entropy values reported in Table 7.2 were propagated using three times the standard deviation in transition enthalpy and an estimated absolute error ±3 K in the determination of transition temperature. This method of error estimation was adopted to compensate for any

systematic errors introduced in the empirical determination of the transition temperatures and enthalpies.

The transition temperatures T_{RR} and T_{PF} determined from the heat capacity data acquired on heating are shown in Figure 7.4. In this figure, the present experimental data are superimposed on the conventional composition-temperature phase diagram constructed by Jaffe, *et al*. using data taken from assembled from several separate investigations[8]. As seen in this figure, the transition temperatures determined from the heat capacity data reported here showed excellent agreement with those shown on the conventional phase diagram. The enthalpies of the PE-FE phase transitions determined from the heat capacity data as acquired on both heating and cooling are shown in Figure 7.10a).

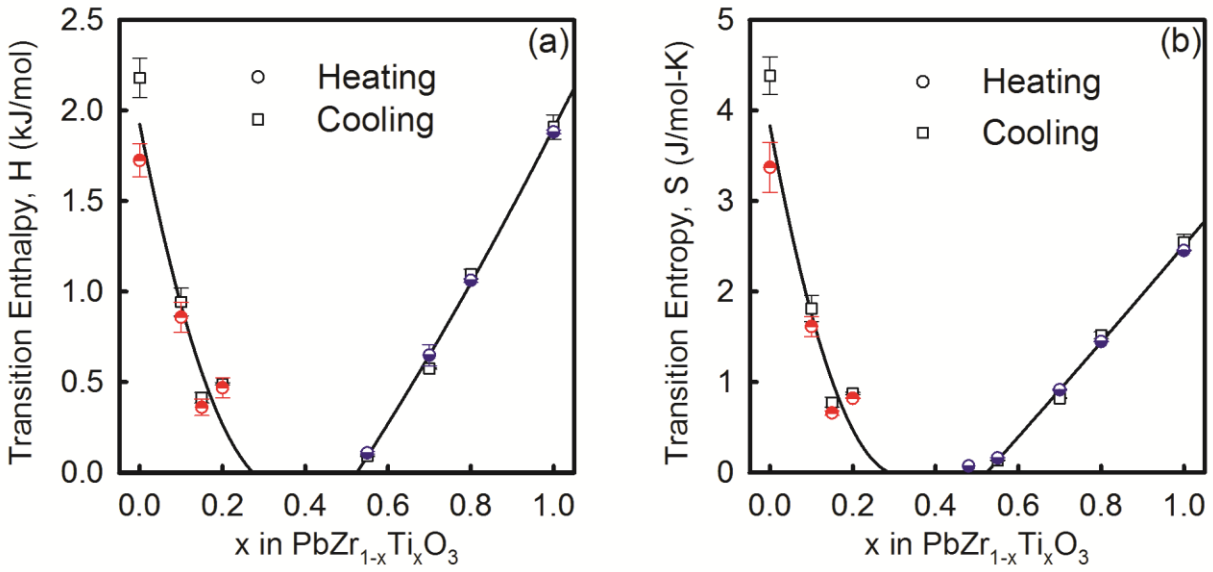

Figure 7. 10 (a) Transition enthalpies and (b) transition entropies *versus* composition collected in both heating and cooling heat capacity measurements. The solid lines shown are least-squares fits to both sets of data.

Several observations can be made from the data presented in this figure. First, as expected for reversible transitions, the transition enthalpies determined from data acquired on heating agreed with those acquired on cooling within experimental error. Further, the good agreement between the heating and cooling measurements confirms the reproducibility of the empirical method used to determine the transition enthalpies. Second, the transition enthalpies for both end member compounds are nearly equal ($\Delta H_{FP} \approx 2\,\mathrm{kJ/mol}$) and are in good agreement with those determined in prior heat capacity investigations of lead zirconate[15] and lead titanate[12,15]. Third, as is apparent from Figure 7.3, Figure 7.5 and Figure 7.6, the enthalpies of the PE-FE phase transitions decrease markedly on approaching the center of the phase diagram from either end member compound. For the compositions $0.60 \leq x \leq 1.0$ the enthalpies of the PE-FE phase transitions shown in Figure 7.10(a) are in good qualitative agreement with those determined from heat capacity made on powder specimens[12]. Finally, for the compositions $0.30 < x < 0.55$, the enthalpies of the PE-FE transitions are zero within experimental error. Here it is important to note that much smaller enthalpies than the smallest values shown on Figure 7.10(a) could be determined at the resolution of the measurements. As reported in Table 7.2, for the rhombohedral cell doubling transitions, enthalpies $\Delta H_{RR} < 0.1\,\mathrm{kJ/mol}$ could be measured, although with a higher relative error. This observation suggests that there are indeed two tricritical points along the line of PE-FE phase transitions in the range of composition $0.25 \leq x \leq 0.55$.

7.3.4 **Thermal analysis**

The experimental transition entropy data was analyzed using a Landau polynomial that describes a binary ferroelectric solid solution having two tricritical points along the lines of R3*m* $\leftrightarrow$ P*m*3*m* and P4*mm* $\leftrightarrow$ P*m*3*m* PE-FE phase transitions.[16,17] At high temperatures near the line of

Curie temperatures, $T_C(x)$, the truncated 2-4-6 Landau polynomial is asymptotically accurate. For this situation the excess non-equilibrium free energy ,G^{XS}, for weak first-order transitions close to second order can be written

$$G^{XS} = G(x,T,\boldsymbol{n},P) = \frac{1}{2}A_0(x)[T - T_C(x)]P^2 + \frac{1}{4}B(x,\boldsymbol{n})P^4 + \frac{1}{6}C_0P^6, \qquad (7.2)$$

where $\boldsymbol{n}$ is a unit vector in the direction of spontaneous polarization $\boldsymbol{P}$, and P is its absolute value. The dielectric stiffness is given by the Curie-Weiss law, $A_0(x) = 1/\varepsilon_0 C_{CW}(x)$, where $C_{CW}(x)$ is the Curie-Weiss constant and ε_0 is the permittivity of free space. The quartic term in Equation 7.2 is assumed to have the following form,

$$B(x,\boldsymbol{n}) = B_0[(x - x_0) - \xi(x - x_m)(n_1^4 + n_2^4 + n_3^4)] \qquad (7.3)$$

where B_0 and ξ are constants and x_0 and x_m are the compositions where the quartic isotropic and quartic anisotropic contributions to the free energy vanish, respectively. Figure 7.11(a) and Figure 7.11(b) shows the predicted linear dependence of composition through tricritical points in PZT. The coefficient of the sextic term, C_0, is taken to be a constant, independent of *x, T* and $\boldsymbol{n}$. After minimizing Equation 7.2 with respect to $\boldsymbol{n}$ and *P*, below $T_C(x)$ the rhombohedral phase with $\boldsymbol{n}_R^{eq} = \{1/\sqrt{3}, 1/\sqrt{3}, 1/\sqrt{3}\}$ is stable for $x < x_m$ and the tetragonal phase with $\boldsymbol{n}_T^{eq} = \{0,0,1\}$ is stable for $x > x_m$. Hence, Equation 7.3 becomes,

$$B(x,\boldsymbol{n}_{eq}) = \begin{cases} B_0[(x - x_0) - (x - x_m)\xi/3] & \text{if } x < x_m \\ B_0[(x - x_0) - (x - x_m)\xi] & \text{if } x > x_m \end{cases} \qquad (7.4)$$

It is apparent from Equation 7.4 that x_m is the composition where the morphotropic boundary line intersects the line of Curie temperatures, *i.e.*, a triple point with coordinates (x_m, $T_C(x_m)$). It is

further evident that if the PE-FE phase transitions for the two end members are both of first order, the constant ξ in Equation 7.4 must adopt a value $1 \le \xi \le 3$.

A tricritical point is defined by the condition that the entire quartic term in by Equation 7.2 turns out to be zero,

$$\min[B(x,\boldsymbol{n})] = 0 \tag{7.5}$$

It follows from Equation 7.4 and Equation 7.5 that there is one such point in the rhombohedral phase having coordinates ($x_R^{CR}, T_C(x_R^{CR})$) with

$$x_R^{CR} = \frac{x_0 - x_m \xi/3}{1-\xi/3}, \tag{7.6}$$

and a second such point in the tetragonal phase having coordinates ($x_T^{CR}, T_C(x_T^{CR})$) with

$$x_T^{CR} = \frac{x_0 - x_m \xi}{1-\xi}. \tag{7.7}$$

From Equation 7.6 and Equation 7.7 there is one line of second-order PE-FE phase transitions for $x_R^{CR} < x < x_T^{CR}$ and two lines of first-order PE-FE phase transitions with $x < x_R^{CR}$ and $x > x_T^{CR}$. Along the two lines of first-order transitions, jumps in polarization $\Delta P(x)$ occur at the temperatures $T_0(x)$, where the ferroelectric and paraelectric phases are in equilibrium,

$$\Delta P^2(x,T_0) = -\frac{3}{4}\frac{B(x,\boldsymbol{n}_{eq})}{C_0}. \tag{7.8}$$

The jump in polarization can be related to the entropy change at $T_0(x)$ by taking the temperature derivative of Equation 7.2,

$$\left.\frac{\partial G^{XS}}{\partial T}\right|_{T_0(x)} = -S^{XS}(x,T_0) = \frac{1}{2}A_0(x)\Delta P^2(x,T_0). \tag{7.9}$$

Equating the jumps in polarization in Equation 7.8 and Equation 7.9 and associating the excess entropy with the experimentally measured values $-S^{XS}(x,T_0) \approx \Delta S(x,T_{FP})$ results in,

$$\frac{B(x,\boldsymbol{n}_{eq})}{C_0} = -\frac{8}{3}\frac{\Delta S(x,T_{FP})}{A_0(x)} \quad . \tag{7.10}$$

In Equation 7.10 $\Delta S(x,T_{FP}) = \Delta S_i(x)\rho_M(x)$, where $\Delta S_i(x)$ is the measured transition entropy reported in Table 7.1 in units of kJ/mol and $\rho_M(x) = M(x)/\rho_X(x)$ is the molar density in which $M(x)$ is the molecular weight and $\rho_X(x)$ is the measured x-ray density. Using Equation 7.4 and Equation 7.5, Equation 7.10 becomes

$$\frac{B(x,\boldsymbol{n}_{eq})}{C_0} = \begin{cases} \frac{B_0}{C_0}[(x-x_0)-(x-x_m)\xi/3] & \text{if } x < x_R^{CR} \\ \frac{B_0}{C_0}[(x-x_0)-(x-x_m)\xi] & \text{if } x > x_T^{CR} \end{cases} . \tag{7.11}$$

Equation 7.11 predicts that the ratio $B(x,\boldsymbol{n}_{eq})/C_0$ is a linear function of composition. Further, from Equation 7.10, if the transition entropy displays a linear dependence on composition as shown by the data in Figure 7.10(b), then the dielectric stiffness $A_0(x)$ must also vary linearly with x.

To compute values for the ratio $B(x,\boldsymbol{n}_{eq})/C_0$, the experimental transition entropies reported in Table 7.2 were inserted in Equation 7.10, together with dielectric stiffness $A_0(x)$ taken as the linear interpolation between the measured values for single crystals of lead titanate[18] and zirconium-rich ($x \leq 0.06$) single crystals of $PbZr_{1-x}Ti_xO_3$,[19]

$$A_0(x) = 5.66\times10^5(1-x) + 8.70\times10^5 x \quad \text{(V-m/C-K)} \tag{7.12}$$

The variation of $B(x,\boldsymbol{n}_{eq})/C_0$ with composition is shown in Figure 7.11(d). In this figure, the symbols show the ratio $B(x,\boldsymbol{n}_{eq})/C_0$ computed using Equation 7.10 and the solid lines are the least-squares fits to the computed values. The intersections of the fitted lines with the horizontal

axis gave the compositions of the two tricritical points, $x_R^{CR} = 0.22$ and $x_T^{CR} = 0.51$, while the intersection of the two lines with each other gave the location of the triple point, $x_m = 0.28$.

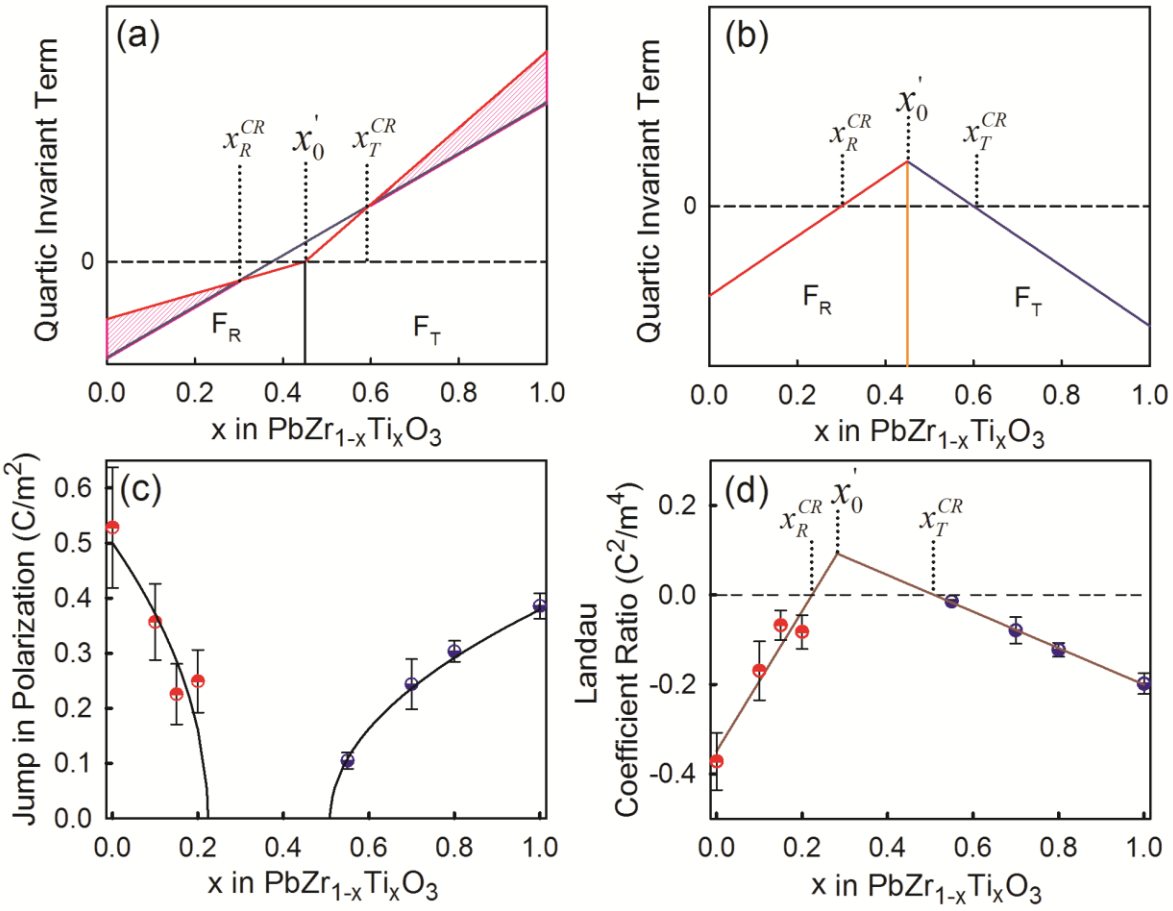

Figure 7. 11 (a) Individual variation of the isotropic and anisotropic quatic invariant terms as a function of composition. (a) Predicted linear dependence of the isotropic and anisotropic contribution to the quartic Landau coefficient. (b) Predicted quartic and sextic Landau coefficient ratio in PZT obtained from Rossetti et al.[20] (c) The jump in polarization at the ferroelectric to paraelectric transition for unannealed $PbZr_{1-x}Ti_xO_3$ powders (x = 0.00, 1.00) and sintered disks ($0.10 \le x \le 0.80$) *versus* composition (half-filled circles). The half-filled circles represent the values computed from the measured transition entropy using Equation 7.8. The solid lines are computed from Equation 7.11 using the Landau parameters of unannealed samples given in the text. (d) The Landau coefficient ratio $[B(x,\boldsymbol{n}_{eq})/C_0]$ of unannealed $PbZr_{1-x}Ti_xO_3$ powder (x = 1.00) and sintered disks ($0.10 \le x \le 0.80$) *versus* composition (half-filled circles). The value of the Landau coefficient ratio was computed from the measured transition entropy using Equation 7.8. and Equation 7.11. The solid lines shown represent linear least-squares fits to the data of unannealed samples

These values were substituted into Equation 7.6 and Equation 7.7, which when solved simultaneously, returned values of $x_0 = 0.25$ and $\xi = 1.16$. By substituting these parameters into Equation 7.11 the scale factor $B_0/C_0 = 2.44 \pm 0.22$ was found that best reproduced the fitted lines shown on Figure 7.11d. Using these parameters, the jumps in polarization along the lines for first-order transitions were predicted by inserting Equation 7.11 into Equation 7.8 and the results are shown on Figure 7.11(c). For comparison, the jumps in polarization computed directly from Equation 7.9 using the experimentally measured entropies and dielectric stiffnesses are also shown. As the latter computation makes no assumptions concerning the forms of the quartic and sextic terms, except that they are independent of temperature, the results shown on Figure 7.11 verify that the truncated 2-4-6 Landau polynomial of Equation 7.2 with quartic term given by Equation 7.3 provides an excellent approximation for the $PbZr_{1-x}Ti_xO_3$ system at high temperatures near the Curie line.

It had been demonstrated that the excess heat capacity goes as $\Delta C_P \propto (T_o - T)^{-1/2}$ or similarly that the excess entropy goes as $S^{XS} = (T_0 - T)^{1/2}$ as T_0 approach T_C or as $T_0 - T_C$ goes to zero.[21,22] The exponent $\beta = 1/2$ in both expressions had been also associated with the tricritical point exponent. It is demonstrated in Figure 7.12 the deviation from $\beta = 1/2$ as moving far from $x_R^{CR} = 0.22$ and $x_T^{CR} = 0.51$. Figure 7.12(b) shows compositions x = 0.3 and x = 0.48 close to such compositions. For the compositions in Figure 7.12(a) and 7.12(c) obvious deviation was observed of the deviation from $\beta = 1/2$. Similarly, a linear behavior is expected for the excess entropy as approaching the tricritical point, where it deviate from linearity as moving far from those points.

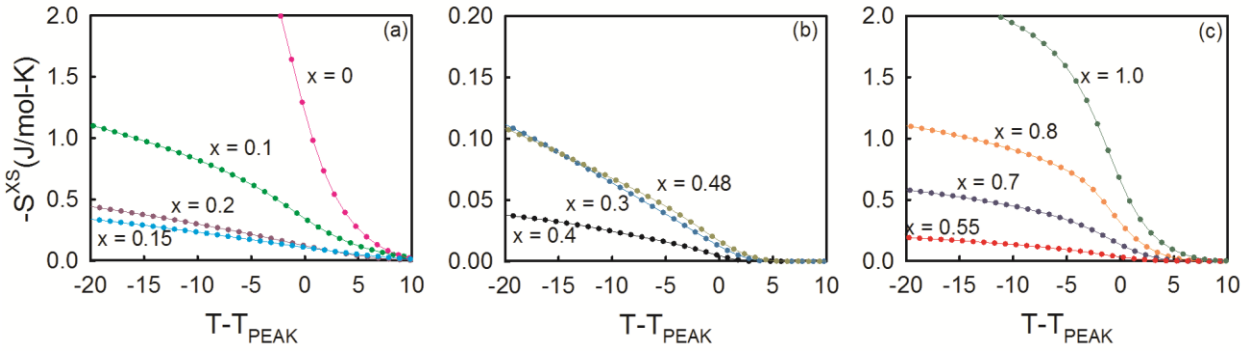

Figure 7. 12 Excess entropy behavior around the PE-FE phase transition as function of $T - T_{peak}$ of the unannealed $PbZr_{1-x}Ti_xO_3$ powder (x = 0.0, 1.00) and sintered disks ($0.10 \leq x \leq 0.80$). (a) Composition in the F_R-phase, (b) compositions around the MPN and (c) compositions in the F_T-phase.

7.4 **Summary**

A heat capacity study was presented in several *Pb(Zr$_{1-x}$Ti$_x$)O$_3$* compositions that range through all the phase diagram. Empirical analysis of the heat capacity data shows the transition from a first to a second order phase transition associated with a tricritical point. Those critical points were found as approaching the MPB form both end members. It was also confirmed from the derivative of the heat capacity which shows a step function at phase transition showing second order behavior. The enthalpy associated with the phase transitions were determined from integration of the excess heat capacity by a subtraction of a linear background related to the low temperature heat capacity data. By using these enthalpies, predictions to the both tricritical points from a modified Landau theory was verify. Due to the linear compositional dependence of the Landau free energy this theory was easy applied which results in the location of the tricritical point at $x_R^{CR} = 0.22$ and $x_T^{CR} = 0.51$. Also the critical exponent to the excess entropy associated with the tricritical point was experimentally demonstrated.

7.5 **References**

1. Chung, C.-C. Microstructural Evolution in Lead Zirconate Titanate (PZT) Piezoelectric Ceramics. 88–106 (2013).

2. Kakegawa, K., Arai, K., Sasaki, Y. & Tomizawa, T. Homogeneity and properties of lead zirconate titanate prepared by a combination of thermal spray decomposition method with solid-phase reaction. *J. Am. Ceram. Soc.* **71,** (1988).

3. Wilkinson, A. P., Speck, J. S. & Cheetham, A. K. In Situ X-rya Diffraction Study of Crystallization Kinetics in PbZr1-xTixO3 (PZT, x = 0.0, 0.55, 1.0). *Chem. Mater.* **6,** 750–754 (1994).

4. Jona, F., Shirane, G., Mazzi, F. & Pepinsky, R. X-Ray and Neutron Diffraction Study of Antiferroelectric Lead Zirconate, PbZrO3. *Phys. Rev.* **105,** 849–856 (1957).

5. Miyake, S. & Ueda, R. On Polymorphic Change of $BaTiO_3$. *J. Phys. Soc. Japan* **1,** 32–33 (1946).

6. Gray, R. B. No Title. 486–560 (1949).

7. Devonshire, A. F. CIX . Theory of barium titanate — Part II. *Philos. Mag. Ser. 7* **42,** 1065–1079 (1951).

8. Jaffe, B., Cook, W. R. & Jaffe, H. *Piezoelectric Ceramics*. 53–183 (Academic Press, 1971).

9. G. A. Rossetti, Zheng, W. & Khachaturyan, A. G. Phase coexistence near the morphotropic phase boundary in lead zirconate titanate solid solutions. *Appl. Phys. Lett.* **88,** 072912 (2006).

10. Eremkin, V. V., Smotrakov, V. G. & Fesenko, E. G. Structural Phase Transitions in PbZr1-xTixO3 Crystals. *Ferroelectrics* **110,** 137=144 (1990).

11. Rane, M. V, Navrotsky, A. & Rossetti, G. A. Enthalpies of Formation of Lead Zirconate Titanate (PZT) Solid Solutions. *J. Solid State Chem.* **161,** 402–409 (2001).

12. Rossetti, G. A. & Navrotsky, A. Calorimetric Investigation of Tricritical Behavior in Tetragonal Pb (Zr x Ti 1 ⁄ x) O 3. *J. Solid State Chem.* **144,** 188–194 (1999).

13. Robie, R. A. & Hemingway, B. S. *Thermodynamic Properties of Minerals and Related Substances at 298.15K and 1 Bar (105 Pascals) Pressure and at Higher Temperatures.* (Geological Survey Bulletin, 1995).

14. Barin, E. & Knacke, O. *Thermochemical Properties of Inorganic Substances*. (Springer-Verlag, 1973).

15. Yoshida, T. *et al.* HEAT CAPACITY AT CONSTANT PRESSURE AND THERMODYNAMIC PROPERTIES OF PHASE TRANSITIONS IN PbMO3 (M = Ti , Zr AND Hf). *J. Therm. Anal. Calorim.* **95,** 675–683 (2009).

16. Rossetti, G. A., Khachaturyan, A. G., Akcay, G. & Ni, Y. Ferroelectric solid solutions with morphotropic boundaries: Vanishing polarization anisotropy, adaptive, polar glass, and two-phase states. *J. Appl. Phys.* **103,** 114113 (2008).

17. Heitmann, A. A. & Rossetti, G. A. Thermodynamics of polar anisotropy in morphotropic ferroelectric solid solutions. *Philos. Mag.* **90,** 71–87 (2010).

18. Rossetti, G. a & Maffei, N. Specific heat study and Landau analysis of the phase transition in PbTiO 3 single crystals. *J. Phys. Condens. Matter* **17,** 3953–3963 (2005).

19. Whatmore, R. W., Clarke, R. & Glazer, A. M. Tricritical behaviour in PbZrxTi1-xO3 solid solutions. *J. Physic C Solid State Phys.* **11,** 3089 (1978).

20. Khachaturyan, A. G. Ferroelectric solid solutions with morphotropic boundary: Rotational instability of polarization, metastable coexistence of phases and nanodomain adaptive states. *Philos. Mag.* **90,** 37–60 (2010).

21. E. Salje. in *Phys. Prop. Thermodyn. Behav. Miner.* (Salje, E.) 75–119 (Dordrecht: Reidel, 1988).

22. Lines, M. E. & Glass, A. M. *Principles and Applications of Ferroelectrics and Related Materials*. (Clarendon Press, 1977).

CHAPTER 8

PHASE TRANSITON ENERGETICS IN RELAXOR-PT FERROELECTRIC MATERIALS (PZN-PT AND PMN-PT) AND ASSOCIATED PHENOMANA TO THE POLARIZATION.

8.1 Introduction

A new method for energy harvesting has recently been demonstrated in which electrical energy is generated by using the ferroelectric to ferroelectric (inter-ferroelectric) transition at the MPB of the ternary solid solution engineering domain relaxor ferroelectric single crystal $xPb(In_{1/2}Nb_{1/2})O_3$ - $(1-x-y)Pb(Mg_{1/3}Nb_{2/3})O_3$ - $yPbTiO_3$ (PIN-PMN-PT).[1,2] . This ferroelectric material has a higher Curie temperature (T_C) and larger coercive field (E_C) when compared with the pseudobinary MPB solid solutions relaxor ferroelectrics.[3–5] In this new energy harvesting method, the simultaneous application of stress and electric field generates a polarization rotation between ferroelectric phases. The energy corresponding to the change in polarization ($\Delta P_{\mathrm{FR-FO}} \approx 0.02\ to\ 0.03\ C/m^2$) at the inter-ferroelectric transition might be harvested under cyclic loading conditions.

The polarization rotation at the inter-ferroelectric transition is a function of both the modulus and direction of the polarization. It had been demonstrated that the ΔP of the inter-ferroelectric phase transition at the MPB of solid solution ferroelectric systems is associated with a low crystallographic anisotropy of polarization.[6] If ΔP is very small, then the crystallographic anisotropy of polarization at the inter-ferroelectric transition vanishes. It means that the polarization between ferroelectric phases at the MPB is almost continuous or there is an easy

polarization rotation at the inter-ferroelectric transition.[6–11] This is the most "inexpensive" mode of the ground state perturbation.[11]

Nanoscale inhomogeneities of local short-range order, or polar nanoregions (PNR), are also considered to explain the nature of the polarization rotation in relaxor ferroelectrics. The concept of polar local regions was proposed by Burns and Dacol from the temperature dependence of the index of refraction $n(T)$ in the relaxor prototypes PMN and PZN.[12] They observed a deviation from linearity of $n(T)$ in temperatures way above a broad maximum in dielectric constant (T_{max}). This deviation from linearity of $n(T)$ is known as the depolarization temperature (T_d), or the Burns temperature (T_B), or the onset in polarization for relaxor ferroelectrics. This transition temperature has been also observed from acoustic emission measurements,[13] thermal expansion,[14] heat capacity and thermal conductivity,[15,16] birefringence,[17] neutron scattering,[18] etc. The diffuse phase transition in relaxor ferroelectrics is associated with a built-in disorder related with the presence of PNR's. This PNRs damp the polar transverse optic phonon mode that drop precipitously into the transverse acoustic branch.[18–21] Order-disorder-like ordering of PNRs, as a function of PT concentration, has been proposed in relaxor ferroelectrics due to observation of no change in local structure, in overall, as the crystal structure undergoes a series of R-O-T ferroelectric phase transitions.[22,23]

In this chapter, it is investigated the phase transition energetics and polarization contributions in PZN-PT and PMN-PT pseudobinary solid solutions relaxor ferroelectric single crystal materials with compositions around the MPB. A wide temperature range C_P measurement of all compositions were used to determine the contributions from the diffuse and structural phase transformations. A method was developed to separate both contributions, and to determine their entropies, enthalpies, and polarizations based on thermodynamic relations that follow the low

order approximation of the Landau theory. Additional contributions associated with an induced phase transition as a result of a poled state in PMN-PT will also be discussed.

8.2 Experimental

Commercial [001] oriented PZN-x%PT (x = 4.5, 6, 7 and 8) single crystals, originally (4 x 4 x 12 mm) poled and along z-direction supplied from Microfine Materials Technology Pte Ltd, Singapore, were sectioned along z-direction into about 1 mm thick. High temperature flux growth process with PbO based fluxes were used to grow these crystals.[24,25] Also, commercially [001] oriented PMN-28%PT single crystal, originally (13.27 x 6.6 x 1.75 mm) poled along z-direction from TRS Technology, was sectioned along x- and y- plane for different measurement condition with thickness of 1.75 mm. The sample were sectioned by using a South Bay Technology Model 650 low speed diamond wheel saw and then thermally depoled at 250 ^{o}C for 2 hours.

The specimens were characterized by a weak-field dielectric permittivity measurement as a function of temperature by using the HP Agilent 4282A LCR meter under 0.1 volts at 1 kHz. The specimens were coated with colloidal silver paste allowed to cure for 24 hours at room temperature before measurement. The temperature dependence of dielectric permittivity was obtained by placing the specimens along the c-direction (1.0 mm) in a two pin custom-built fixture inside a 9100 Delta Design oven for a temperature range from 129 to 473 K at 3 K temperature increment. Polarization versus electric field loop were obtained from a sawyer-tower bridge at room temperature at different voltage.

The same experimental set up were used to measure the pyroelectric current from -50 °C to 250 °C at 1 degree per minute. However, the a HP Agilent 4140B picoammeter connected to the low side of the sample, while the connection to the high side was terminated to a 50 Ω ground,

used to measure the charge build up. The pyroelectric current was subsequently measured at every half degree. The change in polarization as a function of temperature was determined by following the Byer-Rondy method.[26]

Differential Scanning Calorimeter (DSC) 404 F1 Pegasus from Netzsch, in a temperature range from 100 to 1000 K at 10 K/min with 20 points per degree Kelvin, was used to measure the heat capacity (C_P) of the relaxor ferroelectric single crystals PZN-x%PT (x = 4.5, 6, 7 and 8) and PMN-28%PT. The specimens were placed in good thermal contact within covered platinum crucibles. In order to accurately determine the C_P, the ASTM E 1269 ratio method was used with NIST SRM-720 data for a single crystal Al_2O_3 as the calibration standard. Two sets of data (at the low and high temperature ranges) were stitched together after careful calibration of the baseline. The accuracy of the data (absolute average error ~1 %) was verified by comparing the measured C_P of Alumina with the C_P-standard (NSB standard table). The low temperature range (100 to 823 K) was conducted under Helium using the Silver-furnace with the E-type sensor (calibrated with Bi, CsCl, Hg, In, Sn and Zn). Liquid Nitrogen was used during the cooling process with the low temperature range experimental conditions. The high temperature range (303 to 1000 K) was carried out under Argon using the Platinum-furnace with the S-type sensor (calibrated with In, Bi, Al, Ag and Au). The gas flow rates, in both temperature ranges, was 50 ml/min.

Thermal Measurement Analyzer (TMA) Q400 V7.4 thermochemical analyzer from 278 to 803 K at 2 K/min was used for the thermal expansion measurements. The Nitrogen gas flow rate and mechanical load were 100 mL/min and 0.05 N, respectively. ASTM E-831 was used to calibrate the system with Sn, In, Zn, Al standards. The absolute average experimental error for the thermal expansion was ~5.0%.

PART A: SEPARATION OF THE REVERSIBLE AND RELAXOR CONTRIBUTIONS TO THE POLARIZATOIN AND THEIR ENERGETICS

8.3 Results and Discussion

8.3.1 Sample characterization by dielectric measurement

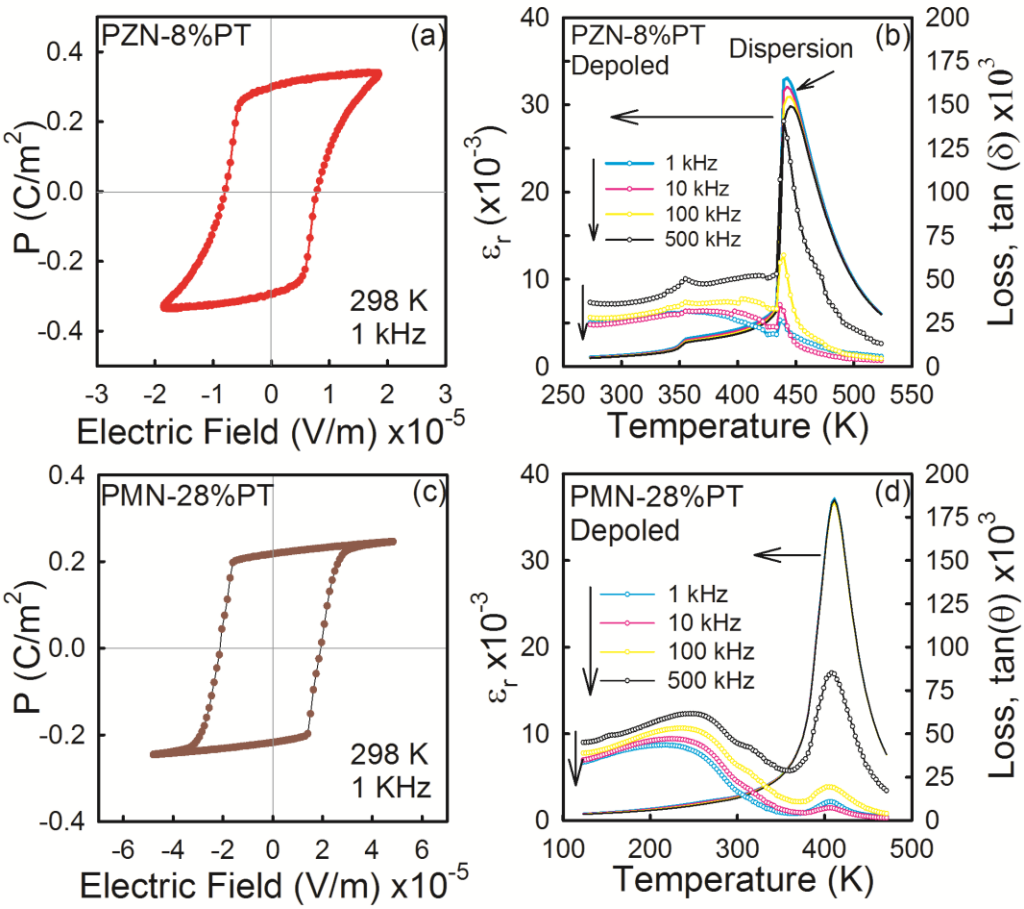

Figure 8.1 (a) Characterization of depoled PZN-8%PT, (a) and (b), and PMN-28%PT, (c) and (d) relaxor ferroelectric single crystals. (a) and (c) Polarization as a function of electric field and (b) and (d) relative dielectric permittivity and electric loss as a function of temperature for different frequencies.

The polarization as function of electric field (P-E loop) and the relative dielectric permittivity (ε_r) and electrical loss ($\tan\delta$) as a function of temperature were used to characterize the relaxor ferroelectric single crystal materials PZN-8%PT (as a representation of the PZN-x%PT

specimens) and PMN-28%PT, both shown in Figure 8.1. The P-E hysteresis of both relaxor ferroelectrics is an indication of the good quality of the investigated single crystals. The spontaneous polarization (P_s) was observed at 0.29 C/m^2 and at 0.22 C/m^2 for PZN-8%PT and PMN-28%PT, respectively. The dielectric permittivity of both single crystals reveals sharp peaks at the paraelectric to ferroelectric (PE-FE) phase transition. These peak temperatures were found at 442.6 K and 408.2 K for PZN-8%PT and PMN-28%PT, respectively. They agree well with the Curie line.[27,28] The inter-ferroelectric phase transition, ferroelectric tetragonal to ferroelectric rhombohedra (F_T-F_R), was observed for PZN-8%PT corresponding to the phase transition across the MPB. The temperature of the F_T-F_R transitions agree with the data of Amin et al.[29,30] The electrical loss decreases as the temperature increases, in general, and follows similar trend as the dielectric permittivity. High electrical losses were observed at high frequencies. Also, from the electrical loss it is observe the frequency dependence behavior characteristic of the relaxor behavior.[14]

The order nature of the phase transition in the relaxor ferroelectric single crystals was investigated by their thermal hysteresis. The signature for a first-order phase transition, due to thermal hysteresis at both the PE-F_T and F_T-F_R phase transitions, is shown in the dielectric permittivity of PZN-8%PT in Figure 8.2a. Similar thermal hysteresis from dielectric permittivity has been reported for PMN-32%PT, indicating characteristic of first-order transition..[31] In PZN-8%PT, it was observed that the thermal hysteresis of the inter-ferroelectric phase transition was about 35 to 40 degrees, as shown in inset of Figure 8.2a. It was confirmed from the thermal hysteresis of the C_P-data, shown in Figure 8.2b.

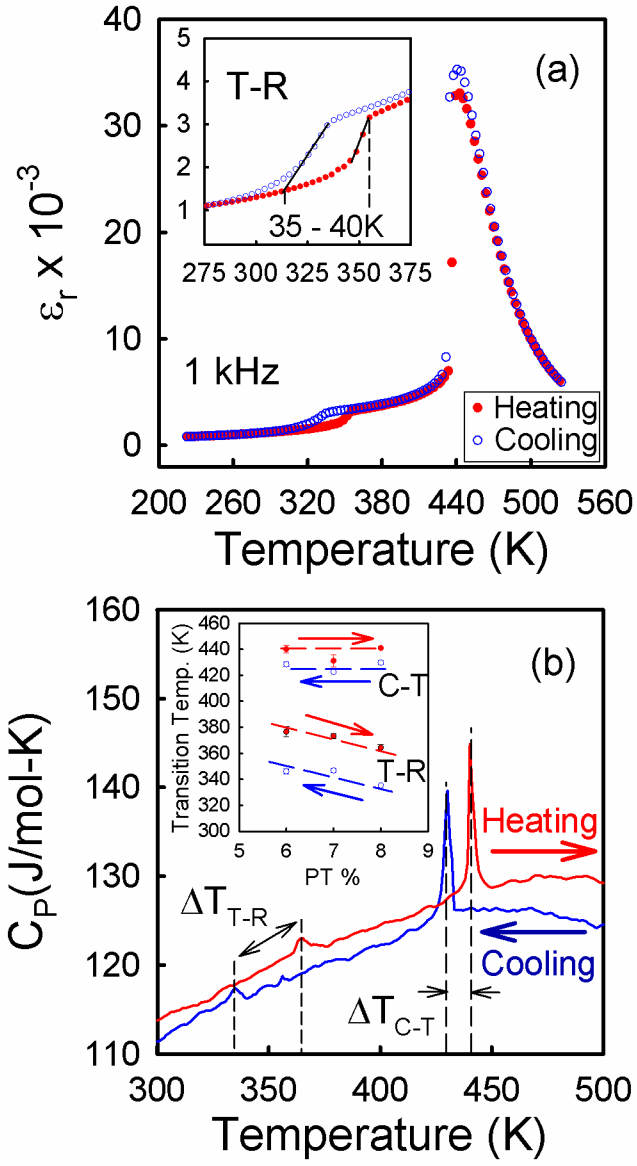

Figure 8.2 Thermal hysteresis of the depoled PZN-8%PT from: (a) relative dielectric permittivity at 1 kHz (inset: inter-ferroelectric phase transition) and (b) heat capacity (inset: depoled 6, 7 and 8 % PT single crystals) as a function of temperature.

The thermal hysteresis in both PE-F_T and F_T-F_R phase transitions observed from the C_P-data confirmed their first-order nature. In PZN-8%PT, the thermal hysteresis of the PE-F_T transition was found to be about 11 degrees while for the F_T-F_R transition was about 30 degrees. Similar thermal hysteresis of 10 K and 40 K has been revealed from acoustic emission in PZN-

9%PT indicating very small elastic strain energy from a gradual growth of the tetragonal into the monoclinic (M_C) phase and an abrupt PE-FE first order phase transition, respectively.[13] The thermal hysteresis of compositions across the MPB in PZN-PT (4.5, 6 and 7%) were also investigated, shown in the inset of Figure 8.2b. It was found that at the PE-F_T transition the thermal hysteresis was about 6.5 degrees while 28.5 degrees for the F_T-F_R transition. The error bars in the data correspond to the standard deviation on more than fifteen DSC runs to each single crystals. It is to be noted that, in average the thermal hysteresis remains constant for the different compositions for both the PE-F_T and F_T-F_R phase transitions. It is an indication of a compositional independence of the energy barrier for both phase transitions. Similar behavior had been observed in PMN-32%PT single crystal as a function of electric field during an induced F_R-F_O phase transformation.[32] Also, it has been found in PIN-PMN-PT single crystal[1,2] as a function of electrical, mechanical and thermal driving energies. In PIN-PMN-PT the hysteretic region between the F_R and F_O phases appears to remain constant, indicating that the energy barrier between these two phases is nearly constant.[1]

8.3.2 Poled state of relaxor ferroelectric PZN-x%PT at the MPB

A comparison of the C_P-data, in the temperature range around the phase transitions, of the poled (solid line) and depoled (dash line) states of composition across MPB in the PZN-PT phase diagram is shown in Figure 8.3. For all studied poled single crystal compositions (4.5, 6, 7 and 8%), discrete depolarization events were observed in a wide temperature range (~60 K) around the PE-F_T transition. It was observed during the first heating of the as received specimens.

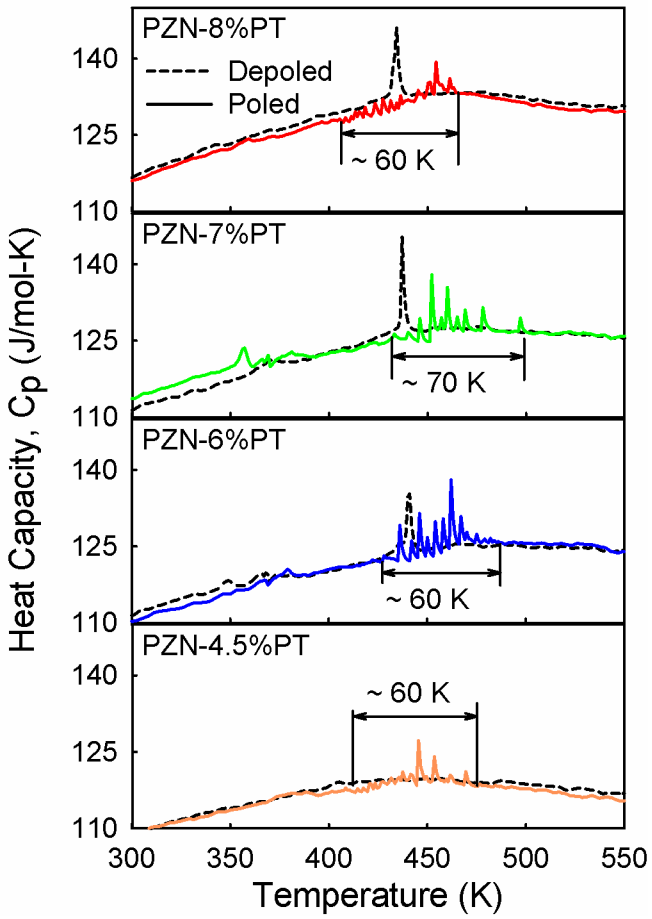

Figure 8.3 Heat capacity comparison of poled and depoled PZN-x%PT single crystals materials.

Those thermal depoling events were associated with competing thermodynamic of metastable states of switching depoling process from domains that were poled in a particular direction to a non-polar paraelectric phase as the temperature increase. Nevertheless, it is possible that these depoling events, corresponding to PNRs clusters, will appear randomly distributed in the same temperature range if the material is repoled. Guo et al. shows conglomeration of PNRs clusters in PMN-28%PT by birefringence data in a transmission optical polarization microscopy close to the mean T_c, that can be oriented in a partially random way by an induced electric field, which vanished as approaching T_d,.[23]

8.3.3 Heat capacity of PZN-x%PT with composition at the MPB and decouple of energy and polarization contributions

The C_P-data for the PZN-PT single crystals, in all measured temperature range is shown in Figure 8.4a. It is to be noted the consistency of the hard-mode behavior of the C_P-data for the different PZN-xPT compositions studied. The C_P-data for each individual single crystal is shown as inset in Figure 8.4a. Here, the PE-F_T (*) and F_T-F_R (+) phase transitions were clearly identified and they transition temperatures, enthalpies and entropies were tabulated in Table 8.1. The enthalpies at both transitions were determined from the thermal analysis software, "Proteus Analysis Software" from Netzsch. The method to determine those energies was by considering the integration area limited by the point where the derivative of the C_P differs from zero ($dC_P/dT \neq 0$) from the left and from the right of the phase transition. As well as for the transition temperatures, inset Figure 8.2b, the error of the enthalpy values corresponds to the standard deviation of more than fifteen DSC runs to each single crystals. The entropy was then calculated as ($\Delta H^{XS}/T_t$), where T_t is the corresponding phase transition temperature. The average enthalpies and entropies, excluding PZN-4.5%PT due to the high uncertainty in this particular sample (possible a non-translucent sample due to crack propagation), were of 30 J/mol and 0.07 J/mol-K, 10 J/mol and 0.026 J/mol-K for the PE-F_T and F_T-F_R phase transitions, respectively. Both F_T-F_R and PE-F_T transitions have small intensities but show hysteresis consistent with first-order behavior as was previously shown in Figure 8.2b.

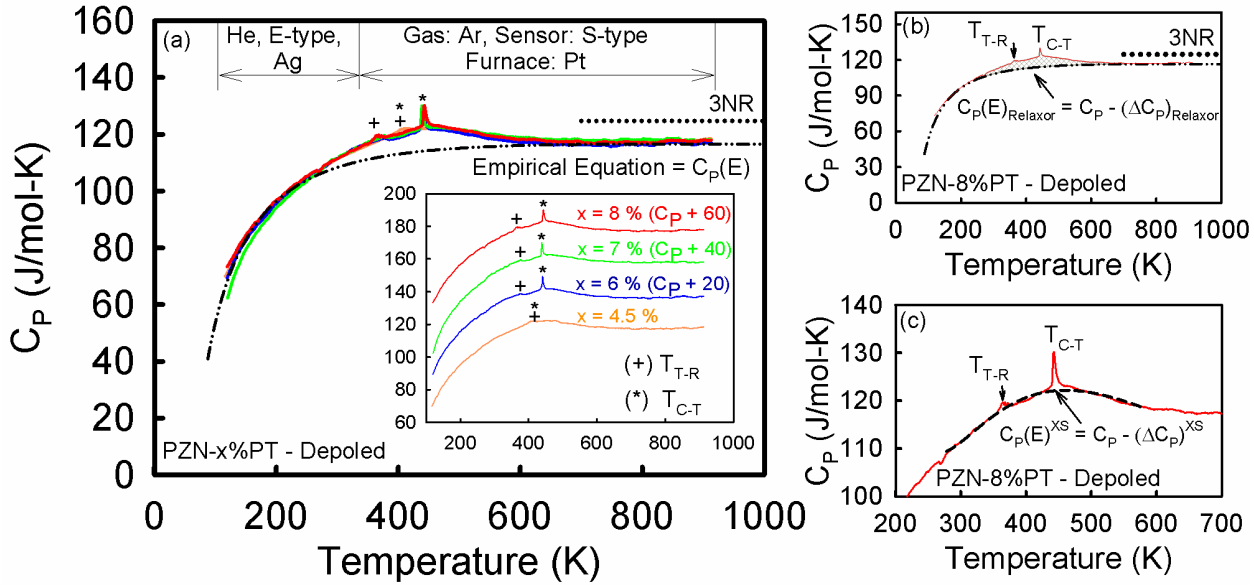

Figure 8.4 (a) Comparison of the heat capacity of the PZN-x%PT single crystals in a wide temperature range (inset: heat capacity of each single crystal), (b) Separation of the relaxor contribution to the polarization. (c) Separation of the reversible contribution to the polarization.

The high temperature C_P above T_d in the PE-phase, for PZN-x%PT specimen was observed below the Dulong-Petit Limit (3NR) (dot line). The number of atoms per unit cell is represented by $N = 5$ and $R = 8.314\ J/mol - K$ is the gas constant. Similar result has been found in $PbZr_{1-x}Ti_xO_3$ (PZT) with compositions around the MPB.[7,33] In this particular case, it was associated with higher degree of close-packing for the PZT samples, which may alter the elastic or electrostrictive properties and lead to a change in the character of the PE-F_T transition.[7] As a consequence an empirical equation, $C_{P-Empirical}$, was used to fit the hard-mode C_P instead of the Debye function, shown in Equation 8.1.

$$\boldsymbol{C_{P-Empirical} = a + bT^{-1} + cT^{\frac{1}{2}} + dT + eT^{2} + fT^{-2}} \quad (8.1)$$

The hard-mode behavior is associated with the C_P where there is no contribution to phase transitions. In this way, low temperature symmetry ferroelectric phase to the high temperature stable PE-phase were fitted to the empirical equation. During this process, it was found that the

relaxor ferroelectrics shown a characteristic anomalous deviation from the expected hard-mode behavior which manifest as a hump in a wide temperature range, not observed in normal ferroelectric such as $BaTiO_3$ and $PbTiO_3$. The regions outside that hump were consider as those found in normal ferroelectrics. Similar hump has been observed by Tachibana et al.[16]

Table 8.1. Properties of PZN-x%PT single crystals obtained from C_P measurement.

	PE-FT - Transition				FT-FR - Transition				
x%	T (K)	ΔH^{XS} (J/mol)	ΔS^{XS} (J/mol-K)	ΔP^{XS} (C/m^2)	T (K)	ΔH^{XS} (J/mol)	ΔS^{XS} (J/mol-K)	ΔP^{XS} (C/m^2)	T_d (K)
4.5	410 (±5.5)	5.80 (±3.9)	0.014 (±0.009)	0.025 (±0.014)	406 (±1.6)	- (-)	- (-)	0.007 (±0.001)	680 (±5.0)
6.0	440 (±2.9)	27.5 (±4.8)	0.062 (±0.010)	0.059 (±0.006)	376 (±3.9)	9.9 (±2.8)	0.026 (±0.007)	0.018 (±0.003)	690 (±5.0)
7.0	431 (±4.5)	27.9 (±4.2)	0.064 (±0.009)	0.059 (±0.005)	373 (±2.1)	12.3 (±5.1)	0.032 (±0.013)	0.015 (±0.001)	708 (±5.0)
8.0	440 (±0.9)	37.3 (±4.4)	0.084 (±0.010)	0.060 (±0.002)	364 (±2.5)	7.8 (±2.7)	0.021 (±0.007)	0.016 (±0001)	685 (±5.0)

In order to determine the enthalpy, entropy and polarization of the phase transitions, another empirical equation around the phase transition was applied. Figure 8.4b shows the fit of the empirical equation (dash-dot-dot line) to the hard mode behavior, as a Debye-like manner, in which the pre-factors in Equation 8.1 were given by: $a = 176.2$, $b = -1.0x10^4$, $c = -2.4$, $d = 0.03$, $e = 0.0$ and $f = 1.0x10^4$. The empirical equation around the phase transitions (dash line) is shown in Figure 8.4c where the pre-factors in Equation 8.1 correspond to: a = $3.1x10^3$, b = $-4.6x10^6$, c = -142.2, d = 1.93, e = 0.0 and f = $3.8x10^7$. By using this empirical method, the excess thermal properties (excess entropy = $S^{XS}(T) = \int \frac{\Delta C_P}{T} dT$, excess enthalpy = $H^{XS}(T) = \int \Delta C_P dT$ and excess free energy = $G^{XS}(T) = H^{XS}(T) - TS^{XS}(T)$) and the polarization corresponding to the anomalous deviation of the hard mode C_P and to the region at phase transitions was determined. The excess energy not associated with the hard-mode contribution is the excess heat capacity,

$\Delta C_P = C_P - C_{P-Empirical}$. It is the purpose of this paper to show the contributions of the energy of both phase transition and the anomalous deviation.

By using the low order approximation of the Ginzburg-Landau thermodynamic theory, it is may be possible to calculate the polarization from the C_P-data.[34,35] This approximation consider the high order temperature Landau coefficients and may give a representation to the polarization behavior. However, since the energetics at both phase transition are extremely small, especially at the inter-ferroelectric transition, a continuity in polarization from one ferroelectric phase to another may be assumed.[6–11] In fact, it was theoretically proposed by A. Heitmann and G. A. Rossetti that the crystallographic anisotropy of polarization at inter-ferroelectric transitions vanished.[8] Having that in consideration, the free energy associated with the above system may be represented as in Equation 8.2:

$$\boldsymbol{G^{XS}(T) = \frac{1}{2}A_o(T - T_C)P^2 + \frac{1}{4}BP^4 + \frac{1}{6}CP^6} \tag{8.2}$$

where B and C are the high order Landau coefficients and $A_o = 2.8\,x10^6\,\frac{Jm}{C^2K}$ is related to the Curie-Weiss constant obtained from Kuwata et al.[36] on PNZ-9%PT at 300 K. Then, the polarization, proportional to the excess entropy $(-S^{XS}(T) = (\partial G^{XS}/\partial T)_P)$, is given by Equation 8.3:

$$\boldsymbol{P(T) = \sqrt{\frac{-2S^{XS}(T)}{A_o}}} \tag{8.3}$$

Figure 8.5a shows the calculated polarization from the energetic region around the phase transition (over the hump), and from the anomalous deviation of the C_P (over the hard-mode C_P), compared with the determined polarization from pyroelectric measurement in PZN-8%PT, as an example. From this method, it can be observed how polarization contributions can be decouple from the C_P-data in relaxor-PT ferroelectric single crystal materials.

This treatment has some implications to the calculated thermodynamic properties and the polarization of these relaxor ferroelectric single crystal materials. First, the calculated polarization from the phase transitions region revealed the exact polarization jumps (ΔP^{XS}) at the phase transitions when compared with the polarization determined from pyroelectric measurement. In the case of PZN-8%PT, the polarization at the PE-F_T and F_T-F_R phase transitions were found to be $\Delta P^{XS} = 0.06\ \mathrm{C}/m^2$ and $\Delta P^{XS} = 0.016\ \mathrm{C/m^2}$, respectively. As was previously mention and theoretically proposed by Adam and Rossetti,[6,8] the ΔP^{XS} at the inter-ferroelectric transition in solid solution ferroelectric system is extremely small. Then, this polarization behavior determined from this region may be associated with the reversible polarization (P_{rev}(T)) or the excess polarization ($P^{XS}(T)$). The determined P_{rev}(T) is comparable with that of a normal ferroelectric material such as $BaTiO_3$.[34,37]

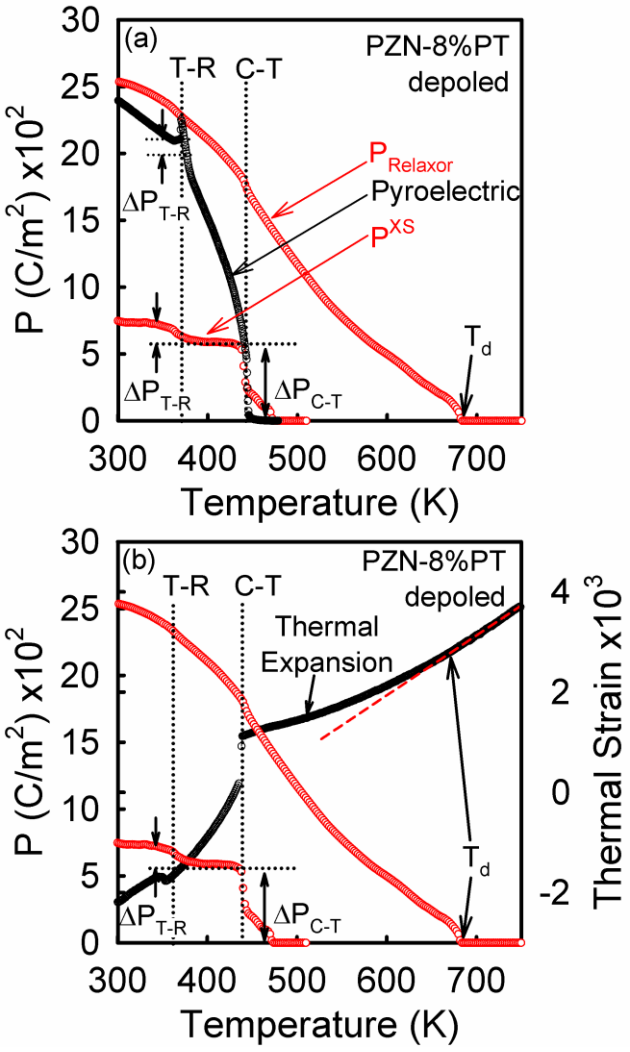

Figure 8.5 Relaxor and reversible contributions of the determine polarization determined from heat capacity compare with: (a) pyroelectric measurements and (b) thermal expansion measurements. (Hash line: linear fit to the high temperature cubic phase).

In the other hand, the low temperature polarization calculated from the anomalous deviation of the hard-mode C_P, or from the hump, compares favorably with the low temperature polarization determined by the pyroelectric measurement. It validates the method of determine the relaxor contribution from the fitting of the $C_P(Empirical)$ along the low and high symmetry phases. It is to be mention, that P_{rev}(T) also contributes to this area. The jump at the phase transition from P_{rev}(T), observed from the anomalous deviation of the C_P, appears as a continuous

function of the polarization. It is may be due to the low crystallographic anisotropy of the polarization at the phase transition between the two low symmetry ferroelectric phases. As a consequence, the entropy might be associated with the square of the polarization, follow the low order approximation of the Landau theory. In reality, the reversible behavior of the polarization is embedded in the relaxor contribution of the polarization. However, the onset of polarization for the relaxor contribution vanishes far away (233 temperature degrees) from the PE-F_T phase transition or far away where the pyroelectric polarization vanish. The temperature for this onset of polarization has been associated with a depolarization temperature, T_d or T_B, commonly observed in relaxor ferroelectrics materials.[12,14] It has been observed from birefringence[12] thermal expansion data,[14] heat capacity and thermal conductivity,[15,16] neutron scattering data,[18] etc. As a consequence, the polarization contribution to this area may be associated with the root mean square (RMS) polarization, P_{RMS}, which was obtained relative to the expected hard-mode C_P. The behavior of P_{RMS} relates the PNRs contributions in relaxor ferroelectric materials.

In order to verify T_d, determined by the above decouple method also described in Figure 8.4 and Figure 8.5, a thermal expansion measurement technique was conducted. In thermal expansion, the deviation from linear of the high temperature Cubic phase define the onset of polarization, as the temperature is decreased, for relaxor ferroelectric materials.[14] Figure 8.5b shows the thermal expansion of the PZN-8%PT single crystal. The phase transitions were observed at the same temperatures as those determined from the C_P-data and the change in thermal strain at the PE-F_T and F_T-F_R phase transitions were found to be $9.4\,x10^{-4}$ and $7.6\,x10^{-5}$, respectively. The high temperature cubic thermal expansion was fitted to a linear equation (dash line). It should be noted that T_d determined from thermal expansion correlated well with depolarization of the PZN-8%PT determined from P_{RMS} in the thermodynamic analysis of the C_P-data.

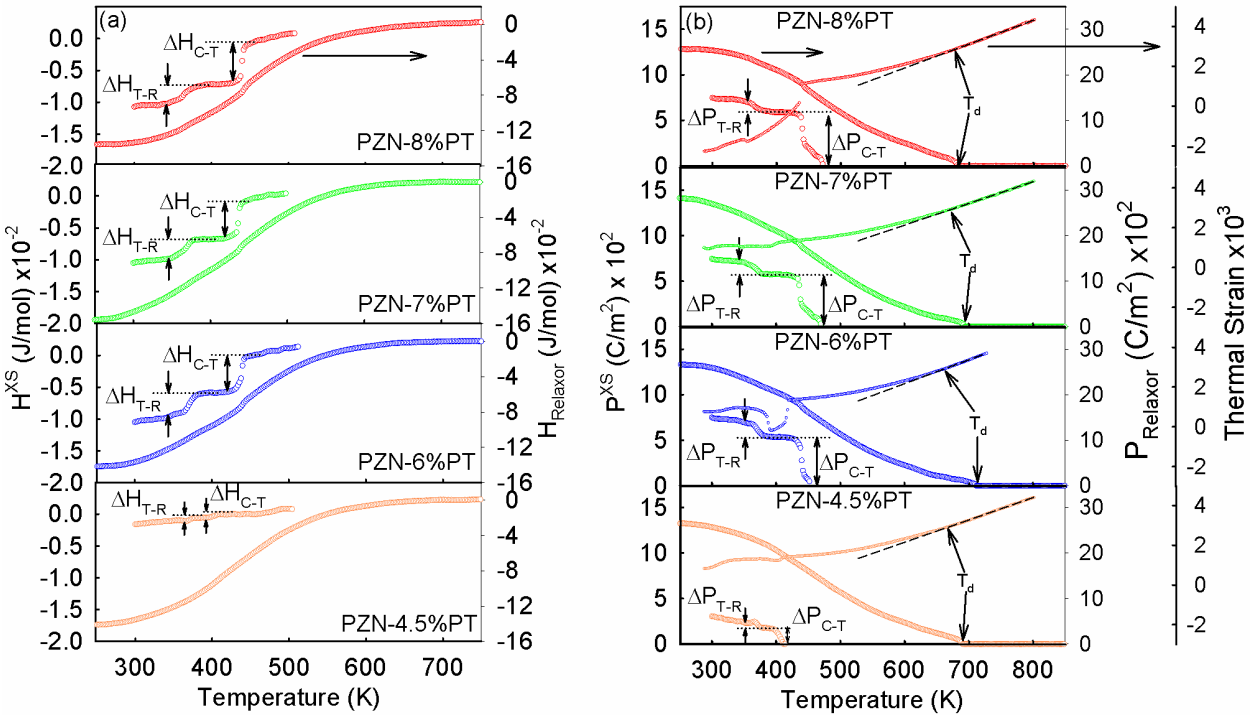

Figure 8.6 (a) Enthalpy of the excess and relaxor contribution in PZN-x%PT single crystals. (b) Determined polarization of the excess and relaxor contribution and the thermal expansion (external right axis) in the PZN-x%PT single crystals.

Figure 8.6 shows the enthalpy and polarization contribution in studied PZN-x%PT compositions (4.5, 6, 7, and 8%). Figure 8.6a shows the separation of the enthalpy corresponding to P_{rev}, (H^{XS}) and the enthalpy associated with P_{RMS}, $H_{Relaxor}$. The enthalpy change at phase transitions from H^{XS}, shown in Table 8.1, and the total energy corresponding to the anomalous deviation above the hard-mode C_P were determined. In average, the $H_{Relaxor}$, was found to be constant as a function of composition ($\approx 1.38\ kJ/mol$). The corresponding $S_{Relaxor}$ was found to be ($\approx\ 3.35\ Jmol^{-1}K^{-1}$).

Figure 8.6b shows the contribution of P_{rev} and P_{RMS} from the polarization decouple method and the comparison of determined T_d from P_{RMS} and thermal strain for the studied solid solution compositions in PZN-x%PT. From P_{rev}, it was possible to determine the jump in polarization at

the phase transitions, in particular at the inter-ferroelectric one. The values of the change in polarization (ΔP) for both PE-F_T and F_T-F_R are shown in Table 8.1. These small ΔP values and the thermal hysteresis of both phase transitions, shown in Figure 8.2b, are characteristic of weak first-order phase transition for this MPB solid solution compositions. Since $H_{Relaxor}$ was approximately similar in all studied PZN-x%PT compositions and their low temperature F_R-phase lies on each other, as shown Figure 8.4a, the average low temperature polarization determined from $P_{RMS}(298\ K) \approx 0.26 \frac{C}{m^2}$, as was found for PZN-8%PT. This polarization is in good agreement the remanent polarization found for PZN-8%PT, as shown in Figure 8.1a.

The thermal strain for each studied PZN-x%PT compositions is also shown in Figure 8.6b, external right axis. Similar approach was fallowed to determine T_d, in which a deviation from the linear thermal expansion of the Cubic phase defined the onset of polarization for relaxor ferroelectric materials. This temperature agree well with that found from P_{RMS} for the same solid solution compositions. In general, directly from the C_P-data, the onset of polarization in relaxor ferroelectric materials can be obtained where the entropy of the system, as the temperature is decrease, deviate from zero or from the PE-phase.

PART B: PHASE TRANSITOIN ENERGETIC FROM AN FIELD-INDUCED PHASE TRANSITION

The solid solution relaxor-PT ferroelectric single crystal material PMN-28%PT ($A_0 = 4.5x10^5 \frac{Jm}{C^2K}$)[38] was also investigated in their poled and depoled states. Figure 8.7a shows the C_p of the depoled PMN-28%PT single crystal in the same temperature range as for the solid solution PZN-x%PT compositions. The transition temperature, excess enthalpy and excess entropy are shown in Table 8.2.The PE-F_T transition temperature was found at the left of the MPB and it agree well with the PMN-x%PT phase diagram.[28] In general, similar behavior was observed. The high temperature C_p-data of the PE-phase in PMN-28%PT was observed below the Dulong-Petit Limit. It seems to be a characteristic of solid solutions compositions around the MPB and may be associated with a constraint in degree of freedom due to coexistence of ferroelectric phases.[6,7] The polarization decouple method was also applied by subtracting the C_p-data from two empirical equations fitted to the two regions, across the phase transition (dash line: $a = -901.8$, $b = 4.2x10^4$, $c = 77.8$, $d = -1.6$, $e = 0.0$ and $f = 5.6x10^5$) and relative to the expected hard-mode behavior (dash-dot-dot line: $a = 379.8$, $b = -3.7x10^4$, $c = -13.1$, $d = -13.1$, $e = 0.0$ and $f = 1.7x10^7$).

Figure 8.7b shows the P_{RMS} of PMN-28%PT and it is compared with the measured thermal strain. Similar phase transitions were obtained. The onset of polarization is also revealed and compares favorably with that from thermal strain and literature.[39] The associated excess enthalpy and entropy were found to be ($1.08\ kJmol^{-1}$) and ($2.67\ Jmol^{-1}K^{-1}$), respectively. The excess entropy is on the range of previously reported by Moriya ($3.3\ Jmol^{-1}K^{-1}$)[40] and Tachibana ($1.9\ Jmol^{-1}K^{-1}$)[16] for PMN.

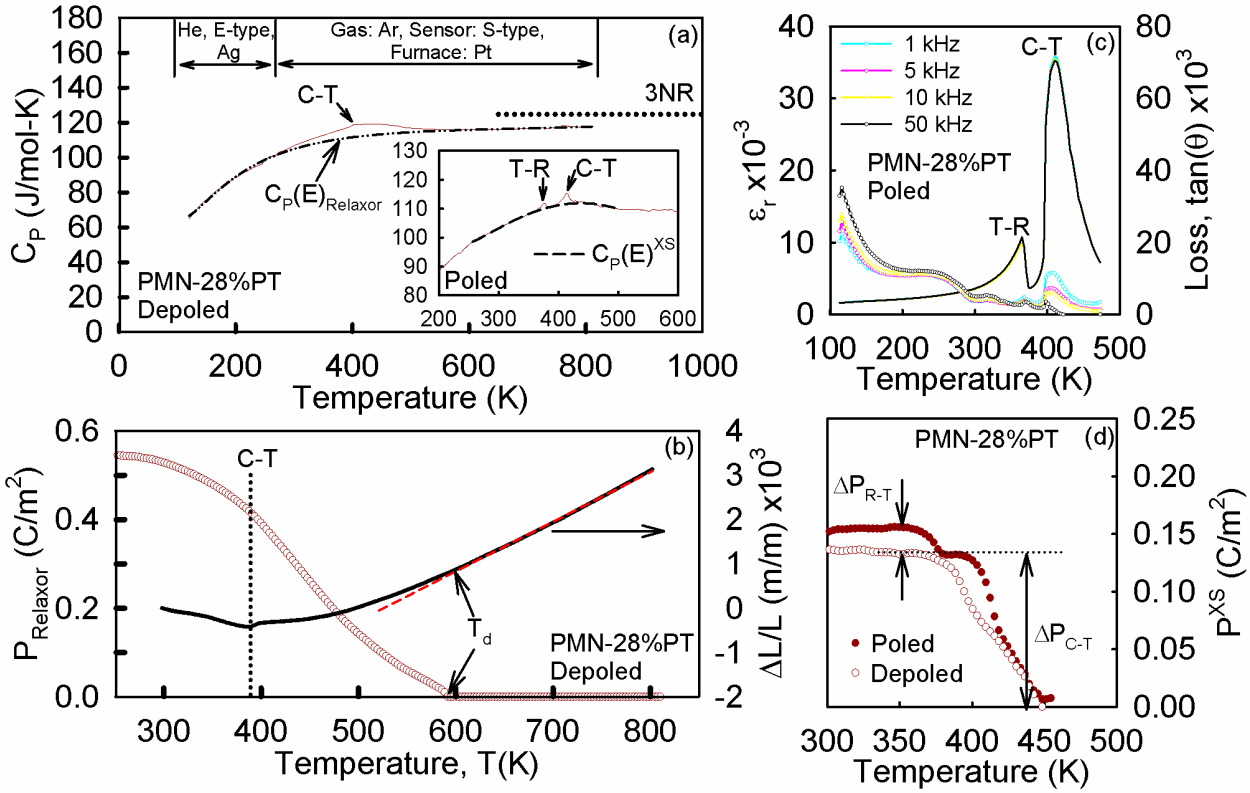

Figure 8.7 Heat capacity and analysis of PMN-28%PT single crystals as a function of temperature. (a) Wide temperature range heat capacity of depoled single crystal (inset: poled single crystal). (b) Relaxor contribution of the determined polarization and the thermal expansion of the depoled single crystal (Dash line: linear fit to the high temperature cubic phase). (c) Relative dielectric permittivity and loss of the poled single crystal. (d) Reversible contribution of the determined polarization for the poled and depoled single crystals.

The behavior of the P_{rev} is shown, as open cycles, in Figure 8.7d. It is to be mentioned that the decouple method allows to directly calculated ΔP at the phase transition. The values of ΔP_{C-T} for PMN-28%PT in its depoled state is shown in Table 8.2. However, the C_P of the poled state in PMN-28%PT, inset Figure 8.7a, shows different depolarization events as those observed in the MPB solid solutions of PZN-xPT, shown in Figure 8.3. In this particular case, the polarized state of PMN-28%PT single crystal shows a very small peak closed to the PE-F_T phase transition. It is associated with an induced inter-ferroelectric phase transition from the F_R to the ferroelectric orthorhombic (F_O) due to its monodomain poled state. This peak disappears when the sample is thermally depoled after the first C_P-measurement. An anomaly at 438 K was reported for PMN-

29%PT attributed the PNRs with tetragonal symmetry existing above T_C in the poled relaxor ferroelectric state.[41]

In order to confirm this observation the relative dielectric permittivity for the polarized state was also measured, shown in Figure 8.7c. The induced ferroelectric transition was also observed close to the PE-F_T phase transition. Since this first dielectric measurement was done to a temperature above Curie temperature, T_C, the second dielectric measurement does not show the induced phase transition peak , shown previously in Figure 8.1d for the depole state. It was the same experimental situation as for the measurement. From the ΔC_P associated with the phase transitions in the polarized state, it is possible to determined change in polarization associated with the induced inter-ferroelectric transition. Figure 8.7d shows the P_{rev} for the polarized state of PMN-28%PT. This polarization different, $\Delta P_{T-R} = 0.023\ C/m^2$. Similar magnitude had been found for the ternary ferroelectric.[1,2] From the adaptive state theory, a gradual polarization rotation is still possible near MB if the material is in the adaptive state because of easy rearrangement of nanodomains under the condition of reduced polar anisotropy.[11]

Table 8.2. Properties of PMN-28%PT single crystal obtained from CP measurement.

		PE-FT - Transition				FT-FR - Transition				T_d (K)
	x%	T (K)	ΔH (J/mol)	ΔS (J/mol-K)	ΔP (C/m^2)	T (K)	ΔH (J/mol)	ΔS (J/mol-K)	ΔP (C/m^2)	
Poled[a]	28	413	34.4	0.083	0.119	376	10.5	0.027	0.023	
Depoled[b]	28	397 (±2.76)	8.7 (±3.16)	0.022 (±0.007)	0.116 (±0.002)	- (-)	- (-)	- (-)	- (-)	589 (±5.0)

[a]The data for the poled sample correspond to the first DSC run.
[b]The data for the depoled sample correspond to the average of several DSC runs in which the standard deviation is indicated.

It is of relevant to mention the high sensitivity of a C_P-measurement to detect these polarization events occurring in the polarized state of the relaxor ferroelectric single crystal

materials. This small jumps in polarization at the MPB were predicted by Rossetti et. al., where the free energy between inter-ferroelectric phases are degenerate (F_R and F_T in the PZT phase diagram) with respect to the direction of the polarization at any temperature along the MPB and as a consequence, the crystallographic anisotropy of polarization vanishes as an energy cost of the polarization rotation.[7]

8.4 Summary

The heat capacity of the solid solutions relaxor-PT ferroelectric single crystal materials PZN-x%PT (x = 4.5, 6, 7 and 8) and PMN-28%PT was measured and analyzed by a direct thermal analysis software and by the low order approximation of the Ginzburg-Landau thermodynamic theory. The poled and depoled states of the single crystals were characterized by dielectric permittivity, electrical loss and P-E loop measurements. In the poled state of the single crystals different thermal depoling events were observed, respectively. For the case of PZN-x%PT, those thermal depoling events were associated with competing thermodynamic of metastable states of switching depolarization process from domains that are polarized in a particular direction to a non-polar paraelectric phase as the temperature increase. In the case of PMN-28%PT it was associated with an induced F_R-F_O phase transition previously observed in other relaxor-PT single crystals.

The C_P-data in the wide measured temperature range for both single crystals, allows to detect an anomalous deviation that manifest as a hump from the expected hard-mode behavior away from the phase transition points extending to the Burns temperature. A method was developed to decouple the reversible and root mean square polarization contributions relative to an empirical equation across the phase transitions area and from the low temperature ferroelectric to the high temperature paraelectric stable phases. From this method, the enthalpies, entropies and

polarization at the phase transition and from the hump were determined. The first order nature of the phase transitions was also confirmed from the observed thermal hysteresis. The energy and polarization at the inter-ferroelectric transition validate the low crystallographic anisotropy of polarization.[7,8]

The room temperature P_{RMS} compares favorably with pyroelectric measurement and the remanent polarization from the P-E loop. This polarization contribution was found to vanishes at the Burns temperature and agree well with thermal expansion data. As related to the C_P-data, the onset of polarization in relaxor ferroelectric materials can be obtained where the entropy of the system, as the temperature is decrease, deviates from zero or from the PE-phase. This anomalous deviation was then related with PNRs contributions in relaxor ferroelectric materials.

These findings are associated with an intrinsic characteristic of inter-ferroelectric transitions and with an easy rotation of polarization between ferroelectric phases of different symmetry. Comparing these results with the polarization obtained from PIN-PMN-PT at zero electric field during the energy harvesting cycling around F_O-F_R phase transition the change in polarization was also very small (P = 0.02 to 0.03 C/m^2).[1,2] These values match very closely with the measured polarization values, in this work, determined from heat capacity. These results show that the change in polarization measured during the energy harvesting under cyclic stress loading is intrinsic to the stress-free crystal. These results provide a framework for the understanding of the phase transition mechanism and energy harvesting capabilities of relaxor ferroelectric single crystal materials during cyclic operation in an energy harvesting process.

8.5 References

1. Dong, W. D., Finkel, P., Amin, A. & Lynch, C. S. Giant electro-mechanical energy conversion in [011] cut ferroelectric single crystals. *Appl. Phys. Lett.* **100,** 042903 (2012).

2. Dong, W. D., Finkel, P., Amin, A. & Lynch, C. S. Stress dependence of thermally driven pyroelectric charge release during FER-FEO phase transformations in [011] cut relaxor ferroelectric crystals. *Appl. Phys. Lett.* **100,** 262909 (2012).

3. Amin, A., McLaughlin, E., Robinson, H. & Ewart, L. Mechanical and thermal transitions in morphotropic PZN-pT and PMN-PT single crystals and their implication for sound projectors. *IEEE Trans. Ultrason. Ferroelectr. Freq. Control* **54,** 1090–5 (2007).

4. Zhang, S., Luo, J., Hackenberger, W. & Shrout, T. R. Characterization of Pb(In(12)Nb(12))O(3)-Pb(Mg(13)Nb(23))O(3)-PbTiO(3) ferroelectric crystal with enhanced phase transition temperatures. *J. Appl. Phys.* **104,** 64106 (2008).

5. Zhang, S. *et al.* Electromechanical characterization of [Formula: see text] crystals as a function of crystallographic orientation and temperature. *J. Appl. Phys.* **105,** 104506 (2009).

6. Rossetti, G. A., Khachaturyan, A. G., Akcay, G. & Ni, Y. Ferroelectric solid solutions with morphotropic boundaries: Vanishing polarization anisotropy, adaptive, polar glass, and two-phase states. *J. Appl. Phys.* **103,** 114113 (2008).

7. Rossetti, G. A. & Navrotsky, A. Calorimetric Investigation of Tricritical Behavior in Tetragonal Pb (Zr x Ti 1 ⁄ x) O 3. *J. Solid State Chem.* **144,** 188–194 (1999).

8. Heitmann, A. A. & Rossetti, G. A. Polar Anisotropy and Inter-Ferroelectric Transitions in Barium Titanate and its Solid Solutions. *Integr. Ferroelectr.* **126,** 155–165 (2011).

9. Heitmann, A. A. & Rossetti, G. A. Thermodynamics of polar anisotropy in morphotropic ferroelectric solid solutions. *Philos. Mag.* **90,** 71–87 (2010).

10. Ishibashi, Y. Theory of the Morphotropic Phase Boundary. *Ferroelectrics* **267,** 191–199 (2002).

11. Khachaturyan, a. G. Ferroelectric solid solutions with morphotropic boundary: Rotational instability of polarization, metastable coexistence of phases and nanodomain adaptive states. *Philos. Mag.* **90,** 37–60 (2010).

12. Burns, G. & Dacol, F. H. Crystalline ferroelectrics with glassy polarization behavior. *Phys. Rev. B* **28,** 2527–2530 (1983).

13. Dul'kin, E., Roth, M., Janolin, P.-E. & Dkhil, B. Acoustic emission study of phase transitions and polar nanoregions in relaxor-based systems: Application to the PbZn1⁄3Nb2⁄3O3 family of single crystals. *Phys. Rev. B* **73,** 012102 (2006).

14. Cross, L. E. Relaxor Ferroelectrics. *Ferroelectrics* **76,** 241–267 (1987).

15. Tachibana, M. & Takayama-Muromachi, E. Thermal conductivity and heat capacity of the relaxor ferroelectric [PbMg1/3Nb2/3O3]1−x[PbTiO3]x. *Phys. Rev. B* **79,** 100104 (2009).

16. Tachibana, M., Sasame, K., Kawaji, H., Atake, T. & Takayama-Muromachi, E. Thermal signatures of nanoscale inhomogeneities and ferroelectric order in [PbZn1/3Nb2/3O3]1−x[PbTiO3]x. *Phys. Rev. B* **80,** 094115 (2009).

17. Ziębińska, a, Rytz, D., Szot, K., Górny, M. & Roleder, K. Birefringence above T c in single crystals of barium titanate. *J. Phys. Condens. Matter* **20,** 142202 (2008).

18. Gehring, P. M., Park, S. & Shirane, G. Soft Phonon Anomalies in the Relaxor Ferroelectric Pb(Zn1/3Nb2/3)0.92Ti0.08O3. *Phys. Rev. Lett.* **84,** 5216–5219 (2000).

19. Gehring, P., Wakimoto, S., Ye, Z.-G. & Shirane, G. Soft Mode Dynamics above and below the Burns Temperature in the Relaxor Pb(Mg1/3Nb2/3)O3. *Phys. Rev. Lett.* **87,** 277601 (2001).

20. Gehring, P., Park, S.-E. & Shirane, G. Dynamical effects of the nanometer-sized polarized domains in Pb(Zn1/3Nb2/3)O3. *Phys. Rev. B* **63,** 224109 (2001).

21. Hirota, K., Wakimoto, S. & E. Cox, D. Neutron and X-ray Scattering Studies of Relaxors. *J. Phys. Soc. Japan* **75,** 111006 (2006).

22. Jeong, I.-K., Lee, J. K. & Heffner, R. H. Local structural view on the polarization rotation in relaxor ferroelectric (1−x)Pb(Zn1⁄3Nb2⁄3)O3–xPbTiO3. *Appl. Phys. Lett.* **92,** 172911 (2008).

23. Guo, Z. *et al.* X-ray probe of the polar nanoregions in the relaxor ferroelectric 0.72Pb(Mg1⁄3Nb2⁄3)O3–0.28PbTiO3. *Appl. Phys. Lett.* **91,** 081904 (2007).

24. Lim, L. C. & Rajan, K. K. High-homogeneity High-performance flux-grown Pb(Zn1/3Nb2/3)O3–(6–7)%PbTiO3 single crystals. *J. Cryst. Growth* **271,** 435–444 (2004).

25. Rajan, K. K., Zhang, M. J. & Lim, L.-C. Optimum Compositions for Pb(Zn 1/3 Nb 2/3)O 3 –PbTiO 3 Single Crystal for High-Performance Applications. *Jpn. J. Appl. Phys.* **44,** 264–266 (2005).

26. Byer, R. L. & Roundy, C. B. Pyroelectric coefficient direct measurement technique and application to a nsec response time detector. *Ferroelectrics* **3,** 333–338 (1972).

27. Kuwata, J., Uchino, K. & Nomura, S. Phase transitions in the Pb(Zn1/3Nb2/3)O3-PbTiO3 System. *Ferroelectrics* **37,** 579–82 (1981).

28. Noheda, B., Cox, D., Shirane, G., Gao, J. & Ye, Z.-G. Phase diagram of the ferroelectric relaxor (1-x)PbMg1/3Nb2/3O3-xPbTiO3. *Phys. Rev. B* **66,** 054104 (2002).

29. Okawara, C., Robinson, H., Stace, J. & Amin, A. Electromechanical Properties of High-Coupling (1-x)Pb(Zn1/3Nb2/3)O3-(x)PbTiO3 Single Crystals for Sound Projectors. *IEEE Trans. Ultrason. Ferroelectr. Freq. Control* **57,** 1497–1504 (2010).

30. Rajan, K. K., Shanthi, M., Chang, W. S., Jin, J. & Lim, L. C. Dielectric and piezoelectric properties of [001] and [011]-poled relaxor ferroelectric PZN–PT and PMN–PT single crystals. *Sensors Actuators A Phys.* **133,** 110–116 (2007).

31. Li, Z., Xi, Z., Xu, Z. & Yao, X. I. Dielectric/ferroelectric response and phase transition of PMN0.32PT single crystal. *J. Mater. Sci. Lett.* **21,** 1325–1327 (2002).

32. McLaughlin, E. A., Liu, T. & Lynch, C. S. Relaxor ferroelectric PMN-32%PT crystals under stress, electric field and temperature loading: II-33-mode measurements. *Acta Mater.* **53,** 4001–4008 (2005).

33. Eremkin, V. V., Smotrakov, V. G. & Fesenko, E. G. Structural Phase Transitions in PbZr1-xTixO3 Crystals. *Ferroelectrics* **110,** 137=144 (1990).

34. Devonshire, A. F. XCVI. Theory of barium titanate. *Philos. Mag. Ser. 7* **40,** 1040–1063 (1949).

35. Lines, M. E. & Glass, A. M. *Principles and Applications of Ferroelectrics and Related Materials*. (Clarendon Press, 1977).

36. Kuwata, J., Uchino, K. & Nomura, S. Dielectric and Piezoelectric Properties of 0.91Pb(Zn1/3Nb2/3)O3-0.09PbTiO9 Single Crystals. *Jpn. J. Appl. Phys.* **21,** 1298–1302 (1982).

37. Bell, a. J. Phenomenologically derived electric field-temperature phase diagrams and piezoelectric coefficients for single crystal barium titanate under fields along different axes. *J. Appl. Phys.* **89,** 3907 (2001).

38. Uchino, K., Nomura, S., Cross, L. E. & Newnham, R. R. Electrostriction in Perovskite Crystals and its Applications to Transducers. *J. Phys. Soc. Japan* **49,** 45–48 (1980).

39. Wongmaneerung, R., Guo, R., Bhalla, A., Yimnirun, R. & Ananta, S. Thermal expansion properties of PMN–PT ceramics. *J. Alloys Compd.* **461,** 565–569 (2008).

40. Moriya, Y., Kawaji, H., Tojo, T. & Atake, T. Specific-Heat Anomaly Caused by Ferroelectric Nanoregions in Pb(Mg1/3Nb2/3)O3 and Pb(Mg1/3Ta2/3)O3 Relaxors. *Phys. Rev. Lett.* **90,** 205901 (2003).

41. Yansue, T., Xiangyong, Z., Xiqi, F., Weiqin, J. & Haosu, L. Pyroelectric properties of [111]-oriented Pb(Mg1/3Nb2/3)O3-PbTiO3 crystals. *Appl. Phys. Lett.* **86,** 082901 (2005).

CHAPTER 9

COMPARATIVE STUDY OF THE THERMAL AND TRANSPORT PROPERTIES IN NORMAL AND RELAXOR PEROVSKITE-TYPE STRUCTURE FERROELECTRIC SINGLE CRYSTAL MATERIALS

9.1 Introduction

Thermal properties in relaxor ferroelectric materials has been demonstrated to be comparable with those of glasses or amorphous materials where short range dipolar interaction are involved.[1–7] Tachibana et al., show the temperature dependence of the thermal conductivity (k) and heat capacity (C_P) for PMN-PT relaxor single crystals grown by flux method for several compositions in the composition-temperature phase diagram.[2,3] They show a plateau transition in thermal conductivity and a shift to the left in C_P/T^3 behavior associated with similar behavior in glasses. In the suppressed plateau region a nanoscale inhomogeneity matrix of PNRs may provide a thermal boundary resistant at the boundary of ferroelectric domain given rise to the glasslike thermal conduction.[2,8] Also from high temperature C_P of PZN-PT single crystals, they show the transition from glass to crystalline behavior as a function of composition.[3] Here, they found an anomaly in C_P associated with nucleation and growth of PNRs which completely merged into ferroelectrics domains below the transition.

These observations, especially for the relaxor ferroelectric materials, had been brought by many different authors in literature, however the basis of comparison to these thermal and transport observations may lead to diverging conclusions. This may be as a consequence of inaccurate experimental measurements, specific requirements to the samples and to the measurement

techniques, assumptions to temperature dependence variables or lack of experimental data or theoretical models for the description of the transport phenomena.

The main purpose of this chapter is to compare the temperature dependence of the thermal conductivity between normal and relaxor perovskite-type crystal structure ferroelectric materials from accurate measurements of the heat capacity, thermal expansion and thermal diffusivity, especially in the temperature near the phase transitions. In particular, the atypical behavior to the temperature dependence of the thermal and transport properties in relaxor ferroelectric materials, PZN-PT and PMN-PT with composition around the MPB, are compared with the well known ferroelectric material $BaTiO_3$. Also in this chapter the thermal and transport data for all three single crystal are provided, as well as empirical polynomials that describe the C_P-background data and the measured thermal expansion.

9.2 Experimental Procedure

The commercial single crystal ferroelectric materials $BaTiO_3$ (from MTI), PZN-6%PT (from Microphine) and PMN-28%PT (from Microphine) were investigated. Their original parameters are given in Table 9.1. In order to meet the different measurement system requirements, all original samples were sectioned by using a South Bay Technology Model 650 low speed diamond wheel saw. The minimum sample requirement for each different measurement systems, in all three crystals, are also shown in Table 9.1. All samples were thermally depoled, in a temperature above its Curie temperature for 2 hours before the measurements. Electrodes were removed for the heat capacity and thermal expansion measurements. The experimental method for the heat capacity, $C_P(T)$, thermal expansion, $e(T)$, and thermal diffusivity, $D(T)$, measurements were previously discussed and can be found in Chapter 4.

Table 9.1. Material parameters required for each different measurement.

Ferroelectric Material	Thermal Diffusivity $D(m^2/s)$	Heat Capacity $C_P(J/mol-K)$	Thermal Strain $\varepsilon_{ij} = \Delta L/L_0$	Thermal Conductivity $k(Wm/K)$
BaTiO3 [100] (5.0x5.0x1.0 mm) from MTI	(1.03x5.0x5.0 mm) ρ = 6.02 g/cm^3	(1.03x2.93x2.68 mm) m = 43.63 mg	(1.03x2.32x1.49 mm) Lo[100] = 1.03 mm Lo[001] = 1.49 mm	Measured C_P Measured ε_{ij} k[001] = Lo(1.03 mm) k[100] = Lo(1.49 mm)
PZN-6%PT [001] (7.4x8.61x1.1 mm) Microfine	(6.22x6.10x1.1 mm) ρ = 8.03 g/cm^3	(3.76x3.78x1.1 mm) m = 97.2 mg	(4x3.99x1.1 mm) Lo = 1.1 mm	Measured C_P Measured ε_{ij}
PMN-28%PT [001] (13.27x6.5x1.73 mm) Microfine	(5.86x5.40x1.73) ρ = 7.71 g/cm^3	(3.66x3.76x1.73 mm) m = 191.2 mg	(3.66x1.91x 1.73 mm) Lo =1.73 mm	Measured C_P Measured ε_{ij}

9.3 Results and Discussion

The characterization of the commercial single crystal materials ($BaTiO_3$, PZN-6%PT and PMN-28%PT) was already shown in Chapter 4 and Chapter 7. For an accurate determination of the thermal conductivity of the normal ferroelectric single crystal $BaTiO_3$ and the relaxor ferroelectric single crystals PZN-6%PT and PMN-28%PT, the heat capacity (Figure 9.1), thermal expansion (Figure 9.2) and the thermal diffusivity (Figure 9.3) were measured. The raw data to all the three measurements of the investigated ferroelectric single crystal materials are shown in the Appendix in Table A.1-A.3, Table A.4-A.6 and Table A.7-A.9, respectively. A typical behavior of the thermal and transport properties of the relaxor ferroelectric crystals was observed, different from the normal ferroelectric. In the case of the heat capacity, additional contributions to the excess heat capacity, above the hard-mode behavior and characteristic features at the high temperature paraelectric phase (PE-phase) were observed in the relaxor ferroelectric single crystal materials, when compared with the normal ferroelectric $BaTiO_3$. Similar basis of comparison were applied to the heat capacity of all three ferroelectric single materials.

9.3.1 Heat capacity comparison of normal and relaxor ferroelectric materials

The heat capacity was computed by the application of the ASTM E 1269 ratio method using NIST SRM-720 data for a single crystal Al_2O_3 calibration standard. The accuracy of the data (absolute average experimental error was ~1 %) was verified by comparing the measured C_P of Alumina with the C_P-standard (NSB standard table) for each DSC run. The two set of data (low and high temperature ranges) were stitched together after careful calibration of the baseline. The stitch of both measured temperature regions allows to capture its complete behavior from the low temperature rhombohedral ferroelectric phase, F_R-phase, to the high temperature PE-phase.

At the high temperature PE-phase, the C_P-data of $BaTiO_3$ approaches the Dulong-Pettit limit (3NR) while for the relaxor ferroelectric materials it was found below it (~2.88NR). This finding has been also observed in the solid solution $Pb(Zr_{1-x}Ti_x)O_3$ (PZT) with compositions near the MPB.[9,10] It was associated with higher degree of close-packing for the PZT samples, which may alter the elastic or electrostrictive properties and lead to a change in the character of the PE-FT transition.[9] As a consequence, and in order to be consistent, the C_P-data were fitted to a polynomial empirical equation, Equation 9.1, from the low temperature F_R-phase ($\leq 200\ K$) to the high temperature PE-phase ($\geq 700\ K$). The empirical equation is given by

$$C_{P-Empirical} = a + bT^{-1} + cT^{\frac{1}{2}} + dT + eT^2 + fT^{-2} \quad (9.1)$$

where the pre-factors a, b, c, d, e and f are given for two temperature ranges in the case of $BaTiO_3$: for the low temperature range $(C_{P-Empirical})_L$ (0 to 305 K) a = -118.22, b = -926.286, c = 23.0536, d = -0.5756, e = 0, f = 0, and for the high temperature range $(C_{P-Empirical})_H$ (305 to 1012 K) a = 365.6705, b = -32.719, c = -13.2313, d = 0.2147, e = 0 and f = 1,210,44.0. For the relaxor ferroelectric materials the pre-factors for the all measured temperature ranges are given by: $a = 360.7$, $b = -3.1x10^4$, $c = -12.3$, $d = 0.18$, $e = 0.0$ and $f = 1.2x10^6$ for PZN-6%PT,

and $a = 379.8$, $b = -3.7x10^4$, $c = -13.1$, $d = -13.1$, $e = 0.0$ and $f = 1.7x10^7$) for PMN-28%PT.

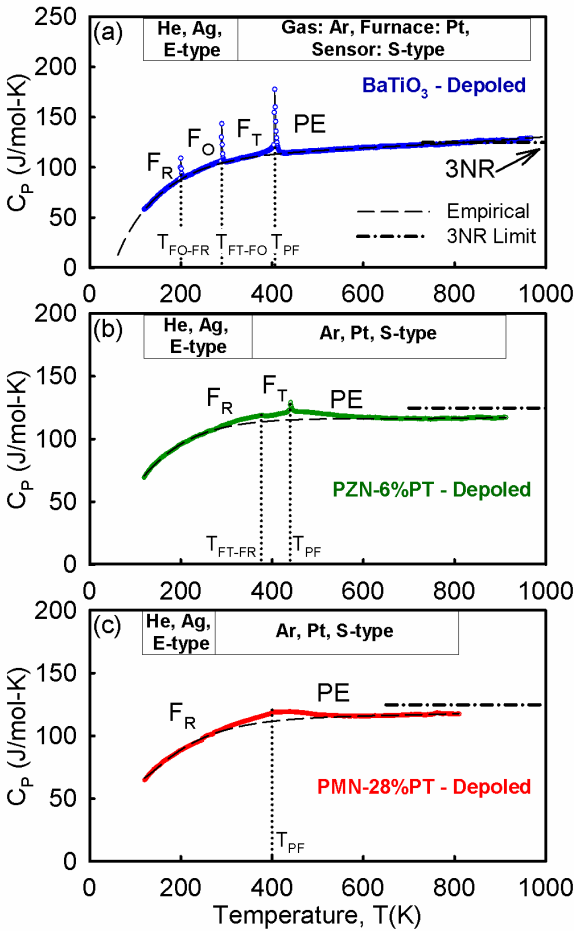

Figure 9.1 Comparison of the heat capacity of normal and relaxor ferroelectric single crystals: (a) Depoled $BaTiO_3$, (b) depoled PZN-6%PT and (c) depoled PMN-28%PT.

By using the empirical equation in all temperature ranges, a continuity of the free energy toward lower symmetry phases is assumed. As previously demonstrated in Chapter 6 and Chapter 8, the energetics at phase transition between lower symmetry ferroelectric phases was extremely small. It was shown that the thermodynamic properties of these materials, based on the perovskite-type crystal structure, can be described by assuming a vanishing in the crystallographic anisotropy of polarization at the ferroelectric to ferroelectric (inter-ferroelectric) phase transitions.[6,11–16] The

enthalpies, entropies and further analysis to the phase transitions are given in Chapter 5, Chapter 7 and Chapter 8. However, our main focus in this chapter is to compare the obvious differences from the relaxor and normal ferroelectric materials. Thereby, if all three empirical equations for each ferroelectric materials are compared, in general they share similar Debye-like behavior. As a consequence, the observed hump above those empirical equations in the PMN-28%PT and PZN-6%PT indicates excess contributions from the relaxor materials. Similar contributions has been observed by other references.[1,3] Especially, it had been shown that the transverse acoustic phonon mode in PMN appears in a similar temperature region.[17] The intersection of the empirical equation with the C_P-data at high temperature paraelectric phase is an indication of the depolarization temperature, T_d (T_d ($BaTiO_3$) = 446 K, T_d (PZN-6%PT) = 690 K and T_d (PMN-28%PT) = 589 K).

9.3.2 Thermal expansion comparison of normal and relaxor ferroelectric materials

The depolarization temperature have been very well described by the index of refraction[18] and thermal expansion measurements.[4] From thermal expansion measurements it has been defined as the deviation from linearity as the temperature decreases from the high temperature PE-phase.[4] This deviation define the onset of polarization for the relaxor ferroelectric materials. The measured thermal expansion is shown in Figure 9.2. The thermal expansion of $BaTiO_3$ single crystal was used as the basis of comparison. For comparison, the high temperature PE-phase was fitted to a linear equation where its slope defines the thermal expansion coefficient, $\alpha(\mu m/mK)$, and its extrapolation to the temperature axis gives T_{PF}, $e_{ij}(T = T_{PF}) = 0$. By comparing all three single crystals, $\alpha \approx 12\ \mu m/mK$, as a typical thermal expansion coefficient for ceramic materials. From the deviation of the fitted line to the thermal expansion data, the T_d of the studied relaxor ferroelectric materials were found, which agree very well with literature.[18–20] Also, this critical

temperatures are in good agreement with the T_d found from heat capacity where the empirical equation, as decreasing the temperature from the high temperature PE-phase, deviates from the C_P-data as the temperature is decreased. Surprisingly, it was also found a small deviation in the $BaTiO_3$ single crystal in spite of being a normal ferroelectric material.

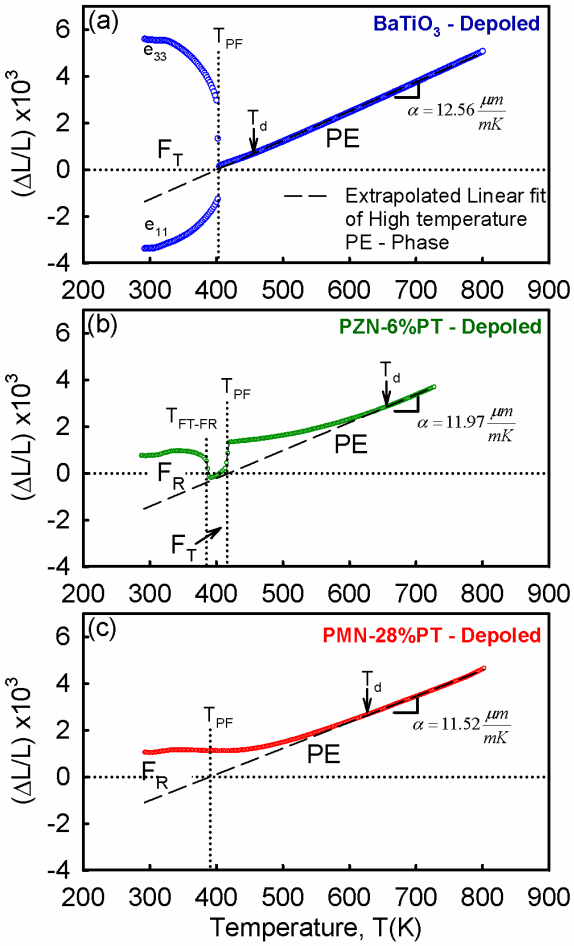

Figure 9.2 Comparison of the thermal expansion of normal and relaxor ferroelectric single crystals: (a) Depoled $BaTiO_3$, (b) depoled PZN-6%PT and (c) depoled PMN-28%PT.

Depolarization temperatures for $BaTiO_3$ had been found from birefringence[20,21] thermal expansion,[4,22] second harmonic generation,[23] Brillouin frequency shit,[24,25] and had been associated with the appearance of local polar nanoregions in the symmetric paraelectric phase.[20,26,27] In

general, it was demonstrated, in Chapter 8, that this deviation is a consequence of the total entropy of the system which is proportional to the square of polarization. Additionally, in the measured temperature range of the thermal expansion, it was possible to obtain the PE-F_T phase transition in all three ferroelectric single crystals and inter-ferroelectric transition in the relaxor ferroelectric single crystals. It is to be noted that the jumps at the PE-F_T phase transition decreases as a function of the relaxor contributions from $BaTiO_3$ to PZN-PT to PMN-PT. As a note, for the input to the thermal conductivity calculations, the thermal expansion data fitted to T_{PF} was used, shown in Figure 9.2.

9.3.3 Thermal diffusivity comparison of normal and relaxor ferroelectric materials

In order to finally determine the thermal conductivity, the measurement of the thermal diffusivity was required, shown in Figure 9.3. To verify the accuracy of the thermal diffusivity measurement (~1 % Error), a polycrystalline Al_2O_3 sample (room temperature thickness 0.989 mm and density 3.91 g/cm^3) was also run at the same time with the same experimental conditions as the single crystals. The standard deviation was defined by seven acceptable shots. Cowan plus pulse correction was used for thermal diffusivity calculation. The thermal diffusivity was then determined by the half time $(t_{1/2})$ of the maximum temperature at the back of the slab surface.[28,29] After solving the transient equation of energy, the transport property of thermal diffusivity is given by Equation 9.2:

$$D(T) = 0.1388 \frac{L_0^2}{t_{1/2}} \tag{9.2}$$

where L_o is the thickness of the slab and the pre-factor 0.1388 comes from the dimensionless solution of the temperature profile obtained from solving the transient energy equation of this particular problem with x = L as the boundary condition. In this measurement technique, the heat

losses are minimized by making the measurement in a very short time enough so that very little cooling can take place.[28] The thickness for the thermal diffusivity measurement for all three ferroelectric materials are given in Table 9.1.

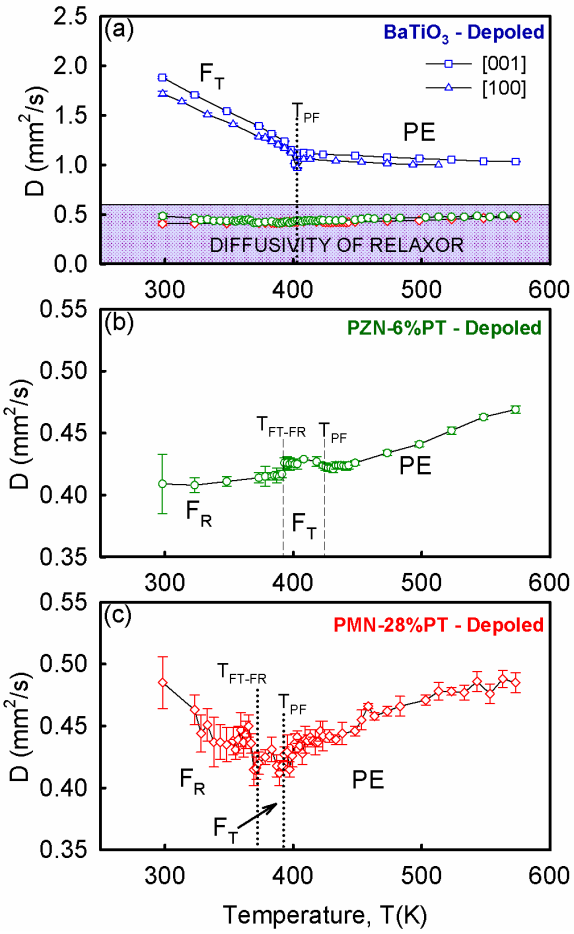

Figure 9.3 Comparison of the thermal diffusivity of normal and relaxor ferroelectric single crystals: (a) Depoled $BaTiO_3$, (b) depoled PZN-6%PT and (c) depoled PMN-28%PT.

Again, the basis of comparison is always the temperature behavior of $BaTiO_3$ single crystal. The thermal diffusivity of $BaTiO_3$ single crystal is one order of magnitude higher than the relaxor one in all measure temperature range. The slopes of thermal diffusivity at the different phases of the relaxor single crystal materials appear to have an opposite behavior to what was obtained for

$BaTiO_3$ single crystal. Especially at the PE-phase the thermal diffusivity of the relaxor ferroelectric single crystal appears to increase while for the $BaTiO_3$ single crystal is decreasing. It is important to mention that the allowed temperature range in the LFA lies results in the region where the hump in the heat capacity and the curvature associated with the deviation from linearity in the thermal expansion occurs. Taking this in consideration, the heat of diffusion in this region of the relaxor ferroelectric single crystal must be as a consequence of a particular phonon mode.

9.3.4 Thermal conductivity comparison of normal and relaxor ferroelectric materials

To have a better picture, it will be of interest to finally determine the thermal conductivity in these ferroelectric single crystals since it takes into account all thermal and transport contributions ($\Delta L(T)/L_0$, $C_P(T)$ and D(T)). The temperature dependence of the thermal conductivity is given by:

$$k(T) = \rho(T) * D(T) * C_P(T) \tag{9.3}$$

where $\rho(T)$ is the temperature dependence of the density. For polymorphic phase transformation the temperature dependence of the density is a function of the material thermal expansion, given by Equation 9.4.

$$\rho(T) = \rho_0 \left(1 + \frac{\Delta L}{L_0}(T)\right)^{-3} \tag{9.4}$$

where L_0 and ρ_0 are the room temperature thickness and density of the material, respectively.

The thermal conductivity of $BaTiO_3$, PZN-6%PT and PMN-28%PT depoled ferroelectric single crystals is shown in Figure 9.4a, Figure 9.4c and Figure 9.4e, respectively. Also, respectively in Figure 9.4b, Figure 9.4d and Figure 9.4f, it is shown an expanded region of the thermal conductivity data at the PE-phase as a function of the 1/T.

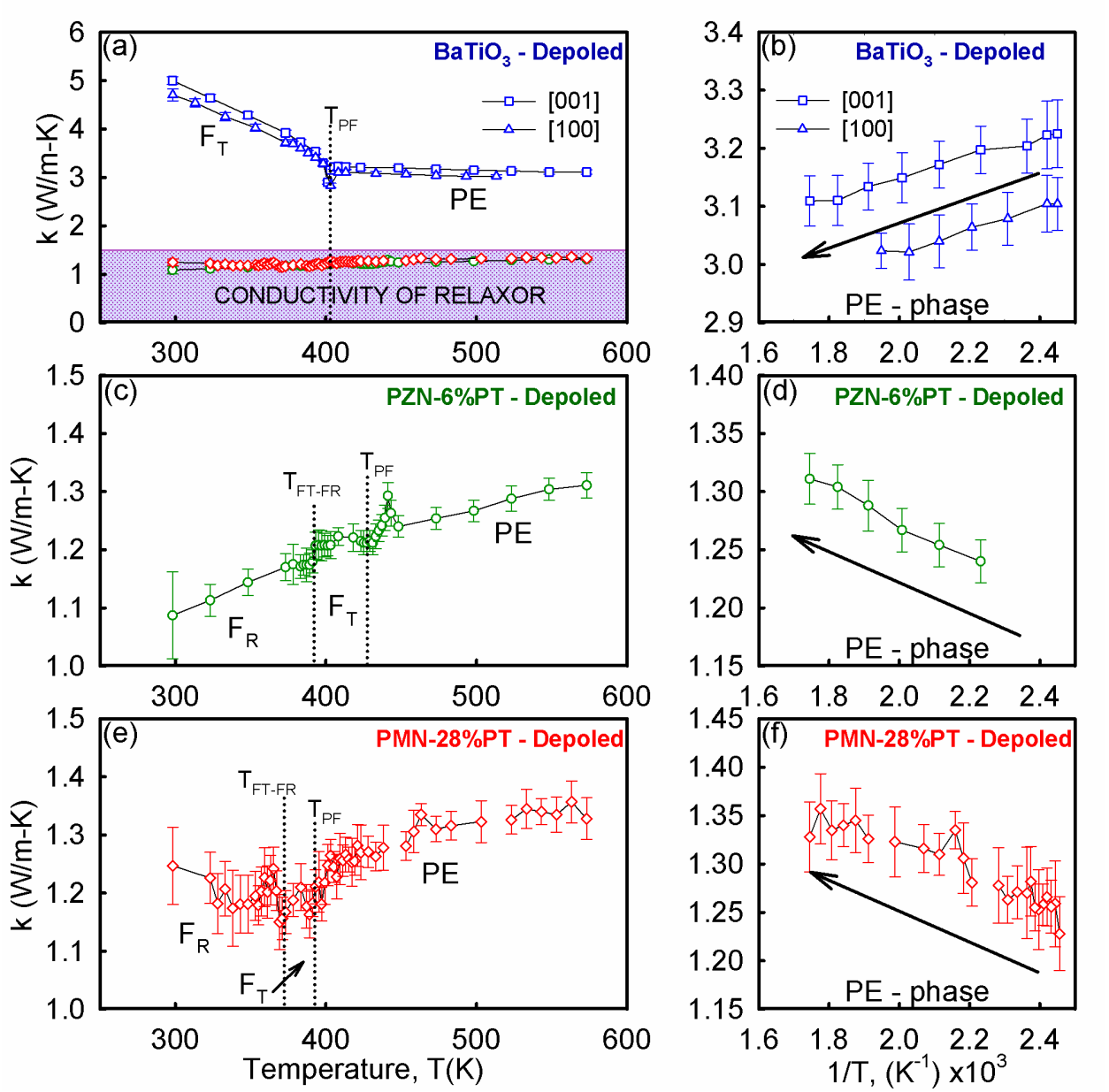

Figure 9.4 Comparison of the calculated thermal conductivity and the normal and relaxor ferroelectric single crystals: (a) Depoled $BaTiO_3$, (c) depoled PZN-6%PT and (e) depoled PMN-28%PT. Figures in the right are the 1/T behavior of the paraelectric phase for each ferroelectric system, respectively.

From typical ceramic materials the 1/T behavior is related to an increase in Umklapp process.[30] The thermal conductivity of $BaTiO_3$ follow a 1/T tendency but not exactly as can be observed from the F_T-phase close to the PE-F_T transition. However, at the PE-phase the $BaTiO_3$ single crystal material seems to leveling off to the 1/T behavior. This behavior is expanded in

Figure 9.4b. The calculated thermal conductivity in $BaTiO_3$ single crystal agree well with that obtained by Mante et al.[31] in the high temperature range and by Suemune[32] in the low temperature range. Suemune stayed that the thermal conductivity shows a high deviation from the Umklapp process, indicating that the anharmonicity accompanied by the lattice distortion dominates that causing Umklapp process. It is even more evident in the temperature dependence of the thermal conductivity in the relaxor ferroelectric materials PZN-PT and PMN-PT.

The thermal conductivity calculated for the relaxor ferroelectric materials appears to increase including the thermal conductivity in the PE-phase. In this type of ferroelectric materials the thermal conductivity at high temperatures cannot be described by the Umklapp process. It is important to remember again that the calculated thermal conductivity for these relaxor ferroelectric materials is in the range where a hump in the heat capacity was observed and the deviation from linearity in the thermal expansion was also perceived. Thereby, the heat transfer through the material must be interacting with the diffuse phase transitions cause by polar nanoregions.

There is an intimate relation of the thermal conductivity with the ferroelectricity, resulting from a singular behavior of the thermal vibration of ions shifted to cause the ferroelectricity.[33] In the case of the relaxor materials some polar nanoregions (PNRs) had been demonstrated where its onset of polarization, or the T_d, had been determined from acoustic emission measurements,[26] thermal expansion,[4] heat capacity and thermal conductivity,[2,3] birefringence,[20] neutron scattering,[34] etc. A built-in disorder is related with the diffuse phase transition in relaxor compounds associated with the presence of PNR's which damp the polar transverse optic phonon mode that drop precipitously into the transverse acoustic branch.[17,34–36] Order-disorder-like ordering of PNRs as a function of PT concentration had been proposed in this materials due to observation of no change in local structure, in overall, as the crystal structure undergoes a series

of R-O-T phase transitions.[37,38] Nevertheless, the thermal properties in relaxor ferroelectric materials had been demonstrated to be comparable with that of glasses or amorphous materials where short range dipolar interaction are involved.[1–7]

9.4 Summary

The thermal conductivity of normal ferroelectric $BaTiO_3$, intermediate relaxor PZN-6%PT and the relaxor PMN-28%PT single crystals was calculated by accurate measurements of heat capacity, thermal expansion and thermal diffusivity. The data from all measurements, as well as the calculated thermal conductivity, is provided for all three ferroelectric single crystals, as well as the actual dimensions use during the different measurements.

Different characteristics were observed from the different measurements which helped to understand the non-Umklapp behavior observed in the ferroelectric single crystals especially in the relaxor ferroelectrics. Different observation addressed these conclusions. From the heat capacity, at the high temperature PE-phase the C_P-data for $BaTiO_3$ approaches the Dulong-Pettit limit (3NR) while for the relaxor ferroelectric materials it was found below it (~2.88NR). Also, it was observed a hump above the hard mode behavior heat capacity in the relaxor ferroelectrics single crystal when compared with the $BaTiO_3$. These excess contributions to the heat capacity vanish where the empirical equation intercepts with the C_P-data or where there is a change in the slope of the PE-phase as the temperature is decreased. This point was associated with the depolarization temperature. From thermal expansion measurements, this critical temperature was validated from the deviation from linearity in the high temperature PE-phase. For comparison purpose, the fitted line to the high temperature PE-phase was set to zero at T_{PF}. In the case of the thermal diffusivity, it was determined from very short time heat diffusion measurement technique.

A Cowan plus pulse corrections was used for final calculation. Opposite behaviors were observed in the slopes at the different phases when compared $BaTiO_3$ with the relaxor single crystals. Especially at the PE-phase, the thermal diffusivity of the relaxor ferroelectric single crystal appears to increase while for the $BaTiO_3$ single crystal it is decreasing.

Finally, the thermal conductivity was calculated as function of the temperature dependence of the density, heat capacity and thermal diffusivity. It is important to mention that the calculated thermal conductivity is in the measured temperature range around the MPB in the relaxor ferroelectric materials. The Umklapp process was not exactly observed which it may be due to the built-in disorder from lattice distortions, anharmonicity, the presence of polar nanoregions and the presence of the transverse acoustic branch.[17,34–36]

9.5 References

1. Moriya, Y., Kawaji, H., Tojo, T. & Atake, T. Specific-Heat Anomaly Caused by Ferroelectric Nanoregions in Pb(Mg1/3Nb2/3)O3 and Pb(Mg1/3Ta2/3)O3 Relaxors. *Phys. Rev. Lett.* **90,** 205901 (2003).

2. Tachibana, M. & Takayama-Muromachi, E. Thermal conductivity and heat capacity of the relaxor ferroelectric [PbMg1/3Nb2/3O3]1−x[PbTiO3]x. *Phys. Rev. B* **79,** 100104 (2009).

3. Tachibana, M., Sasame, K., Kawaji, H., Atake, T. & Takayama-Muromachi, E. Thermal signatures of nanoscale inhomogeneities and ferroelectric order in [PbZn1/3Nb2/3O3]1−x[PbTiO3]x. *Phys. Rev. B* **80,** 094115 (2009).

4. Cross, L. E. Relaxor Ferroelectrics. *Ferroelectrics* **76,** 241–267 (1987).

5. Viehland, D., Jang, S. J., Cross, L. E. & Wuttig, M. Freezing of the polarization fluctuations in lead magnesium niobate relaxors. *J. Appl. Phys.* **68,** 2916 (1990).

6. Rossetti, G. A., Khachaturyan, A. G., Akcay, G. & Ni, Y. Ferroelectric solid solutions with morphotropic boundaries: Vanishing polarization anisotropy, adaptive, polar glass, and two-phase states. *J. Appl. Phys.* **103,** 114113 (2008).

7. Phillips, W. A. *Amorphous Solids: Low Temperature Properties*. (Springer, 1981).

8. Swartz, E. & Pohl, R. Thermal boundary resistance. *Rev. Mod. Phys.* **61,** 605–668 (1989).

9. Rossetti, G. A. & Navrotsky, A. Calorimetric Investigation of Tricritical Behavior in Tetragonal Pb (Zr x Ti 1 ⁄ x) O 3. *J. Solid State Chem.* **144,** 188–194 (1999).

10. Eremkin, V. V., Smotrakov, V. G. & Fesenko, E. G. Structural Phase Transitions in PbZr1-xTixO3 Crystals. *Ferroelectrics* **110,** 137=144 (1990).

11. Heitmann, A. A. & Rossetti, G. A. Polar Anisotropy and Inter-Ferroelectric Transitions in Barium Titanate and its Solid Solutions. *Integr. Ferroelectr.* **126,** 155–165 (2011).

12. Heitmann, A. A. & Rossetti, G. A. Thermodynamics of polar anisotropy in morphotropic ferroelectric solid solutions. *Philos. Mag.* **90,** 71–87 (2010).

13. Ishibashi, Y. Theory of the Morphotropic Phase Boundary. *Ferroelectrics* **267,** 191–199 (2002).

14. Khachaturyan, a. G. Ferroelectric solid solutions with morphotropic boundary: Rotational instability of polarization, metastable coexistence of phases and nanodomain adaptive states. *Philos. Mag.* **90,** 37–60 (2010).

15. Rossetti, G. A. & Khachaturyan, A. G. Inherent nanoscale structural instabilities near morphotropic boundaries in ferroelectric solid solutions. *Appl. Phys. Lett.* **91,** 072909 (2007).

16. G. A. Rossetti, Zheng, W. & Khachaturyan, A. G. Phase coexistence near the morphotropic phase boundary in lead zirconate titanate solid solutions. *Appl. Phys. Lett.* **88,** 072912 (2006).

17. Hirota, K., Wakimoto, S. & E. Cox, D. Neutron and X-ray Scattering Studies of Relaxors. *J. Phys. Soc. Japan* **75,** 111006 (2006).

18. Burns, G. & Dacol, F. H. Crystalline ferroelectrics with glassy polarization behavior. *Phys. Rev. B* **28,** 2527–2530 (1983).

19. Gorev, M. V., Flerov, I. N., Sciau, P. & Guillemet-Fritsch, S. Thermal Expansion of (Ba1-xLax)Ti1-x/4O3 Solid Solutions. *Phys. Solid State* **51,** 746–752 (2009).

20. Ziębińska, a, Rytz, D., Szot, K., Górny, M. & Roleder, K. Birefringence above T c in single crystals of barium titanate. *J. Phys. Condens. Matter* **20,** 142202 (2008).

21. Takagi, M. & Ishidate, T. Anomalous birefringence of cubic $BaTiO_3$. *Solid State Commun.* **113,** 423–426 (2000).

22. Rusek, K. *et al.* Non-Linear Properties of BaTiO 3 above T C. *Ferroelectrics* **375,** 165–169 (2008).

23. Pugachev, a. M. *et al.* Broken Local Symmetry in Paraelectric BaTiO_{3} Proved by Second Harmonic Generation. *Phys. Rev. Lett.* **108,** 247601 (2012).

24. Ko, J.-H. *et al.* Elastic softening and central peaks in BaTiO[sub 3] single crystals above the cubic-tetragonal phase-transition temperature. *Appl. Phys. Lett.* **93,** 102905 (2008).

25. Ko, J.-H., Kim, T. H., Roleder, K., Rytz, D. & Kojima, S. Precursor dynamics in the ferroelectric phase transition of barium titanate single crystals studied by Brillouin light scattering. *Phys. Rev. B* **84,** 094123 (2011).

26. Dul'kin, E., Roth, M., Janolin, P.-E. & Dkhil, B. Acoustic emission study of phase transitions and polar nanoregions in relaxor-based systems: Application to the PbZn1⁄3Nb2⁄3O3 family of single crystals. *Phys. Rev. B* **73,** 012102 (2006).

27. Namikawa, K. *et al.* Direct Observation of the Critical Relaxation of Polarization Clusters in $BaTiO_3$ Using a Pulsed X-Ray Laser Technique. *Phys. Rev. Lett.* **103,** 197401 (2009).

28. Parker, W. J., Jenkins, R. J., Butler, C. P. & Abbott, G. L. Flash Method of Determination Thermal Diffusivity, Heat Capacity, and Thermal Conductivity. *J. Appl. Phys.* **32,** (1961).

29. Carslaw, H. S. & Jaeger, J. C. *Conduction of Heat in Solids*. 101 (Oxford University, 1959).

30. Poirier, D. R. & Geiger, G. H. *Transport Phenomena in Material Processing*. (The Minerals, Metals & Materials Society, 1998).

31. Mante, A. J. H. & Volger, J. The Thermal Conductivity of $BaTiO_3$ in the Neighbourhood of its Ferroelectric Transition Temperatures. *Phys. Lett. A* **24,** 139–140 (1967).

32. Suemune, Y. Thermal Conductivity of $BaTiO_3$ and SrTiO3 from 4.5 to 300 K. *J. Phys. Soc. Japan* **20,** 174–175 (1965).

33. Ikushi, Y., Nomura, S. & Sawada, S. Thermal Conductivity of $BaTiO_3$ Ceramics. *J. Phys. Soc. Japan* **13,** 1550–1551 (1958).

34. Gehring, P. M., Park, S. & Shirane, G. Soft Phonon Anomalies in the Relaxor Ferroelectric Pb(Zn1/3Nb2/3)0.92Ti0.08O3. *Phys. Rev. Lett.* **84,** 5216–5219 (2000).

35. Gehring, P., Park, S.-E. & Shirane, G. Dynamical effects of the nanometer-sized polarized domains in Pb(Zn1/3Nb2/3)O3. *Phys. Rev. B* **63,** 224109 (2001).

36. Gehring, P., Wakimoto, S., Ye, Z.-G. & Shirane, G. Soft Mode Dynamics above and below the Burns Temperature in the Relaxor Pb(Mg1/3Nb2/3)O3. *Phys. Rev. Lett.* **87,** 277601 (2001).

37. Jeong, I.-K., Lee, J. K. & Heffner, R. H. Local structural view on the polarization rotation in relaxor ferroelectric (1−x)Pb(Zn1⁄3Nb2⁄3)O3–xPbTiO3. *Appl. Phys. Lett.* **92,** 172911 (2008).

38. Guo, Z. *et al.* X-ray probe of the polar nanoregions in the relaxor ferroelectric 0.72Pb(Mg1⁄3Nb2⁄3)O3–0.28PbTiO3. *Appl. Phys. Lett.* **91,** 081904 (2007).

CHAPTER 10

PHASE TRANSITION ENERGETIC IN THE PARAELECTRIC TO FERROELECTRIC AND INTER-FERROELECTRIC PHASE TRANSION IN PEROVSKITE-TYPE STRUCTURES.

10.1 Introduction

In this chapter, the phase transition energetics were studied in the ferroelectric materials with perovskite-type parent cubic phase crystal structure. Their ferroelectric behavior range from normal to relaxor ferroelectrics, such as $BaTiO_3$ and the PZT to the PZN-PT and PMN-PT, respectively. $BaTiO_3$ is a line compound ferroelectric material while the last three are solid solutions with a morphotropic phase boundary (MPB).[1–4] The energetics at phase transition were investigated from experimental data of heat capacity (C_P) measurements discussed in Chapter 5, Chapter 7, Chapter 8-Part A and Chapter 8-Part B, respectively. All samples are commercial single crystal ferroelectric materials except for PZT which was a powder ceramic in pellet form processed in the Laboratory at the University of Connecticut by Ching Chang-Chung. However, the high quality of the sample, as reveal by lattice parameters, see Chapter 7, as well as the phase transition temperatures compared with the temperature-composition phase diagram,[1] make it possible to use it for comparison purposed. In the range where the ferroelectric materials were investigated, the phase transition energetics are across the PE-F_T to F_T-F_R. In the case of $BaTiO_3$ it is across the PE-F_T to F_T-F_O to F_O-F_R. It is important to recognize that, in general, at a PE-FE phase transition a spontaneous change in polarization occurs at T_{PF}, the PE-FE phase transition temperature, as a consequence of the atomic displacement of the center atom in the crystal structure.[5] However, at

the inter-ferroelectric phase transition, a polarization rotation between low symmetry ferroelectric phases occurs.[6]

10.2 Results and Discussion

The energies at the ferroelectric phase transitions of the different ferroelectric materials studied were computed by the analysis of the heat capacity, shown in previous chapters. The transition temperatures at the PE-FE phase transition (in this case the PE-FT phase transition), their corresponding entropies, enthalpies and their corresponding spontaneous polarization are shown in Table 10.1. The change in entropy and polarization of this data is plotted in Figure 10.1 as a function of the different ferroelectric materials and compositions. At the inter-ferroelectric phase transition, there were considered the F_T-F_O and F_O-F_R phase transitions in $BaTiO_3$, the F_T-F_R in the MPB solid solutions PZN-PT and PMN-PT, and the F_{R3m}-F_{R3c} phase transition in the PZT. The entropy and polarization, plotted in Figure 10.2, the enthalpy and the phase transition temperatures of these lower symmetry inter-ferroelectric phase transitions are given in Table 10.2. The enthalpies were obtained from the integration of the excess heat capacity (ΔC_P). In the same manner, the entropy was obtained for the integration of $\Delta C_P/T$. The integration limits of the energetic at the phase transitions were considered by the point where the derivative of the ΔC_P differs from zero ($dC_P/dT \neq 0$) from both, the left and right of the phase transition. For an accurate base of comparison, ΔC_P was determined from the subtraction of the C_P-data to a C_P-background determined from an empirical equation fitted to the high temperature PE-phase to the lower temperature ferroelectric symmetry phase, in the measured temperature range as discussed in Chapter 4. The C_P ratio method, ASTM E 1269, was used with accurate C_P-measurements of

Al_2O_3 standard single crystal material and of the ferroelectric material together with the NIST SRM-720 data for Al_2O_3 single crystal.

Table 10. 1 Properties at the paraelectric to the ferroelectric phase transition.

	Transition temperature (K)	ΔH^{XS} (J/mol)	ΔS^{XS} (J/mol-K)	ΔP^{XS} (C/m^2)	Reference
PMN-x%PT					Chapter 8
x = 28 %	397	8.7	0.022	0.116	Part B
x = 30 %	417	11.8	0.028	0.099	
PZN-x%PT					Chapter 8
x = 4.5 %	411	5.8	0.014	0.026	Part A
x = 6.0 %	440	27.6	0.063	0.060	
x = 7.0 %	431	27.1	0.065	0.060	
x = 8.0 %	441	37.3	0.085	0.060	
$PbZr_{1-x}Ti_xO3$					Chapter 7
PT (x = 1)	767	1881.1	2.453	0.373	
PZ (x = 0)	511	1724.1	3.371	0.376	
$BaTiO_3$	405	563.0	1.400	0.184	Chapter 5

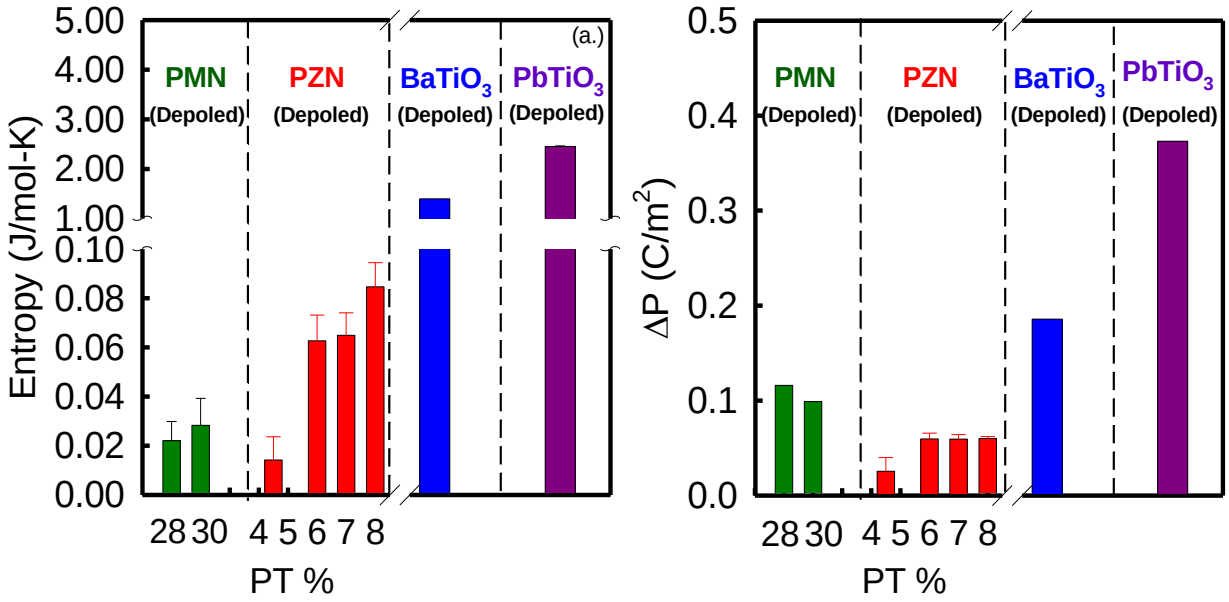

Figure 10.1 Entropy (a) and polarization at the paraelectric to ferroelectric phase transition of different perovskite-type crystal structure ferroelectric materials.

Table 10. 2 Properties at the ferroelectric to ferroelectric phase transition.

	Transition temperature (K)	ΔH^{XS} (J/mol)	ΔS^{XS} (J/mol-K)	ΔP^{XS} (C/m^2)	
PMN-x%PT					Chapter 8
x = 28 %		10.5	0.028	0.024	Part B
x = 30 %		6.5	0.017	0.019	
PZN-x%PT					Chapter 8
x = 4.5 %		-	-	0.007	Part A
x = 6.0 %		10.0	0.027	0.018	
x = 7.0 %		12.3	0.033	0.015	
x = 8.0 %		7.8	0.021	0.016	
$PbZr_{1-x}Ti_xO3$					Chapter 7
PT (x = 0.1)		468.1	0.821	0.011	
PZ (x = 0.2)		857.6	1.614	0.018	
$BaTiO_3$					Chapter 5
T-O	286	174.0000	0.6000	0.0201	
O-R	198	73.0000	0.3600	0.0104	

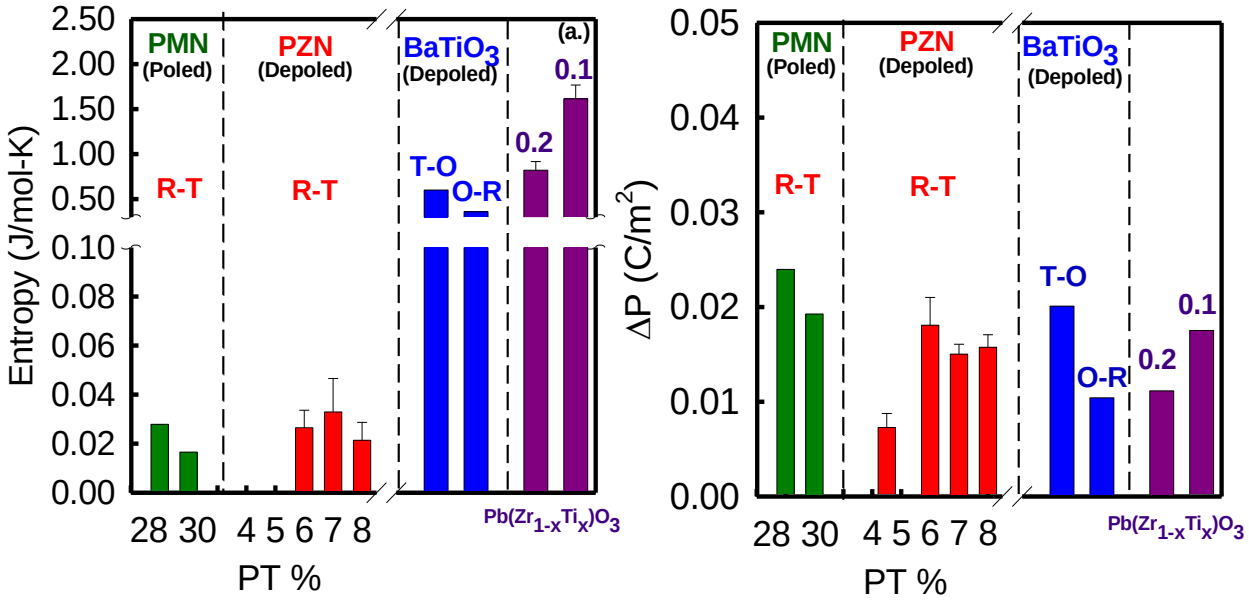

Figure 10.2 Entropy (a) and polarization at the ferroelectric to ferroelectric phase transition of different perovskite-type crystal structure ferroelectric materials.

The phase transition order nature of the all transitions was found to be of the first-order due to thermal hysteresis. The results show that the enthalpies of the inter-ferroelectric transition in the relaxor ferroelectric crystals are quite small (~10 J/mol) when compared with the energies of the inter-ferroelectric transitions in normal ferroelectric $BaTiO_3$ and PZT. A trend follows from the conventional ferroelectric ($BaTiO_3$) to the conventional MPB solid solution (PZT) to the single crystal relaxor (PZN-PT and PMN-PT), showing a decrease in the enthalpy at the phase transitions from normal to relaxor ferroelectric materials. The corresponding polarization jumps at the paraelectric to ferroelectric phase transition also follow similar trends as for the enthalpies. However, remarkably similar values were obtained from the change in polarization at inter-ferroelectric transition for all studied ferroelectric materials.

High piezoelectric and electromechanical properties has been found near the MPB of solid solution ferroelectric single crystals.[7] Observation of different monoclinic phases by X-ray diffraction[8] and the polarization rotation through monoclinic phases[9] had been used to explain the properties around the MPB. However, it has been demonstrated, from diffraction theory to the ferroelectric solid solutions PMN-PT and PZN-PT, that the low symmetry monoclinic ferroelectric phases may be an artifact caused by the automatic diffraction domain averaging when the coherence length of scattering is greater than the typical size of the domains.[10] Diffraction pattern attributed to the monoclinic M_A phase has been demonstrated to consist of nanodomains of the F_R or F_T phases.[11] The observation of the low symmetry ferroelectric phases may be also as a consequence of the invariant conditions that are the fingerprints of stress accommodation in which polar nanodomains (PND) may assemble in geometrical patterns to minimize the elastic energy.[12–14] This fingerprints are present in the vicinity of the MPB having a low domain wall energy density, which is the key requirement for the conformal miniaturization of stress-

accommodation.[12] This nanoscale domain structures have been referred as adaptive states.[10] A natural link between the occurrence of the MPB and the observation of structurally heterogeneous states associated with low-symmetry ferroelectric phases in solid solution systems is a strong reduction in the crystallographic polarization anisotropy energy.[15] The formation of adaptive states that are inherently heterogeneous at the nanometer length scale arises as a consequence of the vanishing polarization anisotropy along a MPB line where a change in symmetry between two ferroelectric phases occurs.[15]

The polarization rotation at the inter-ferroelectric transition will be a function of both the modulus and direction. It had been demonstrated that the difference in polarization (ΔP) between the two ferroelectric phases at the MPB of solid solution ferroelectric systems is associated with a low crystallographic anisotropy of polarization at the inter-ferroelectric phase transition.[15] If ΔP is very small, then the crystallographic anisotropy of polarization at the inter-ferroelectric transition will vanish which means that at the inter-ferroelectric transition the polarization is almost continuous will rotates in an easy polarization rotation path.[15–21] It had been also proposed for $BaTiO_3$ single crystal based on the low-order 2-4-6 Landau polynomial, which might be used as a common parametric scheme for similar perovskite-type ferroelectric materials.[17] Heitmann et al., proposed a relative stability phase diagram of the ferroelectric phases in $BaTiO_3$ formulated from a continuous path of the polarization towards low symmetry ferroelectric phases.

In general, the energy surface with respect to the polarization vector must approaches a spherical form in order to minimize its energy at the inter-ferroelectric transitions. Figure 10.3 shows the surface energies for the F_T-phase, the F_R-phase and the surface energy corresponding to the F_T-F_R inter-ferroelectric phase transition. The polarization vector in the [001] direction dramatically drop in magnitude before it is reoriented along the [111] direction. Similarly occurs

in the inter-ferroelectric transition of the F_T-F_O and F_O-F_R in $BaTiO_3$.[17]This implies that the jumps at the inter-ferroelectric transitions are extremely weak or the crystallographic anisotropy is vanishingly small. Due to these very small differences, shown in Figure 10.2, the direction of the polar vector is easily changed by external forces, such as mechanical stress or electric field.

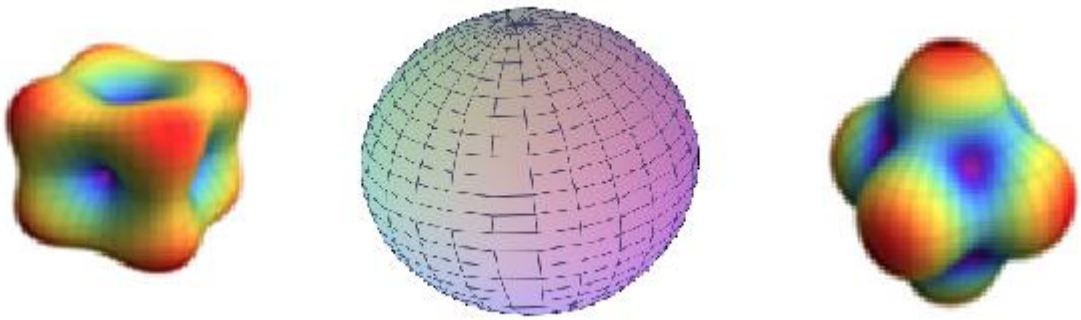

Figure 10.3 Surface free energy of the FT-phase, FR-phase and at the FT-FR phase transition.

It is to be noted that the jump in polarization in PMN-PT single crystal determined at the inter-ferroelectric transition, shown in Figure 10.2, corresponds to the poled state of the single crystal sample during heating. This sample was previously poled along its monodomain state, which corresponds to the 1T engineering domain configuration. However, during the second heating of the C_P-measurement, there is no jump in polarization at the inter-ferroelectric transition, see Chapter 8 part B. The same behavior was confirmed from dielectric permittivity measurements to the same single crystal sample, also shown in Chapter 8 part B. This jump from the poled state of the single crystal has been reported by Choi et al., from dielectric permittivity and pyroelectric data around the same compositions in the PMN-PT system.[22] Then, this jump in polarization is associated with a field induce phase transition from the 1T engineering domain configuration. The field induce phase transition phenomena appear in the particular poled state of the single crystal ferroelectric materials. In this particular case, where there is no energy corresponding to the

depoled state of the sample, the energy associated with the phase transition is a consequence of the rotation of the polarization vector and no change in its magnitude. It implies that there is no thermal energy, or extremely small energy, corresponding to the structural transformation of the sample.

These findings are associated with an intrinsic characteristic of inter-ferroelectric transitions and with an easy rotation of polarization between ferroelectric phases of different symmetry. Comparing these results with the polarization obtained for PIN-PMN-PT single crystal, by Dong et al., at zero electric field during an energy harvesting cycling around F_O-F_R phase transition, the change in polarization was also very small (P = 0.02 to 0.03 C/m^2).[23] These values match very closely with the measured polarization values, in this work, determined from heat capacity. These results show that the change in polarization measured during the energy harvesting under cyclic stress loading conditions is intrinsic to the stress-free crystal. These results provide a framework for the understanding of the phase transition mechanism and energy harvesting capabilities of relaxor ferroelectric single crystal materials during cyclic operation in an energy harvesting process.

10.3 Summary

Comparison of the phase transition energetic at the PE-FE and inter-ferroelectric transition point were investigated for ferroelectric materials with perovskite-type structure at the high symmetry PE-phase. It includes the normal ferroelectrics $BaTiO_3$ single crystal and the MPB solid solution PZT ceramic, and the relaxor ferroelectrics MPB solid solutions PZN-PT and PMN-PT. The transition temperatures, enthalpies, entropies and polarization at both phase transitions were determined from heat capacity measurements as discussed in previous chapters. First, the order

nature of the phase transitions were of first-order due to thermal hysteresis. A decrease trend in the energy of the transition from the normal to relaxor ferroelectric materials was observed in the PE-FE phase transition. However in the inter-ferroelectric transition, remarkably similar polarization values were obtained from the change in polarization at inter-ferroelectric transition for all studied ferroelectric materials. It was associated with a strong reduction in the energy associated with the crystallographic anisotropy of the polarization.[15] Since the change in polarization was found to be very small, then the crystallographic anisotropy of polarization at the inter-ferroelectric transition will vanishes which means that the polarization is almost continuous between ferroelectric phases and the polarization vector will rotate around the easy polarization direction represented as a spherical energy surface.[15–21]

Additionally, a field induced phase transition in PMN-PT crystal was observed from its monodomain engineering state, poled along it crystallographic direction. Since it was not observed in the depoled state, after first heating during the heat capacity measurement, it was associated with a neglected or small transformation energy due to a rotation of the polarization vector and not change in its magnitude. Similar polarization values in the 2R engineering domain PIN-PMN-PT[24,25] during energy harvesting process showing that these result is an intrinsic property of the stress-free crystal.

10.4 References

1. Jaffe, B., Cook, W. R. & Jaffe, H. *Piezoelectric Ceramics*. 53–183 (Academic Press, 1971).

2. Rase, D. E. & Roy, R. Phase Equilibria in the System BaO-TiO2. *J. Am. Ceram. Soc.* **38,** 102–113 (1955).

3. Noheda, B., Cox, D., Shirane, G., Gao, J. & Ye, Z.-G. Phase diagram of the ferroelectric relaxor (1-x)PbMg1/3Nb2/3O3-xPbTiO3. *Phys. Rev. B* **66,** 054104 (2002).

4. Kuwata, J., Uchino, K. & Nomura, S. Phase transitions in the Pb(Zn1/3Nb2/3)O3-PbTiO3 System. *Ferroelectrics* **37,** 579–82 (1981).

5. Strukov, B. A. & Levanyuk, A. P. *Ferroelectric Phenomena in Crystals: Physical Foundations*. (Springer-Verlag, 1998).

6. Lines, M. E. & Glass, A. M. *Principles and Applications of Ferroelectrics and Related Materials*. (Clarendon Press, 1977).

7. Park, S.-E. & Shrout, T. R. Ultrahigh strain and piezoelectric behavior in relaxor based ferroelectric single crystals. *J. Appl. Phys.* **82,** 1804 (1997).

8. Noheda, B. *et al.* Polarization Rotation via a Monoclinic Phase in the Piezoelectric 92% PbZn_{1/3}Nb_{2/3}O_{3}-8% PbTiO_{3}. *Phys. Rev. Lett.* **86,** 3891–3894 (2001).

9. Fu, H. & Cohen, R. Polarization rotation mechanism for ultrahigh electromechanical response in single-crystal piezoelectrics. *Nature* **403,** 281–3 (2000).

10. Khachaturyan, A. G., Shapiro, S. M. & Semenovskaya, S. Adaptive phase formation in martensitic transformation. *Phys. Rev. B* **43,** 10832 (1991).

11. Schönau, K. a. *et al.* Nanodomain structure of Pb[Zr_{1−x}Ti_{x}]O_{3} at its morphotropic phase boundary: Investigations from local to average structure. *Phys. Rev. B* **75,** 184117 (2007).

12. Bai, F., Li, J. & Viehland, D. Domain engineered states over various length scales in (001)-oriented Pb(Mg1⁄3Nb2⁄3)O3-x%PbTiO3 crystals: Electrical history dependence of hierarchal domains. *J. Appl. Phys.* **97,** 054103 (2005).

13. Jin, Y. M., Wang, Y. U., Khachaturyan, A. G., Li, J. F. & Viehland, D. Adaptive ferroelectric states in systems with low domain wall energy: Tetragonal microdomains. *J. Appl. Phys.* **94,** 3629 (2003).

14. Jin, Y. M., Wang, Y. U. & Khachaturyan, a. G. Conformal Miniaturization of Domains with Low Domain-Wall Energy: Monoclinic Ferroelectric States near the Morphotropic Phase Boundaries. *Phys. Rev. Lett.* **91,** 197601 (2003).

15. Rossetti, G. A., Khachaturyan, A. G., Akcay, G. & Ni, Y. Ferroelectric solid solutions with morphotropic boundaries: Vanishing polarization anisotropy, adaptive, polar glass, and two-phase states. *J. Appl. Phys.* **103,** 114113 (2008).

16. Rossetti, G. A. & Navrotsky, A. Calorimetric Investigation of Tricritical Behavior in Tetragonal Pb (Zr x Ti 1 ⁄ x) O 3. *J. Solid State Chem.* **144,** 188–194 (1999).

17. Heitmann, A. A. & Rossetti, G. A. Polar Anisotropy and Inter-Ferroelectric Transitions in Barium Titanate and its Solid Solutions. *Integr. Ferroelectr.* **126,** 155–165 (2011).

18. Heitmann, A. A. & Rossetti, G. A. Thermodynamics of polar anisotropy in morphotropic ferroelectric solid solutions. *Philos. Mag.* **90,** 71–87 (2010).

19. Ishibashi, Y. Theory of the Morphotropic Phase Boundary. *Ferroelectrics* **267,** 191–199 (2002).

20. Khachaturyan, a. G. Ferroelectric solid solutions with morphotropic boundary: Rotational instability of polarization, metastable coexistence of phases and nanodomain adaptive states. *Philos. Mag.* **90,** 37–60 (2010).

21. Rossetti, G. A. & Khachaturyan, A. G. Inherent nanoscale structural instabilities near morphotropic boundaries in ferroelectric solid solutions. *Appl. Phys. Lett.* **91,** 072909 (2007).

22. Choi, S. W., Shrout, T. R., Jang, S. J. & Bhalla, A. S. Dielectric and Pyroelectric Properties in the Pb(Mg1/3Nb2/3)O3-PbTiO3 System. *Ferroelectrics* **100,** 29–38 (1989).

23. Dong, W. D., Finkel, P., Amin, A. & Lynch, C. S. Stress dependence of thermally driven pyroelectric charge release during FER-FEO phase transformations in [011] cut relaxor ferroelectric crystals. *Appl. Phys. Lett.* **100,** 262909 (2012).

24. Dong, W. D., Finkel, P., Amin, A. & Lynch, C. S. Stress dependence of thermally driven pyroelectric charge release during FER-FEO phase transformations in [011] cut relaxor ferroelectric crystals. *Appl. Phys. Lett.* **100,** 262909 (2012).

25. Dong, W. D., Finkel, P., Amin, A. & Lynch, C. S. Giant electro-mechanical energy conversion in [011] cut ferroelectric single crystals. *Appl. Phys. Lett.* **100,** 042903 (2012).

CHAPTER 11

RESONANCE MODE ENERGY HARVESTING IN PIEZOELECTRIC MATERIALS

11.1 Introduction

Energy harvesting is a process in which energy captured from an external source is used to provide power in a device. Parasitic mechanical energy sources from vibration are very attractive for the energy harvesting process, since they generate the highest amount of power when compared with other parasitic energies.[1] In general, a piezoelectric energy harvesting device uses the mechanical vibration to generate electrical energy which is then stored and used to provide power (for example to a wireless sensor network).[2] This energy conversion occurs because the piezoelectric molecular structure is oriented such that the material exhibits a local charge separation.[3]

A typical configuration that enables the piezoelectric energy harvesting process is the bimorph and/or Unimorph cantilever, shown in Figure 11.1. In these configurations, an input mechanical energy, due to the kinetic energy of a proof mass at the tip of the cantilever, produces resonance vibrations generating electrical energy as a result of the direct piezoelectric effect. The electrical energy is collected by the electrodes in contact with the piezoelectric material.[1] The most widely exploited materials currently in use for these applications are the ferroelectric morphotropic phase boundary (MPB) solid solution $PbZrO_3$-$PbTiO_3$ (PZT).[4–9]

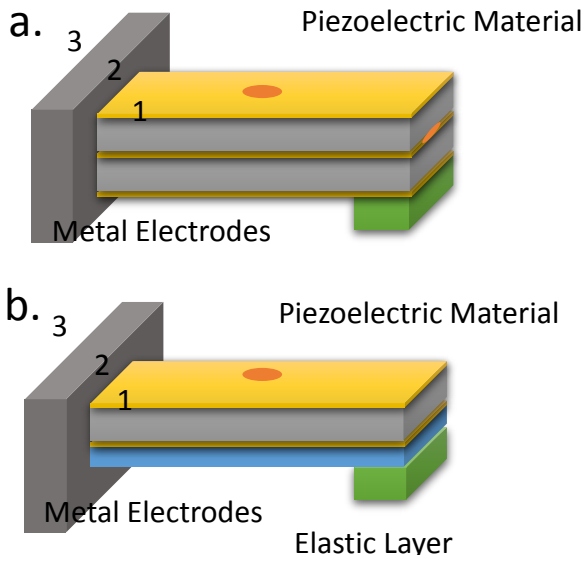

Figure 11.1 Basic configuration for a piezoelectric energy harvesting, (a) Bimorph configuration, (b) Unimorph configuration.[1]

The key material parameters in piezoelectric materials for electromechanical energy conversion are the electromechanical coupling factor (k_{ij}) and the piezoelectric coefficient (d_{ij}). High piezoelectric material properties had been found at the MPB of the solid solutions ferroelectric single crystal materials $Pb(Zr_{1/3}Nb_{2/3})O_3$-$xPbTiO_3$ (PZN-PT) and $Pb(Mg_{1/3}Nb_{2/3})O_3$-$xPbTiO_3$ (PMN-PT).[10,11] Different material-property-configuration had been developed. From the material-property relationship it is included the piezoelectric ceramics (piezoceramics),[8,9] piezoelectric single crystal (piezocrystal),[12,13] piezoelectric polymer and fiber-based piezoelectric (piezofiber).[14] In the material-property-configuration relationship, as an example, high power and voltage output due to high piezoelectric coefficient of PMN-29%PT single crystal and flexibility performance of the cantilever Unimorph bender based on shear mode were obtained as a function of frequencies, load resistances and proof masses.[12] Also, due to the resonance requirements, different geometries of cantilever mode configuration had been studied with the purpose to maximize the piezoelectric energy conversion. S. R. Anton and H. A. Sodano shows a summary

of various piezoelectric geometries investigated.[3] Just to mention some of them, triangular and rectangular cantilever configuration where compared in which the triangular shape generates higher strains and power output.[15] Cantilever configuration with trapezoid geometry had been also investigated, in where the strain is distributed evenly in the beam increasing the power density output.[16]

11.2Methodology

For comparison purpose, of the piezoelectric properties of single crystal and polycrystalline ferroelectric materials, constituent equations were adopted, derived by Q.-M. Wang et al., for symmetrical triple layer piezoelectric benders.[17] These constituent equations allow to easily demonstrate the material-property-configuration relationship of piezoelectric materials in cantilever resonance mode energy harvesting. They were based on a 4x4 matrix where the external momentum (M), external tip force (F), uniform load (p), and applied electric voltage (V) were applied to a cantilever-mode resonance configuration.[17] The bending angle (α), tip deflection (δ), volume displacement (ν), and electrical charge (Q) may be derived as a consequence to the curvature and total internal energies as the cantilever bends. Constituents equations for cantilever triple layer piezoelectric benders with two piezoelectric layers in series, Series Triple Layer (STL), and also in parallel (PTL) have been also derived following a similar approach for a bimorphs configuration under quasi-static conditions using a one dimensional assumption from thermodynamic approach[18] and for Unimorph (UNI) configuration describing its responses under different loading conditions.[19] As an example, the constituent equations for a STL is given in Equation 11.1.[17]

$$\begin{bmatrix}\boldsymbol{\alpha}\\ \boldsymbol{\delta}\\ \boldsymbol{v}\\ \boldsymbol{Q}\end{bmatrix}=\begin{bmatrix}\frac{12s_{11}^{m}s_{11}^{E}L}{Dw} & \frac{6s_{11}^{m}s_{11}^{E}L^{2}}{Dw} & \frac{2s_{11}^{m}s_{11}^{E}L^{3}}{D} & \frac{6s_{11}^{m}d_{31}(t_m+t_p)L}{D}\\ \frac{6s_{11}^{m}s_{11}^{E}L^{2}}{Dw} & \frac{4s_{11}^{m}s_{11}^{E}L^{3}}{Dw} & \frac{3s_{11}^{m}s_{11}^{E}L^{4}}{2D} & \frac{3s_{11}^{m}d_{31}(t_m+t_p)L^{2}}{D}\\ \frac{2s_{11}^{m}s_{11}^{E}L^{3}}{D} & \frac{3s_{11}^{m}s_{11}^{E}L^{4}}{2D} & \frac{3s_{11}^{m}s_{11}^{E}L^{5}w}{5D} & \frac{s_{11}^{m}d_{31}(t_m+t_p)L^{3}w}{D}\\ \frac{6s_{11}^{m}d_{31}(t_m+t_p)L}{D} & \frac{3s_{11}^{m}d_{31}(t_m+t_p)L^{2}}{D} & \frac{s_{11}^{m}d_{31}(t_m+t_p)L^{3}w}{D} & \frac{Lw}{2t_p}e_{33}^{T}\left(1-\frac{D-6s_{11}^{m}t_p(t_m+t_p)^{2}}{D}k_{31}^{2}\right)\end{bmatrix}=\begin{bmatrix}\boldsymbol{M}\\ \boldsymbol{F}\\ \boldsymbol{p}\\ \boldsymbol{V}\end{bmatrix} \quad (11.1)$$

where $D=2s_{11}^{m}\left(3t_m^2t_p+6t_mt_p^2+4t_p^3\right)+s_{11}^{E}t_m^3$, t_m = cantilever metal thickness, t_p = piezoelectric thickness, s_{11}^{E} = the piezoelectric elastic compliance ($1/Y_p$, where Y_p is the piezoelectric Young's modulus), s_{11}^{m} = the metal shim elastic compliance ($1/Y_m$, where Y_m is the metal shim Young's modulus), w and L are the with and length of the cantilever metal and piezoelectric material, d_{31} is the piezoelectric coefficient, k_{31} is the electromechanical coupling factor and e_{33}^{T} is the clamped dielectric constant. An example of a Unimorph configuration is shown in Figure 11.1.

11.3Results and Discussion

The first generation, PZT (soft and hard), the second generation PZN-PT and PMN-PT, and the third generation PIN-PMN-PT ferroelectric material were considered. Table 11.1 shows the piezoelectric material properties d_{31}, k_{31}, Y_p and e_{33}^{T} for the different polycrystalline and single crystal materials, organized as a function of T_C, used for a 31-mode cantilever resonance mode energy harvesting. From this piezoelectric material properties it is might be possible to predict the cantilever sensitivity by using the constituent equations for each configuration. From the constituents equations for STL, PTL and UNI the charge sensitivity ($Q_0=\partial Q/\partial F$), voltage sensitivity ($V_o=\partial V/\partial F$) and the sensor capacitance ($C_P=\partial Q/\partial V$) are determined if only a force F is applied perpendicularly to the free end of the cantilever.[20]

Table 11. 1 Material properties of single crystal and polycrystalline piezoelectric materials organized by the clamp dielectric constant ε_{33}^{T}.

Ferroelectric Materials	T_C (K)	Y_P (GPa)	$-d_{31}$ (pC/N)	k_{31}	$\varepsilon_{33}^{T} = K^{T}\varepsilon_0$
Soft PZT[a]	210	60.6	340.0	0.46	3.45 x10^8
Hard PZT[a]	350	100.0	1000.0	0.33	0.885 x10^8
PZN-4.5%PT[a]	155	12.2	970.0	0.50	4.60 x10^8
PMN-32%PT[a]	166	16.7	1000.0	0.51	7.08 x10^8
PIN-PMN-PT[b]	197	13.3	1337.0	0.65	6.41 x10^8

[a]TRS materials[21], [b]Liu et al.[22]

Figure 11.2 shows the Q_0, V_o and C_P for the three configuration as a function of e_{33}^{T} since the piezoelectric properties relationship: $\left(e_{33}^{T} = d_{31}^{2} Y_p / k_{31}^{2}\right)$. Basically, it is observed how the sensitivity for Q_0, V_o and C_P increase as function of e_{33}^{T} from first generation polycrystalline materials to the third generation single crystal materials.

For the cantilever configurations the Unimorph appears to be an average of the sensitivity between the bimorphs PTL and STL. However, the behavior of the PTL and STL sensitivities is inversely proportional. From the voltage sensitivity and sensor capacitance, the average power output as a function frequency (ω) and electric load (R_L) can be also obtained based on a the ideal voltage generator as the most suitable model for piezoelectric materials to be applied for structural vibration below ultrasonic frequency range.[23] The power output is given by Equation 11.2.

$$\langle \boldsymbol{P} \rangle = \frac{\boldsymbol{V_0^2}}{\boldsymbol{2R_L\left[1+\left(1/\omega C_p R_L\right)^2\right]}} \tag{11.2}$$

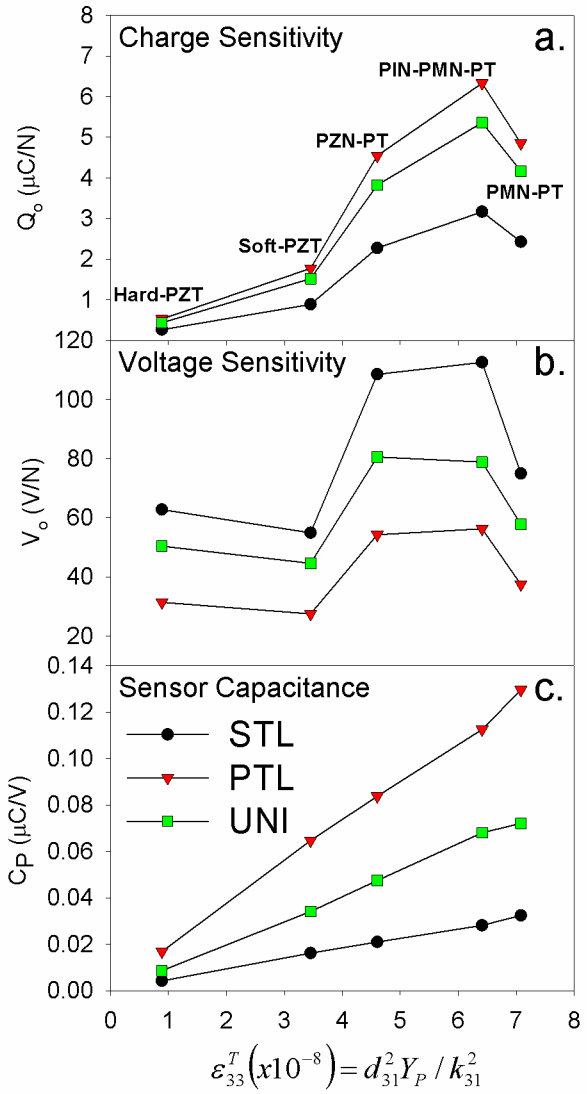

Figure 11.2 (a) Charge sensitivity, (b) voltage sensitivity and (c) the sensor capacitance of the Series Triple Layer (STL), Parallel Triple Layer (PTL) and Unimorph (UNI) configurations as a function of the clamped dielectric constant for single crystal and polycrystalline materials for cantilever resonance mode energy harvesting.

Taking in consideration the soft PZT and our material of interest PIN-PMN-PT, the power output at 10 kHz for both single crystal and polycrystalline materials in all three cantilevers configurations is compared in Figure 11.3. The power output for PIN-PMN-PT single crystal results ~5 times higher that obtained from the soft PZT. In general, the electromechanical coupling

factor and the piezoelectric coefficients will be the piezoelectric material properties of interest for a cantilevers resonance mode energy harvesting application. Nevertheless, those material properties play a role in the cantilever configuration. However, neither of them (piezoelectric and cantilever properties) may be optimized without the modification or alteration of the other due to their material property-configuration relationship or interaction. This tradeoff may be approach by figures of merit (FOM) which reveal behavior tendencies. It is important to mention that FOM display quality than quantity characteristics. It is of interest, by using FOM, the decoupling of contributing factors that enhance the property-configuration performance.

A careful examination to the constituent equations for the three cantilever configurations, especially for Q_0, V_o and C_P, there is three contributing factors that can be extracted related to the sensitivity based on the piezoelectric and resonance mode cantilever properties. All three sensor sensitivities, Q_0, V_o and C_P, show the same decouple relationship:

$$\boldsymbol{Sensitivity} = (\boldsymbol{EPP - Factor})(\boldsymbol{G - Factor})(\boldsymbol{EP - Factor}) \qquad (11.3)$$

The Electromechanical Piezoelectric Properties Factor (EPP-Factor) relates the piezoelectric properties d_{31}, k_{31} and ε_{33}. The Geometrical Factor (G-Factor) reveals the geometrical configuration of the cantilever, in this case a rectangular shape (w and L). The Elastic Properties Factor (EP-Factor) shows the relationship between Y_P and Y_m with t_P and t_m, respectively. These three factors may be use to optimize Q_0, V_o and C_P of the device. Table 11.2 summarized all three factors for the three resonance mode configurations.

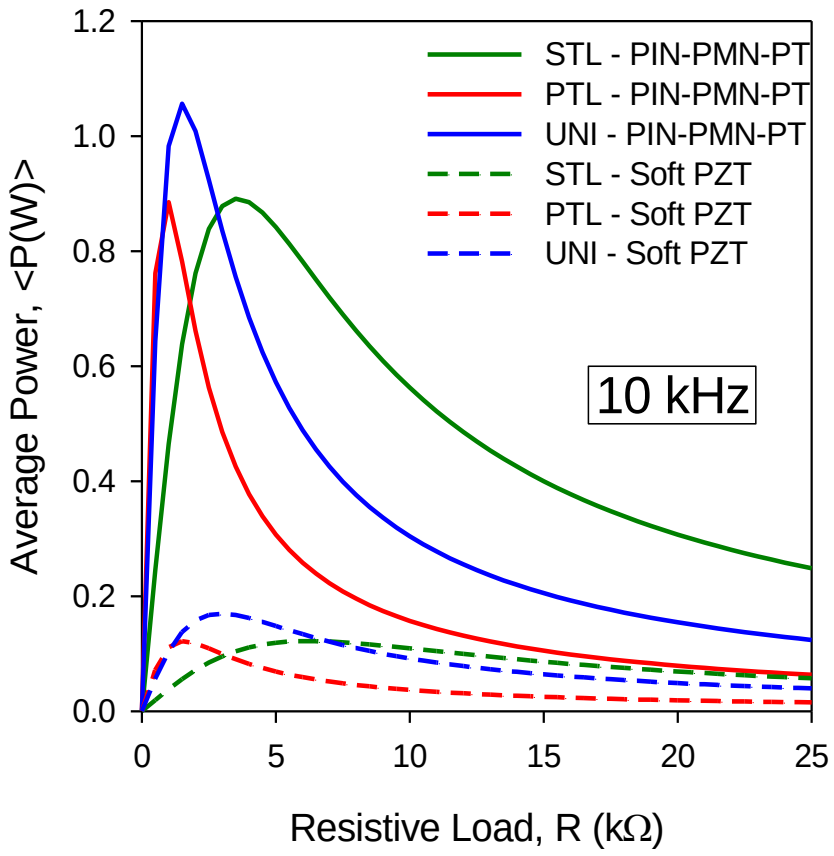

Figure 11.3 Comparison of the average power as a function of electric resistive load for the of a soft PZT polycrystalline material (dash lines) and PIN-PMN-PT single crystal (solid lines) at 10 kHz for a series triple layer, STL (green), parallel triple layer, PTL (red), and Unimorph, UNI (blue) cantilever bimorph resonance mode configurations.

Following Equation 11.3, it is observed that in general

$$\boldsymbol{Q_0(FOM)} \propto (\boldsymbol{3d_{31}})(\boldsymbol{L^2})\left(\frac{\boldsymbol{1}}{\boldsymbol{A+B}}\right) \tag{11.4}$$

$$\boldsymbol{V_o(FOM)} \propto \left(\frac{\boldsymbol{6d_{31}}}{\boldsymbol{\varepsilon_{33}^T(1\pm k_{31}^2)}}\right)\left(\frac{\boldsymbol{L}}{\boldsymbol{w}}\right)\left(\frac{\boldsymbol{1}}{\boldsymbol{A+B}}\right) \tag{11.5}$$

and

$$\boldsymbol{C_P(FOM)} \propto \left(\frac{\boldsymbol{\varepsilon_{33}^T}}{\boldsymbol{2}}\right)(\boldsymbol{Lw})\left(\frac{\boldsymbol{1}}{\boldsymbol{t_p}}\right) \tag{11.6}$$

where $A = \left(t_m + t_p\right)^2$ and $B = \frac{Y_m t_m^3}{Y_p t_p}$.

Table 11.2 Sensitivity (FOM) equations as a function of electromechanical piezoelectric properties, geometrical and elastic properties factors. The sensitivity parameter is obtained by multiply these three factors. FOM for PTL and UNI are related to STL configuration. $A = \left(t_m + t_p\right)^2$, $B = \frac{Y_m t_m^3}{Y_p t_p}$.

Sensitivity	Electromechanical Piezoelectric Properties Factor	Geometrical Factor	Elastic Properties Factor
V_o(STL-FOM)	$\left(\frac{6d_{31}}{\varepsilon_{33}^T(1-k_{31}^2)}\right)$	$\left(\frac{L}{w}\right)$	$\left(\frac{1}{6A+B}\right)$
Q_o(STL-FOM)	$(3d_{31})$	(L^2)	$\left(\frac{1}{6A+B}\right)$
C_p(STL-FOM)	$\left(\frac{\varepsilon_{33}^T}{2}\right)$	(Lw)	$\left(\frac{1}{t_p}\right)$
V_o(PTL-FOM)	$\frac{1}{2}\left(\frac{6d_{31}}{\varepsilon_{33}^T(1-k_{31}^2)}\right)$	$\left(\frac{L}{w}\right)$	$\left(\frac{1}{6A+B}\right)$
Q_o(PTL-FOM)	$2(3d_{31})$	(L^2)	$\left(\frac{1}{6A+B}\right)$
C_p(PTL-FOM)	$4\left(\frac{\varepsilon_{33}^T}{2}\right)$	(Lw)	$\left(\frac{1}{t_p}\right)$
V_o(UNI-FOM)	$\left(\frac{3d_{31}}{\varepsilon_{33}^T(1+k_{31}^2)}\right)$	$\left(\frac{L}{w}\right)$	$\left(\frac{1}{2A+B}\right)$
Q_o(UNI-FOM)	$(3d_{31})$	(L^2)	$\left(\frac{1}{4A+B}\right)$
C_p(UNI-FOM)	$2\left(\frac{\varepsilon_{33}^T}{2}\right)$	(Lw)	$\left(\frac{1}{t_p}\right)$

From these FOM it is clearer to capture the behavior of Q_0, V_o and C_P, previously shown in Figure 11.2, but now based on the material property-configuration relationship of the piezoelectric and resonance mode cantilever parameters. The piezoelectric single crystals shown a higher EPP-factor than the piezoelectric ceramics, revealing a higher sensitivity responses. For charge sensitivity d_{31} is a proportional term which has higher values for piezoelectric single crystals than for piezoelectric ceramics. However the ratio between d_{31} and ε_{33}^T is a strong parameter forV_o. The G-Factor reveals a degree of freedom on the device dimensions. Q_0,V_o C_P and $\langle P \rangle$ increase as the length of the device increase. However, for V_o the $L-w$ ratio will determine G-Factor contribution as fallow: $V_o\left(\left(\frac{L}{w}\right)<1\right) < V_o\left(\left(\frac{L}{w}\right)=1\right) < V_o\left(\left(\frac{L}{w}\right)>1\right)$. The EP-Factor contribution is proportional to the deflection of the cantilever. The (Y_m/Y_P) ratio and the A-term will define Q_0, V_o, C_P and $\langle P \rangle$. Then for an optimum EP-Factor the properties of the

metal shim parameters (Y_m and t_m) should be very small compared with the piezoelectric properties parameters (Y_p and t_p). From this simple approach, which consider FOM relating the material property-configuration relationship of the piezoelectric materials and resonance mode cantilever parameters, the understanding of the behavior polycrystalline and single crystal materials embedded in the Unimorph and bimorphs cantilever resonance mode configuration energy harvesters may be bring some lights to their performance optimization.

11.4 Summary

The 31-mode piezoelectric properties of the ferroelectric materials PZT (Hard and Soft), PZN-PT, PMN-PT and PIN-PMN-PT were qualitatively compared from FOM based on the constituents equations for resonance mode cantilever configuration energy harvesting. The cantilever configuration under comparison were the Unimorph and the bimorph, in series and parallel, benders. The constituent equations are based on the geometrical configuration of the bender from deformation due to a mass at the tip of the cantilever.

The FOM determined in this chapter are useful to control the properties of a piezoelectric material by grouping them in different factors. It was as a consequence of the tradeoff of the individual enhancement of the piezoelectric properties to the enhancement of the configuration. The different factors in the FOM equation were then associated with the geometrical configuration of the cantilever ($G-factor = f(w, L)$), with the properties of the piezoelectric materials ($EPP-factor = f(d_{31}, k_{31}, \varepsilon_{33})$) and with the elastic properties of the cantilever ($EP-factor = f(Y_P, Y_m, t_P, t_m,)$). Qualitatively, the FOM revealed the same behavior for the voltage,

charge and capacitance sensitivity as well as for the power sensitivity of the cantilever resonance mode configuration.

11.5 References

1. Priya, S. Advances in Energy Harvesting Using Low Profile Piezoelectric Transducers. *J. Electroceramics* **19,** 165–182 (2007).

2. Kim, S.-G., Priya, S. & Kanno, I. Piezoelectric MEMS for energy harvesting. *MRS Bull.* **37,** 1039–1050 (2012).

3. Anton, S. R. & Sodano, H. a. A review of power harvesting using piezoelectric materials (2003–2006). *Smart Mater. Struct.* **16,** R1–R21 (2007).

4. Morimoto, K., Kanno, I., Wasa, K. & Kotera, H. High-efficiency piezoelectric energy harvesters of c-axis-oriented epitaxial PZT films transferred onto stainless steel cantilevers. *Sensors Actuators A Phys.* **163,** 428–432 (2010).

5. Muralt, P., Marzencki, M., Belgacem, B., Calame, F. & Basrour, S. Vibration Energy Harvesting with PZT Micro Device. *Procedia Chem.* **1,** 1191–1194 (2009).

6. Hajati, A. PhD thesis. (2010).

7. Fang, H.-B. *et al.* Fabrication and performance of MEMS-based piezoelectric power generator for vibration energy harvesting. *Microelectronics J.* **37,** 1280–1284 (2006).

8. Aktakka, E. E. PhD Thesis. (2012).

9. Park, J. C., Park, J. Y. & Lee, Y. Modeling and Characterization of Piezoelectric d 33 -Mode MEMS Energy Harvester. *J. Microelectromechanical Syst.* **19,** 1215–1222 (2010).

10. Park, S.-E. & Shrout, T. R. Ultrahigh strain and piezoelectric behavior in relaxor based ferroelectric single crystals. *J. Appl. Phys.* **82,** 1804 (1997).

11. Kuwata, J., Uchino, K. & Nomura, S. Dielectric and Piezoelectric Properties of 0.91Pb(Zn1/3Nb2/3)O3-0.09PbTiO9 Single Crystals. *Jpn. J. Appl. Phys.* **21,** 1298–1302 (1982).

12. Ren, B. *et al.* Piezoelectric energy harvesting using shear mode 0.71Pb(Mg(1/3)Nb(2/3))O(3)-0.29PbTiO(3) single crystal cantilever. *Appl. Phys. Lett.* **96,** 083502 (2010).

13. Sun, C., Qin, L., Li, F. & Wang, Q.-M. Piezoelectric Energy Harvesting using Single Crystal Pb(Mg1/3Nb2/3)O3-xPbTiO3 (PMN-PT) Device. *J. Intell. Mater. Syst. Struct.* **20,** 559–568 (2009).

14. Shen, D., Choe, S. Y. & Kim, D. J. Analysis of Piezoelectric Materials for Energy Harvesting Devices under High-g Vibrations. *Jpn. J. Appl. Phys.* **46,** 6755–6760 (2007).

15. Mateu, L. & Moll, F. Optimun Piezoelectric Bending Beam Structures for Energy Harvesting using Shoe Inserts. *J. Intell. Mater. Syst. Struct.* **16,** 835–845 (2005).

16. Baker, J., Roundy, S. & Wright, P. 132 Alternative Geometries for Increasing Power Density in Vibration Energy Scavenging for Wireless Sensor Networks. *Int. Energy Convers. Eng. Conf.* **2,** 1–12 (2005).

17. Wang, Q. M. & Cross, L. E. Constitutive equations of symmetrical triple layer piezoelectric benders. *IEEE Trans. Ultrason. Ferroelectr. Freq. Control* **46,** 1343–51 (1999).

18. Smits, J. G., Dalke, S. I. & Cooney, T. K. The constituent equations of piezoelectric bimorphs. *Sensors Actuators A Phys.* **28,** 41–61 (1991).

19. Smits, J. G. & Choi, W. The constituent equations of piezoelectric heterogeneous bimorphs. *IEEE Trans. Ultrason. Ferroelectr. Freq. Control* **38,** 256–70 (1991).

20. Ng, T. H. & Liao, W. H. Sensitivity Analysis and Energy Harvesting for a Self-Powered Piezoelectric Sensor. *J. Intell. Mater. Syst. Struct.* **16,** 785–797 (2005).

21. Raffi Sahull. High Performance Pieozoceramics. *TRS Technol. Inc.* at <http://www.trstechnologies.com/Materials/piezoceramics.php>

22. Liu, X., Zhang, S., Luo, J., Shrout, T. R. & Cao, W. Complete set of material constants of Pb(In(12)Nb(12))O(3)-Pb(Mg(13)Nb(23))O(3)-PbTiO(3)single crystal with morphotropic phase boundary composition. *J. Appl. Phys.* **106,** 74112 (2009).

23. Park, C. H. On the Circuit Model of Piezoceramics. *J. Intell. Mater. Syst. Struct.* **12,** 515–522 (2001).

CHAPTER 12

PIEZOELECTRIC ENERGY CONVERSION FROM A REVERSIBLE STRESS-INDUCED INTER-FERROELECTRIC PHASE TRANSFORMATION IN PIN-PMN-PT RELAXOR FERROELECTRIC SINGLE CRYSTAL MATERIAL.

12.1 Introduction

Piezoelectric energy harvesting for self-powered devices has attracted interest in the engineering and scientific community due to its many technological applications.[1] For a resonance-mode piezoelectric energy harvesting, such as cantilever-mode, the key material parameters are the electromechanical coupling factors (k_{ij}) and the piezoelectric coefficient (d_{ij}).[2] Extremely high dielectric properties, $d_{33} >= 1500\ pC/N$ and $k_{33} \geq 0.92$ have been demonstrated in the solid solutions relaxor ferroelectric single crystal materials $Pb(Zn_{1/3}Nb_{2/3})O_3$-$PbTiO_3$ (PZN-PT) and $Pb(Mg_{1/3}Nb_{2/3})O_3$-$PbTiO_3$ (PMN-PT) especially around the morphotropic phase boundary (MPB) compared with polycrystalline piezoelectric ceramic materials.[3–5] However, the bandwidth of mechanical vibration, stress levels and temperatures that can lead to depolarization are some of the limitations for a resonance-mode piezoelectric energy harvesting application.[1] For instance, the electrical energy output in the cantilever resonance mode configuration is limited to the bandwidth of resonance mechanical vibrations reducing the active area and volume for energy harvesting. The resonance bandwidth of a linear cantilever beam harvester should be wide enough to accommodate the uncertain variance of ambient vibration.[6] A solution for the cantilever energy harvesting is to increase the bandwidth and to reduce the dielectric constant in order to match the impedance of the vibration material.[1] The bandwidth can be increased from nonlinear resonators energy harvesters by hardening of softening the resonance bandwidth of the beam structure. As a

consequence, nonlinear resonators can extract more electrical energy than linear resonating beams.[6,7] Ultra wide bandwidth (>20%) from the center frequency have been demonstrated in monolithic MEMS-based nonlinear resonant piezoelectric micro energy harvester which generated a power of more than 22 μW with a power density of (1100.0 μW/mm^3).[6]

The piezoelectric energy harvesting in linear or nonlinear resonance mode is operated well below phase transitions in order to avoid large swings in load impedance, high electric field drive, and hysteresis losses.[8] Their thermal stability during operation is limited by their Curie temperature, T_C. Similarly, the poled state must be maintained during operation, which limits the stress levels and temperatures that can lead to depolarization. A new method for electromechanical energy conversion was demonstrated based on the d_{32}-mode ferroelectric to ferroelectric (inter-ferroelectric) phase transition in the engineering domain $xPb(In_{1/2}Nb_{1/2})O_3$-(1-x-y)$Pb(Mg_{1/3}Nb_{2/3})O_3$-$yPbTiO_3$ (PIN-PMN-PT) relaxor ferroelectric single crystal.[9] During an inter-ferroelectric transition, both modulus and direction of polarization change. In this particular case, it was as a result of an induced-electric field in the [011] direction, an induced ferroelectric orthorhombic (F_O) phase[10], due to an inter-ferroelectric polarization rotation from the poled [111] ferroelectric rhombohedral (F_R) phase, a 2R engineering domain state[11], across the MPB.[8] This method is benefitted from the output electric energy that results from an easy polarization rotation across the MPB[12–17] and their engineering polarization orientation.[18]

The polarization orientation and rotation of the [111] engineering domain single crystal is represented in Figure 12.1, where a simultaneous electrical bias along [110] and a uniaxial stress along [001] cause an easy polarization rotation from a poled [111] single crystal, engineering cut along {110}, to [110] direction for composition at the MPB. Then, in this method, the electric energy output was obtained from a reversible cycling process through the F_R-F_O phase transition

triggered by simultaneous application of an electric bias and a reversible mechanical stress drove at 1 Hz, out of the resonance frequency of PIN-PMN-PT single crystal. Essentially, this energy conversion method was based in two isopolarization processes, where mechanical compression and an applied reverse electric field drive the single crystal close to an induced F_O phase transition, and two isobaric process, where the change in polarization and strain are allowed by bleeding charge from the electrodes during the F_R-F_O phase transition.[19] The reversible F_O-F_R transition on decompression could be due to compensation charges on charge domain walls that pull the polarization to the F_R state.[10]

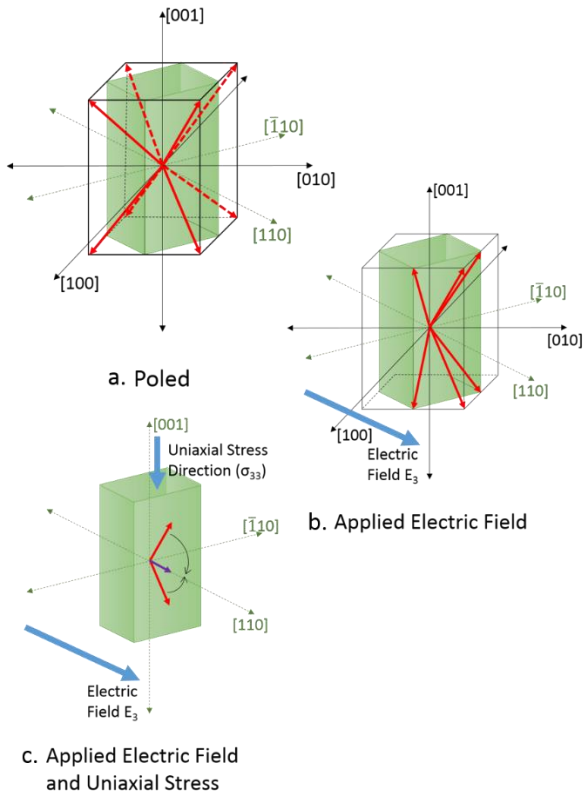

Figure 12.1. Polarization rotation from [111] to [110] in a [111] poled engineering domain ferroelectric.

The polarization rotation through the inter-ferroelectric phase transition may be occurred when subjected to a change of temperature, composition, applied stress and/or applied electric field.[9] A stress-electric field-temperature diagram have been demonstrated for the ferroelectric single crystal materials PMN-32PT[20] and PIN-PMN-PT[9]. Figure 12.2 shows the stress-electric field-temperature diagram for the F_R-F_O inter-ferroelectric transition in PIN-PMN-PT single crystal. It is to be noted that the width of the hysteresis region around F_R-F_O phase transition appears to remain constant, indicating that the energy barrier between the F_R and F_O phases is nearly independent of whether the transformation is thermally, electrically, or mechanically driven within this range of loadings.[9] This diagram shows that the inter-ferroelectric transition can be trigger by the simultaneous application of external fields.

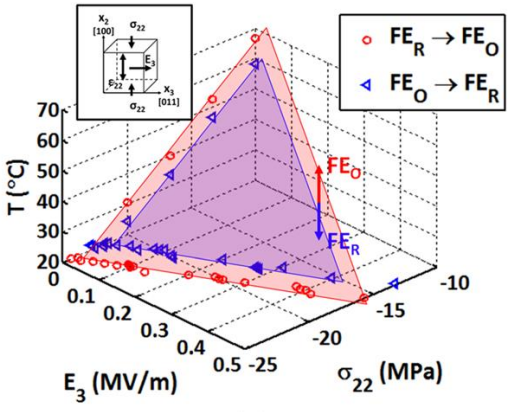

Figure 12.2. Temperature-stress-electric field diagram for PIN-PMN-PT showing the phase transition formation hysteresis.[9]

The objective of this work is to investigate a phase transforming piezocrystal energy conversion process in the engineering domain PIN-PMN-PT single crystal only as a function of an applied mechanical stress. The piezocrystal will be mechanically driven close to an induced F_O phase, a preload, and then the F_R-F_O phase transition will be mechanical triggered by an additional applied cycling mechanical stress allowing a reversible phase transformation. The determination

of energy density, power density and the energy conversion efficiency per cycle will be described, as well as the total input mechanical energy per cycle, and comparison with their corresponding cycling energy conversion process around the F_R-liner region under similar experimental conditions will be discussed. Also, the discussion is extended to compare the phase transforming piezocrystal energy conversion process with the typical cantilever resonance mode energy harvesters.

12.2 Experimental Procedure

The linear F_R-phase region and the phase transforming piezocrystal energy conversion process, driven by a reversible high mechanical stress, were investigated. Due to the non-linearity nature of the inter-ferroelectric transition, an empirical treatment was adopted. For the phase transforming piezocrystal process a d_{32}-mode PIN-24PMN-PT from HC-ceramics ($(length, l = 4), x\ (width, w = 4), x\ (height, h = 12\ mm)$) piezoelectric single crystal material was used. The mechanical preload close to the induced F_O phase transformation in PIN-PMN-PT was able by using a costume built preload fixture, shown in Figure 12.3.

The preload fixture consists of two small parallel metal plates separated by the single crystal height, perpendicular to the plates, connected to two parallel springs, (total net spring constant, k = -72.94 N/mm), which statically compress the piezoelectric single crystal material. Kapton and Teflon tape were placed between the metal plates and the piezoelectric material to avoid arc effects. After the mechanical preload, a reversible mechanical stress through the F_R-phase linear and separately through the induced F_R-F_O phase transition regions was applied. The applied reversible mechanical stress from a load generator (Enduratec: see Figure 12.3) was determined by a calibrated load cell. Low drive frequencies of 10 and 25 Hz were used.

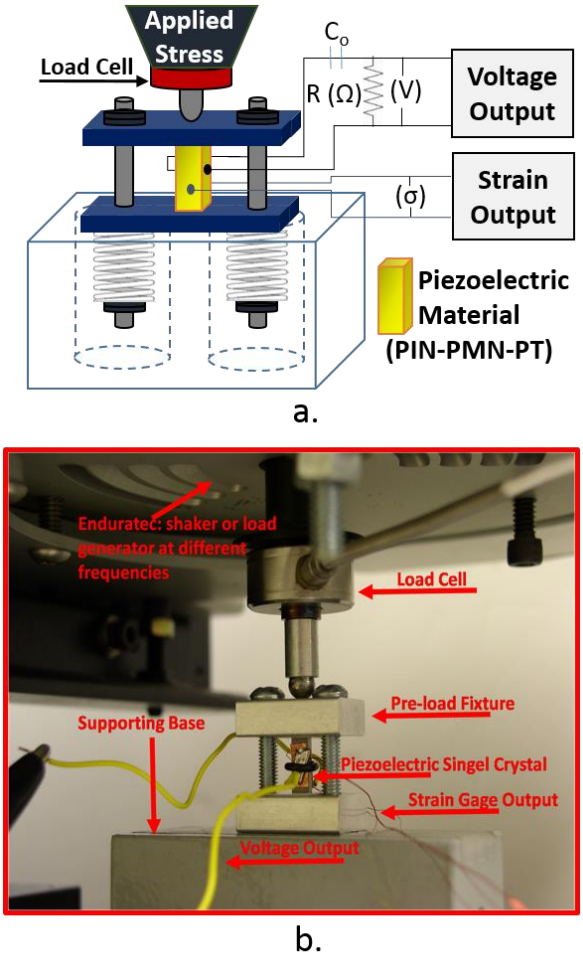

Figure 12.3. Experimental set up during the reversible stress-induced phase transformation process. Designed (left) and built (right) phase transforming piezocrystal energy conversion device.

The strain was measured by strain gages placed in the non-electrode sides of the sample (see Figure 12.3). At the same time, the voltage was measured by using a Tektronix P6015A high voltage prove, for high voltage signals, and by using a 617 Keithley programmable electrometer for low voltage signals. The internal resistance of both measurement devices are 100 MΩ and 1 TΩ, respectively. The experimental data was collected at different resistive loads of 50 kΩ, 100 kΩ, 500 kΩ, 1000 kΩ and 5000 kΩ. The circuit for the measured output voltage is shown in Figure 12.3. The strain and voltage were acquired as a function of the applied cycling stress or mechanical excitation ($\Delta\sigma$) and time ($t(s)$).

12.3 Results and Discussion

For characterization purpose, the stress-strain behavior of the as received material was first verified, shown in Figure 12.4 (black solid line). A very sharp phase transition was observed at -19.0 MPa during compression and at -15.6 MPa during decompression through the F_R-F_O phase transformation. It compares well with the one obtained by Amin et al. at room temperature.[21] Figure 12.4 also shows the strain, ε (left axis) and voltage, V (right axis) output as a function of the applied reversible mechanical stress, σ, at 10 Hz drive frequency and 100 kΩ electric resistive load experimental conditions for one cycle.

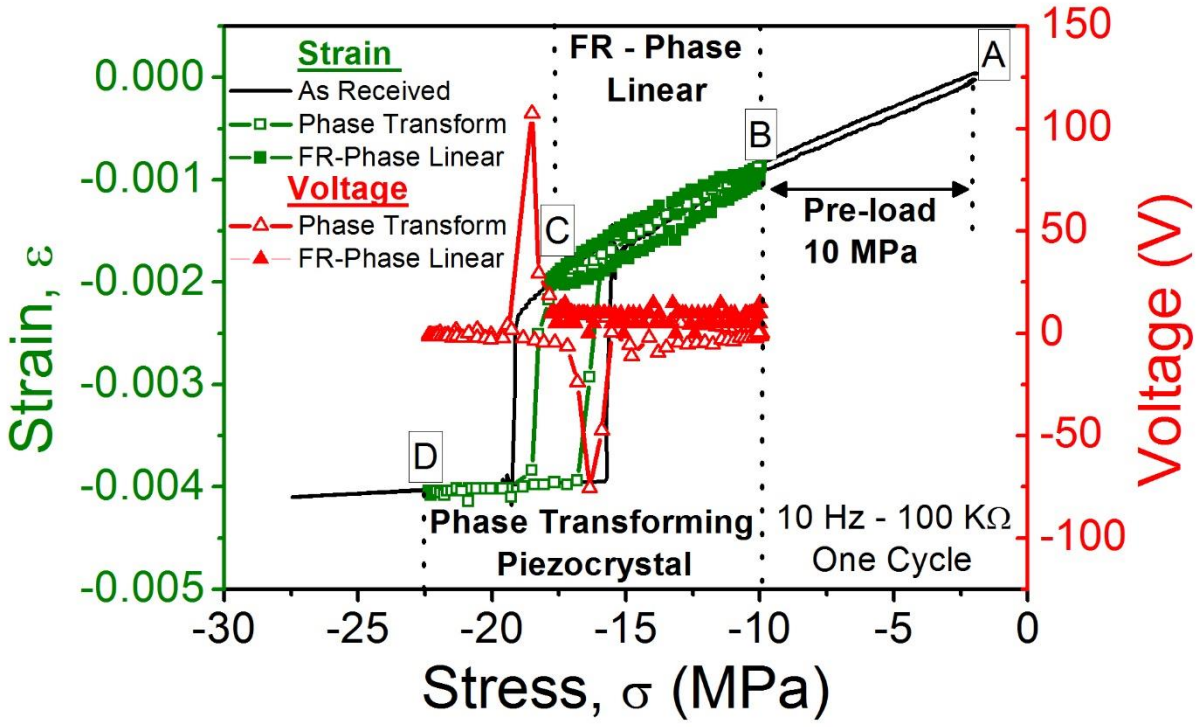

Figure 12.4. Strain (green squares) and voltage (red triangles) output as a function of applied stress at 10 Hz drive frequency and 100 kΩ electric resistive load. FR-Phase linear region (solid symbols) and phase transforming piezocrystal region (open symbols) for one cycle. Stress-strain characterization of as received d32-mode PIN-24PMN-PT single crystal (solid back line).

Three regions were considered during the cycling process, as shown in the Figure 12.4. The pre-load region (step A-B), where the single crystal was pre-stress ($\sigma \approx -10\ MPa$) close to an induced F_R-F_O phase transition; the linear F_R single phase region (step B-C: solid green squares), where a reversible mechanical stress was applied from 10 MPa up to around ~17 MPa; and the phase transforming piezocrystal region (step B-D: open green squares) where a reversibly mechanical stress was applied from 10 MPa to around 23 MPa. The phase transforming piezocrystal region may be reversible tuned in a short mechanical compression-decompression region. However, for comparison purpose, it was set-up from point B to point C. It is to be noted that a pre-load up to point C does not return the F_R-phase after decompression. Taking all this region in consideration , the total input mechanical energy density per cycle (MED) in the phase transforming piezocrystal process is the total energy corresponding to the mechanical pre-load, mechanical compression through the F_R-F_O phase transition (from B to D) and the mechanical energy losses (area inside the loop). It is given by Equation 12.1, respectively.

$$\boldsymbol{MED\ (J/m^3) = \int_A^B \sigma d\varepsilon + \int_B^D \sigma d\varepsilon + \oint \sigma d\varepsilon} \quad (12.1)$$

In the total input, mechanical energy density per cycle for the linear F_R single phase region, the compression was from B to C. As the piezoelectric single crystal was driven through the two different regions (linear F_R single phase region and phase transforming piezocrystal region) the voltage output as a function of different resistive loads was simultaneously determined, see circuit in Figure 12.3. As an example, the voltage output for the 10 Hz drive frequency and 100 kW electric resistive load experimental condition as a function of applied mechanical stress is shown in right axis of Figure 12.4. The voltage output for the linear F_R single phase region is shown as solid red triangles while for the phase transforming piezocrystal region it is shown as open triangles. It is to be noted the huge area corresponding to the phase transforming piezocrystal

region compared to the small linear F_R single phase region. From the voltage output per cycle, the instantaneous power given by $V(t)^2/R_{eq}$ (where the peak power may be obtained), and the polarization *P(C/m²)* may be determined. The polarization is given by:

$$\boldsymbol{Polarization = P(C/m^2) = \frac{Charge}{Area} = \frac{1}{(lxw)(2\pi f)}\int idt = \frac{1}{(lxw)(2\pi f)}\int \frac{V(t)}{R_{eq}}dt} \qquad (12.2)$$

where i is the current, the $2\pi f$ factor defined one cycle and f is the drive frequency. As an example, the applied reversible mechanical stress, or mechanical excitation ($\Delta\sigma$), for the phase transforming piezocrystal region and the corresponding changes in strain ($\Delta\varepsilon$), induced electric field, ($E(V/m) = V/l$), and polarization ($P(C/m^2)$) are plot as a function of time for the investigated drive frequencies10 Hz, Figure 12.5a and 12.5b, and 25 Hz, Figure 12.5c and 12.5d, at 100 kΩ electric resistive load experimental conditions.

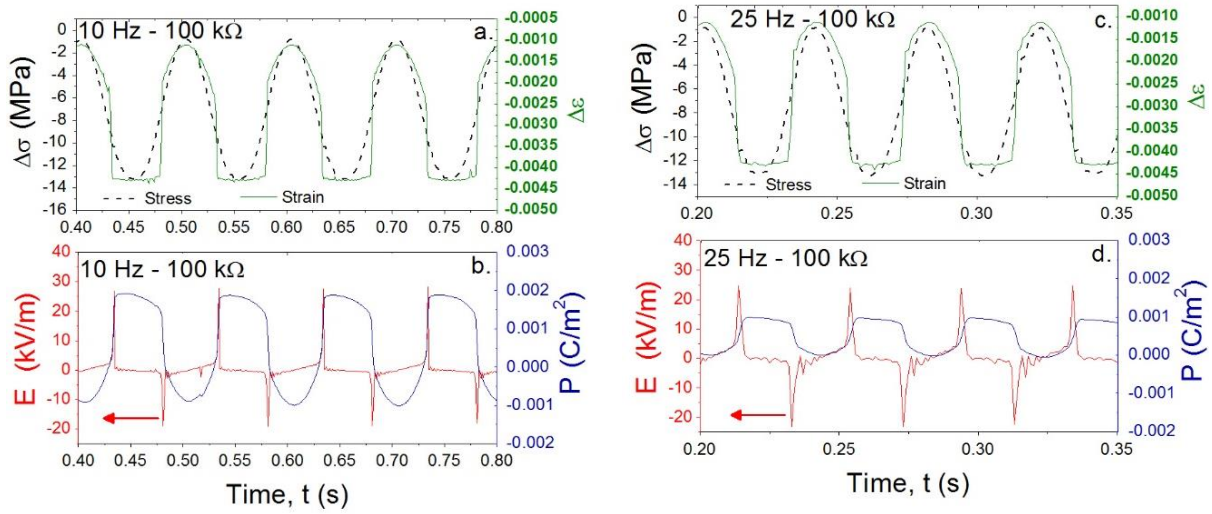

Figure 12.5. a) Mechanical excitation (Δσ) and mechanical strain (Δε) responses and (b) induced electric field (E) and polarization (P) as a function of time for the 10 Hz drive frequency and 100 kΩ electric resistive load experimental conditions during the phase transforming piezocrystal cycling process. (c) P-E loop for different electric resistive loads at 10 Hz for one cycle.

The cycling through the F_R-F_O induced phase transition is demonstrated for an expand region (4 cycles) of the total number of cycles, for clarity. It is clear, from the jump in polarization,

the first-order nature of the induced F_R-F_O phase transition which generates a peak in voltage, or induced electric field, due to the sudden change in strain. Also, it is noted the difference in slope in the induced electric field at the F_R and F_O phases, indicating the capability for energy conversion. It is well know from resonance mode that the energy conversion from the F_O-phase is very small or insignificant, compared with the F_R-phase due to the small strain-stress slope. Similar behavior is observed for the strain responses at 10 and 25 Hz drive frequencies, however small peaks in the induced electric field and small jumps in polarization were observed at 25 Hz compared with the 10 Hz drive frequency indicating a frequency dependence to the voltage output. Using the polarization and the induced electric field, the total output electrical energy density per cycle was determined. The total area inside the polarization as a function of the induced electric field plot (a P-E loop) will determine the total output electrical energy density per cycle (EED). This is given by Equation 12.3:

$$\boldsymbol{EED\ per\ cycle\ (J/m^3) = \oint PdE} \tag{12.3}$$

The power energy density per cycle (PED) was then determined from the EED per cycle by the total time in the cycle. Also, the energy conversion factor (ECF) for the phase transforming piezocrystal and the linear F_R single phase region during the energy conversion process were determined as shown in Equation 12.4.

$$\boldsymbol{ECF}\ (\%) = \frac{\boldsymbol{Output\ Electrical\ Energy\ Density\ (J/m^3)\ per\ cycle}}{\boldsymbol{Input\ Mechanical\ Energy\ Density\ (J/m^3)\ per\ cycle}}\boldsymbol{x100} \tag{12.4}$$

The $\Delta\varepsilon$-$\Delta\sigma$ curve and P-E loop for all investigated experimental conditions at 10 Hz and 25 Hz are shown in Figure 12.6a and 12.6b and Figure 12.6c and 12.6d, respectively. The results for the total input mechanical energy density per cycle, the total output electrical energy density per cycle, the corresponding power density and energy conversion factor per cycle are shown in Table 12.1 and Table 12.2 for the 10 Hz and 25 Hz drive frequencies, respectively.

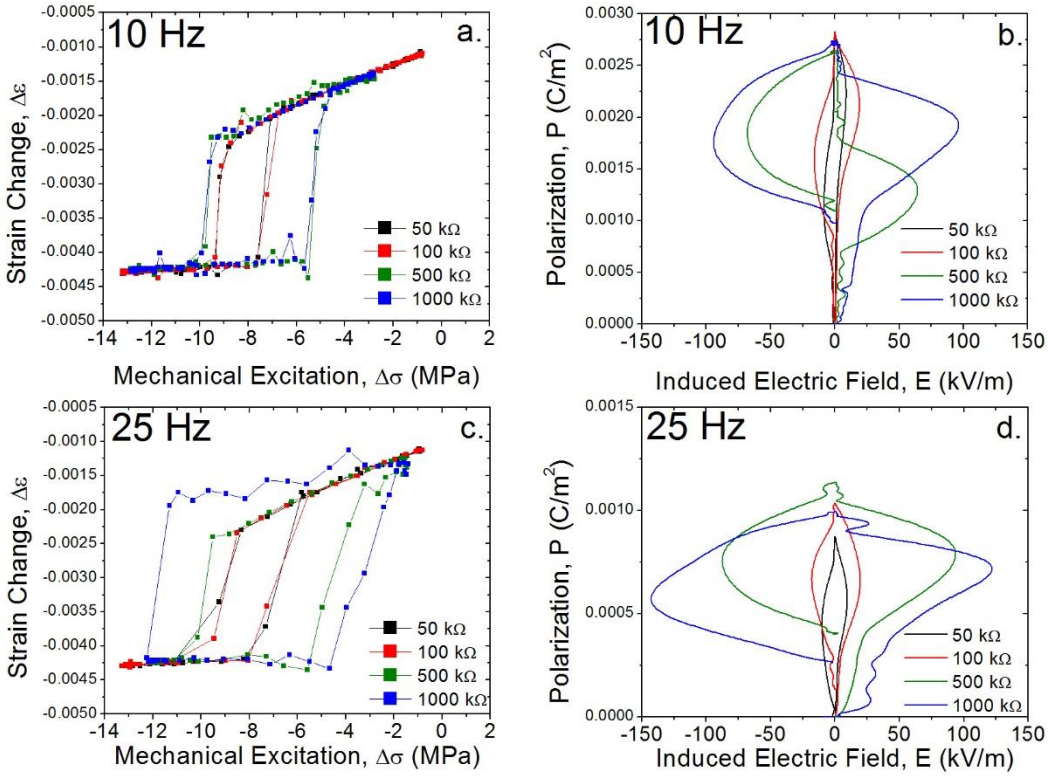

Figure 12.6. Strain vs stress and polarization vs induce electric field as a function of electric resistive load for 10 Hz (a and b) and 25 Hz (c and d), respectively.

It is to be noted from Figure 12.6a and 12.6c, and also from Table 12.1 and Table 12.2, that even though the Δε at phase transition remains constant as a function of electric resistive loads and drive frequencies, due to the intrinsic property nature of the phase transition, the mechanical energy losses increases as function of the electric resistive loads. This widening of the Δε-Δσ curve was observed for resistive loads above 500 kΩ and was consistent during all the experiments. As a consequence the total input mechanical energy also increased. Comparing with the corresponding F_R-phase linear region the total input mechanical energy remains the same in average (~0.88 μJ/cm3) as a function of frequency and resistive load.

Table 12. 1 Analysis of the linear and nonlinear energy conversion at 10 Hz drive frequency.

	Resistive Load (kΩ)	Peak Power (mW)	Peak Power Density ($\mu W/cm^3$)	ΔP (C/m^2)	Input Mechanical Energy per cycle ($\mu J/cm^3$)	Power Density per cycle ($\mu W/cm^3$)	Energy Density per cycle ($\mu J/cm^3$)	Efficiency per cycle (%)
	10	12	5.99x104	0.00084	3.06 x104	53	5	0.018
Phase	50	38	19.7 x104	0.00116	3.21 x104	220	22	0.068
Transform	100	90	46.9 x104	0.00089	3.25 x104	398	42	0.129
Piezocrystal	500	203	106 x104	0.00068	3.40 x104	1274	130	0.382
	1000	182	94.6 x104	0.00095	3.26 x104	2056	212	0.650
	5000	128	66.8 x104	0.00081	4.33 x104	4486	467	1.078
F_R-phase	10	0.02	0.01 x104	-	1.00 x104	3	0.3	0.003
Linear	50	0.39	0.20 x104	-	0.92 x104	9	1	0.010
	100	0.61	0.32 x104	-	0.95 x104	18	2	0.020
	500	0.43	0.23 x104	-	0.88 x104	39	4	0.045
	1000	2.91	1.52 x104	-	0.76 x104	76	8	0.103
	5000	5.13	2.67 x104		0.76 x104	257	27	0.351

Table 12. 2 Analysis the linear and nonlinear energy conversion at 25 Hz drive frequency.

	Resistive Load (kΩ)	Peak Power (mW)	Peak Power Density ($\mu W/cm^3$)	ΔP (C/m^2)	Input Mechanical Energy per cycle ($\mu J/cm^3$)	Power Density per cycle ($\mu W/cm^3$)	Energy Density per cycle ($\mu J/cm^3$)	Efficiency per cycle (%)
Phase	10	2	1.08 x104	0.00006	3.41 x104	10	0.4	0.001
Transform	50	52	27.0 x104	0.00030	3.38 x104	225	10	0.029
Piezocrystal	100	91	47.3 x104	0.00030	3.22 x104	472	20	0.062
	500	401	209 x104	0.00034	3.96 x104	2224	93	0.236
	1000	416	216 x104	0.00041	5.49 x104	3135	129	0.234
	5000	167	87.1 x104	0.00029	5.05 x104	6608	271	0.536
F_R-phase	10	0.08	0.04 x104	-	0.82 x104	1	0.04	0.0005
Linear	50	0.31	0.16 x104	-	0.76 x104	2	0.1	0.001
	100	0.77	0.40 x104	-	0.86 x104	11	0.5	0.005
	500	6.90	3.59 x104	-	0.86 x104	91	4	0.044
	1000	15.05	7.84 x104	-	0.80 x104	128	5	0.066
	5000	2.88	1.50 x104		0.70 x104	393	16	0.230

The widening of the Δε-Δσ curve as a function of the electric resistive loads during the phase transforming piezocrystal process has some implications to the total output electrical energy density as well as the power density per cycle of the system. It is to be noted that the induced

electric field increases considerably (~100kV/m) for resistive loads above 500 kΩ as a consequence of the Δε-Δσ broadening. Nevertheless, the polarization at the phase transition decreases by a factor of three as the frequency is increased from 10 to 25 Hz. It is demonstrated in Figure 12.5b and 12.5d from the jump in polarization at the material is cycled at 10 Hz and 25 Hz for the 100 kΩ electric resistive load, as well as from Figure 12.6b and 12.6d from the polarization of the induced F_O-phase at zero induced electric field as a function of the electric resistive loads.

Table 12.1 and Table 12.2 also show the peak power and the peak power density for the linear F_R single phase region and phase transforming piezocrystal region, as well as the polarization change (ΔP) determined at the F_R-F_O phase transition for the 10, 50 100, 500, 1000 and 5000 kΩ electric resistive loads at both 10 and 25 Hz drive frequencies. The peak power and peak power density increase as a function of the electric resistive load up to a maximum between 500 and 1000 kW for both phase transforming piezocrystal and the linear F_R single phase regions at both measured drive frequencies. The maximum in peak power and peak power density around this range electric resistive load was about two time higher for the 25 Hz compared with 10 Hz indicating a proportional dependency to the drive frequency in both regions. An extremely small change in polarization was revealed from the phase transition, around 0.001 C/m^2 at 10 Hz and 0.0003 C/m^2 at 25 Hz, which appears to be independent of the electric resistive load. This different in polarization from the two investigate frequencies is very small, indicating that the change in polarization measured during the energy conversion under cyclic stress loading conditions is intrinsic to the stress-free crystal. These extremely small values, with the material composition close to the MPB, give evidence of the very low anisotropy at this particular inter-ferroelectric transition. This phenomenon has been also observed by other researches.[13,16]

Figure 12.7 shows the results for the power density and energy density as well as the energy conversion factor per cycle as a function of the electric resistive loads (log scale) and drive frequencies for both phase transforming piezocrystal and the linear F_R single phase regions. All data points in Figure 12.7 are also shown in Table 12.1 and Table 12.2. Huge power and energy density per cycle were obtained when compared with the linear F_R single phase region. At high electric resistive loads (≥500 kΩ) the power and energy density per cycle for the phase transforming piezocrystal region is three order of magnitude higher than those corresponding to cyclic loading in the linear F_R single phase region. The efficiency of the process, or the energy conversion factor, for the phase transforming region results six time higher than the corresponding linear F_R single phase region. In both studied regions the energy and power density per cycle, as well as the energy conversion factor appear not to be frequency dependent, at least at the investigated drive frequencies.

One of the question based on of application viability for this energy conversion process is the fatigue of the piezoelectric single crystal material during the cycling process due to the continuous change in strain at the phase transition. The lack of fatigue on the PIN-PMN-PT single crystal through the F_R-F_O-F_R phase transition was demonstrated by Finkel et al., under less than 0.1 MVm^{-1} applied electric field along [011] to a mechanically clamped single crystal at 14 MPa.[8] They clamp the single crystal close to phase transition and induced it by a small applied sinusoidal electric field. The single crystal material undergoes one million cycle without noticeable degradation. They attributed this unexpected lack of fatigue to the crystallographic direction along which the field was applied where the strain can be elastically accommodated only along (011) direction.

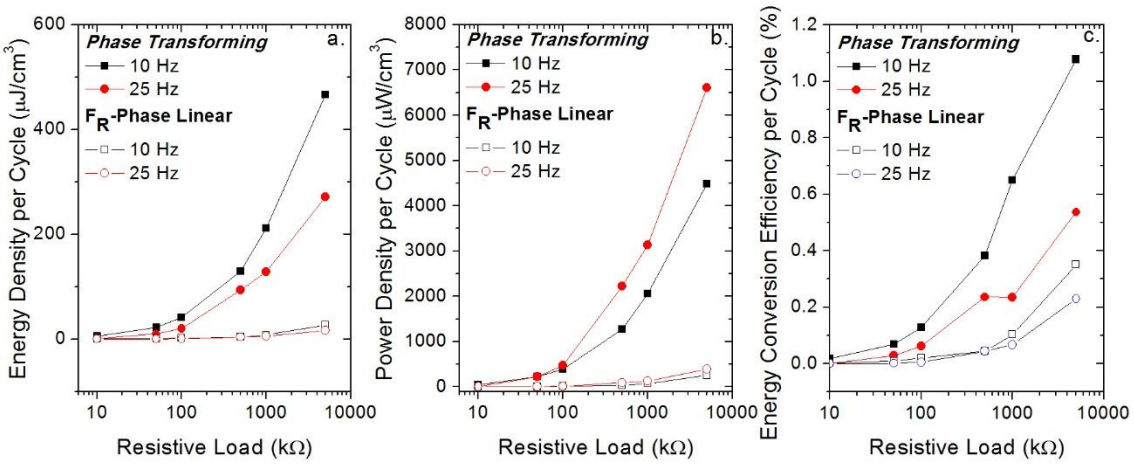

Figure 12.7. Comparison of Energy conversion in Phase-Change and FR-Phase Linear Regions. a. Energy density per cycle, b. power density per cycle and c. energy conversion efficiency per cycle as a function of electric resistive loads.

This new energy conversion method of phase transforming piezocrystal process brings new key material property configuration parameters, different from the cantilever resonance mode configurations. As previously discussed, the key piezoelectric material parameters for the cantilever resonance mode energy harvesters were d_{ij} and k_{ij}. However, for the phase transforming piezocrystal energy conversion method the magnitude of the phase transition and the easy way to trigger and tune it are the key parameters.

Table 12.3 shows a comparison of the power density for both types of configurations. For the phase transforming piezocrystal energy conversion process the power density increases while the energy density decreases, proportionally as a function of frequency. In average, similar power density was found for the phase transforming piezocrystal energy harvester compared to the resonance mode energy harvesters. However, the energy density per cycle results in three order of magnitude compared with the resonance modes. These results bring applications based on very low drive frequencies under high mass loads, enough to cross the phase transition.

Table 12. 3 Comparison of power density and energy density per cycle of the typical cantilever resonance mode and the phase transforming piezocrystal energy harvesters as function of frequency.

Reference	Active Material	Resistive Load (kΩ)	Frequency, Hz	Power Density, $\mu W/mm^3$	Energy density per cycle $(\mu J/mm^3)$
Phase Transforming Piezocrystal Energy Harvesters					
Wen et al. 2012[19]	PIN-PMN-PT	10000	1	0.750	0.750
This study	PIN-PMN-PT	5000	10	4.486	0.467
This study	PIN-PMN-PT	5000	25	6.608	0.271
Cantilever Resonance Mode Energy Harvesters					
Roundy et al. 2004[22]	PZT	170	120	0.975	0.008
Morimoto et al. 2010[23]	PZT, d31	50	126	20.5	0.163
XU et al. 2011[24]	PZT	405	329	0.35	0.001
Park et al. 2010[25]	PZT, d33	2200	528	1.05	0.002
Fang et al. 2006[26]	PZT, d31	21.4	608	2.77	0.005

The values of resonance frequency and power density for the cantilever resonance mode energy harvesters were obtained from Kim et al. 2012.[1]

12.4 Summary

A phase transforming piezocrystal energy conversion device was designed, built and tested under cycling stress loading and as functions of electrical resistive loads and drive frequencies. The reversible stress-induced transition in PIN-PMN-PT relaxor ferroelectric single crystal produces high power and energy densities per cycle as a consequence of easy polarization rotation between ferroelectric phases. The efficiency, power and energy density were six times greater than those in the linear F_R single phase region. Phase-change piezocrystal energy harvesters have much higher power and energy densities compared with conventional materials and can be utilized in applications requiring operation under high load at low frequency.

12.5 References

1. Kim, S.-G., Priya, S. & Kanno, I. Piezoelectric MEMS for energy harvesting. *MRS Bull.* **37,** 1039–1050 (2012).

2. Kim, H., Priya, S., Stephanou, H. & Uchino, K. Consideration of impedance matching techniques for efficient piezoelectric energy harvesting. *IEEE Trans. Ultrason. Ferroelectr. Freq. Control* **54,** 1851–9 (2007).

3. Kuwata, J., Uchino, K. & Nomura, S. Phase transitions in the Pb(Zn1/3Nb2/3)O3-PbTiO3 System. *Ferroelectrics* **37,** 579–82 (1981).

4. Kuwata, J., Uchino, K. & Nomura, S. Dielectric and Piezoelectric Properties of 0.91Pb(Zn1/3Nb2/3)O3-0.09PbTiO9 Single Crystals. *Jpn. J. Appl. Phys.* **21,** 1298–1302 (1982).

5. Park, S.-E. & Shrout, T. R. Ultrahigh strain and piezoelectric behavior in relaxor based ferroelectric single crystals. *J. Appl. Phys.* **82,** 1804 (1997).

6. Hajati, A. & Kim, S.-G. Ultra-wide bandwidth piezoelectric energy harvesting. *Appl. Phys. Lett.* **99,** 083105 (2011).

7. Marinkovic, B. & Koser, H. Smart Sand—a wide bandwidth vibration energy harvesting platform. *Appl. Phys. Lett.* **94,** 103505 (2009).

8. Finkel, P., Amin, A., Lofland, S., Yao, J. & Viehland, D. Phase switching at low field and large sustainable strain output in domain engineered ferroic crystals. *Phys. Status Solidi* **209,** 2108–2113 (2012).

9. Dong, W. D., Finkel, P., Amin, A. & Lynch, C. S. Stress dependence of thermally driven pyroelectric charge release during FER-FEO phase transformations in [011] cut relaxor ferroelectric crystals. *Appl. Phys. Lett.* **100,** 262909 (2012).

10. Amin, A., McLaughlin, E., Robinson, H. & Ewart, L. Mechanical and thermal transitions in morphotropic PZN-pT and PMN-PT single crystals and their implication for sound projectors. *IEEE Trans. Ultrason. Ferroelectr. Freq. Control* **54,** 1090–5 (2007).

11. Matthew, D., Damjanovic, D., Hayem, D. & Setter, N. Domain engineering of the transverse piezoelectric coefficient in perovskite ferroelectrics. *J. Appl. Phys.* **98,** 014102 (2005).

12. Heitmann, A. A. & Rossetti, G. A. Polar Anisotropy and Inter-Ferroelectric Transitions in Barium Titanate and its Solid Solutions. *Integr. Ferroelectr.* **126,** 155–165 (2011).

13. Heitmann, A. A. & Rossetti, G. A. Thermodynamics of polar anisotropy in morphotropic ferroelectric solid solutions. *Philos. Mag.* **90,** 71–87 (2010).

14. Ishibashi, Y. Theory of the Morphotropic Phase Boundary. *Ferroelectrics* **267,** 191–199 (2002).

15. Khachaturyan, a. G. Ferroelectric solid solutions with morphotropic boundary: Rotational instability of polarization, metastable coexistence of phases and nanodomain adaptive states. *Philos. Mag.* **90,** 37–60 (2010).

16. Rossetti, G. A., Khachaturyan, A. G., Akcay, G. & Ni, Y. Ferroelectric solid solutions with morphotropic boundaries: Vanishing polarization anisotropy, adaptive, polar glass, and two-phase states. *J. Appl. Phys.* **103,** 114113 (2008).

17. Rossetti, G. A. & Navrotsky, A. Calorimetric Investigation of Tricritical Behavior in Tetragonal Pb (Zr x Ti 1 ⁄ x) O 3. *J. Solid State Chem.* **144,** 188–194 (1999).

18. Fu, H. & Cohen, R. Polarization rotation mechanism for ultrahigh electromechanical response in single-crystal piezoelectrics. *Nature* **403,** 281–3 (2000).

19. Dong, W. D., Finkel, P., Amin, A. & Lynch, C. S. Giant electro-mechanical energy conversion in [011] cut ferroelectric single crystals. *Appl. Phys. Lett.* **100,** 042903 (2012).

20. McLaughlin, E. A., Liu, T. & Lynch, C. S. Relaxor ferroelectric PMN-32%PT crystals under stress and electric field loading: I-32 mode measurements. *Acta Mater.* **52,** 3849–3857 (2004).

21. Finkel, P., Robinson, H., Stace, J. & Amin, A. Study of phase transitions in ternary lead indium niobate-lead magnesium niobate-lead titanate relaxor ferroelectric morphotropic single crystals. *Appl. Phys. Lett.* **97,** 122903 (2010).

22. S. Roundy, Wright, P. K. & Rabaey, J. M. *Energy Scavenging for Wireless Sensor Networks: With Special Focus on Vibrations*. (Kluwer, 2004).

23. Morimoto, K., Kanno, I., Wasa, K. & Kotera, H. High-efficiency piezoelectric energy harvesters of c-axis-oriented epitaxial PZT films transferred onto stainless steel cantilevers. *Sensors Actuators A Phys.* **163,** 428–432 (2010).

24. Xu, R. *et al.* No Title. in *Proc. 16th Int. Conf. Solid-State Sensors, Actuators Microsystems* 679 – 682 (2011).

25. Park, J. C., Park, J. Y. & Lee, Y. Modeling and Characterization of Piezoelectric d 33 -Mode MEMS Energy Harvester. *J. Microelectromechanical Syst.* **19,** 1215–1222 (2010).

26. Fang, H.-B. *et al.* Fabrication and performance of MEMS-based piezoelectric power generator for vibration energy harvesting. *Microelectronics J.* **37,** 1280–1284 (2006).

CHAPTER 13

CONCLUSIONS AND FUTURE WORK

13.1 Conclusions

i. The nature of all the phase transitions were found to be of first-order due to thermal hysteresis.

ii. The enthalpies of the inter-ferroelectric phase transitions in the relaxor ferroelectric crystals are quite small (~10 J/mol) when compared with the energies of the inter-ferroelectric transitions in normal ferroelectric $BaTiO_3$ and PZT. These findings are associated with an intrinsic characteristic of inter-ferroelectric transitions and with an easy polarization rotation between ferroelectric phases of different symmetry.

iii. The phase transition enthalpies fallows a decreasing trend from the normal ferroelectric $BaTiO_3$ and PZT to the relaxor PZN-PT and PMN-PT. However, remarkable similar small values were obtained from the change in polarization at inter-ferroelectric transition for all studied ferroelectric materials. This finding reveals an outstanding ability of relaxor materials to easily transform from one ferroelectric phase to another with extremely small or minimal thermal energy dissipation.

iv. The expectation of weak crystallographic anisotropy of polarization and an associated easy rotation of polarization for relaxor crystals in the transitions between phases near the morphotropic boundary was demonstrated.

v. A complete set of Landau coefficients for $BaTiO_3$ single crystal were determined from heat capacity measurements and simultaneous solutions to the Landau polynomial for different ferroelectric phases and at several phase transitions. As consequence, the vanishing of crystallographic anisotropy of polarization was confirmed.

vi. Linear dependence of the quartic Landau coefficient on the composition was demonstrated in PZT. As a result, tricritical points were determined at x = 0.30 and x = 0.55 PT concentrations.

vii. Anomalous deviation from the expected hard-mode behavior, found in relaxor ferroelectric materials away from the transition points and where polar nanoregions had been found, was associated with the relaxor behavior of the polarization.

viii. A method was developed to separate the reversible and root mean square (RMS) contributions to the polarization associated with the phase transition and relaxor behavior, respectively. The jumps at the phase transition from the determined reversible polarization and the onset of the RMS polarization agree well with pyroelectric and thermal expansion data, which validate the method.

ix. Thermal depoling events were observed in relaxor ferroelectric materials and were associated with switching depoling process during the polar to non-polar phase transition of particular oriented ferroelectric domains. It reveals the relaxor nature of the transition and competing thermodynamics of metastable states over a broad range of temperature extending to the Burns temperature.

x. The induced inter-ferroelectric phase transitions were also observed in relaxor ferroelectric materials as a consequence of poling conditions.

xi. It was found that the thermal conductivity, in all measured temperature range, of the relaxor ferroelectric materials is much lower ($\cong x2$) than the thermal conductivity of normal ferroelectrics.

xii. The 1/T dependence of the thermal conductivity in the PE-phase was observed in normal ferroelectric materials. However, this relationship was not fallowed by the relaxor ferroelectrics. Instead, the thermal conductivity increase in the high temperature PE-phase

which lies in the region where the heat capacity deviate from the Debye-like hard-mode behavior and where the thermal expansion deviate from linearity. It is may be due to the built-in disorder from lattice distortions, anharmonicity, the presence of polar nanoregions and the presence of the transverse acoustic branch.

xiii. A Figure of Merit (FOM) was generated to understand material-property-configuration relationship for a resonance mode cantilever energy harvesting device. The FOM it is able to separate the factors that contribute to the charge and voltage sensitivity of a resonance mode energy harvesting device. The FOM, demonstrates that the electromechanical piezoelectric property factor, the geometrical factor and the elastic property factor may be individually modified to enhance the power sensitivity.

xiv. A phase transforming piezocrystal energy harvesting device, which may be used for low and out of resonance frequencies and high electrical loads applications, was designed, built and tested under cycling stress loading conditions and as functions of electrical resistive loads and drive frequencies. The efficiency, power and energy density were six times greater than those in the linear F_R single phase region.

xv. The reversible stress-induced inter-ferroelectric phase transition (F_R-F_O) in PIN-PMN-PT relaxor ferroelectric single crystals produces high power and energy densities per cycle compared with resonance mode energy harvesting, as a consequence of an easy polarization rotation between low symmetry ferroelectric phases and insignificant energy dissipation of relaxor ferroelectric materials.

13.2 Future Works

i. **Short-circuit experiments:** effect of electrodes

To investigate the effect of electrodes in the poled and depoled state on the intrinsic properties of the ferroelectric single crystal materials and to compare it with the previously studied single crystals with open-circuit boundary conditions. Specifically, near the inter-ferroelectric phase transition.

ii. **Electrical loading cycling experiment:** degradation effects

To study the degradation in the piezoelectric properties of the ferroelectric single crystal materials by the application of mechanical or electrical cycling loading conditions. Polarization switching in ferroelectric materials may exhibits "fatigue" or irreversible (extrinsic) domain wall motion. The domain wall motion could be affected by stress relaxation, "poling" of charged defect pairs and space-charge accumulation at or near the electrode-ferroelectric interface (nucleation of domains at the electrode-sample interface). The data may be analyzed with the Rayleigh theory applied to ferroelectric materials to identify the intrinsic and extrinsic to the dielectric property.

iii. **Transport properties measurements of short-circuit boundary conditions:** heat diffusion

To study the thermal conductivity of the relaxor ferroelectric single crystal material from an open- and a short-circuit experiments in both the poled and depoled states. To investigate the thermal heat losses associated with degradation process during loading cycles conditions near inter-ferroelectric phase transition.

APPENDIX

Appendix A

Table A.1. Heat Capacity of depoled $BaTiO_3$ single crystal.

F_O-F_R		F_T-F_O		PE-F_T		PE - phase	
T (K)	C_P (J/mol-K)	T (K)	C_P (J/mol-K)	T (K)	C_P (J/mol-K)	T (K)	C_P (J/mol-K)
120	58.4	211	90.5	311	106.3	451	115.0
131	62.6	221	92.5	321	107.7	461	115.2
141	67.6	231	95.2	331	109.1	471	115.6
151	72.1	241	97.1	341	109.8	481	115.9
161	75.8	251	99.2	351	110.7	491	116.3
171	79.8	261	101.2	361	111.8	501	116.5
181	82.5	271	102.9	371	112.8	511	116.6
191	86.2	281	104.9	381	114.4	531	117.5
193	86.9	283	105.4	385	114.9	541	117.7
195	87.5	285	105.6	389	116.1	551	118.0
197	88.1	287	106.0	393	116.8	561	118.3
198	88.7	288	106.1	397	118.1	581	118.8
199	100.0	289	130.0	401	119.9	601	119.3
200	109.0	290	143.4	403	121.3	621	120.0
201	98.6	291	122.5	404	122.3	641	120.6
202	93.8	292	113.3	405	154.5	661	120.6
203	91.4	293	109.2	406	177.6	681	121.2
204	90.4	294	107.3	407	159.9	701	121.5
206	90.0	295	106.3	408	145.6	721	122.2
208	90.2	296	105.8	409	135.9	741	122.8
210	90.4	298	105.4	410	129.3	761	122.8
-	-	302	105.6	411	124.7	781	123.7
-	-	306	106.0	412	121.4	801	124.0
-	-	310	106.3	414	117.9	820	124.8
-	-	-	-	417	115.7	840	125.2
-	-	-	-	421	114.3	860	126.0
-	-	-	-	425	114.2	880	126.5
-	-	-	-	429	114.2	900	126.5
-	-	-	-	433	114.0	920	125.9
-	-	-	-	437	114.4	940	126.9
-	-	-	-	441	114.6	960	128.4
-	-	-	-	445	114.9	980	130.2
-	-	-	-	449	115.0	1000	130.5

Table A.2. Thermal expansion $\varepsilon_{ij} = \Delta L/L_0$ of depoled $BaTiO_3$ single crystal.

PE-F_T						PE - phase			
T (K)	$e_{33}\left(\frac{m}{m}\right)$ X10^{-3}	$e_{11}\left(\frac{m}{m}\right)$ X10^{-3}	T (K)	$e_{33}\left(\frac{m}{m}\right)$ X10^{-3}	$e_{11}\left(\frac{m}{m}\right)$ X10^{-3}	T (K)	$\frac{\Delta L}{L}\left(\frac{m}{m}\right)$ X10^{-3}	T (K)	$\frac{\Delta L}{L}\left(\frac{m}{m}\right)$ X10^{-3}
292	5.61	-3.37	349	5.16	-2.86	404	0.15	470	0.86
295	5.57	-3.36	352	5.09	-2.81	406	0.19	480	0.98
298	5.57	-3.36	355	5.02	-2.76	408	0.21	490	1.10
301	5.56	-3.36	358	4.94	-2.71	410	0.23	500	1.22
304	5.56	-3.35	361	4.86	-2.65	412	0.25	520	1.47
307	5.55	-3.34	364	4.78	-2.59	416	0.30	540	1.72
310	5.55	-3.32	367	4.69	-2.53	420	0.33	560	1.97
313	5.55	-3.30	370	4.59	-2.44	424	0.37	580	2.22
316	5.55	-3.27	373	4.48	-2.37	428	0.41	600	2.47
319	5.55	-3.23	376	4.38	-2.28	432	0.45	620	2.72
322	5.54	-3.20	379	4.26	-2.20	436	0.49	640	2.98
325	5.53	-3.16	382	4.14	-2.11	440	0.53	660	3.24
328	5.50	-3.13	385	4.00	-2.02	444	0.57	680	3.50
331	5.47	-3.10	388	3.85	-1.91	448	0.62	700	3.75
334	5.43	-3.07	391	3.69	-1.80	452	0.66	720	4.03
337	5.38	-3.03	394	3.50	-1.68	456	0.70	740	4.29
340	5.33	-2.99	397	3.27	-1.54	460	0.75	760	4.55
343	5.27	-2.94	400	2.98	-1.38	464	0.80	780	4.81
346	5.22	-2.91	402	1.34	-1.25	468	0.84	800	5.07

`

Table A.3. Thermal diffusivity (D) and thermal conductivity (k) of depoled $BaTiO_3$ single crystal.

[001] oriented					[100] oriented				
T (K)	D (mm^2/s)	Standard Deviation	k (W/m-K)	Standard Deviation	T (K)	D (mm^2/s)	Standard Deviation	k (W/m-K)	Standard Deviation
298	1.882	0.013	5.00	0.085	298	1.719	0.028	4.70	0.124
323	1.706	0.011	4.64	0.076	313	1.638	0.014	4.54	0.084
348	1.544	0.009	4.28	0.068	333	1.509	0.015	4.26	0.085
373	1.391	0.006	3.92	0.056	353	1.410	0.012	4.03	0.075
383	1.316	0.008	3.73	0.060	373	1.285	0.012	3.71	0.072
393	1.240	0.005	3.53	0.050	378	1.275	0.005	3.69	0.051
398	1.154	0.004	3.30	0.044	383	1.240	0.004	3.60	0.048
401	1.014	0.003	2.90	0.038	388	1.205	0.007	3.50	0.055
403	1.096	0.005	3.15	0.046	393	1.169	0.008	3.41	0.058
405	1.120	0.005	3.22	0.047	398	1.122	0.007	3.28	0.053
408	1.121	0.009	3.23	0.058	403	0.968	0.006	2.83	0.046
413	1.118	0.009	3.22	0.058	408	1.059	0.005	3.10	0.046
423	1.107	0.005	3.20	0.047	413	1.057	0.006	3.10	0.049
448	1.096	0.003	3.20	0.041	433	1.040	0.005	3.08	0.046
473	1.079	0.003	3.17	0.041	453	1.029	0.003	3.06	0.040
498	1.065	0.004	3.15	0.043	473	1.015	0.005	3.04	0.045
523	1.052	0.003	3.13	0.040	493	1.003	0.006	3.02	0.048
548	1.038	0.004	3.11	0.043	513	1.000	0.000	3.02	0.030
573	1.034	0.004	3.11	0.043	-	-	-	-	-

Table A.4. Heat Capacity of depoled PZN-6%PT single crystal.

F_R - phase		F_R-F_T		F_T-P_E		PE - phase	
T (K)	C_P (J/mol-K)	T (K)	C_P (J/mol-K)	T (K)	C_P (J/mol-K)	T (K)	C_P (J/mol-K)
120	69.87	361	117.67	421	120.25	491	120.98
130	75.15	363	117.80	426	120.44	501	120.66
140	79.33	365	117.92	431	121.02	521	119.79
150	82.55	367	117.96	432	121.13	541	118.80
160	86.00	369	118.04	434	121.40	561	118.26
170	88.58	371	118.31	436	122.40	581	117.58
180	90.87	373	118.57	438	123.10	601	117.09
190	93.21	375	118.56	439	123.41	621	117.14
200	95.78	377	118.73	440	127.12	641	116.74
210	97.72	379	118.55	441	129.28	661	116.44
220	99.51	381	118.60	442	126.89	681	116.24
230	101.47	383	118.32	443	125.61	701	116.31
240	103.15	385	118.17	444	124.36	721	116.17
250	104.27	387	118.27	445	123.73	741	116.08
260	106.23	389	118.32	447	122.63	761	116.02
270	107.16	391	118.42	449	122.19	781	116.46
280	108.62	393	118.37	451	121.92	801	116.45
290	110.59	395	118.49	453	121.85	821	116.30
300	111.43	397	118.62	455	121.81	841	116.91
310	112.84	399	118.72	457	121.81	861	117.35
320	114.17	401	118.72	459	121.81	881	116.33
330	115.30	406	119.09	461	121.69	901	116.97
340	116.03	411	119.55	271	107.16	911	117.29
351	116.83	416	119.91	481	121.27		

Table A.5. Thermal Expansion $\varepsilon_{ij} = \Delta L/L_0$ of depoled PZN-6%PT single crystal.

F_R-phase		F_T-F_R		PE-F_T		PE -phase	
T (K)	$\frac{\Delta L}{L}\left(\frac{m}{m}\right) x10^{-3}$	T (K)	$\frac{\Delta L}{L}\left(\frac{m}{m}\right) x10^{-3}$	T (K)	$\frac{\Delta L}{L}\left(\frac{m}{m}\right) x10^{-3}$	T (K)	$\frac{\Delta L}{L}\left(\frac{m}{m}\right) x10^{-3}$
287	0.766	371	0.851	406	0.036	470	1.510
290	0.762	374	0.817	409	0.100	480	1.540
293	0.751	377	0.771	410	0.135	490	1.590
296	0.769	380	0.702	411	0.156	500	1.640
302	0.768	381	0.689	412	0.195	510	1.680
308	0.782	382	0.659	413	0.224	520	1.740
314	0.806	383	0.612	414	0.271	530	1.790
317	0.834	384	0.567	415	0.454	540	1.860
320	0.864	385	0.524	416	0.702	550	1.940
323	0.891	386	0.407	417	0.862	560	2.010
326	0.907	387	0.210	418	1.230	570	2.090
329	0.932	388	0.007	419	1.340	580	2.160
332	0.953	389	-0.114	420	1.350	590	2.240
338	0.963	390	-0.159	421	1.350	600	2.320
341	0.966	391	-0.174	422	1.350	610	2.410
347	0.961	392	-0.180	425	1.350	620	2.500
350	0.960	393	-0.175	428	1.370	630	2.590
353	0.954	394	-0.167	431	1.370	640	2.690
356	0.945	395	-0.154	437	1.390	650	2.800
359	0.933	396	-0.146	443	1.410	660	2.910
362	0.921	397	-0.135	449	1.430	680	3.130
365	0.902	400	-0.085	455	1.450	700	3.370
368	0.875	403	-0.035	460	1.460	727	3.700

Table A.6. Thermal diffusivity (D) and thermal conductivity (k) of depoled PZN-6%PT single crystal.

T (K)	D (mm^2/s)	Standard Deviation	k (W/m-K)	Standard Deviation
298	0.409	0.024	1.087	0.075
323	0.408	0.006	1.113	0.028
348	0.411	0.004	1.144	0.023
373	0.414	0.004	1.17	0.023
378	0.415	0.008	1.175	0.034
383	0.415	0.003	1.171	0.020
389	0.415	0.003	1.174	0.020
391	0.417	0.003	1.18	0.020
393	0.426	0.004	1.207	0.023
395	0.426	0.005	1.208	0.026
397	0.425	0.005	1.207	0.026
399	0.426	0.003	1.208	0.021
401	0.425	0.002	1.207	0.018
403	0.425	0.004	1.208	0.023
408	0.429	0.001	1.223	0.015
418	0.427	0.004	1.221	0.024
423	0.424	0.002	1.215	0.018
425	0.423	0.003	1.212	0.021
427	0.422	0.003	1.212	0.021
429	0.422	0.002	1.215	0.018
431	0.421	0.003	1.212	0.021
433	0.424	0.003	1.223	0.021
435	0.424	0.002	1.233	0.018
437	0.424	0.002	1.242	0.019
439	0.424	0.003	1.255	0.022
441	0.423	0.003	1.293	0.022
443	0.424	0.003	1.263	0.022
448	0.426	0.002	1.24	0.018
473	0.434	0.002	1.254	0.019
498	0.441	0.002	1.267	0.019
523	0.452	0.003	1.288	0.022
548	0.463	0.002	1.304	0.019
573	0.469	0.003	1.311	0.022

Table A.7. Heat Capacity C_P of depoled PMN-28%PT single crystal.

F_R - phase		F_T-F_R		PE-F_T		PE - phase	
T (K)	C_P (J/mol-K)	T (K)	C_P (J/mol-K)	T (K)	C_P (J/mol-K)	T (K)	C_P (J/mol-K)
120	64.8	350.4	112.7	382	116.1	435	119.1
140	73.1	352.4	112.9	384	116.3	445	119.1
160	79.1	354.4	113.2	386	116.5	455	118.8
180	84.0	356.4	113.4	388	116.7	465	118.4
200	88.6	358.4	113.6	390	117.0	475	118.0
210	90.5	360.4	113.8	392	117.2	480	117.8
220	92.3	362.4	114.1	394	117.5	485	117.5
230	94.2	364.4	114.3	396	117.8	490	117.2
240	95.7	366.4	114.5	398	118.1	495	117.0
250	98.6	368.4	114.7	400	118.5	500	116.8
260	100.4	370.4	114.9	402	118.8	520	116.4
270	101.7	372.4	115.1	404	118.8	540	116.1
280	103.7	374.4	115.3	406	118.8	560	115.8
290	105.2	376.4	115.5	408	118.8	580	115.8
300	106.9	378.4	115.7	410	118.8	600	115.7
310	108.2	380.4	115.9	412	118.8	620	115.9
320	109.3	-	-	414	118.9	640	115.9
330	110.5	-	-	416	118.9	660	116.3
340	111.7	-	-	418	119.0	680	116.4
345	112.2	-	-	420	119.0	700	116.7
-	-	-	-	422	119.0	720	117.1
-	-	-	-	424	119.0	740	116.8
-	-	-	-	426	119.1	760	118.3
-	-	-	-	428	119.1	780	117.7
-	-	-	-	430	119.1	800	117.2
-	-	-	-			810	117.4

Table A.8. Thermal expansion $\varepsilon_{ij} = \Delta L/L_0$ of depoled PMN-28%PT single crystal.

F_R-phase		FT-FR		PE-F_T		PE -phase	
T (K)	$\frac{\Delta L}{L_0}\left(\frac{m}{m}\right)x10^{-3}$	T (K)	$\frac{\Delta L}{L_0}\left(\frac{m}{m}\right)x10^{-3}$	T (K)	$\frac{\Delta L}{L_0}\left(\frac{m}{m}\right)x10^{-3}$	T (K)	$\frac{\Delta L}{L_0}\left(\frac{m}{m}\right)x10^{-3}$
292	1.059	350	1.161	382	1.133	435	1.151
296	1.056	352	1.164	384	1.131	445	1.178
300	1.051	354	1.160	386	1.125	455	1.222
302	1.049	356	1.156	388	1.123	465	1.266
304	1.049	358	1.155	390	1.128	475	1.322
306	1.056	360	1.155	392	1.131	480	1.353
308	1.062	362	1.156	394	1.129	485	1.386
310	1.069	364	1.156	396	1.129	490	1.418
312	1.078	366	1.151	398	1.131	495	1.454
311	1.076	368	1.151	400	1.128	500	1.491
314	1.089	370	1.150	402	1.124	520	1.644
313	1.080	372	1.147	404	1.126	540	1.822
316	1.092	374	1.147	406	1.127	560	2.015
315	1.089	376	1.145	408	1.129	580	2.204
318	1.105	378	1.143	410	1.129	600	2.407
322	1.122	380	1.136	412	1.130	620	2.608
324	1.127	-	-	414	1.127	640	2.812
326	1.141	-	-	416	1.127	660	3.027
328	1.145	-	-	418	1.130	680	3.246
330	1.156	-	-	420	1.127	700	3.459
332	1.157	-	-	422	1.134	720	3.670
334	1.156	-	-	424	1.131	740	3.889
336	1.160	-	-	426	1.135	760	4.119
340	1.166	-	-	428	1.140	780	4.348
342	1.166	-	-	430	1.139	800	4.623
344	1.159	--	-	-	-	802	4.657

Table A.9. Thermal diffusivity (D) and thermal conductivity (k) of depoled PMN-28%PT single crystal.

T (K)	D (mm^2/s)	Standard Deviation	k (W/m-K)	Standard Deviation
298	0.485	0.021	1.247	0.067
323	0.463	0.012	1.226	0.044
328	0.444	0.015	1.182	0.052
333	0.451	0.013	1.207	0.047
338	0.437	0.02	1.174	0.066
353	0.438	0.011	1.195	0.042
355	0.431	0.008	1.179	0.034
361	0.437	0.012	1.202	0.045
365	0.45	0.009	1.242	0.037
367	0.436	0.008	1.204	0.034
369	0.415	0.013	1.15	0.048
383	0.431	0.01	1.21	0.04
389	0.412	0.01	1.163	0.04
391	0.418	0.004	1.183	0.023
395	0.429	0.014	1.219	0.052
397	0.415	0.006	1.181	0.029
403	0.441	0.005	1.265	0.027
407	0.428	0.009	1.228	0.038
413	0.441	0.006	1.266	0.03
417	0.437	0.01	1.253	0.041
421	0.446	0.008	1.282	0.036
433	0.439	0.004	1.263	0.024
438	0.444	0.009	1.278	0.039
448	0.446	0.004	1.281	0.024
458	0.466	0.002	1.335	0.019
463	0.458	0.003	1.31	0.022
473	0.462	0.004	1.316	0.025
503	0.471	0.004	1.326	0.025
513	0.478	0.007	1.345	0.033
533	0.477	0.006	1.335	0.03
543	0.486	0.008	1.357	0.036
553	0.476	0.008	1.328	0.036
563	0.488	0.007	1.361	0.034
573	0.485	0.008	1.352	0.036